University of Nevada, Reno

Seismic Response Control Of Structures Using Semi-Active and Passive Variable Stiffness Devices

A dissertation submitted in partial fulfillment of the requirements for the degree of Doctor of Philosophy in Civil and Environmental Engineering

by

Mohamed M. A. Salem

Dr. Gökhan Pekcan /Dissertation advisor
Dr. Ahmad Itani /Co advisor

May , 2014

THE GRADUATE SCHOOL

University of Nevada, Reno
Statewide · Worldwide

We recommend that the dissertation
prepared under our supervision by

MOHAMED M. A. SALEM

entitled

**Seismic Response Control Of Structures Using Semi-Active
And Passive Variable Stiffness Devices**

be accepted in partial fulfillment of the
requirements for the degree of

DOCTOR OF PHILOSOPHY

Gokhan Pekcan, Ph.D., Advisor

Ahmad Itani, Ph.D., Committee Member

Ian G. Buckle, Ph.D., Committee Member

M. Sami Fadali, Ph.D., Committee Member

John Anderson, Ph.D., Graduate School Representative

Marsha H. Read, Ph. D., Dean, Graduate School

May, 2014

Abstract

Controllable devices such as Magneto-Rheological Fluid Dampers, Electro-Rheological Dampers, and controllable friction devices have been studied extensively with limited implementation in real structures. Such devices have shown great potential in reducing seismic demands, either as smart base isolation systems, or as smart devices for multistory structures. Although variable stiffness devices can be used for seismic control of structures, the vast majority of research effort has been given to the control of damping.

The primary focus of this dissertation is to evaluate the seismic control of structures using semi-active and passive variable stiffness characteristics. Smart base isolation systems employing variable stiffness devices have been studied, and two semi-active control strategies are proposed. The control algorithms were designed to reduce the superstructure and base accelerations of seismically isolated structures subject to near-fault and far-field ground motions. Computational simulations of the proposed control algorithms on the benchmark structure have shown that excessive base displacements associated with the near-fault ground motions may be better mitigated with the use of variable stiffness devices. However, the device properties must be controllable to produce a wide range of stiffness changes for an effective control of the base displacements. The potential of controllable stiffness devices in limiting the base displacement due to near-fault excitation without compromising the performance of conventionally isolated structures, is illustrated.

The application of passive variable stiffness devices for seismic response mitigation of

multistory structures is also investigated. A stiffening bracing system (SBS) is proposed to replace the conventional bracing systems of braced frames. An optimization process for the SBS parameters has been developed. The main objective of the design process is to maintain a uniform inter-story drift angle over the building's height, which in turn would evenly distribute the seismic demand over the building. This behavior is particularly essential so that any possible damage is not concentrated in a single story. Furthermore, the proposed design ensures that additional damping devices distributed over the building's height work efficiently with their maximum design capacity, leading to a cost efficient design. An integrated and comprehensive design procedure that can be readily adopted by the current seismic design codes is proposed. An equivalent lateral force distribution is developed that shows a good agreement with the response history analyses in terms of seismic performance and demand prediction. This lateral force pattern explicitly accounts for the higher mode effect, the dynamic characteristics of the structure, the supplemental damping, and the site specific seismic hazard. Therefore, the proposed design procedure is considered as a standalone method for the design of SBS equipped buildings.

Acknowledgments

I would like to take the chance to show my great appreciation to my committee chair, Dr. Gökhan Pekcan. This work could not have been done without his support and guidance. Thank you for teaching me special tools that were so helpful in completing my dissertation. I'm also thankful to Dr. Ian Buckle, Dr. M. Sami Fadali, and Dr. John Anderson for their participation as committee members. Special thanks to Dr. Ahmad Itani for his guidance and support throughout this work. My beloved wife, thank you for your love, patience, unlimited support, and understanding during happy and hard times that we've gone through. To my family and siblings, I'm grateful to your encouragement and kindness. Finally, I dedicate this dissertation to my parents, may Allah forgive them and grant them paradise. The tuition and stay for the duration of this study was funded by the Egyptian government, which is gratefully acknowledged.

Table of Contents

List of Tables

List of Figures

Chapter 1

Introduction

Seismic mitigation is not only essential for buildings and bridges to ensure life safety, but also to ensure functionality. Critical facilities should remain functional during and after severe seismic events. Seismic mitigation can be achieved by several different methods and applications. These include, but are not limited to, permitting parts of the structure to undergo inelastic deformation that allows for energy dissipation through hysteretic behavior of the material. Yielding structures are usually designed for a distinct performance level that should at least ensure life safety, but may suffer significant yielding and permanent deformations that could be costly to repair. In critical facilities, where immediate occupancy of the structure and the functionality of its sensitive contents are important, this may not be a desirable solution. As an alternative to the yielding structures, supplemental energy dissipation devices are used to provide a desired energy dissipation mechanism so that the damage to the main structural elements is minimized or eliminated (Soong and Spencer Jr., 2002; Constantinou et al., 1998). Another innovative seismic mitigation procedure is seismic isolation (Buckle and Mayes, 1990; Naeim and Kelly, 1999; Komodromos, 2000). These devices are of special interest for their ability to decouple the isolated structure from the ground shaking. This behavior is achieved through the relatively flexible bearings that are placed mostly between the superstructure and the foundation, so

that large amount of seismic energy is dissipated through the deformation and damping properties of the isolators. However, conventional isolation systems alone under the effect of near-fault ground motions may exhibit large displacements at the isolation level that can lead to structural instability. Despite the fact that supplemental energy dissipation systems placed in parallel to the seismic isolation systems may reduce the base displacement, the added damping may result in increased seismic demand on the superstructure (Kelly, 1999; Jangid and Kelly, 2001; Mazza and Vulcano, 2004; Providakis, 2008). To overcome this problem, smart base isolation systems have been introduced during the last few decades. With the capability of regulating the mechanical properties (stiffness and/or damping) of the controllable devices, the seismic isolation systems incorporating the so-called smart base isolation systems are more likely to overcome the unfavorable large base displacement under the effect of near-fault excitation, while retaining the merits of the conventional seismic isolation systems (Ramallo et al., 2002; Narasimhan and Nagarajaiah, 2006). There are several controllable devices that have been used and investigated for this purpose, such as the Magneto-Rheological Fluid (MRF) based devices (Carlson and Spencer Jr., 1996; Jolly et al., 1998; Yang et al., 2002), Magneto-Rheological Elastomer (MRE) devices (Davis, 1999; Jung et al., 2009; Usman et al., 2009; Li et al., 2013a,b; Yang et al., 2013; Eem et al., 2013; Behrooz et al., 2014a,b), and variable stiffness devices (Nagarajaiah et al., 2006; Usman et al., 2009). Although variable stiffness devices are available, the vast majority of research effort has been given to controllable damping devices (Johnson et al., 1998; Sadek and Mohraz, 1998; Symans et al., 2000; Jansen and Dyke, 2000; Bani-Hani and Sheban, 2006).

To avoid yielding of the structural elements (beams, columns), supplemental damping devices can be used within the structure itself as well. These devices provide mechanism to dissipate seismic energy through the relative velocity between the

floors that they are attached to, as in the case of velocity dependent devices (viscous dampers), or through the relative displacement as in the cases of displacement dependent devices such as Added Damping and Stiffness (ADAS) devices (Tsai et al., 1993; Hanson et al., 1992). However, for a better performance of structures equipped with such devices, uniform distribution of the inter-story drift, and hence the inter-story velocity, becomes an important factor. For this reason, structures with poorly distributed strength and stiffness may not gain the best benefits from the supplemental energy dissipation devices distributed in the building (Mohammadi et al., 2004). Therefore, structural design methods that would lead to a proper distribution of stiffness throughout the building's height to achieve uniform inter-story drift result in a better performance and more cost effective structures. This is especially true for structures equipped with supplemental energy dissipation devices.

1.1 Research Objectives

Conventional seismic isolation systems, as described in the previous section, may not be efficient for near-fault sites. With the technological advances in manufacturing smart controllable devices, it has been proved that smart base isolation systems are more likely to be implementable. Although variable stiffness devices and variable stiffness isolation bearings may be suitable for near-fault seismic isolation, the vast majority of studies have focused on controllable damping devices. Therefore, it is essential to investigate the efficiency of variable stiffness strategies for structures that may be subjected to far-field and near-fault motions. Near-fault motions may result in a permanent deformation in the isolation system. This can be mitigated by a semi-active control law that minimizes the residual displacement of smart base isolated systems. The second objective is to find a proper stiffness distribution method that would result in more favorable uniform inter-story drift for multistory structures. This

is particularly beneficial for avoiding concentrated damage in one floor (soft story mechanism). In addition, uniform inter-story drift throughout the building's height minimizes bending moments in the columns. While adhering to an acceptable level of inter-story drift also reduces the second order effect, such as the $P - \Delta$. Another important aspect of the uniform inter-story drift is that the structure gets the most benefits from passive energy dissipation devices (if any). In other words, structures equipped with energy dissipation devices together with proper stiffness distribution, allow all the energy dissipation devices to work with their highest efficiency. To achieve this objective, the variable stiffness behavior is again employed as a stiffening bracing system (SBS) for multistory structures. A design methodology for the stiffness distribution throughout the building's height is developed for a specified performance objective.

1.2   Dissertation Overview

This dissertation focuses on the seismic control of structures using semi-active and passive variable stiffness characteristics. Chapter 2 covers some of the relevant research studies on base isolation systems, smart base isolation systems, and semi-active devices, algorithms, and their implementation. In addition, the chapter covers studies related to the optimal stiffness and/or damping distribution, and the equivalent lateral force procedure.

In Chapter 3, a Magneto-Rheological Elastomer (MRE) base isolation device is considered. Two semi-active control algorithms are developed to control such a device in real-time. Both far-field and near-fault ground motions are applied to a benchmark structure equipped and controlled with the proposed system.

Chapter 4 proposes a new stiffening bracing system (SBS) for multistory structures. The proposed bracing system is a passive system where the measurement of the

structural response quantities is not required for the control decision. Instead, performance based design is developed and a procedure for the optimal stiffness distribution and controlling parameters is illustrated. Then the adequacy of the proposed SBS in seismic control of structures is demonstrated by considering benchmark structures with different heights.

Chapters 5 investigates the efficiency of the proposed system for seismic control of tall buildings. In Chapter 6, an integrated design procedure is proposed for the design of structures incorporating the SBS. The performance of structures designed according to the proposed procedure is investigated under a wide variety of earthquake excitations, and for a number of different height structures. The dissertation conclusion and suggested future work is given in Chapter 7.

1.3   Contribution of this Dissertation

The contribution to the state-of-the-art of this dissertation can be summarized in two parts. In the first part, two semi-active control algorithms have been developed for variable stiffness smart base isolation system, employing a variable stiffness device such as Magneto-Rheological Elastomer (MRE) isolator. The two control algorithms have shown significant improvement to the structural performance of seismically isolated structures compared to the conventional Lead Rubber Bearings (LRB) isolation system. However, the minimal acceleration control (MAC) algorithm has shown tendency to leave residual displacement in the isolation level. This shortcoming has been resolved with the proposed acceleration gain control (AGC), which resulted in desirable response under both far-field and near-fault ground motions. In addition, the AGC has shown that the unfavorable large base displacement associated with near-fault excitations can be significantly reduced without altering the superstructure response achieved by conventional base isolation strategies.

In the second part, a new stiffening bracing system (SBS) is proposed to replace the conventional bracing systems of multistory structures. The parameters of the proposed system are optimized through a simple optimization process that achieves the target performance of uniform inter-story drift distribution over the building's height. The performance of structures incorporating the proposed system is investigated through nonlinear time history analyses on benchmark structures with different heights under the effect of a wide variety of far-field and near-fault ground motions. Subsequently, an integrated design procedure has been developed for structures employing the proposed SBS. The design process has shown that the predicted equivalent lateral force distribution as well as the overall seismic performance of the structure are in good agreement to that obtained through the nonlinear time history analyses. This fact has been proven for a wide range of building heights under the effect of different levels of recorded seismic events, which implies that the proposed design methodology is robust and could be easily implemented in the seismic design provisions.

Chapter 2

Literature Review

2.1   Seismic Isolation Systems

Seismic isolation is one of the most effective mitigation strategies for structural and nonstructural components (Buckle and Mayes, 1990; Naeim and Kelly, 1999; Komodromos, 2000). In general, seismic isolation systems depend on shifting the fundamental period of the isolated structure away from the range of predominant excitation periods, which results in reduced acceleration demand on the isolated structure. As a result of the lengthened period, the base displacement of the isolated system becomes larger, and in some cases may lead to loss of stability of the isolation system. For this reason, many of the isolation systems provide some damping capacity to overcome the unacceptably large isolation deformations (Buckle, 1985). This damping capacity may be provided by the isolator directly or by means of supplemental damping devices. However, increasing the damping capacity of the isolated structures by means of supplementary dampers leads to an increase in the superstructure's accelerations and inter-story drifts (Kelly, 1999).

Researchers put in a great effort in the area of seismic isolation of relatively lightweight structural and nonstructural components. For instance, an experimental study carried out by Cui et al. (2010) to investigate the behavior of bidirectional spring unit

used in isolated floor systems. The test results showed that the spring behavior was stable and not sensitive to the motion velocity. An unconventional hysteretic behavior of the spring unit was observed. A physical model was then developed to simulate the experimentally observed behavior. Tsai (2012) developed an experimental and theoretical study on advanced isolation systems for protecting light-weight structures from earthquake damage. The systems considered consist of rolling and sliding type bearings. Two types of isolation systems were investigated; the ball pendulum and the directional-optimized friction pendulum. The ball pendulum system is composed of sliding ball enveloped by a natural rubber to improve the damping capacity of the isolator by the deformation of the coating rubber. The directional-optimized friction pendulum system consists of a concave trench on one plate and a spherically concave surface on the other plate of the bearing. The two concave surfaces can be of different radii, and an articulated slider is located in between them. Both systems were experimentally evaluated with light-weight equipment and they outperformed the fixed base unit.

Through the last few decades, investigation and implementation of the smart materials in the field of civil engineering and structures, particularly in seismic isolation strategies have been increasing. Among these materials is the Shape Memory Alloy (SMA), which is capable of recovering large strains through a heating process (Otsuka and Wayman, 1998). The most interesting superelastic property of this material improves the re-centering and damping capacity when used in buildings or other structural systems. Numerous studies have investigated seismic isolation systems utilizing SMAs. For instance, Jalali et al. (2010) developed a smart restorable base isolation system employing flat sliding bearing and superelastic shape memory alloy wires. The role of the SMA was to provide horizontal stiffness and restoring capability. Residual displacement of the proposed isolator can be restored by temperature

treatment. Dolce and Marnetto (2000) proposed a seismic isolation device composed of different groups of SMAs placed in a configuration such that energy dissipation as well as re-centering effects could be achieved. Their analysis showed that the structure equipped with the SMA bearing outperformed the one isolated with conventional rubber bearing. Wilde et al. (2000) proposed a laminated rubber bearing combined with SMA bars as a base isolation system for elevated bridges. The SMA bars plays a role in providing additional damping to the system, as well as displacement control.

2.2   Smart Base Isolation and Structural Control

In many circumstances, conventional base isolation systems, such as rubber bearings and friction pendulum, may not be the best alternative for seismic mitigation of structures and non-structural components (equipment). This issue arises in case of near-fault ground motions, which are dominated by long velocity pulses. For the case of long period structures, e.g. base isolated, the velocity pulse tends to develop large displacements (Hall et al., 1995). The pulse displacement is usually associated to the fault-normal direction, where high spectral acceleration components are observed in the long period range (Jangid and Kelly, 2001). This long period spectral acceleration components tend to resonate with conventionally isolated structures, leading to an excessive base displacement that may destabilize the structure. On the other hand, base isolation systems that utilize rubber-based technologies present limitations in case of light-weight equipment with relatively stiff and highly damped systems, and hence hinder of significant isolation.

Hybrid systems, where the conventional isolation system is combined with active controllable device (Kelly et al., 1987; Inaudi and Kelly, 1993; Nagarajaiah et al., 1993), may be used to overcome the shortcomings of the conventional base isolation systems. Barbat et al. (1995) designed a feedback control law to determine the

required active forces to be applied at the base level of seismically isolated structures. The goal of this hybrid system is to reduce the large base displacements encountered with the purely passive base isolated system. The drawback of this method is the slight increase in the superstructure's inter-story drifts and absolute accelerations. However, with advances in smart materials, smart base isolation systems employing stiffness and/or damping controllable devices are becoming more attractive for seismic mitigation purposes. Devices such as Magneto-Rheological Damper (MR Damper) and Magneto-Rheological Elastomers (MRE) have been recently investigated and implemented in seismic isolation systems. The mechanical properties of these devices can be regulated in real-time to achieve more favorable performance of the isolated structure.

The Electro-Rheological Fluid (ERF) that was discovered by Willis Winslow in 1947, has the ability of changing the viscosity from liquid to semi-solid state instantly upon the application of an electric field; this is due to its composition of non-conducting tiny particles of the size of a few microns suspended in an electrically insulating fluid (Winslow, 1947, 1949). Because of the controllable viscosity, the ERF is being used in manufacturing controllable damping devices and vibration isolators (Morishita and Ura, 1993).

Magneto-Rheological Fluid (MRF) is quite similar to the ERF but the viscosity of the fluid is changed by the application of a magnetic field, as it is composed of tiny magnetic particles suspended in a carrier fluid. Upon the application of the magnetic field, the magnetic particles align consistent with the magnetic field flux. This alignment results in restricting the fluid movement and hence increasing the apparent viscosity of the fluid. This material was discovered by Jacob Rabinow in 1948 (Jolly et al., 1998). The viscosity of the MRFs is found to be linearly proportional to the applied magnetic field intensity (Roszkowski et al., 2008). Due to

the high load carrying capacity of the MRFs, they are considered more versatile in construction of controllable dampers than the ERFs, especially for civil structures, where high load capacity is often favorable. The controllability of the MRFs and the Magneto-Rheological Elastomers (MREs) encouraged the researchers to develop smart controllable devices, particularly to help protecting structures and nonstructural components from seismic hazard.

In the area of seismic isolation, Makris (1997) presented a comprehensive analytical study to show that Electro-Rheological Dampers (ER-Damper) can be used with base isolated structures to provide rigidity to the flexible base isolated structures subjected to near-fault ground motions. This rigidity, which is introduced through friction-type forces, reduces the accelerations. The friction mechanism, however, leads to permanent displacements. Therefore, it was proposed to use controllable ER-Dampers to eliminate the residual displacement by removing the friction-type force at the end of the pulse excitation. Symans et al. (2000) analytically and experimentally investigated an adaptive seismic isolation system composed of sliding bearings and a controllable damper. The damping force of the controllable damper is adjusted in real-time based on a sliding mode semi-active control algorithm. It was shown that the adaptive base isolation system reduces the response of substructure and superstructure for a variety of earthquake characteristics. Madden et al. (2003) analytically studied a smart base isolation system with an adaptive fluid damper. It was found that the near-fault ground motions result in large displacements in base isolated structures if no supplementary damping is incorporated. However, with the use of an adaptive fluid damper, the damping capacity could be adjusted in real-time so that base displacement is controlled and the superstructure accelerations are minimized. Li and Ou (2006) carried out a design approach for semi-active control of MR-Dampers. They showed that the semi-active control forces generate most of the required control

forces of an active control. Furthermore, they concluded that passive systems can be designed to perform like actively controlled systems. Usman et al. (2009) proposed and evaluated a controllable stiffness Magneto-Rheological Elastomer (MRE) base isolation system. The numerical simulation carried out in their work showed that the controlled MREs outperformed conventional isolation systems.

Implementation of active and semi-active control strategies requires structural response measurements. The acceleration measurement is considered more reliable and inexpensive compared to the measurement of displacements or velocities. Dyke et al. (1994, 1996a) addressed the need of acceleration feedback control strategies to replace the full-state based control algorithms. The H_2/LQG control design strategy was used to develop different control algorithms with different performance objectives for a three-story active tendon experiment. In addition, the interaction between the actuator dynamics and the controlled structure was taken into account. The experimental results showed that controllers based on acceleration feedback are effective and robust. Further extension of the acceleration feedback control strategy was carried out experimentally on semi-actively controlled structure by Dyke et al. (1996b). The MR-Damper is implemented in a three-story model building for uniaxial shake table test. Clipped-optimal control was proposed by Dyke et al. (1996c) and employed for the control design. This approach depends on designing a linear optimal controller that determines the desired control force based on structural response and force measurements. The MR-Damper is then provided with the maximum or minimum voltage to provide the desired control force as closely as possible. The experimental study proved the efficacy of the clipped-optimal control strategy based on acceleration feedback in semi-actively controlled structures with an MR damper. The H_∞ control was employed by Jabbari et al. (1995) to control the floor accelerations as well as the inter-story drifts. In addition, the capability of using the absolute ac-

celeration measurements as the output feedback was addressed. This control relies on weighting desired floor accelerations or inter-story drifts that need to be minimized. A numerical simulation on six-story building showed the effectiveness of the presented control method. In addition, it was shown that the control algorithm can give almost the same effect as full state feedback control. Schmitendorf et al. (1994) showed the robustness of the control method and its practical implementation on full-scale structures. The study showed that the control can rely on a limited number of observations and yet recover the full state feedback control. Additionally, the actuator dynamics was incorporated into the control method to account for the time-delay that may be associated with the servo-hydraulic to develop the desired force, which for large scale actuators may lead to structural instability.

Yoshioka et al. (2002) conducted an experimental study to test the efficacy of smart base isolation system employing MR Damper. It is well known that conventional isolation systems are designed for a particular seismic hazard. Smart dampers can widen the range of the seismic hazard under which the isolated structure behaves favorably. In their study, linear behavior is considered to take place for both the structure and the isolation bearings. The time lag between the control command and the development of the damper force was taken into account by considering a first order differential equation between the controllable voltage and a parameter α, which is involved in calculating the MR damper force. The clipped optimal control proposed by Dyke et al. (1996c) employing the H_2/LQG strategy was used to regulate the damping force of the MR damper. The Kalman filter was used to estimate the state variables and hence the optimal damper force. A significant acceleration reduction for both structure and base was observed.

The MR damper was also implemented by Sahasrabudhe and Nagarajaiah (2005b) in an experimental study on sliding base isolated bridge. A Lyapunov control algo-

rithm was used to control the MR damper. It was shown that the MR damper can successfully reduce the bearing displacements of the isolated bridges subjected to near-fault ground motions, compared to the passive low and high damping cases, without increasing the forces at the isolation level.

Semi-active friction dampers have two phases during their motion; the sticking phase and the slipping phase. The sticking phase results when the relative velocity across the damper is zero or when the driving force is less than the frictional resistance of the damper. The slipping phase takes place when there is a relative velocity across the damper and the two plates are in motion relative to each other. The slipping phase however, is the one responsible for the energy dissipation, while the sticking phase is responsible for possible acceleration spikes. Therefore, for a better performance, it is desirable to maintain the semi-active damping device in the slipping phase as much as possible. To achieve this, He et al. (2003) introduced a linear boundary layer semi-active friction (LBLSAF) controller, which varies the controllable friction force linearly around the domain of zero relative velocity. The simulation results for five-story smart isolated building indicated that the proposed algorithm successfully eliminates the acceleration spikes and gives a smooth hysteresis. However, under the effect of near-fault ground motions, the semi-active friction device with the proposed control law fails to limit the base displacement and must be accompanied by a passive viscous damper. It should be noted that increasing the friction capacity of the semi-active friction damper may lead to unfavorable behavior during less severe earthquakes. Consistent with this observation, Yang and Agrawal (2002) showed that the conventional passive seismic isolation strategies alone are not suitable for near-fault earthquakes with long period, high velocity pulse. The study suggests different hybrid systems in which the passive bi-linear seismic isolation systems are combined with passive or semi-active energy dissipation devices, such as the semi-active friction

damper, to limit the deformation of the isolation system to an acceptable safe range.

Control theory can be used to design passive devices to replace the active or semi-active control devices used for seismic mitigation of structures and equipment. In most cases when the passive device is designed to mimic the behavior of the active or semi-active device, the performance of the passively controlled system may be similar to the actively or semi-actively controlled one.

Agrawal and Yang (1999) proposed a methodology for the design of passive viscous damper devices based on the constrained static output linear quadratic regulator (LQR), where the control force vector can be expressed by amplifying the output state vector $\mathbf{Y}(t)$ by the output feedback gain $\mathbf{G}_y$. Note that the output vector here includes the relative displacements and relative velocities at the damper locations. By defining the output feedback gain, the damper parameters can be evaluated by

$$\mathbf{G}_y = [\mathbf{K}_d \ , \ \mathbf{C}_d] \tag{2.1}$$

where $\mathbf{K}_d$ and $\mathbf{C}_d$ are diagonal matrices with the ith diagonal elements correspond to the desired equivalent stiffness and damping coefficient for the ith damper, respectively. However, the structure of the static output LQR gain is not the same as assumed for the gain matrix given by Equation 2.1. An iterative optimization process based on the constrained static LQR method takes place to converge to the desired output feedback gain matrix. This optimization process involves extensive and time consuming iterative solutions of highly nonlinear equations. Thus, another approach based on suboptimal LQR method is used. In this method, the full state feedback system is derived first, then the desired damper matrix $\mathbf{G}_y$ is designed to minimize the error between the full state feedback system and the corresponding system with the assumed properties.

Li et al. (2008) found that the active and semi-active control of cables in a cable-

stayed bridge result in a negative stiffness behavior for the relationship between the control force and the displacement. The characteristics and effect of this negative stiffness was quantified by means of three indices. Then pseudo-viscoelastic (P-VE) damper is suggested to replace the active device as it can provide similar force-deformation characteristics. The force developed in the equivalent P-VE damper can be expressed as

$$F_{ed} = -k_d v(x_d) - c_d \dot{v}(x_d) \tag{2.2}$$

in which k_d and c_d are the stiffness and damping coefficient of the equivalent P-VE damper, respectively, and $v(x_d)$ and $\dot{v}(x_d)$ are the relative displacement and velocity at point x_d where the damper is attached. In order to find the appropriate parameters (k_d and c_d) of the equivalent P-VE damper, the force developed by the damper must be equal to the control force $u(t)$ developed by employing the LQR method. The numerical results showed that the P-VE damper designed according to the proposed equivalent method, can achieve the behavior of the active and semi-active control devices when the system vibrates in one dominant mode.

2.3   Variable Stiffness Devices

Various types of semi-active stiffness and damping devices have been recently studied for seismic control of civil structures. The semi-active stiffness damper (Figure 2.1) consists of a hydraulic damper equipped with a controllable valve on the bypass tube connecting the two sides of the piston. The device is intended to be attached to bracing members, so that when the valve is closed the hydraulic damper provide stiffness to the system determined by the bulk modulus of the oil. When the valve is open, it provides damping to the system without increase in the stiffness. Yang and Agrawal (1999) presented two control laws for resetting the energy stored in the fluid
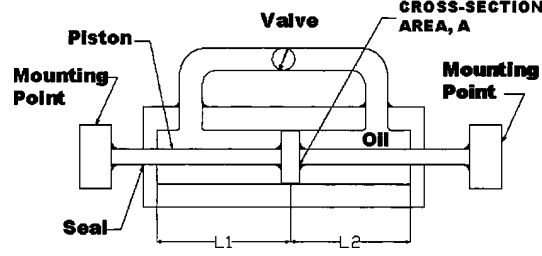
Figure 2.1: Schematic diagram of the semi-active stiffness damper (Agrawal et al., 2003)

by pulse opening and closing the valve. In addition, a switching control law for active variable stiffness (AVS) was derived. The two resetting control logics were based on the classical Lyapunov function consisting of the potential and kinetic energies of the system. To ensure that the system energy reduces with time, the derivative of the Lyapunov function must be a semi-definite real negative value. This led to the following control logic

$$x_{si}(t) = x_i(t) \begin{cases} \text{if } \dot{x}_i = 0 \\ \\ \text{or } \dot{x}_i x_i = 0 \end{cases} \tag{2.3}$$

where $x_{si}(t)$ is the piston position of the ith semi-active stiffness damper (SASD), and $x_i(t)$ is the relative displacement across the damper rod. Note that $x_{si}(t) = x_i(t)$ means that no force (stiffness) is participating in the system. The first control logic in Equation 2.3 is consistent with the one derived by Thai et al. (1997). In the switching control law, it is assumed that the SASD can be turned on and off at any time. The control force vector of the SASD can be represented as

$$\mathbf{U}(t) = \sum_{i=1}^{n} K_{di} v_i \mathbf{X}(t) \tag{2.4}$$

where K_{di} is the effective stiffness of the ith damper, v_i is the control parameter, and $\mathbf{X}(t)$ is the relative displacement vector. The switching control logic is then given by

$$v_i(t) = \begin{cases} 1 & \text{if } \dot{x}_i x_i \geq 0 \\ 0 & \text{otherwise} \end{cases} \tag{2.5}$$

A numerical study on three and eight story structures showed that the control logics are effective in reducing the inter-story drifts. However, the floor accelerations are significantly increased in some cases. In addition, it was found that the performance of the controlled structure depends on the control method and on the type of excitation. The control law given by Equation 2.5 was also derived by Yang et al. (1996) based on the sliding mode control theory with static output feedback (limited number of sensors). The simulation results showed the robustness of the control method, and also indicated that active variable stiffness (AVS) systems can significantly reduce the inter-story drifts but may lead to increased floor accelerations.

Yang et al. (2000) developed control laws for resetting the SASD where two extra terms were added to the classical Lyapunov function. One term was added to preserve the properties of the energy function and the other term to account for the ground acceleration. The simulation carried out on three and eight story buildings showed that the resetting control law successfully reduces both inter-story drifts and floor accelerations of the three story building. However, the accelerations of the lower floors of the eight story building were significantly increased but were reduced for the upper floors.

As a comparison of active, semi-active and passive control systems on a benchmark cable-stayed bridge, Agrawal et al. (2003) tested the performance of the benchmark bridge equipped with the semi-active stiffness damper and semi-active friction damper compared to linear and nonlinear viscous dampers as well as to an actively controlled bridge. Based on the simulation results, the overall performance of the passive systems as well as the semi-active friction damper were found to be comparable to the actively

controlled bridge. The resetting semi-active stiffness damper came last in terms of the overall performance enhancement.

Kobori et al. (1993); Nasu et al. (2001) used active variable stiffness (AVS) device for seismic control of structures. By placing the AVS device between the braces and the floor beam, it can continuously provide a non-resonant state by instantaneously altering the building's stiffness. Only small power supply is needed to operate the AVS. This system was installed in a trial building and it was shown through the structural monitoring and the analytical work that the AVS system provides substantial reduction to the seismic demands. Response estimation, which relies on estimating the structural response with different stiffness profiles, was employed for the selection of the appropriate stiffness in real-time. The response estimation method was further improved by Nasu et al. (2001) to account for structural nonlinearities. After more than 30 earthquakes hit the controlled building in ten years, the recorded and analyzed data confirmed the efficiency and reliability of AVS control.

Jabbari and Bobrow (2002) studied the resetting approach for vibration suppression. The study showed that by providing high stiffness, reliability and safety are not compromised and the resisting force is always at its maximum value. Furthermore, the number of times energy is extracted is higher in the resetting technique than in the variable stiffness technique, leading to faster and more effective vibration suppression. Furthermore, the resetting approach maintains the natural frequency and mode shapes of the system.

In order to overcome the limitations of conventional on/off type variable stiffness systems, a new semi-active independently variable stiffness (SAIVS) device was developed by Nagarajaiah and Mate (1998). The SAIVS device (Figure 2.2) is capable of changing the stiffness continuously and smoothly between minimum and maximum stiffness. The device consists of four springs, where joints 3 and 4 slide on a guide rail.

By changing the device angle, θ, with the electromechanical actuator connected to joint 1, the device stiffness can be smoothly changed. It was demonstrated through the experimental study that by switching the stiffness continuously and smoothly, a non-resonant state can be achieved, leading to significant seismic response reduction. The effectiveness of the device was evaluated by Nagarajaiah and Sahasrabudhe (2006) in reducing the seismic response of sliding base isolated buildings. The SAIVS device was incorporated into the sliding isolation system of the building experimental model. A moving average non-linear tangential stiffness control algorithm was developed to regulate the device stiffness in real-time. This algorithm however, is based on making the spring force of the device a non-linear function of the relative base displacement. The study showed the effectiveness of the SAIVS in reducing the base displacement compared to the passive cases. These passive cases are corresponding to the device being operated at its maximum or minimum stiffness. In addition to the reduced base displacement, the base shear of the passive system with minimum stiffness was not exceeded by the SAIVS device. Although near-fault ground motions were considered in their study, the response enhancement was verified only for the fault-parallel direction, and a better semi-active control algorithm is needed to reduce the seismic response due to fault-normal direction.

Narasimhan and Nagarajaiah (2005) developed a short time Fourier transformation (STFT) to track the excitation properties in terms of energy spectrum and frequency distribution to reduce the seismic response of base isolated buildings. The energy of the excitation corresponding to the fundamental period of the isolated structure is used to regulate the variable stiffness of the SAIVS. The suggested control algorithm was numerically investigated for near-fault ground motion effect on a five story reinforced concrete building equipped with the SAIVS at the isolation level. It was shown that the proposed algorithm successfully reduces the base dis-
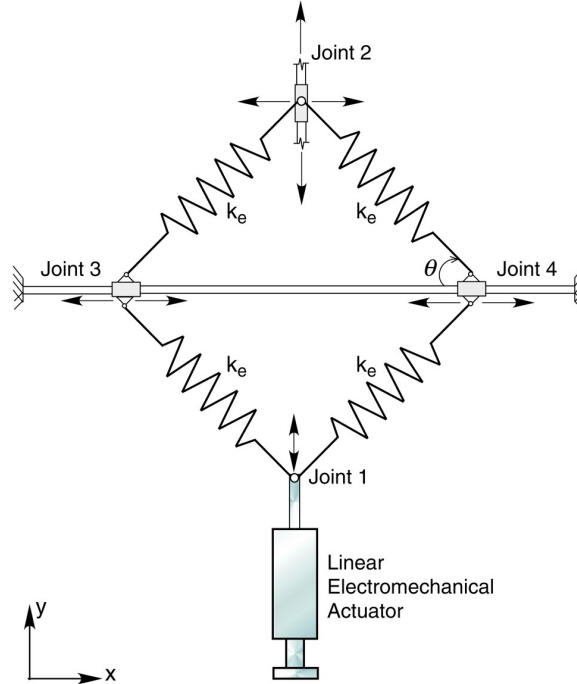
Figure 2.2: Analytical model of the SAIVS device (Narasimhan and Nagarajaiah, 2005)

placement and inter-story drifts without increasing the accelerations. Sahasrabudhe and Nagarajaiah (2005a) implemented the semi-active independently variable stiffness device in a experimental study on a sliding base isolated bridge for near-fault ground motions. The moving average non-linear tangential stiffness control algorithm, discussed earlier, was used to control the stiffness of the SAIVS device. It was shown that the proposed system is capable of reducing the bearing displacement compared to the passively isolated cases, which implies that the SAIVS can improve the seismic performance of sliding base isolated bridges.

2.4   Stiffness and Equivalent Lateral Force Distribution

For design purpose, it is essential to reliably determine the seismic demand on structural systems. One of the most common methods establishes equivalent lateral forces that are assumed to apply statically for the design of members and for the prediction of the structural performance under the effect of seismic loads. However, the equivalent lateral force procedures adopted by most of the seismic design codes (International Code Council, 2006; NEHRP, 2003) do not precisely take into account the nonlinear behavior of structures. Instead, the elastic seismic demands are reduced to account for the structural ductility, while the elastic structural deformations are magnified for the same reason. This method does not lead to a reliable seismic performance prediction, especially for structures experiencing high nonlinearity and those with supplemental damping devices. Furthermore, the equivalent lateral force procedures are mostly dependent on the first mode of vibration, but the effect of higher modes is not explicitly considered. Researchers realize the need for more rigorous methods for different types of structures. In this regard, Lee et al. (2004) proposed a new seismic lateral force distribution for steel moment frames based on nonlinear dynamic analyses. The seismic base shear was derived from a modified energy balance equation. The proposed seismic base shear and lateral force distribution showed good agreement with the nonlinear dynamic response analysis, and hence, it is more favorable for the purpose of seismic design and seismic performance prediction of steel moment frames. Chao et al. (2007); Chao and Goel (2005, 2008) investigated the adequacy of the proposed lateral force distribution on a number of framed structures under a wide variety of earthquake ground motions. It was shown that the proposed lateral force pattern is more rational and gives a reliable prediction of inelastic seismic demands

on different structures. It was also concluded that the structures designed according to the proposed loading pattern experience maximum story shear that agrees well with the expected values. In addition, they experience more uniform maximum inter-story drifts compared to those design according to the code's equivalent lateral force procedure.

In an attempt to account for the effect of higher modes, Gupta and Kunnath (2000) proposed an enhanced modal site-specific spectra-based pushover analysis. The proposed procedure has shown capability of predicting the inter-story drift as well as the failure mechanism. Most importantly, the method is suitable for structures with irregular strength/stiffness distribution. Chopra and Goel (2001a) developed a Modal Pushover Analysis (MPA) procedure to account for the effect of higher modes for a better prediction of the seismic demand on inelastic structures. The response history analysis of a selected 9-story building proved that the proposed methodology is more accurate in estimating the drift demands and plastic hinge rotations than all FEMA's force distribution patterns. In order to evaluate the accuracy of the proposed MPA, Chopra and Goel (2001b) applied the procedure to six SAC buildings to predict the seismic demands and compare them to the nonlinear response history analyses results. It was found that the MPA underestimates the seismic demand on most of the considered structures, particularly for the upper floors.

In terms of optimal stiffness distribution over the building's height, Takewaki (2000) proposed a procedure for stiffness and damping simultaneous optimization by minimizing the sum of mean square responses to stationary random excitations with the maximum capacity of the stiffness and damping devices being considered. Mo-hammadi et al. (2004) investigated the adequacy of various loading patterns, such as rectangular, triangular, parabolic, on shear buildings. According to this investiga-tion, it was found that the equivalent lateral force patterns specified by design codes

do not help achieving uniform ductility demand over the building's height. However, the study proposed an iterative method for optimal distribution of strength, and it was found that the lateral loading pattern strongly depends on the type of structure as well as on the excitation. With the proposed methodology, the stiffness distribution of buildings with hysteretic dampers could lead to a uniform inter-story drift throughout the building's height. Park and Medina (2007); Park (2007) proposed a lateral force distribution pattern for the conceptual seismic design of moment frames. The loading pattern takes into account the inelastic behavior of the structure. Uniform story ductility ratios are expected to result with the proposed loading pattern obtained through an iterative procedure. Ganjavi et al. (2007) investigated the effect of the equivalent static and spectral dynamic loading patterns on the distribution of drift, hysteretic energy and damage of reinforced concrete buildings. It was found that buildings designed according to those patterns, when subjected to strong earthquakes, are more likely to experience structural damage that is concentrated in one or two stories rather than uniformly distributed along the stories. In all of the considered models, the amount of the hysteretic energy dissipated through the top story was negligible.

Chapter 3

Smart Base Isolation Systems

Controllable devices incorporating smart materials, such as Magneto-Rheological Elastomers (MREs) and Magneto-Rheological Fluids (MRFs) have attracted the researchers interest for their reliability, adaptability and feasibility. Despite limitations, they provide potentially feasible seismic mitigation alternative to active control strategies. It is possible to change their mechanical properties when they are subjected to a magnetic field, which can be developed and controlled by low external power. This feature makes the semi-active devices especially attractive, as they overcome the high external power needed to operate their counterpart active control devices. Furthermore, semi-active control devices do not add energy to the structure and hence they do not destabilize the controlled system as may be the case in actively controlled structures.

This chapter presents two semi-active control algorithms for smart base isolated structures incorporating controllable stiffness devices, such as Magneto-Rheological Elastomers (MREs). The performance of the smart base isolated systems is compared to the conventionally isolated systems using Lead Rubber bearing (LRB) and to one that implements linear quadratic regulator (LQR) control subjected to near-fault and far-field ground motions.

3.1 Variable Stiffness Devices

The Variable stiffness devices (VSD) are assumed to be multi-linear elastic devices that have different stiffness branches in their force-deformation relationship. The devices that possess this variable stiffness behavior can be mechanical devices (passive devices) or controllable smart-material based variable stiffness devices. A summary of different variable stiffness devices, such as the semi-active stiffness damper (SASD) or the active variable stiffness (AVS) device (Kobori et al., 1993; Yang et al., 1996; Yang and Agrawal, 1999; Yang et al., 2000; Nasu et al., 2001; Agrawal et al., 2003) and the semi-active independently variable stiffness (SAIVS) device (Nagarajaiah and Mate, 1998; Narasimhan and Nagarajaiah, 2005; Sahasrabudhe and Nagarajaiah, 2005a; Nagarajaiah and Sahasrabudhe, 2006) is given in Section 2.3. The controllable VSD incorporating Magneto-Rheological Elastomer (MRE), which was numerically investigated by Usman et al. (2009) will be used as the smart base isolation system for the illustration of the control algorithms developed in this chapter. The stiffness of the considered device can be adjusted by controlling the magnitude of the applied magnetic field. The proposed device was investigated for implementation as a semi-active base isolation system. According to preliminary experimental tests conducted on the MRE device (Usman et al., 2009), the maximum achievable stiffness adjustment is about $\pm 70\%$ of the base material stiffness k_0 (Recent experimental studies have shown that higher stiffening ratios are achievable (Yang et al., 2013)). However, a wider range is assumed to demonstrate potential benefits of the proposed control algorithms, which are also applicable to any similar stiffness controllable devices.

3.2   Benchmark Structure

The benchmark structure proposed by Kelly et al. (1987) is considered herein for the illustration of the performance of different control algorithms. The benchmark structure represents a five story base isolated building, as shown in Figure 3.1a. The proposed semi-active control devices (bearings) are assumed to replace the conventional Lead Rubber Bearings (LRB) isolation system (Figure 3.1b). The benchmark system properties are illustrated in Table 3.1. Note that the postyielding stiffness, k_b, of the isolation system was originally selected so that the fundamental period of the structure is 2.5 sec once the lead plug yields. In the following sections, the postyield stiffness, k_b, will remain unchanged, while the bilinear properties that define the hysteretic behavior of the LRB are defined based on average response of isolated building under moderate and sever seismic events. Ramallo et al. (2002) performed nonlinear response history analyses on the considered benchmark structure to define the effect of the LRB parameters on the peak response. Different values of the characteristic strength, Q_y, and the postyield to preyield stiffness ratio, α, were considered. Figure 3.2 shows the structural acceleration and the base drift peak response under moderate and sever seismic events (Ramallo et al., 2002). It should be noted that the legend in Figure 3.2 is used in that study, where they specified two different systems such that LRB1, with ($Q_y = 0.05W$) for far-field and LRB2, with ($Q_y = 0.15W$) for the near-fault motions. However, in this study, Figure 3.2 is used to define the LRB parameters so that unified isolation system is used for both far-field and near-fault excitations. The characteristic strength, Q_y, is selected to be 10% of the building's weight and the postyield to preyield stiffness ratio, α, is taken as 8.5%. As can be seen from the figure, these values provide sufficient control of the base displacement without excessive structural accelerations for both moderate and sever seismic events.
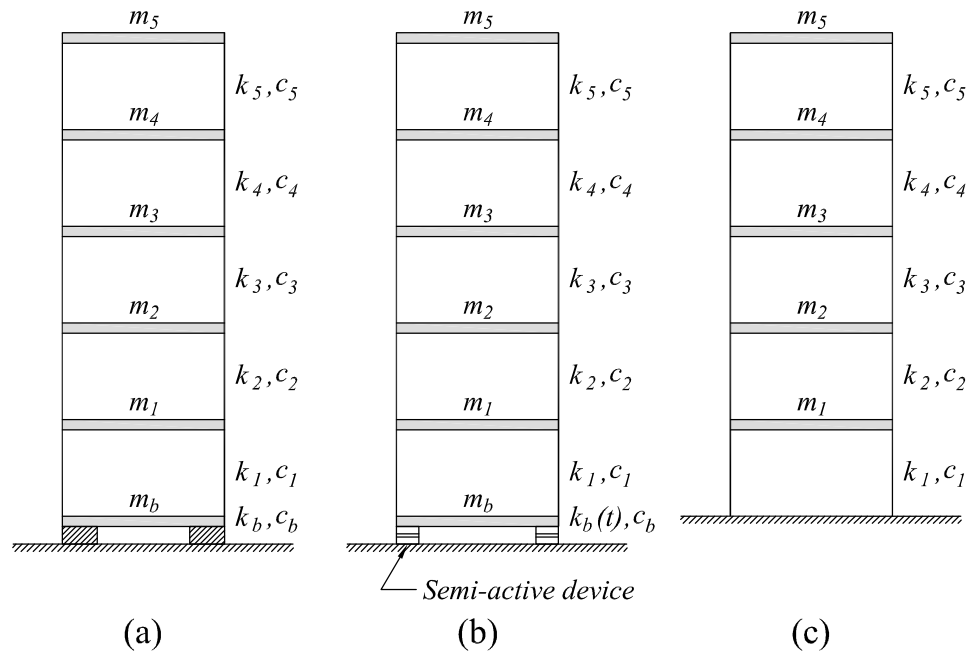
Figure 3.1: Benchmark five-story structure; (a) Conventionally isolated, (b) Semi-actively isolated (c) Fixed base

Table 3.1: Properties of the benchmark structure (Kelly et al., 1987).

Floor mass (kg)	Stiffness coefficients (kN/m)	Damping coefficients (kN.s/m)
$m_b = 6800$	$k_b = 232$	$c_b = 3.74$
$m_1 = 5897$	$k_1 = 33732$	$c_1 = 67$
$m_2 = 5897$	$k_2 = 29093$	$c_2 = 58$
$m_3 = 5897$	$k_3 = 28621$	$c_3 = 57$
$m_4 = 5897$	$k_4 = 24954$	$c_4 = 50$
$m_5 = 5897$	$k_5 = 19059$	$c_5 = 38$
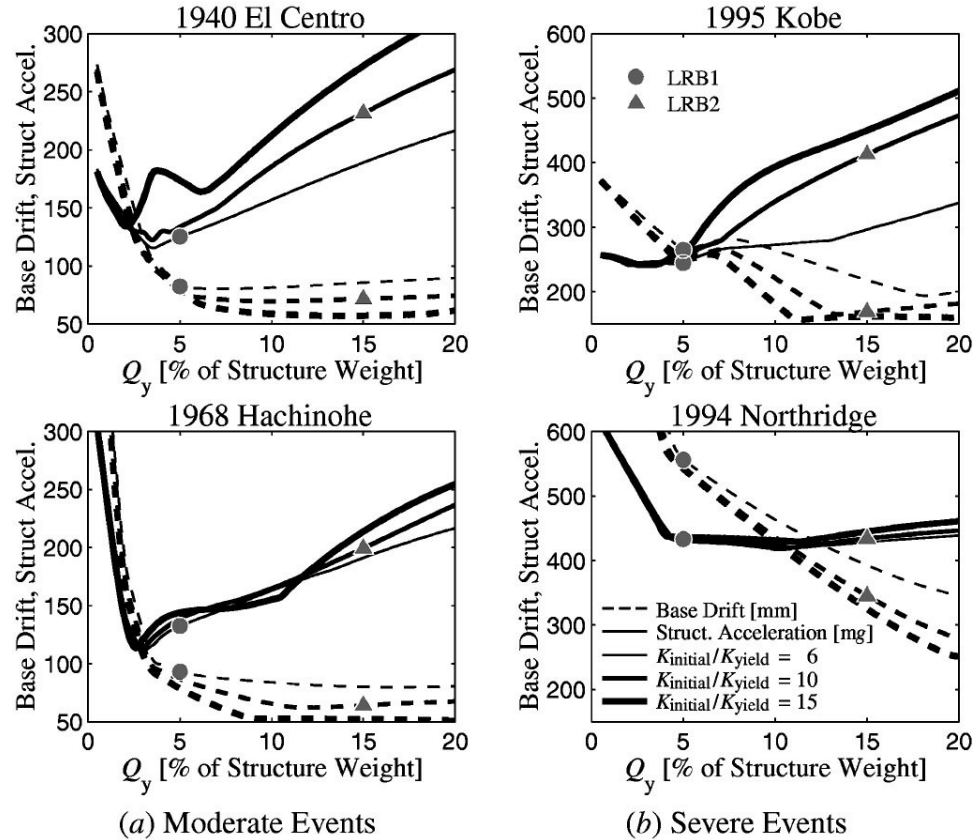
Figure 3.2: Peak response of LRB isolated building under moderate and sever seismic events (Ramallo et al., 2002)

3.3 Equations of Motion

The equations of motion of the smart base isolated structure shown in Figure 3.3 can be written as

$$\mathbf{M}_s\ddot{\mathbf{u}}_s^t + \mathbf{C}_s\dot{\mathbf{u}}_s + \mathbf{K}_s\mathbf{u}_s = 0 \tag{3.1a}$$

$$m_b\ddot{u}_b^t + F_d(c_b, \dot{u}_b) + F_s(u_b, \dot{u}_b, z) - \mathbf{I}_s^T\mathbf{V}_s = 0 \tag{3.1b}$$

Equation 3.1a defines the motion of the superstructure, while Equation 3.1b defines the base slab motion. $\mathbf{M}_s$, $\mathbf{C}_s$ and $\mathbf{K}_s$ are the mass, damping and stiffness matrices for the superstructure, respectively. m_b, is the base slab mass, $F_d(c_b, \dot{u}_b)$ and $F_s(u_b, \dot{u}_b, z)$
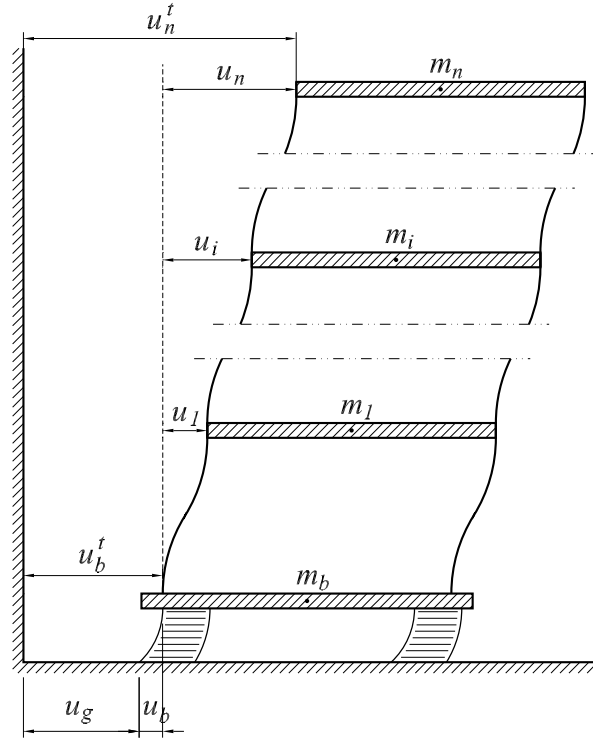
Figure 3.3: Schematic view of base isolated system

are the damping force and the restoring force of the isolation system, respectively. $\ddot{\mathbf{u}}_s$, $\dot{\mathbf{u}}_s$ and $\mathbf{u}_s$ are the acceleration, velocity and displacement vectors of the superstructure, respectively, with respect to the base slab, as shown in Figure 3.3, where $s = 1, ..., n$. $\ddot{u}_b$, $\dot{u}_b$ and u_b are the acceleration, velocity and displacement vectors of the base slab with respect to the ground, respectively. The superscript t indicates the total displacement with respect to a fixed reference, as shown in the figure. $\mathbf{I}_s^T$ represents the influence array of the superstructure motion on the motion of the base slab and $\mathbf{V}_s$ is the vector of shear forces induced by the superstructure. In other words, $\mathbf{I}_s^T \mathbf{V}_s$ is the total shear force acting on the base slab due to the motion of the superstructure. $\mathbf{V}_s$ can be written as

$$\mathbf{V}_s = -\mathbf{M}_s \ddot{\mathbf{u}}_s^t \tag{3.2}$$

The total displacement vectors of the structure shown in Figure 3.3 can be expressed as

$$\mathbf{u}_s^t = \mathbf{u}_s + \mathbf{I}_b u_b + \mathbf{I}_1 u_g \tag{3.3a}$$

$$u_b^t = u_b + \mathbf{I}_2 u_g \tag{3.3b}$$

where $\mathbf{I}_b$ is the influence array of the base slab motion on the DOFs of the superstructure, $\mathbf{I}_1$ and $\mathbf{I}_2$ are the influence arrays of the ground motion on the superstructure and base slab DOFs, respectively, and u_g is the total ground displacement. Substituting $\mathbf{u}_s^t$ and u_b^t from Equations 3.3 into 3.1 and rearranging, the governing equations of motion can be written as

$$\mathbf{M}_s\ddot{\mathbf{u}}_s + \mathbf{C}_s\dot{\mathbf{u}}_s + \mathbf{K}_s\mathbf{u}_s = -\mathbf{M}_s(\mathbf{I}_b\ddot{u}_b + \mathbf{I}_1\ddot{u}_g) \tag{3.4a}$$

$$m_b\ddot{u}_b + F_d(c_b, \dot{u}_b) + F_s(u_b, \dot{u}_b, z) = -m_b\mathbf{I}_2\ddot{u}_g - \mathbf{I}_s^T\mathbf{M}_s(\ddot{\mathbf{u}}_s + \mathbf{I}_b\ddot{u}_b + \mathbf{I}_1\ddot{u}_g) \tag{3.4b}$$

In the preceding equation, the damping force, $F_d(c_b, \dot{u}_b)$, can be evaluated based on whether the isolation system possesses controllable damping device or inherent viscous damping only. Thus,

$$F_d = \begin{cases} c_b\dot{u}_b, & \text{uncontrolled damping} \\ c_b(t)\dot{u}_b, & \text{controlled damping} \end{cases} \tag{3.5}$$

In this study, the isolation systems are modeled with inherent damping only, with damping coefficient, c_b, as specified per the benchmark building (Table 3.1). This coefficient provides 2% equivalent damping ratio to the first mode of the isolated benchmark structure. The restoring force, $F_s(u_b, \dot{u}_b, z)$ represents the bilinear hysteretic behavior of conventional LRB isolation system. The Bouc-Wen model is used

to approximate this behavior (Ikhouane and Rodellar, 2007). Thus the restoring force, F_s, used to model the LRB is determined as

$$F_s = k_b u_b + (1 - \alpha)k_e x_y z \tag{3.6a}$$

$$x_y \dot{z} = A\dot{u}_b - \beta|\dot{u}_b|z|z|^{n-1} - \gamma\dot{u}_b|z|^n \tag{3.6b}$$

where α is the ratio of the postyield stiffness (k_b) to the preyield stiffness (k_e) of the LRB isolation system, x_y is the yield displacement of the isolators, and z is dimensionless parameter that defines the hysteresis loops of the LRB. It is found by solving the nonlinear differential Equation 3.6b, in which $(n > 1)$ is a parameter that defines the sharpness of the transition zone between preyield and postyield stiffness, A, β, and γ are constant parameters that control the shape of the hysteresis loops. For the elastic stiffness to be modeled properly $(A = \beta + \gamma)$, and for the unloading to follow the elastic stiffness $(\beta = \gamma)$. The effect of the aforementioned parameters on the hysteresis loops is shown in Figures 3.4 and 3.5. Equation 3.4 can be rewritten in matrix form as

$$\overbrace{\begin{bmatrix} \mathbf{M}_s & \mathbf{M}_s\mathbf{I}_b \\ \mathbf{I}_s^T\mathbf{M}_s & m_b + \mathbf{I}_s^T\mathbf{M}_s\mathbf{I}_b \end{bmatrix}}^{\tilde{\mathbf{M}}} \begin{bmatrix} \ddot{\mathbf{u}}_s \\ \ddot{u}_b \end{bmatrix} + \overbrace{\begin{bmatrix} \mathbf{C}_s & \mathbf{0} \\ \mathbf{0} & c_b \end{bmatrix}}^{\tilde{\mathbf{C}}} \begin{bmatrix} \dot{\mathbf{u}}_s \\ \dot{u}_b \end{bmatrix} + \overbrace{\begin{bmatrix} \mathbf{K}_s & \mathbf{0} \\ \mathbf{0} & k_b \end{bmatrix}}^{\tilde{\mathbf{K}}} \begin{bmatrix} \mathbf{u}_s \\ u_b \end{bmatrix} = $$
$$\underbrace{\begin{bmatrix} -\mathbf{M}_s\mathbf{I}_1 \\ -m_b\mathbf{I}_2 - \mathbf{I}_s^T\mathbf{M}_s\mathbf{I}_1 \end{bmatrix}}_{\mathbf{E}_g} \ddot{u}_g + \underbrace{\begin{bmatrix} \mathbf{0} \\ -\mathbf{I}_c \end{bmatrix}}_{\mathbf{E}_c} f_c \tag{3.7}$$
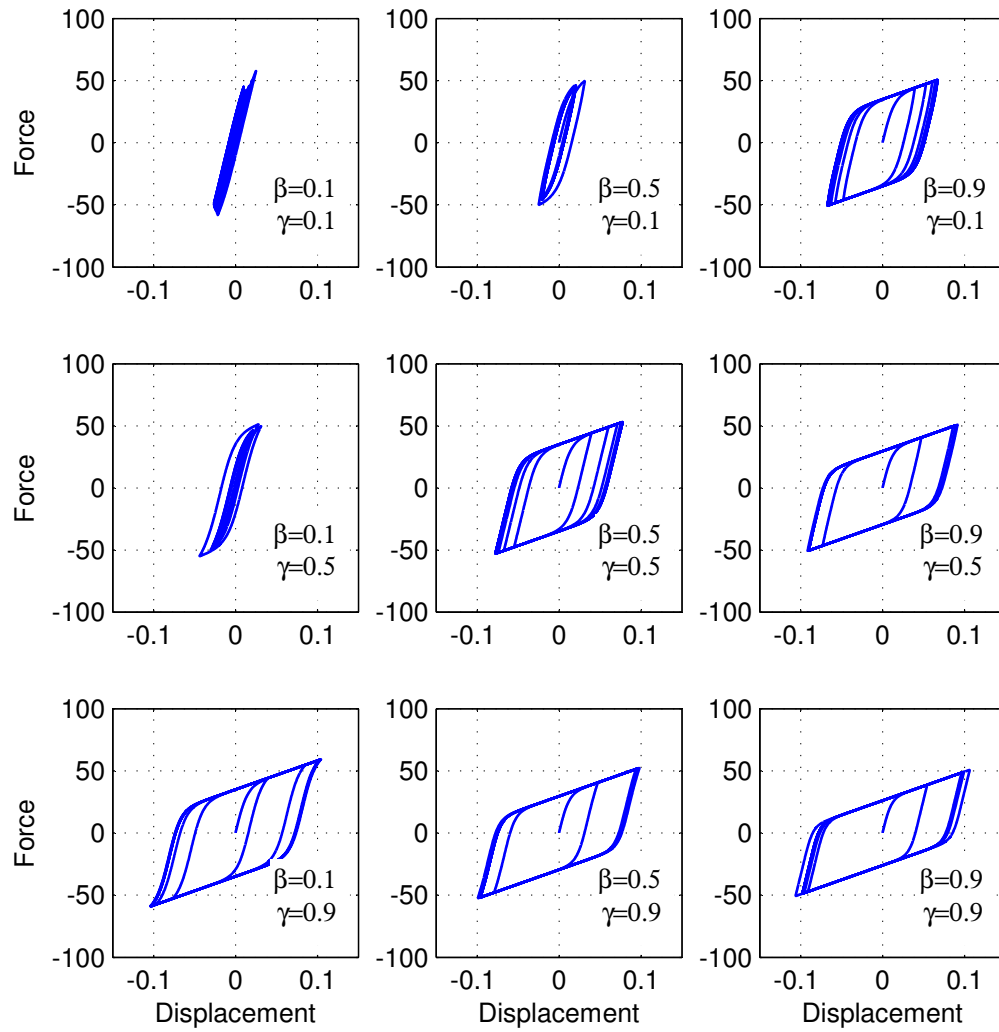
Figure 3.4: Effect of the Bouc-Wen parameters on the hysteresis loop shapes, ($n = 2$, $A = 1$)
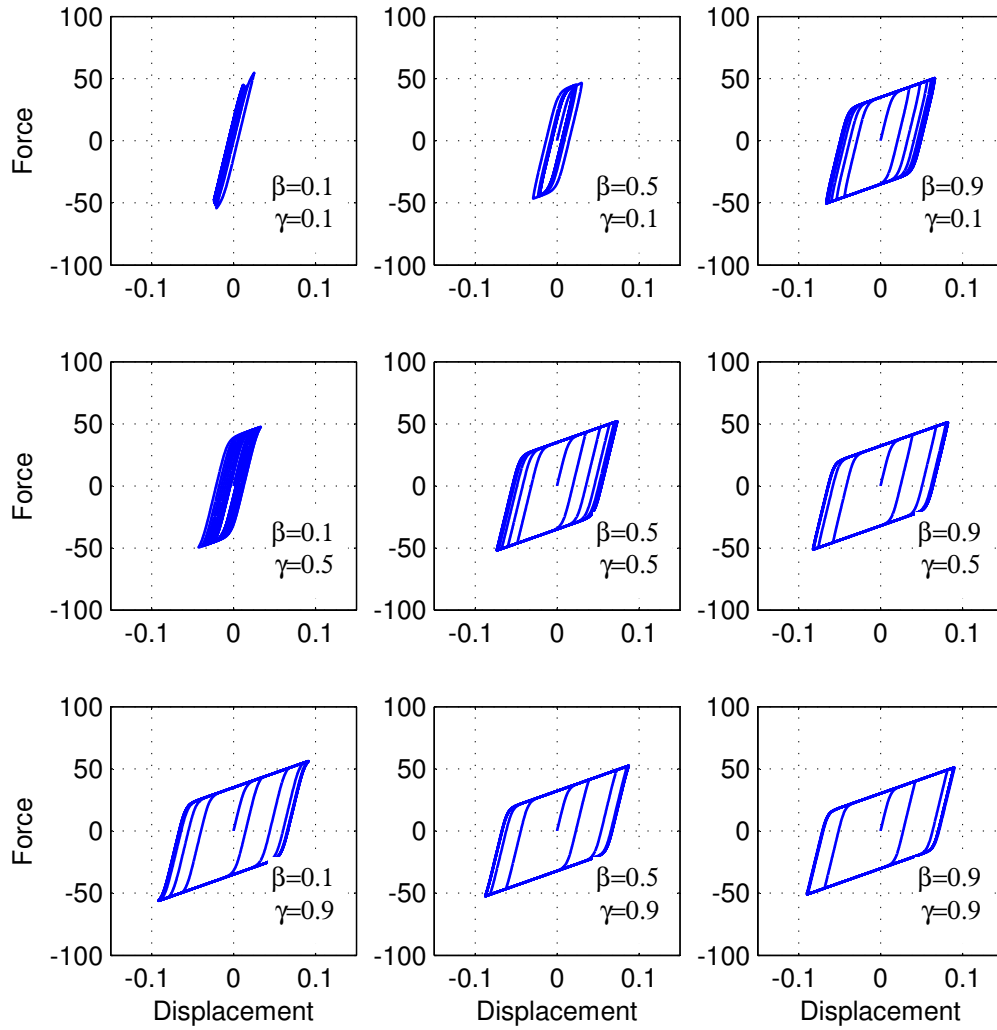
Figure 3.5: Effect of the Bouc-Wen parameters on the hysteresis loop shapes, ($n = 4$, $A = 1$)

where $\mathbf{I}_c$ is the location matrix of the restoring force of the isolation system. Equation 3.7 can be written in the state space representation as

$$\dot{\mathbf{x}} = \mathbf{A}\mathbf{x} + \mathbf{B}f_c + \mathbf{E}\ddot{u}_g \tag{3.8a}$$

$$\mathbf{y} = \mathbf{C}_y\mathbf{x} + \mathbf{D}_yf_c + \mathbf{E}_y\ddot{u}_g \tag{3.8b}$$

where $\mathbf{x} = [\mathbf{u}_s^T \ u_b \ \dot{\mathbf{u}}_s^T \ \dot{u}_b]^T$ is the state vector, and $\mathbf{y}$ represents the vector of measurements. The state matrices are defined as

$$\mathbf{A} = \begin{bmatrix} \mathbf{0} & I \\ -\tilde{\mathbf{M}}^{-1}\tilde{\mathbf{K}} & -\tilde{\mathbf{M}}^{-1}\tilde{\mathbf{C}} \end{bmatrix} \ , \ \mathbf{B} = \begin{bmatrix} \mathbf{0} \\ \tilde{\mathbf{M}}^{-1}\mathbf{E}_c \end{bmatrix} \ , \ \mathbf{E} = \begin{bmatrix} \mathbf{0} \\ \tilde{\mathbf{M}}^{-1}\mathbf{E}_g \end{bmatrix} \tag{3.9}$$

while $\mathbf{C}_y$, $\mathbf{D}_y$ and $\mathbf{E}_y$ are obtained based on the measured state variables. For instance, if the floors and base slab accelerations are measured, the measurement equation matrices become

$$\mathbf{C}_y = \begin{bmatrix} -\bar{\mathbf{M}}^{-1}\tilde{\mathbf{K}} & -\bar{\mathbf{M}}^{-1}\tilde{\mathbf{C}} \end{bmatrix} \ , \ \mathbf{D}_y = \begin{bmatrix} \bar{\mathbf{M}}^{-1}\mathbf{E}_c \end{bmatrix} \ , \ \mathbf{E}_y = 0 \ , \ \bar{\mathbf{M}} = \begin{bmatrix} \mathbf{M}_s & \mathbf{0} \\ \mathbf{I}_s^T\mathbf{M}_s & m_b \end{bmatrix}$$
$$\tag{3.10}$$

In case of passive isolators, $(f_c = (1 - \alpha)k_e x_y z)$ represents the hysteretic behavior, otherwise, f_c is the control force determined according to the control laws that are presented in Section 3.5.

3.4   Ground Motions and Scaling

To illustrate the effectiveness of the proposed semi-active control algorithms, the benchmark building (Figure 3.1) is subjected to a series of recorded far-field and near-fault ground motions. Ten far-field and fourteen near-fault pulse type recorded

Table 3.2: Far-filed ground motion details and scaling.

EQ ID	Earthquake Name	Year	M	Recording Station Name	Owner	Scale Factor
02	Northridge	1994	6.70	Canyon Country-WLC	USC	1.42
03	Duzce, Turkey	1999	7.10	Bolu	ERD	1.09
05	Imperial Valley	1979	6.50	Delta	UNAM	2.23
06	Imperial Valley	1979	6.50	El Centro Array No.11	USGS	2.75
08	Kobe, Japan	1995	6.90	Shin-Osaka	CUE	2.13
09	Kocaeli, Turkey	1999	7.50	Duzce	ERD	1.86
11	Landers	1992	7.30	Yermo Fire Station	CDMG	2.60
13	Loma Prieta	1989	6.90	Capitola	CDMG	1.46
16	Superstition Hills	1987	6.50	El Centro Imp. Co.	CDMG	2.45
19	Chi-Chi, Taiwan	1999	7.60	CHY101	CWB	1.48

ground motions are selected from the record sets provided in FEMA (2009). These motions are scaled so that the average of the square root of the sum of squares (SRSS) spectrum, constructed for each pair of the ground motions by taking the SRSS of the 5% damped response spectra of the scaled components, does not fall below 1.4 the design response spectra in the range of the period of interest. For isolated structures, this period range is considered $0.5T_D$ to $1.25T_M$ (ASCE, 2010), where T_D and T_M are the effective periods of the isolated structure at the design displacement and the maximum displacement, respectively. The scaling of the ground motion records is performed to match 1.4 the design response spectra of a hypothetical site, where the mapped values of the short period and 1-second spectral accelerations are ($S_S = 2.1g$), and ($S_1 = 0.93g$), respectively, and the site is assumed of class D. Tables 3.2 and 3.3 show the far-field and near-fault ground motion sets and their scale factors, respectively. Figures 3.8 and 3.9 show the 5% damped spectral acceleration, spectral velocity and spectral displacement for the far-field and the near-fault ground motion sets, respectively. The average SRSS spectrum of the scaled motions overlaid on the 1.4 design response spectra are shown in Figures 3.6 and 3.7.

Table 3.3: Near-fault pulse type ground motion details and scaling.

EQ	Earthquake			Recording Station		Scale
ID	Name	Year	M	Name	Owner	Factor
01	Imperial Valley-06	1979	6.50	El Centro Array No.6	CDMG	1.73
02	Imperial Valley-06	1979	6.50	El Centro Array No.7	USGS	1.35
03	Irpinia, Itali-01	1980	6.90	Sturno	ENEL	2.50
04	Superstition Hills-02	1987	6.50	Parachute Test Site	USGS	1.22
05	Loma Prieta	1989	6.90	Saratoga - Aloha	CDMG	2.36
06	Erzican, Turkey	1992	6.70	Erzincan	–	1.36
07	Cape Mendocino	1992	7.00	Petrolia	CDMG	0.93
08	Landers	1992	7.30	Lucerne	SCE	2.35
09	Northridge-01	1994	6.70	Rinaldi Receiving Sta	DWP	0.79
10	Northridge-01	1994	6.70	Sylmar - Olive View	CDMG	1.02
11	Kocaeli, Turkey	1999	7.50	Izmit	ERD	3.48
12	Chi-Chi, Taiwan	1999	7.60	TCU065	CWB	0.99
13	Chi-Chi, Taiwan	1999	7.60	TCU102	CWB	1.57
14	Duzce, Turkey	1999	7.10	Duzce	ERD	1.29
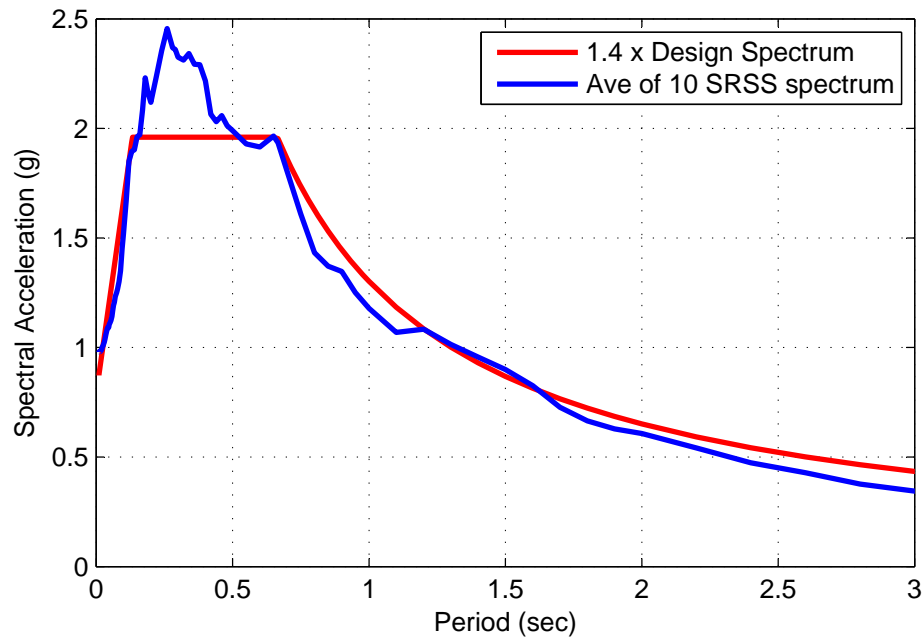
Figure 3.6: Average of 10 SRSS scaled spectrum for the far-field motions
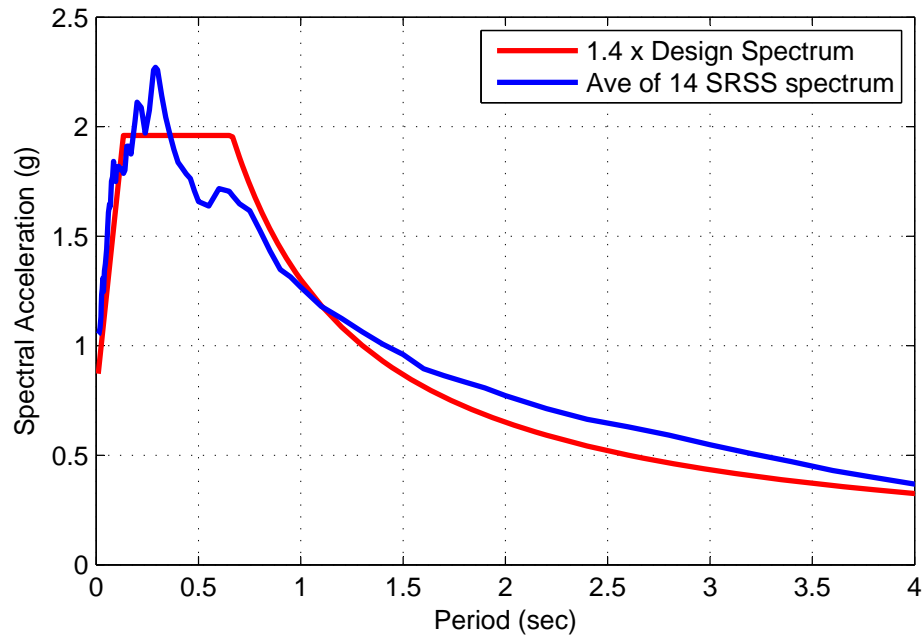
Figure 3.7: Average of 14 SRSS scaled spectrum for the near-fault motions

3.5   Semi-Active Control Algorithms

3.5.1   Minimal Acceleration Control (MAC)

The Minimal Acceleration Control (MAC) presented in this section, is designed to reduce the total structural acceleration primarily by controlling the isolation system's stiffness. Consider a system with an inherent viscous damping, so that $(F_d = c_b \dot{u}_b)$, and a controllable stiffness device, such as the one described in Section 3.1, the time variant stiffness of this controllable device can be described as

$$k_b(t) = k_0 + k_v(t) \tag{3.11}$$

where k_0 is the base material stiffness, and $k_v(t)$ is the variable stiffness controlled in real-time based on command signals that alter the intensity of the magnetic field applied to the device. Considering Equation 3.11, the restoring force, F_s, of the
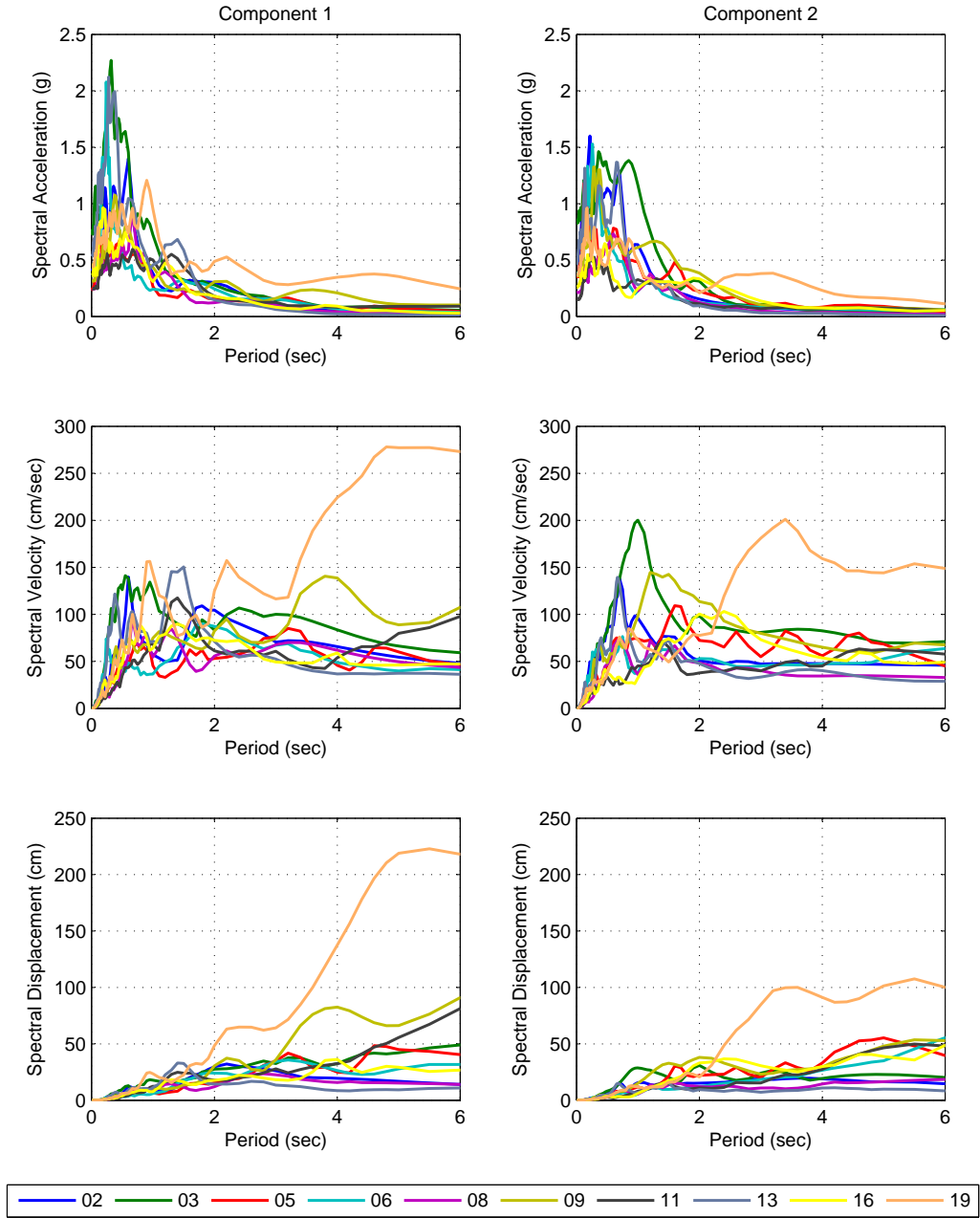
Figure 3.8: 5% Damped response spectrum of the far-field motions
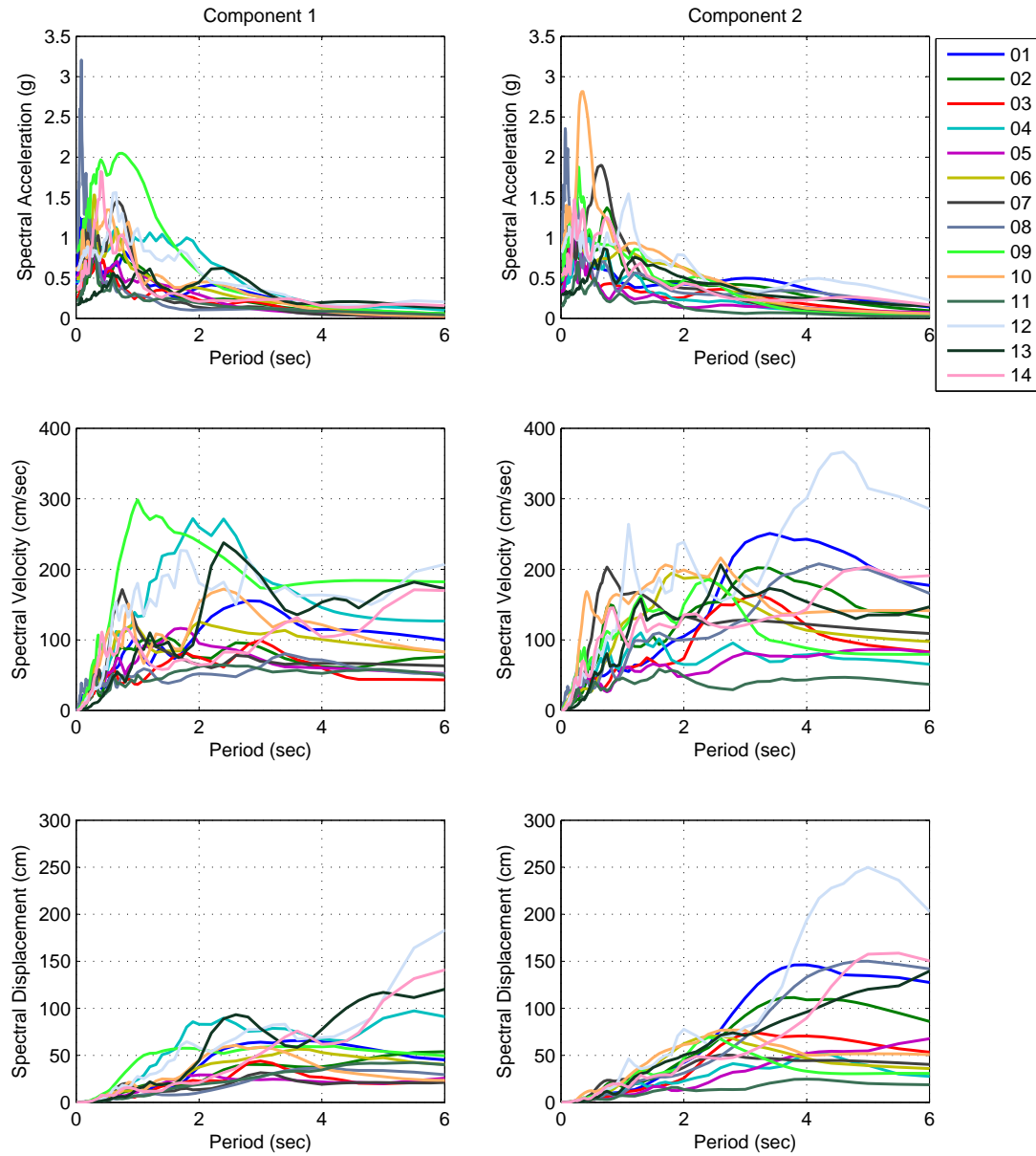
Figure 3.9: 5% Damped response spectrum of the near-fault motions

isolation system can be written as

$$F_s(t) = k_0 u_b + f_c \tag{3.12}$$

where f_c is the controllable term of the restoring force as a result of the regulated stiffness. Substituting for F_d and F_s into Equation 3.4b, leads to

$$m_b \ddot{u}_b^t + \mathbf{I}_s^T \mathbf{M}_s \ddot{\mathbf{u}}_s^t = -c_b \dot{u}_b - k_0 u_b - f_c \tag{3.13}$$

In order to minimize or even theoretically eliminate the structural accelerations, the right hand side of Equation 3.13 should be minimized. Therefore, the controlled restoring force $f_c(t)$ can be adjusted in real-time such that

$$f_c(t) = -c_b \dot{u}_b(t) - k_0 u_b(t) \tag{3.14}$$

The desired control force $f_c(t)$ obtained in Equation 3.14 is not necessarily achievable with the practical limitations on the maximum and minimum controllable stiffness, k_v. Therefore, an approximate first-order variable stiffness for a discrete time system can be calculated as

$$k_v^{min} \le k_v(t_i) = \frac{f_c(t_i) - f_{act}(t_{i-1})}{u_b(t_i) - u_b(t_{i-1})} \le k_v^{max} \tag{3.15}$$

where $f_c(t_i)$ is the desired restoring (control) force at the current time step (t_i), $f_{act}(t_{i-1})$ is the actually achieved control force in the previous time step (t_{i-1}) and $(u_b(t_i) - u_b(t_{i-1}))$ is the change in the base displacement from time t_{i-1} to t_i. The actual restoring/control force obtained at time step t_i by regulating the variable

stiffness of the isolation system can be written as

$$f_{act}(t_i) = f_{act}(t_{i-1}) + k_v(t_i)[u_b(t_i) - u_b(t_{i-1})] \tag{3.16}$$

Equation 3.14 is equivalent to Equation 2.2, which is used by Li et al. (2008) to find the appropriate properties of pseudo viscoelastic (P-VE) damper that could replace the active or semi-active control devices, so that the passive P-VE damper would behave the same as the active control device. However, Equation 2.2 is based on prior knowledge of the desired control force, determined through active control theory. In the proposed control algorithm, Equation 3.14 determines the desired unknown control force based on local measurements of the velocity and displacement of the base slab, with known stiffness and damping parameters. The implementation of this control law does not need any state predictor, as the control law depends only on local measurements of the base slab response, as shown in Figure 3.10. Thus, the obtained measurements $\mathbf{y}$ of the structure's response along with the instantaneous controlled restoring force, f_{act}, are fed back to the controller. The controller then uses these measurements to directly determine the desired control force so that the stiffness of the isolation system is regulated accordingly.

3.5.2 Acceleration Gain Control (AGC)

Consider the structure of Figure 3.3, under the effect of seismic excitation, the total shear force in the foundation system due to inertia forces is evaluated as

$$V_{found} = -m_b \ddot{u}_b^t - \mathbf{I}_s^T \mathbf{M}_s \ddot{\mathbf{u}}_s^t \tag{3.17}$$

where $\mathbf{I}_s^T$ is the influence array of the motion of the superstructure on the DOFs of the base slab. In order to reduce the shear force in the foundation level, and consequently
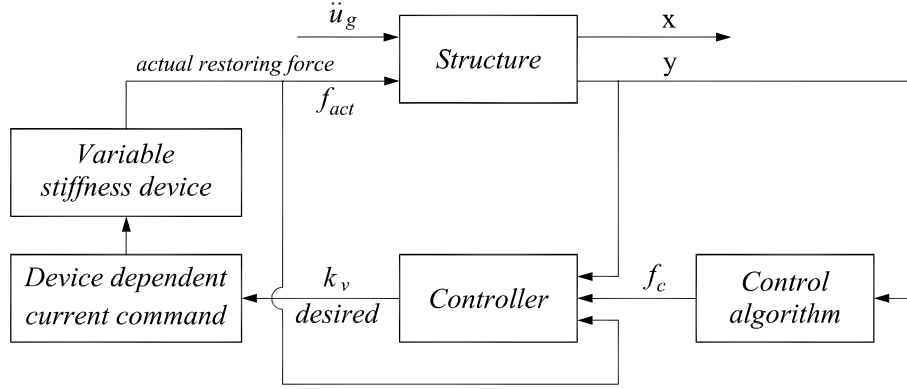
Figure 3.10: Block diagram of an output feedback semi-active control used with the MAC

the accelerations, it is desired to adjust the properties of the variable stiffness semi-active control device, used for the isolation system, so that it minimizes the total base shear at the foundation level. Therefore, the Acceleration Gain Control (AGC) presented in this section is designed so that the summation of the semi-active control force and the inertia forces $(f_c(t) + V_{found}(t))$ is minimized in real-time by regulating the stiffness of the isolation system. Thus, the desired semi-active control force must be evaluated in real-time as follows

$$f_c(t) \simeq m_b \ddot{u}_b^t + \mathbf{I}_s^T \mathbf{M}_s \ddot{\mathbf{u}}_s^t \tag{3.18}$$

Expanding the superstructure's accelerations according to Equation 3.3a, and considering a two-dimensional analysis (uniaxial excitation), Equation 3.18 can be written as

$$f_c(t) \simeq m_b \ddot{u}_b^t + \mathbf{I}_s^T \mathbf{M}_s (\ddot{\mathbf{u}}_s + \mathbf{I}_b \ddot{u}_b + \mathbf{I}_1 \ddot{u}_g) \tag{3.19}$$

with the $n - dimensional$ unit vectors, $\mathbf{I}_b = \mathbf{I}_1$, where n is the total number of DOFs of the superstructure, the evaluation of the control force can be simplified to

$$f_c(t) \simeq m_b \ddot{u}_b^t + \mathbf{I}_s^T \mathbf{M}_s \mathbf{I}_b \ddot{u}_b^t + \mathbf{I}_s^T \mathbf{M}_s \ddot{\mathbf{u}}_s \qquad (3.20)$$

In Equation 3.20, the term $(\mathbf{I}_s^T \mathbf{M}_s \mathbf{I}_b)$ represents the total mass of the superstructure and the last term in the equation represents the summation of the floor mass times the floor acceleration relative to the base slab, $\ddot{\mathbf{u}}_s$. To eliminate the relative floor accelerations and rely only on the base acceleration, an acceleration gain is applied to the relative base acceleration, and the control force is thus evaluated as

$$f_c(t) \simeq m_b \ddot{u}_b^t + \mathbf{I}_s^T \mathbf{M}_s \mathbf{I}_b \ddot{u}_b^t + G \ddot{u}_b \sum_{i=1}^{n} m_i \qquad (3.21)$$

where m_i is the mass of the ith floor, and n is the total number of floors, as shown in Figure 3.3. With the desired control force, f_c, calculated according to Equation 3.21 at time instant, i, the variable stiffness of the controllable device is regulated according to Equation 3.15.

In the Acceleration Gain Control (AGC), the acceleration gain, G, is intended to estimate the total inertia forces developed in a vibrating superstructure with respect to a steady base slab in terms of the relative acceleration of the base slab. Therefore, setting the value of the gain G to zero means ignoring the relative vibration of the superstructure with respect to the base slab, in other words, converting the structural system to a single degree of freedom (SDF) or isolated rigid system with a mass equals to the total mass of the superstructure and base slab. If this is the case, the AGC algorithm will always pick the minimum stiffness for the isolation system, as this will be the only available choice to reduce the single parameter in the control law namely the total base acceleration, $\ddot{u}_b^t$, as can be observed from Equation 3.21.

This is consistent with the fact that the effect of the superstructure on the overall performance of an isolated system becomes less significant as the isolation system becomes softer. On the other hand, there will be no control on the base displacement, which is the most critical parameter for near-fault base isolated structures. For this reason, the value of the gain G needs to be nonzero at all times, especially for smart base isolated structures subjected to near-fault ground motions. It should be noticed that the higher the value of G, the higher the shear capacity of the isolation system will be. Consequently, this would allow for a controllable system that provides some control on the base displacement, but of course at the expense of the accelerations.

The most interesting merit of the AGC given by Equation 3.21 is that it is completely decentralized (depends on only local measurements), where only the ground acceleration and the absolute base slab acceleration are needed (measured) for the implementation of the control law, as shown in Figure 3.11. In addition, acceleration measurement is considered the most reliable and readily used measurements (Spencer Jr. et al., 1994; Jabbari et al., 1995; Dyke et al., 1996b) that can be accurately achieved by means of inexpensive accelerometers. This fact makes the AGC robust and reliable as the uncertainties of the structural system modeling do not affect the performance of the controller.

3.5.2.1   Selection of the Acceleration Gain

In order to investigate the effect of the acceleration gain, G, selection on the overall performance of the controlled structure, a sensitivity analysis has been carried out using the most critical seismic events of the far-field and near-fault ground motion records.

Under the near-fault ground motions, with stiffening ratio $(-0.7 \leq \alpha \leq 0.7)$, the base displacement is controlled by increasing the value of G, as shown in Figure 3.12,
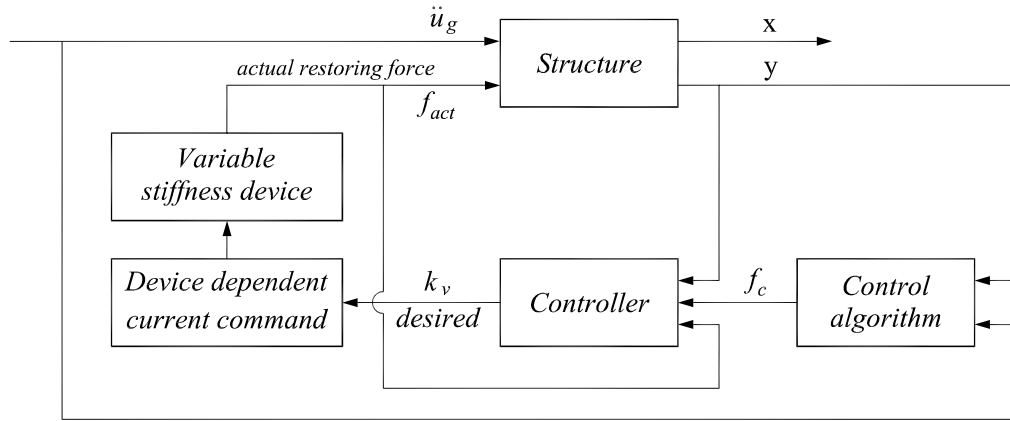
Figure 3.11: The block diagram used with the AGC

which show the peak responses normalized to the corresponding LRB peak responses. However, the peak response of the base displacement reaches its minimum achievable value at $G \approx 5.0$. Hence, any further increase of G does not lead to any enhancement of the base displacement. On the other hand, the base acceleration and the super-structure acceleration and drifts reach their minimum achievable values at $G \approx 0.8$, and any further increase of G leads to slight increase in the superstructure response. Beyond the value of 5, the overall structural response does not change, as the high value of the acceleration gain allows the isolation system to reach its maximum shear capacity, which is bounded by the maximum stiffening ratio.

With stiffening ratio $(-0.7 \leq \alpha \leq 2.0)$, the same observations regarding the effect of G on the controlled structure performance remain true, as shown in Figure 3.13. The figure demonstrates how the increased stiffening ratio leads to a better structural performance. With stiffening ratio $(-0.7 \leq \alpha \leq 10)$, the same observations regarding the effect of G on the controlled structure performance remain true, as shown in Figure 3.14. It can be concluded from the figure that if the stiffening ratio can be as high as 10, more than 50% reduction of the base displacement is possible. However, with the same base displacement, the seismic demands on the superstructure may
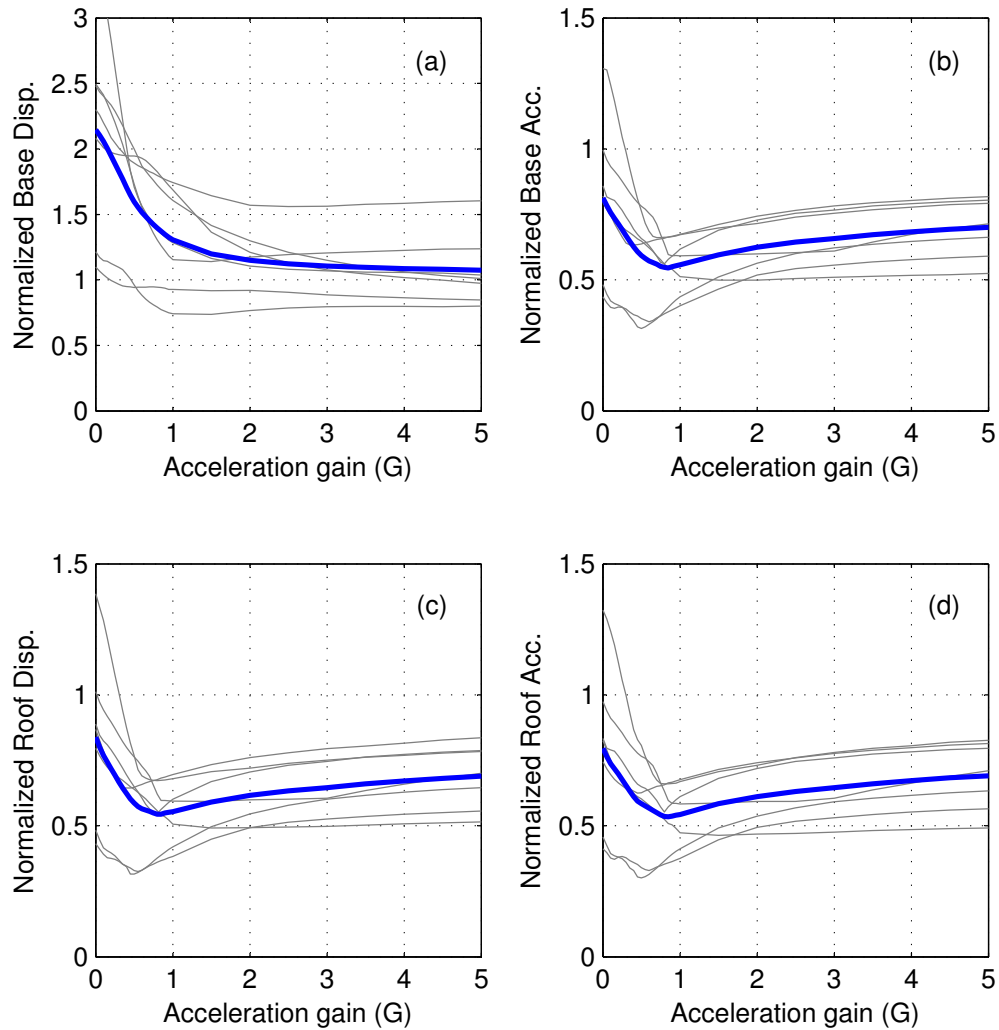
Figure 3.12: Effect of the acceleration gain selection on the performance of the AGC with $\alpha_{max} \leq 0.7$. The grey and bold curves are events and average normalized peak response, respectively. (a) base displacement, (b) base acceleration, (c) roof displacement, and (d) roof acceleration
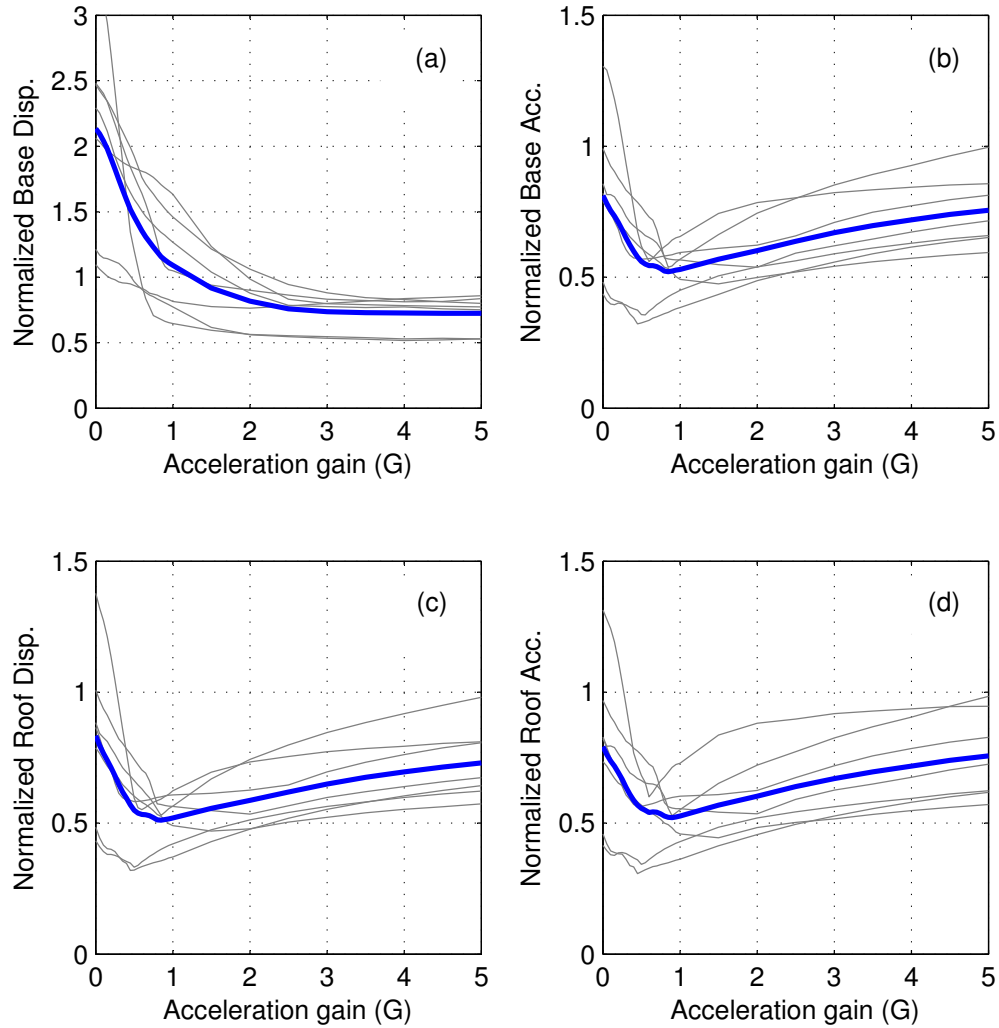
Figure 3.13: Effect of the acceleration gain selection on the performance of the AGC with $\alpha_{max} \leq 2.0$. The grey and bold curves are events and average normalized peak response, respectively. (a) base displacement, (b) base acceleration, (c) roof displacement, and (d) roof acceleration

be reduced by up to 50%. Under the far-field ground motions, the same behavior is observed regarding the sensitivity of the control algorithm to the stiffening ratio and the acceleration gain.
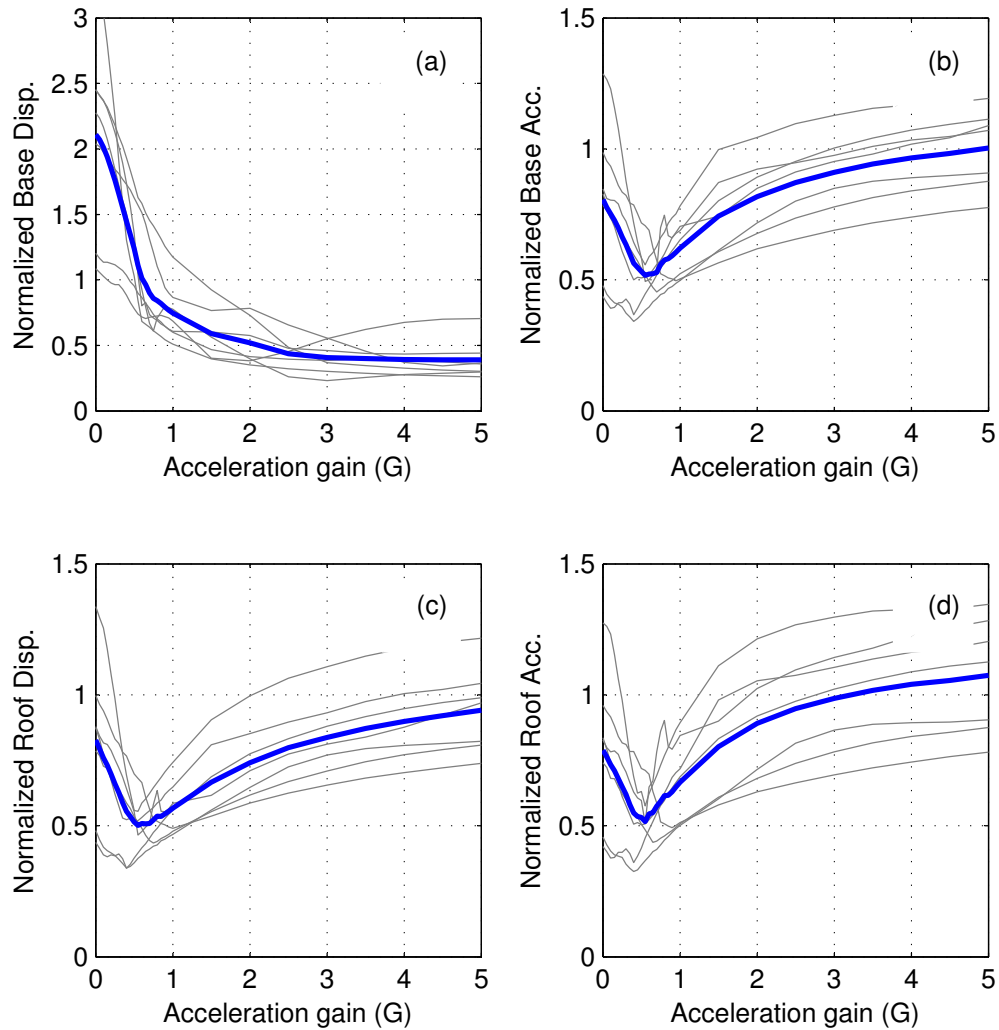
Figure 3.14: Effect of the acceleration gain selection on the performance of the AGC with $\alpha_{max} \leq 10$. The grey and bold curves are events and average normalized peak response, respectively. (a) base displacement, (b) base acceleration, (c) roof displacement, and (d) roof acceleration

3.5.3 Acceleration Feedback Control (AFB)

In the acceleration gain control, only the base and ground accelerations are the required measurements for the control algorithm to operate. The AGC regulates the lateral force resistant capacity of the isolation system based on the instantaneous base shear (approximated by the first two terms of Equation 3.21) and the relative motion between the base slab and the ground. This relative motion is essential for the AGC to perform as desired. According to the desired trade-off between the structural response and the base displacement, an appropriate gain is applied to the relative base slab acceleration. However, control algorithm that depends only on the instantaneous base shear may not result in the desired control of the near-fault base displacement. To illustrate this idea, consider the acceleration feedback control (AFB) determined according to Equation 3.18. In this equation, the control force is regulated to always minimize the shear force in the isolation system. Accordingly, the controller will always use the minimum stiffness of the isolator regardless of the upper stiffening ratio, and hence provides no control over the base displacement. In order for this control logic to provide some controllability to the base displacement, the shear force needs to be exaggerated. This is done by multiplying the total base shear by the base shear gain, G', as follows

$$f_c(t) \simeq G'\{m_b \ddot{u}_b^t + \mathbf{I}_s^T \mathbf{M}_s \ddot{\mathbf{u}}_s^t\} \tag{3.22}$$

In the AFB control given by Equation 3.22, the base slab as well as the floor accelerations need to be measured. Figure 3.15 shows the effect of the base shear gain selection on the structural response. An upper stiffening ratio of ten is considered for this analysis. As can be noticed from the figure, the AFB control can achieve more than 50% reduction to the superstructure demands. However, the base displacement in comparison to the LRB system cannot be reduced. In contrast, the AGC (Figure 3.14) with the same controllable device can substantially reduce the
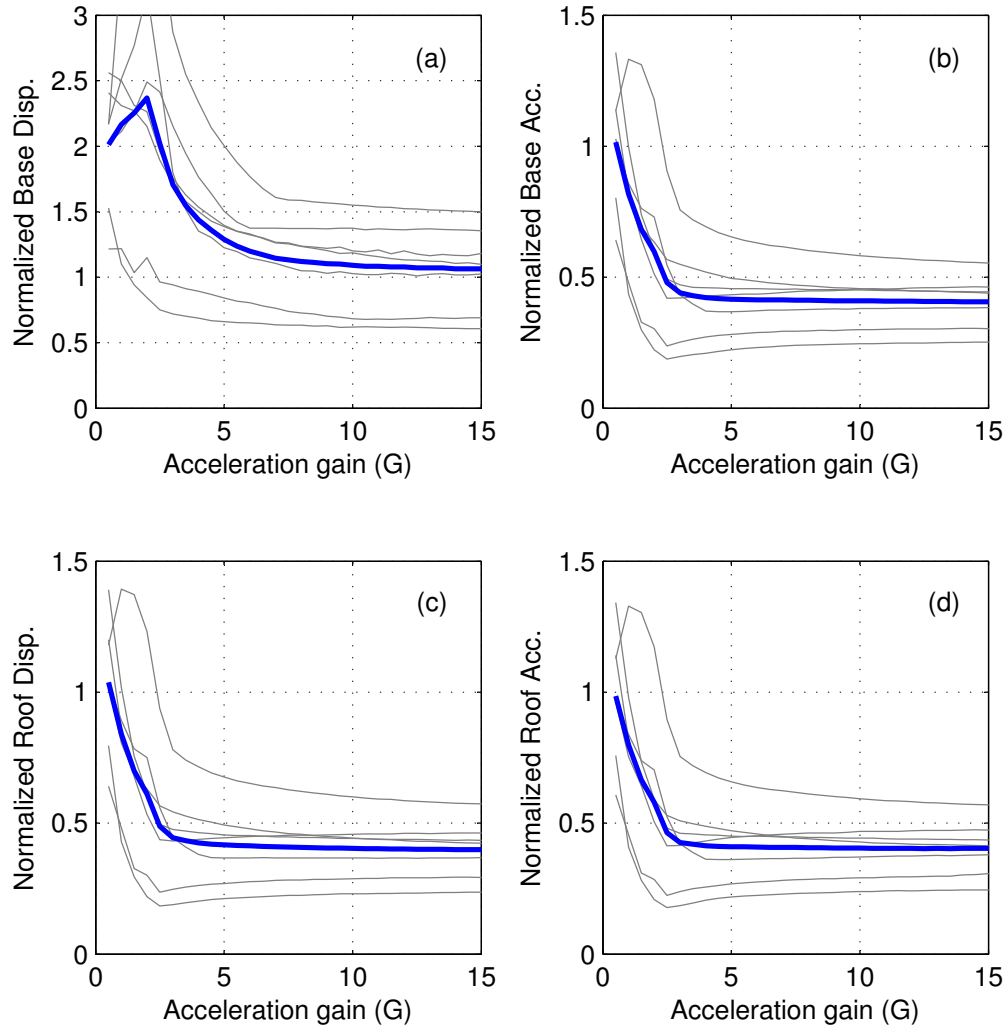
Figure 3.15: Effect of the base shear gain selection on the performance of the AFB control with $\alpha_{max} \leq 10$. The grey and bold curves are events and average peak responses normalized to the LRB, respectively. (a) base displacement, (b) base acceleration, (c) roof displacement, and (d) roof acceleration

near-fault base displacement demand without compromising the performance of the conventionally isolated structure.
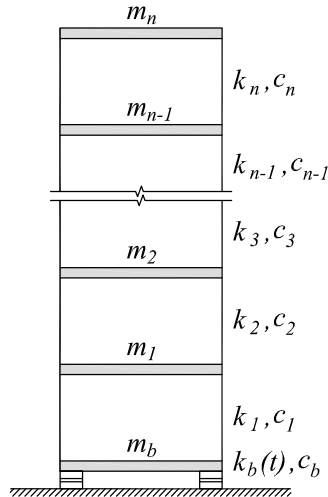
Figure 3.16: Semi-actively controlled smart base isolated structure

3.6   Stability of the Control Algorithms

In the preceding sections, different semi-active control algorithms were suggested for controllable stiffness base isolation systems. Unlike the active control devices, the semi-active devices do not destabilize the controlled structure, as they do not add any external forces to the system. However, it is essential to study the stability robustness of the controlled structure. Consider the semi-actively controlled structure shown in Figure 3.16, the equation of motion for this structure is given by

$$\mathbf{M}\ddot{\mathbf{x}} + \mathbf{C}\dot{\mathbf{x}} + \mathbf{K}\mathbf{x} = -\mathbf{M}\mathbf{I}\ddot{u}_g \tag{3.23}$$

where $\mathbf{M}$, $\mathbf{C}$, and $\mathbf{K}$ are the mass, damping, and stiffness matrices, respectively, $\mathbf{x}$, $\dot{\mathbf{x}}$, and $\ddot{\mathbf{x}}$ are the vectors of displacement, velocity, and acceleration with respect to the ground, respectively, $\ddot{u}_g$ is the ground acceleration, and $\mathbf{I}$ is n-dimensional unit vector. The energy in the system is determined by

$$V = \frac{1}{2}\left[\dot{\mathbf{x}}^T\mathbf{M}\dot{\mathbf{x}} + \mathbf{x}^T\mathbf{K}\mathbf{x}\right] \tag{3.24}$$

which can be considered a Lyapunov function for this system only if $\mathbf{M}$ and $\mathbf{K}$ are positive definite matrices. However, $\mathbf{M}$ is definitely positive definite matrix, as it is a diagonal matrix of the floor mass. The question is whether $\mathbf{K}$ is a positive definite or not, as it has the time variant stiffness term, $k_b(t)$. The stiffness matrix $\mathbf{K}$ for the shown structure is calculated as

$$\mathbf{K} = \begin{bmatrix} k_n & -k_n & 0 & \cdots & 0 \\ -k_n & k_n + k_{n-1} & -k_{n-1} & \cdots & 0 \\ 0 & \ddots & \ddots & \ddots & 0 \\ 0 & \cdots & -k_2 & k_2 + k_1 & -k_1 \\ 0 & \cdots & 0 & -k_1 & k_1 + k_b(t) \end{bmatrix} \tag{3.25}$$

For the $\mathbf{K}$ matrix to be positive definite, it must satisfy the following condition

$$\mathbf{z}^T \mathbf{K} \mathbf{z} > 0 \tag{3.26}$$

where $\mathbf{z}$ is a non-zero n-dimensional vector of real numbers. This condition is satisfied if the time variant base stiffness is positive, ($i.e$ $k_b(t) > 0$) for ($t \geq 0$). The base stiffness $k_b(t)$ is defined by Equation 3.11, and repeated here for convenience

$$k_b(t) = k_0 + k_v(t) \tag{3.27}$$

in which $k_v(t)$ is the variable stiffness part and is bounded by the maximum and minimum stiffness ratios so that

$$\alpha_{min} k_0 \leq k_v(t) \leq \alpha_{max} k_0 \tag{3.28}$$

Therefore, $k_b(t)$ is always positive as long as $(\alpha_{min} > -1)$. Since the lower bound in this study is $(\alpha_{min} = -0.7)$, Equation 3.24 can be considered as a Lyapanov function. Its derivative can be expressed as

$$\frac{dV}{dt} = \dot{\mathbf{x}}^T \mathbf{M}\ddot{\mathbf{x}} + \dot{\mathbf{x}}^T \mathbf{K}\mathbf{x} \tag{3.29}$$

For the system to be asymptotically stable, the rate of change of the system energy should be decreasing with time. In other words, Equation 3.29 needs to be negative definite. Substituting from Equation 3.23 into Equation 3.29, the derivative of the Lyapanov function can be written as

$$\frac{dV}{dt} = -\dot{\mathbf{x}}^T \mathbf{C}\dot{\mathbf{x}} - \dot{\mathbf{x}}^T \mathbf{M}\mathbf{I}\ddot{u}_g \tag{3.30}$$

In Equation 3.30, the last term on the right hand side can be disregarded for the stability analysis, as $(\lim_{t\to\infty}(\ddot{u}_g) = 0)$. The damping term of the right hand side represents the energy dissipated in the system. However, this term implies that the rate of change of system energy is negative semi-definite as $(-\dot{\mathbf{x}}^T \mathbf{C}\dot{\mathbf{x}} = 0 \ when \ \dot{\mathbf{x}} = 0)$. From the system dynamics (Equation 3.23), $(\dot{\mathbf{x}} = 0)$ implies that when $t \to \infty$

$$\mathbf{M}\ddot{\mathbf{x}} = -\mathbf{K}\mathbf{x} \tag{3.31}$$

It can be inferred form Equation 3.31 that the system cannot reach an equilibrium state unless when $(\mathbf{x} = 0)$. Using LaSalle's invariant principle indicates that the origin is a locally asymptotically stable point and hence the system is asymptotically stable.

3.7 Response History of the Base Isolated Systems

In this section, the response history analyses are performed on the benchmark structure described in Section 3.2 subject to far-field and near-fault scaled ground motion records listed in Tables 3.2 and 3.3. In order to evaluate the effectiveness of the semiactive control algorithms proposed for base isolation systems incorporating MRE controllable stiffness isolators, the isolation system for the benchmark structure was obtained first using conventional lead rubber bearing (LRB). The response is compared to the counterpart structures equipped with MRE isolation system using the minimal acceleration control (MAC) and the acceleration gain control (AGC). The base material stiffness of the MRE bearing, k_0, is taken as the postyielding stiffness of the isolation system of the benchmark building (*i.e.* $k_0 = k_b = 232kN/m$). As discussed earlier, the proposed control algorithms have limited control on the base displacement, as they were original designed to reduce the structural acceleration. In addition, the maximum upper limit of the stiffening ratio of the MRE base isolation system, which was experimentally obtained by Usman et al. (2009), puts an extra limitation to the controllability of the base displacement. However, in order to evaluate the effectiveness of the proposed control algorithms, it is assumed that the MRE device or another similar one, can achieve a higher stiffening ratio, α. Based on the results of the sensitivity analyses given in Section 3.5.2.1, the maximum and minimum stiffening ratios, α, and the gain, G, used for the controls are shown in Table 3.4. The table summarized values are selected for the highest base displacement control as well as the best performance of the superstructure.

The median, which is defined as the geometric mean and given by the exponential of the average of the natural log values of the data points, as well as the 84th percentile, defined as the median times the exponent of the standard deviation of the natural log of the data points (Shome et al., 1997; Gupta and Krawinkler, 1999; FEMA, 2000), are

Table 3.4: Semi-active control notations and details.

Control ID	Stiffening Ratio		Acceleration Gain
	α_{min}	α_{max}	G
MAC-1	-0.7	0.7	N/A
MAC-2	-0.7	2.0	N/A
AGC-1	-0.7	0.7	0.8
AGC-2	-0.7	2.0	0.8
AGC-3	-0.7	0.7	2.0
AGC-4	-0.7	2.0	2.0

used to represent the statistical values of the peak quantities of the response history analyses under the effect of the considered ground motions. Theses parameters are calculated based on Shome et al. (1997) definition as

$$\hat{x} = e^{\frac{1}{n}\sum_{i=1}^{n}\ln x_i} \tag{3.32a}$$

$$\delta = \sqrt{\frac{\sum_{i=1}^{n}(\ln x_i - \ln \hat{x})^2}{n-1}} \tag{3.32b}$$

$$84^{th}\ percentile = \hat{x}e^{\delta} \tag{3.32c}$$

where $\hat{x}$ is the median value of total of n data points, and δ is the standard deviation of the natural logs of the data. These parameters are used to represent the coefficient of variation in the data series and are useful for the probabilistic and performance-based design.

3.7.1 Response to the Far-Field Records

The ten pairs of the scaled ground motions given in Table 3.2 are used in this section to evaluate the efficacy of the proposed semi-active control algorithms under the far-field excitations. The displacement response-history and the isolation system

force-displacement relationship with the MAC against the passive LRB subjected to the *1994 Northridge, Canyon Country*, EQ02, are shown in Figures 3.17 and 3.18, respectively. Figures 3.19 and 3.20 show the displacement response-history and the isolation system force-displacement relationship for the system with AGC, under the same earthquake record. The same response quantities due to the *1992 Landers*, EQ11, are also shown in Figures 3.21 to 3.24. The MAC algorithm results in residual displacement in the isolation level, and this behavior was observed under most of the considered ground motions. In addition, increasing the maximum stiffening ratio (from $\alpha_{max} = 0.7$ to $\alpha_{max} = 2.0$) neither helps reducing the base displacement nor the residual displacement. In contrast, the AGC was found to be self-centering under the effect of all the considered ground motions. On the other hand, the effect of higher stiffening ratio is remarkable on the base displacement, as can be observed in Figures 3.19 and 3.23.

The base displacement can be controlled by increasing the acceleration gain used for the AGC, as discussed in Section 3.5.2.1. However, increasing the gain will only allow the control law to reach the full capacity of the isolation system, which is bounded by the maximum stiffening ratio, and should lead to less reduction in the superstructure response quantities. This can be observed from Figures 3.12, 3.13, and 3.14. By comparing the isolation system force-displacement relationships for the systems with the same upper bound of stiffening ratio (*e.g.* algorithms AGC-1 versus AGC-3 and AGC-2 versus AGC-4) that is shown in Figures 3.20 and 3.24, it is obvious that the increased acceleration gain, G, reduces the base displacement. However, comparing the systems with the same acceleration gain (*e.g.* algorithms AGC-1 versus AGC-2 and AGC-3 versus AGC-4), it can be noticed that the upper bound of the stiffening ratio, α, is more effective in reducing the base displacement. The acceleration gain only defines the trade-off between the base displacement and the
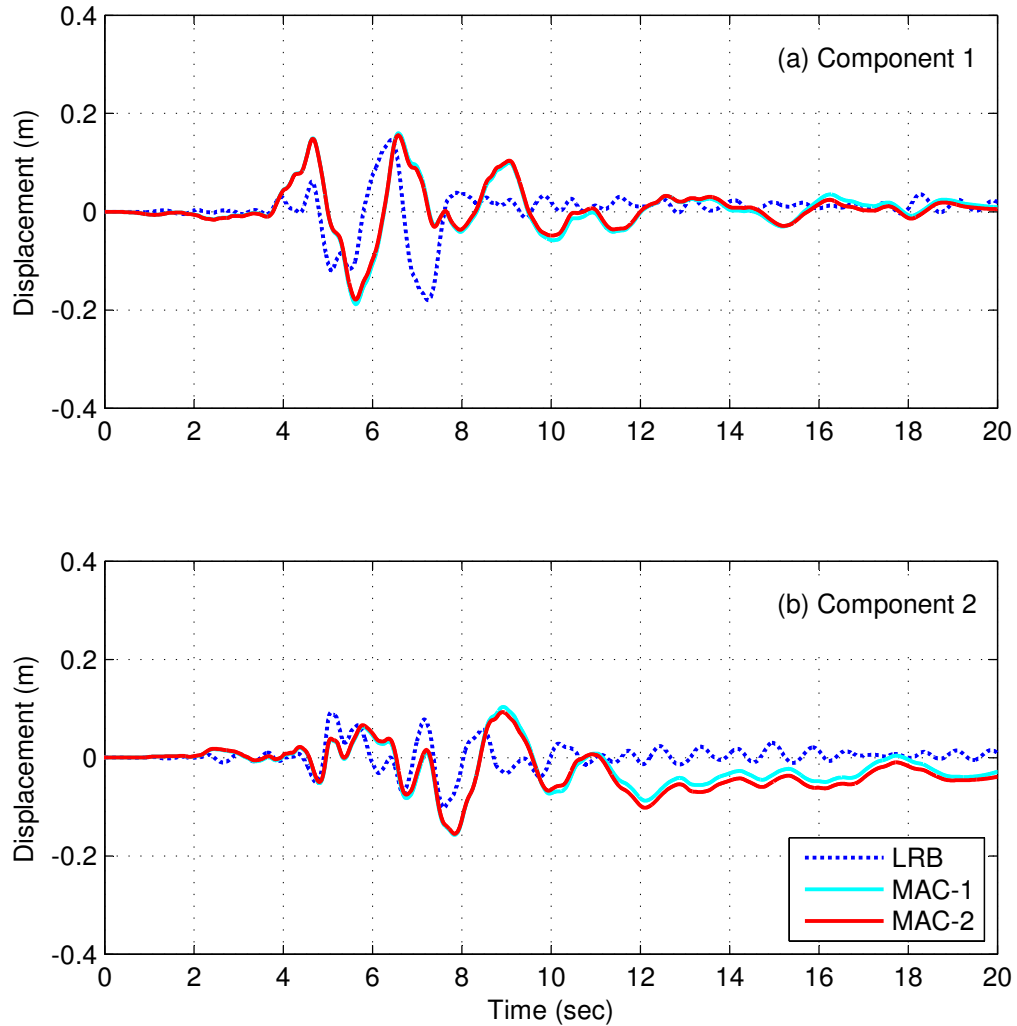
Figure 3.17: Base displacement response history for MAC systems versus LRB under far-field EQ02 (Northridge, Canyon Country)

superstructure response. Based on this observation, it can be concluded that variable stiffness devices that possess a wider range of variable stiffness are more likely to provide adequate control on the base displacement with the acceleration gain control, as will be seen in the following section with AGC-5.

Studying the statistical summary of the base displacement peak responses that is shown in Figure 3.29, the same observation regarding the effect of the increased
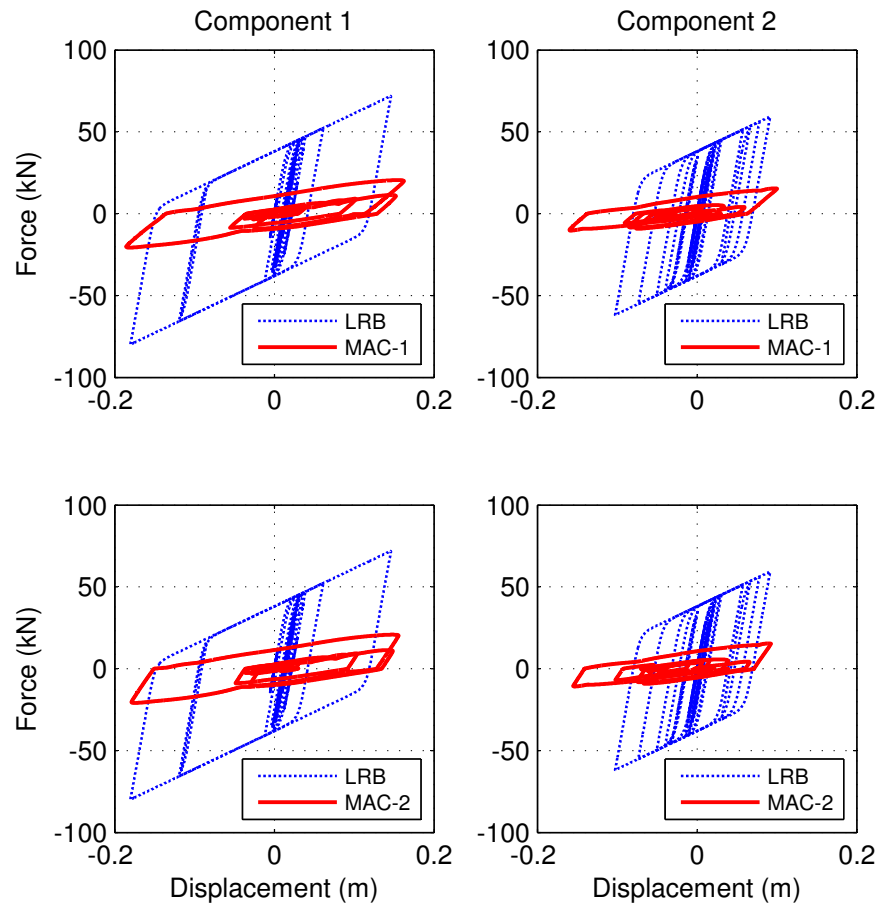
Figure 3.18: Passive LRB vs MAC isolation systems force-displacement relationship, under far-field EQ02 (Northridge, Canyon Country)
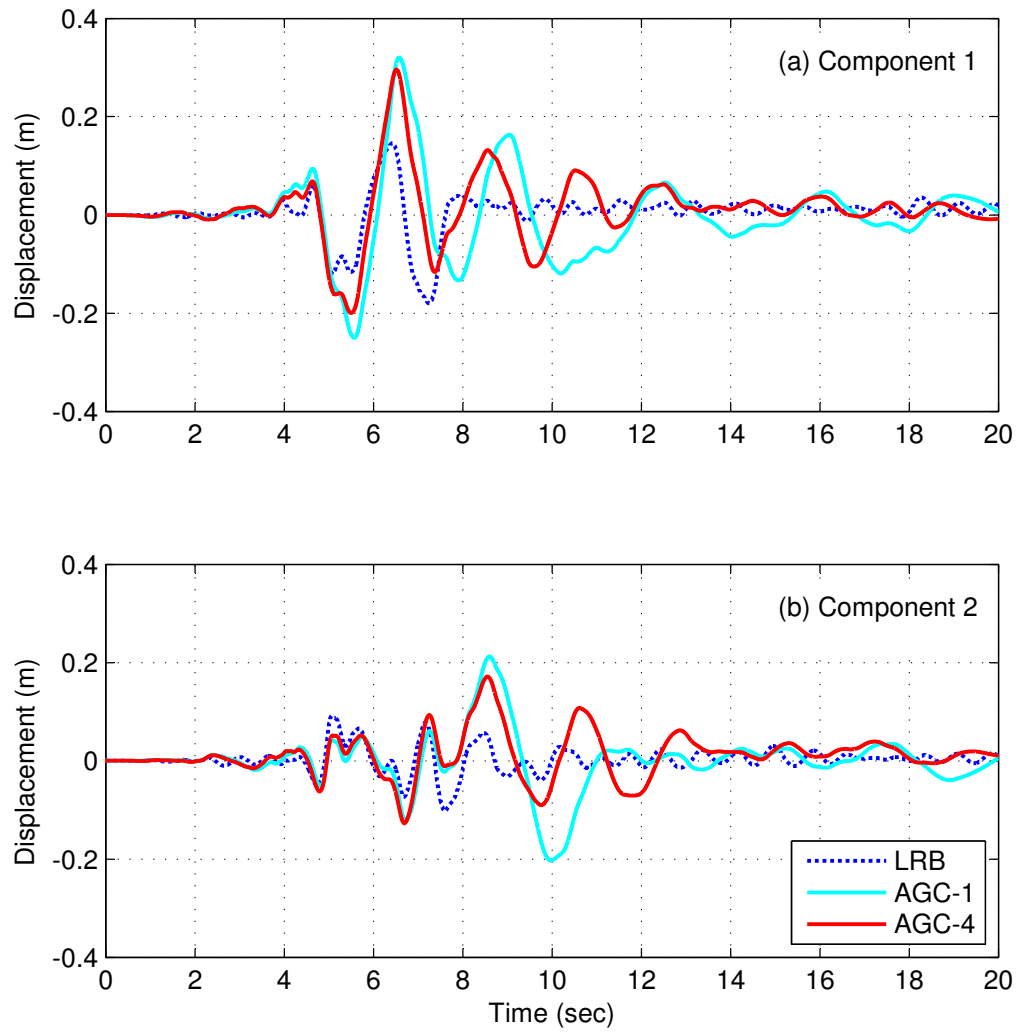
Figure 3.19: Base displacement response history for AGC systems versus LRB under far-field EQ02 (Northridge, Canyon Country)
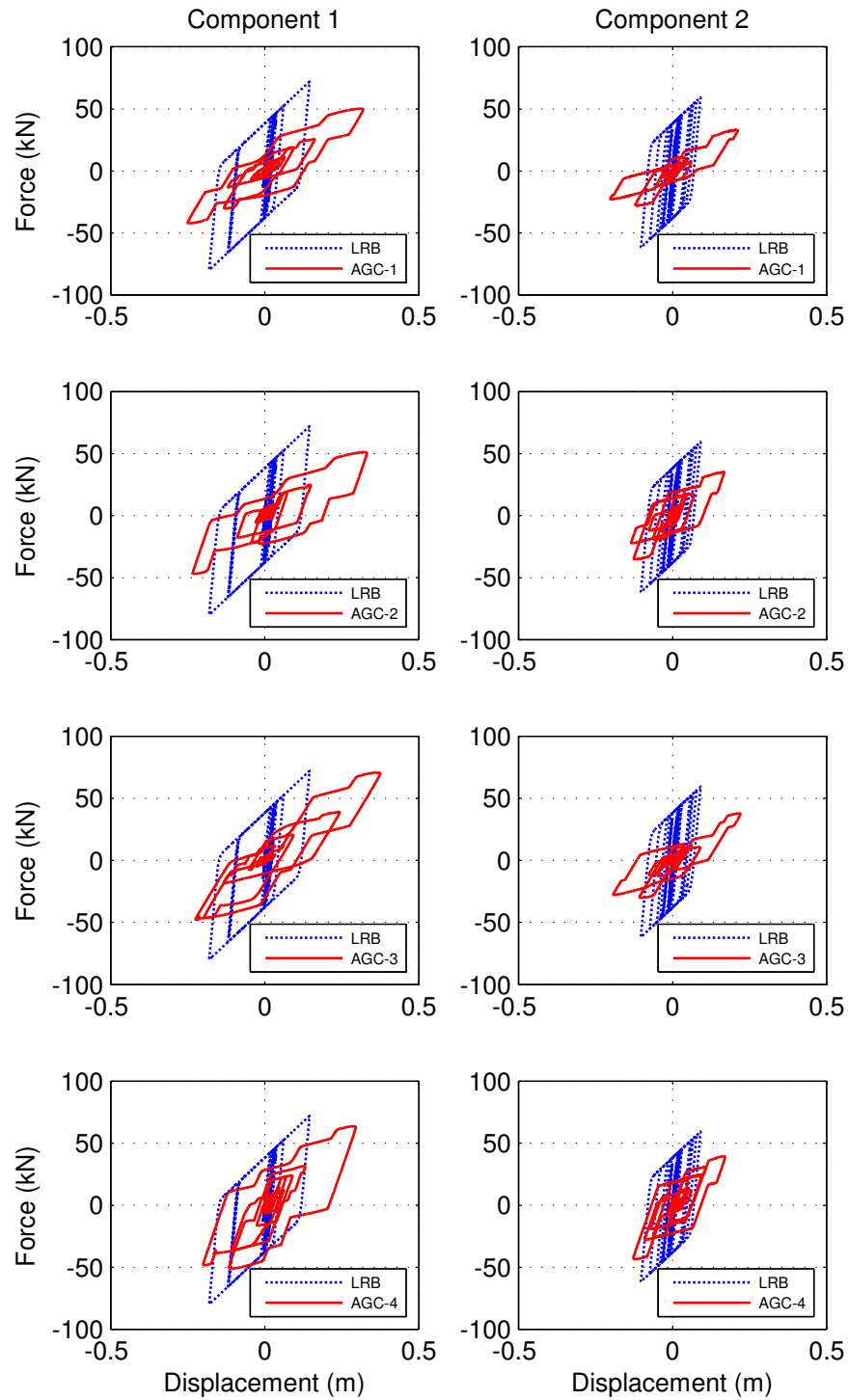
Figure 3.20: Passive LRB vs AGC isolation systems force-displacement relationship, under far-field EQ02 (Northridge, Canyon Country)
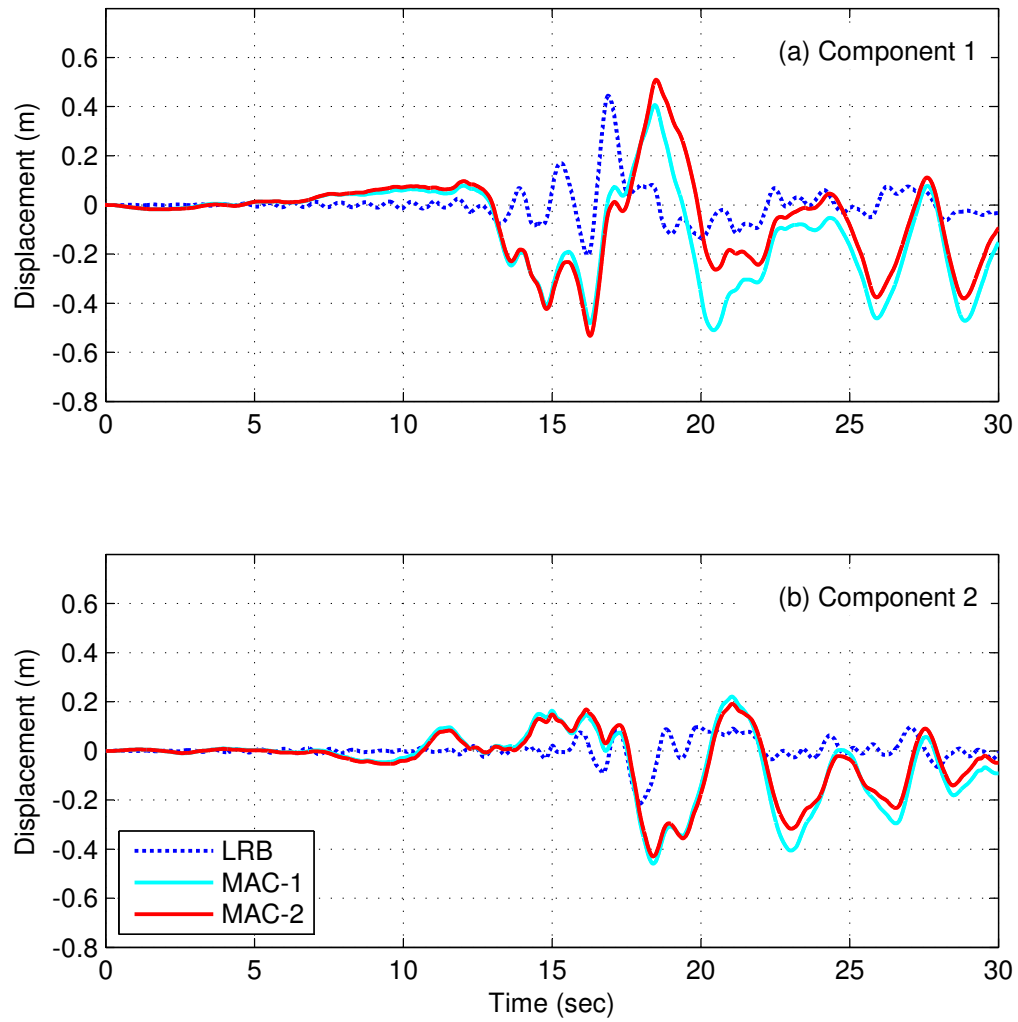
Figure 3.21: Base displacement response history for MAC systems versus LRB under far-field EQ11 (Landers)
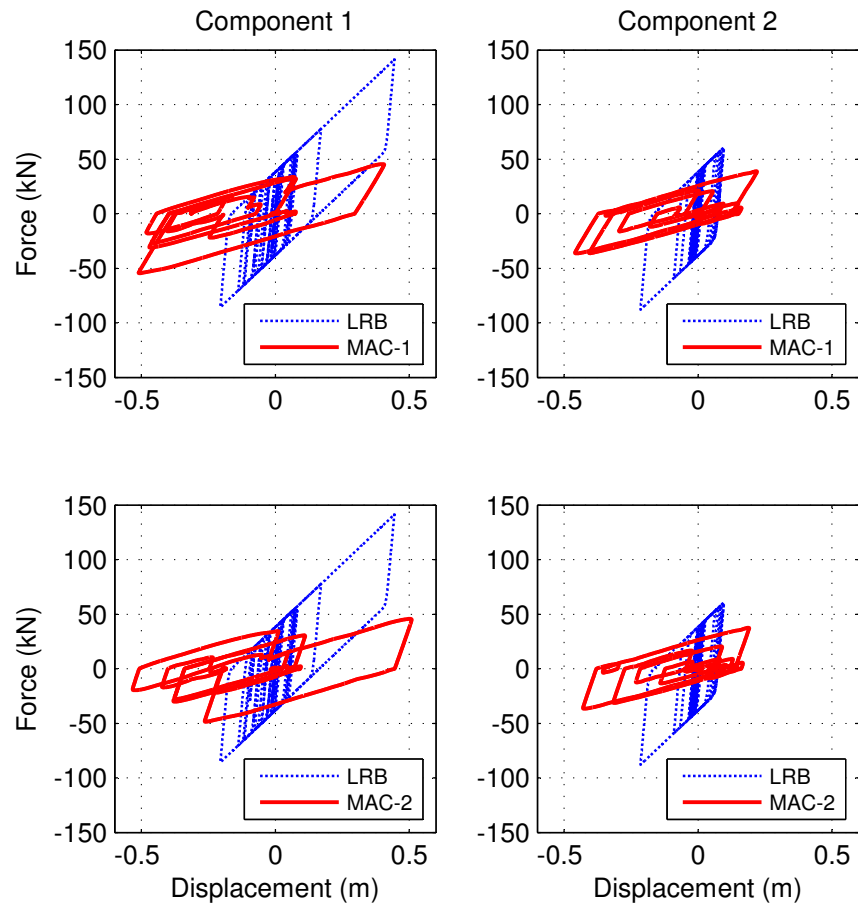
Figure 3.22: Passive LRB vs MAC isolation systems force-displacement relationship, under far-field EQ11 (Landers)
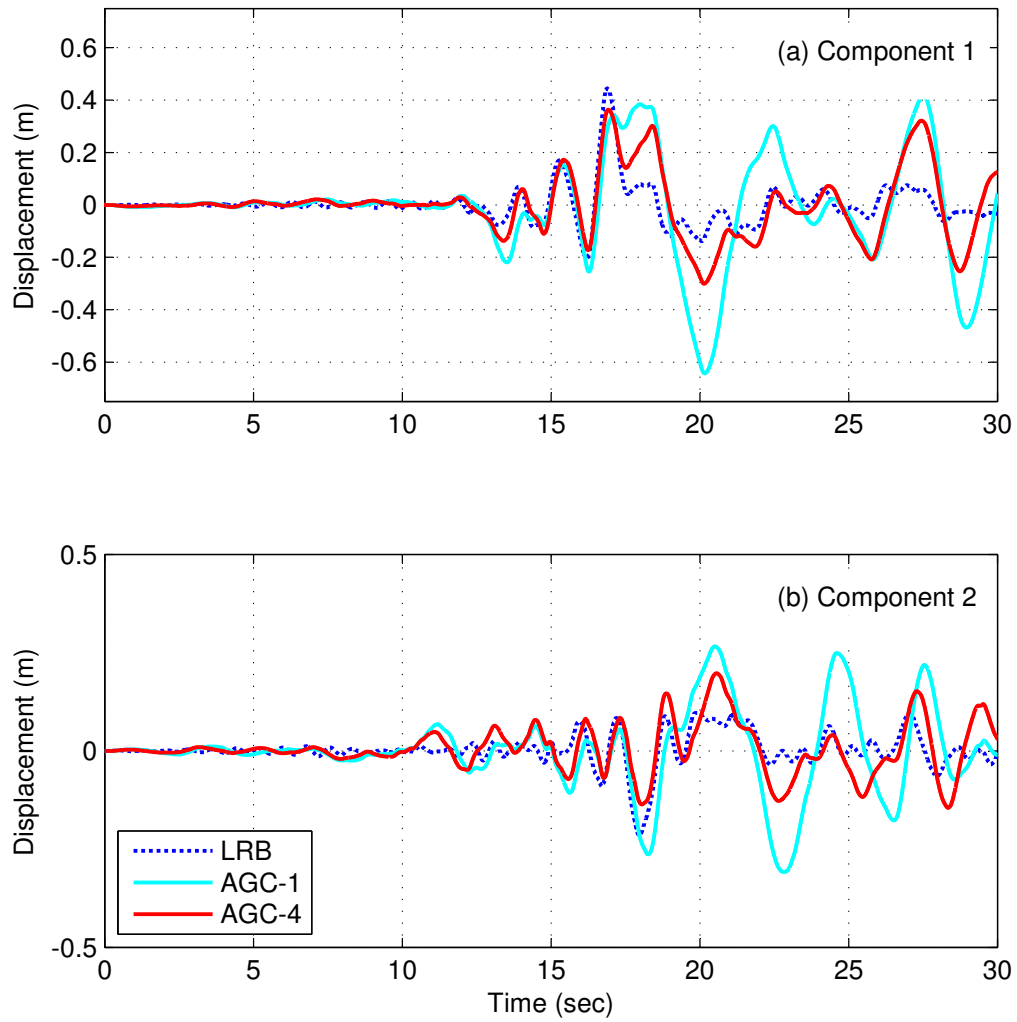
Figure 3.23: Base displacement response history for AGC versus LRB under far-field EQ11 (Landers)
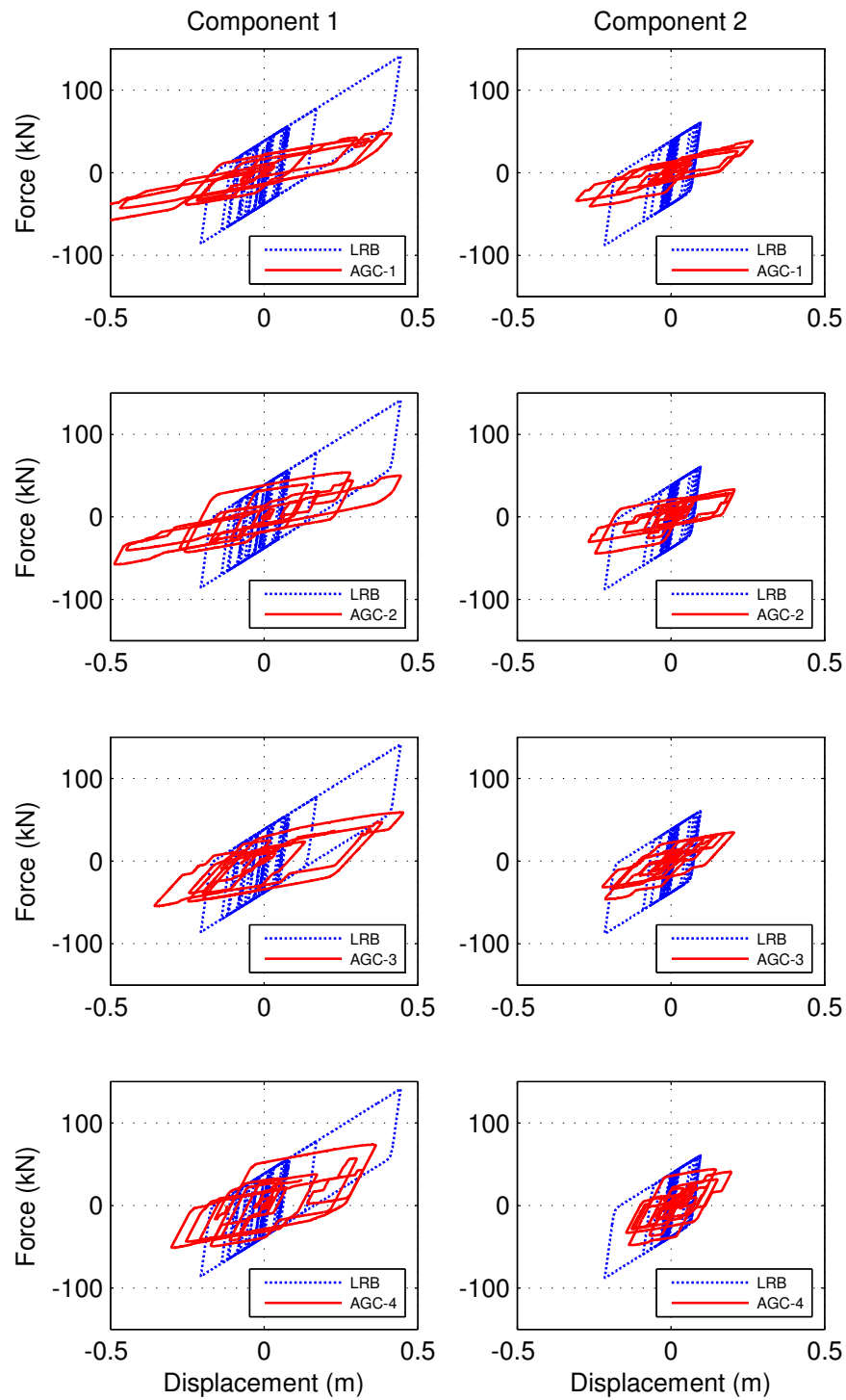
Figure 3.24: Passive LRB vs AGC isolation system force-displacement relationship, under far-field EQ11 (Landers)

acceleration gain and the upper bound of the stiffening ratio, holds true. On the other hand, the effect of the upper bound of stiffening ratio on the base acceleration is insignificant with the MAC law, but may slightly help controlling the base displacement. With AGC, as can be seen in Figure 3.30, the base acceleration slightly increases with the increase of the stiffening ratio upper limit, α_{max}.

In terms of the base acceleration demand, the MAC systems are capable of achieving up to 75% reduction in the base acceleration compared to the LRB system. The AGC systems provide less reduction of up to 60% only, as can be seen from Figures 3.25 to 3.28 that show the base acceleration response history for EQ02 (1994 Northridge, Canyon Country) and EQ11 (1992 Landers). On the other hand, the effect of increased stiffening ratio on the base acceleration response history is not significant on the system with the MAC algorithms. However, a slight increase in the base acceleration, compared to the passive LRB system, is noticeable when the stiffening ratio and/or the acceleration gain are increased.

In terms of the superstructure seismic demands, the MAC law provides significant reduction in both the acceleration and displacement demands on the superstructure, as shown in Figures 3.31 to 3.33. A comparison of the superstructure seismic demands normalized to the demands on the fixed base structure is given in Table 3.5, while the structural seismic demands of the proposed control strategies normalized to the seismic demands of the LRB system are given in Table 3.6. As can be inferred from the tables, the proposed smart base isolation strategies provide significant reduction to the seismic demands on both the fixed base and the conventionally isolated structures subjected to the far-field ground motion records.
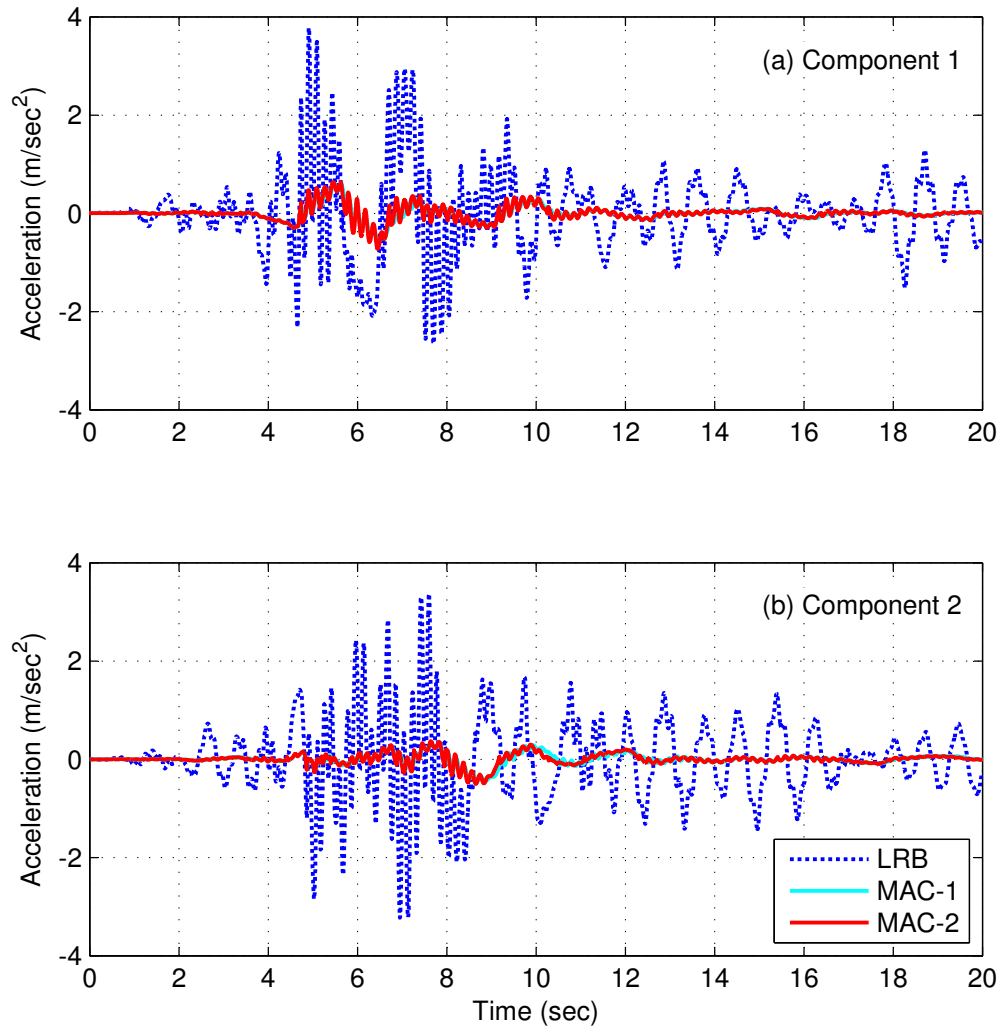
Figure 3.25: Base acceleration response history for LRB versus MAC under far-field EQ02 (Northridge, Canyon Country)

Table 3.5: Superstructure seismic demands normalized to the fixed base structure under the far-field records.

Demand	LRB	MAC-1	MAC-2	AGC-1	AGC-2	AGC-3	AGC-4
Roof Displacement	0.161	0.037	0.038	0.073	0.080	0.087	0.104
Roof Acceleration	0.171	0.032	0.035	0.066	0.074	0.079	0.096
1st floor shear	0.162	0.042	0.042	0.081	0.087	0.097	0.112
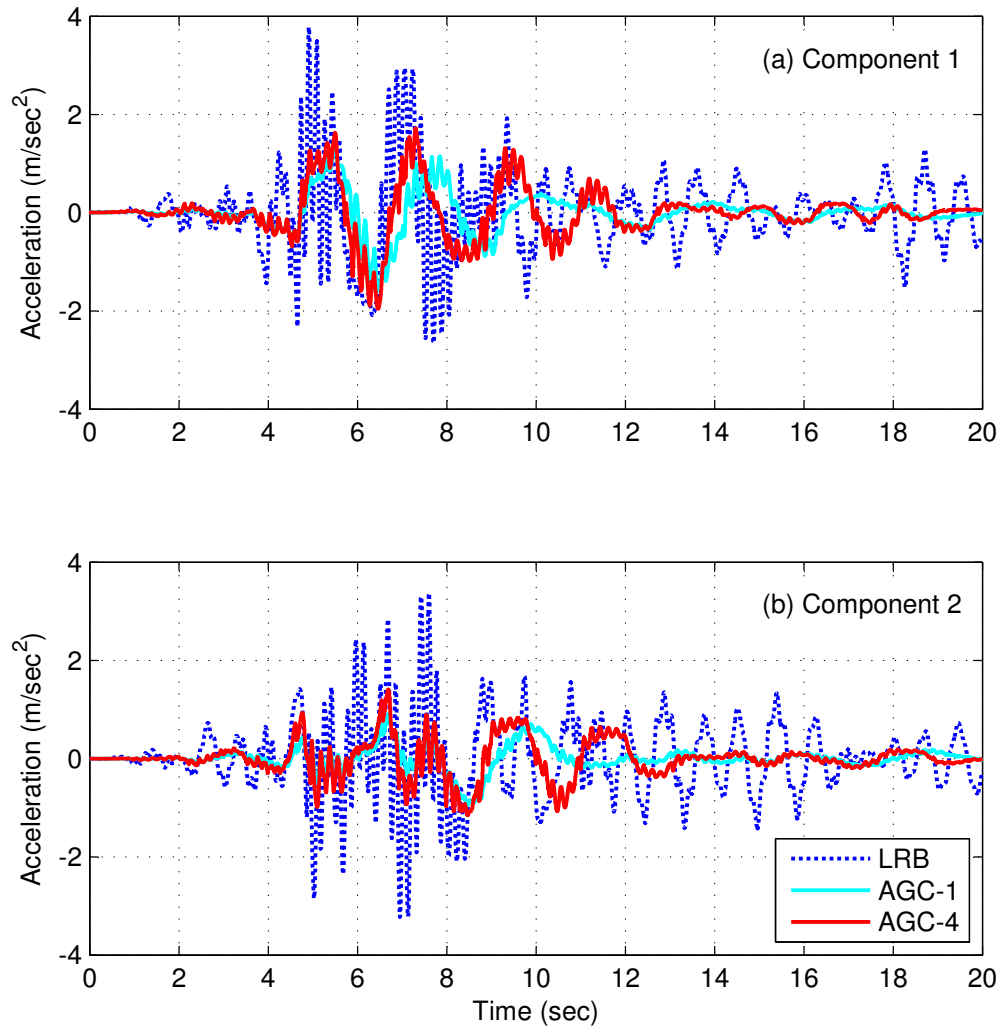
Figure 3.26: Base acceleration response history for LRB versus AGC under far-field EQ02 (Northridge, Canyon Country)

Table 3.6: Structural seismic demands normalized to the LRB system under the far-field records.

Demand	MAC-1	MAC-2	AGC-1	AGC-2	AGC-3	AGC-4
Base Displacement	1.372	1.279	1.446	1.268	1.412	1.185
Base Acceleration	0.201	0.213	0.409	0.453	0.489	0.589
Roof Displacement	0.231	0.236	0.452	0.494	0.543	0.643
Roof Acceleration	0.189	0.203	0.387	0.434	0.462	0.564
1st floor shear	0.260	0.259	0.497	0.538	0.595	0.692
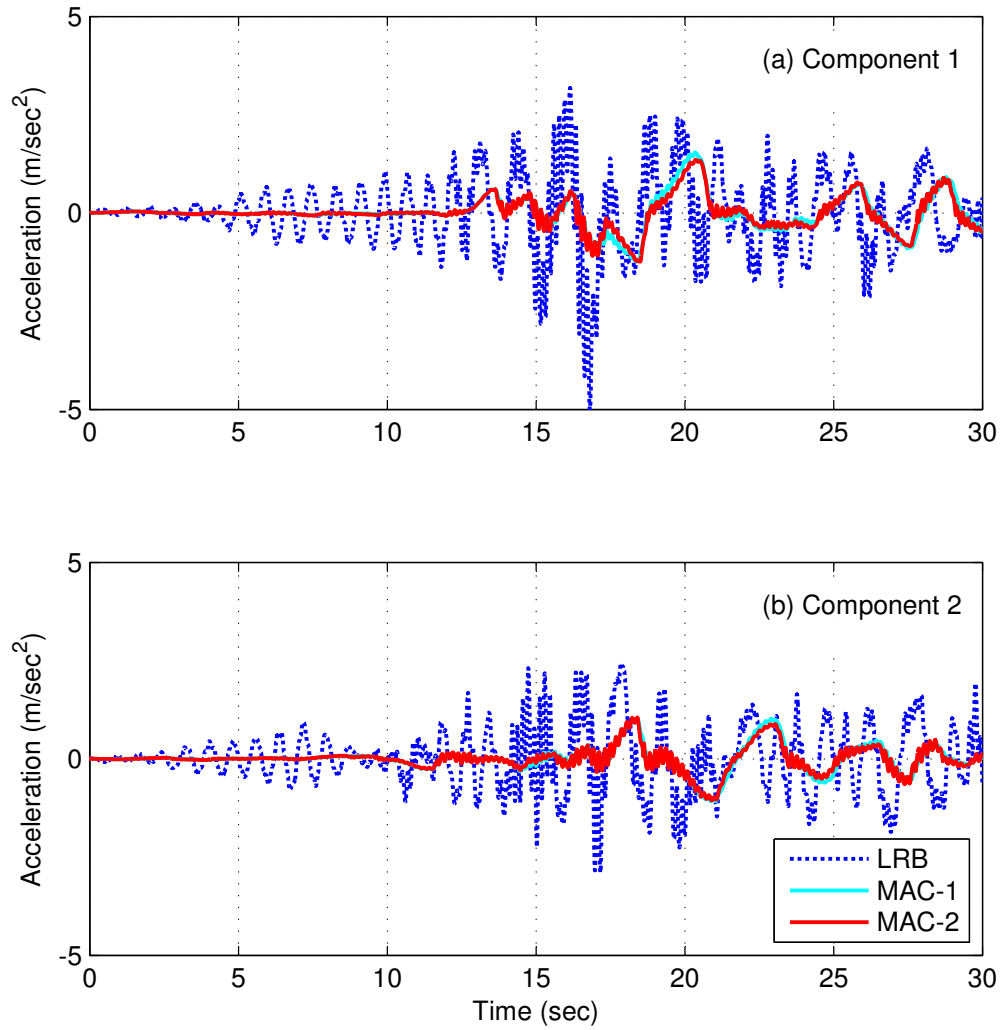
Figure 3.27: Base acceleration response history of LRB versus MAC under far-field EQ11 (Landers)
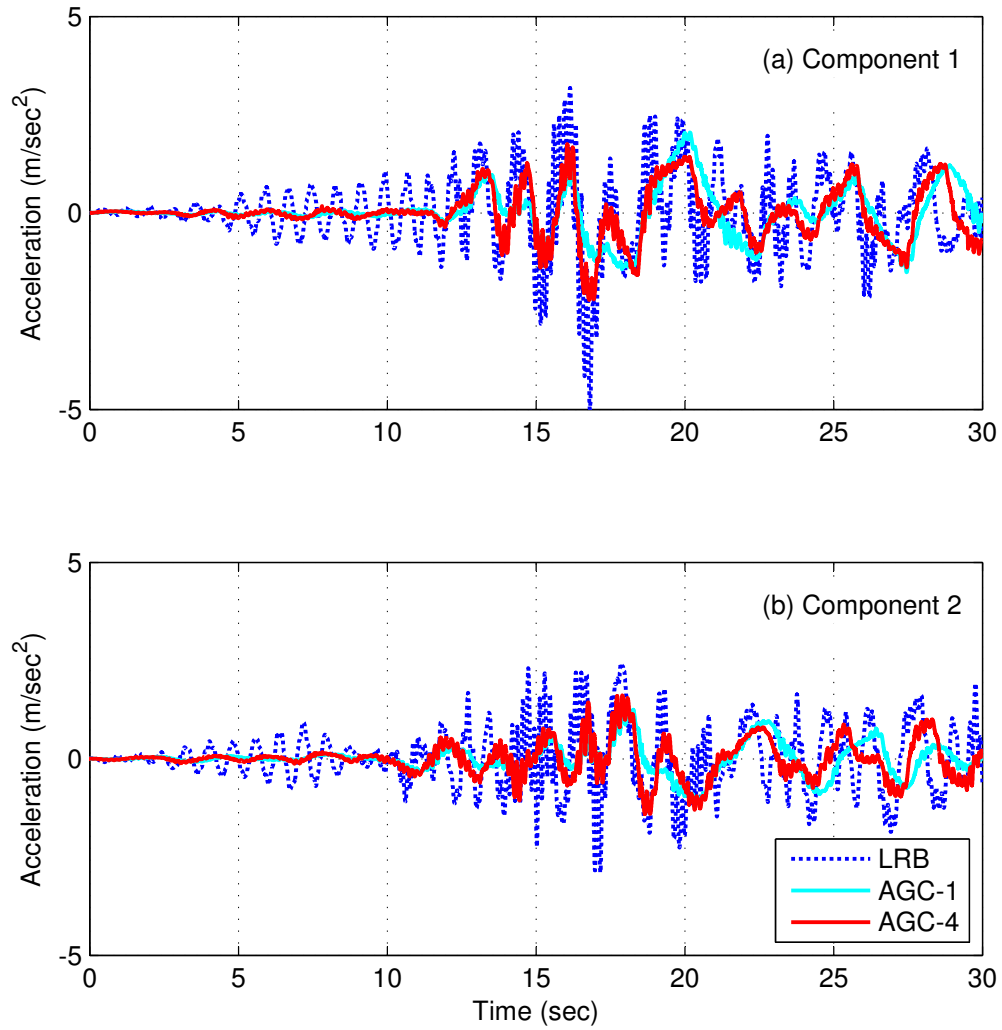
Figure 3.28: Base acceleration response history of LRB versus AGC under far-field EQ11 (Landers)
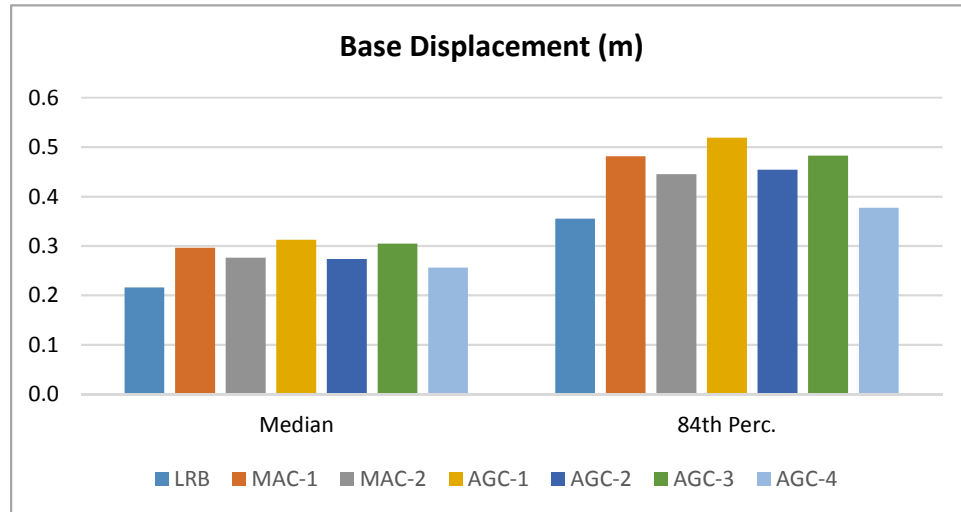
Figure 3.29: Summary of the far-field base displacement response.
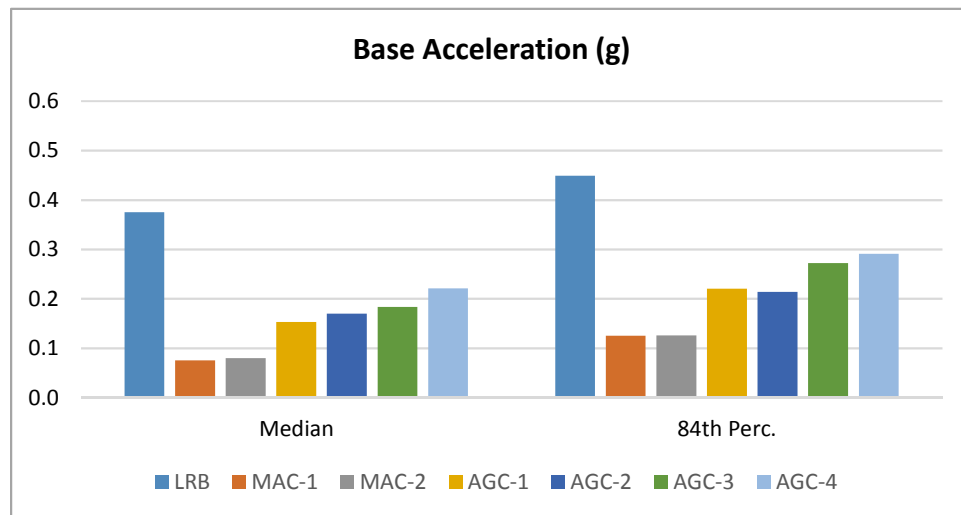
Figure 3.30: Summary of the far-field base total acceleration response.
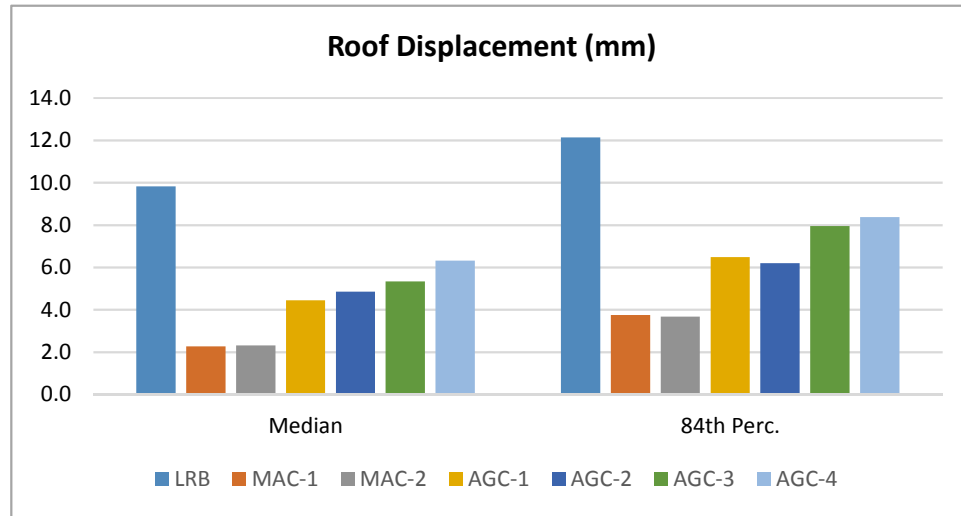
Figure 3.31: Summary of the far-field roof displacement response relative to the basemat.
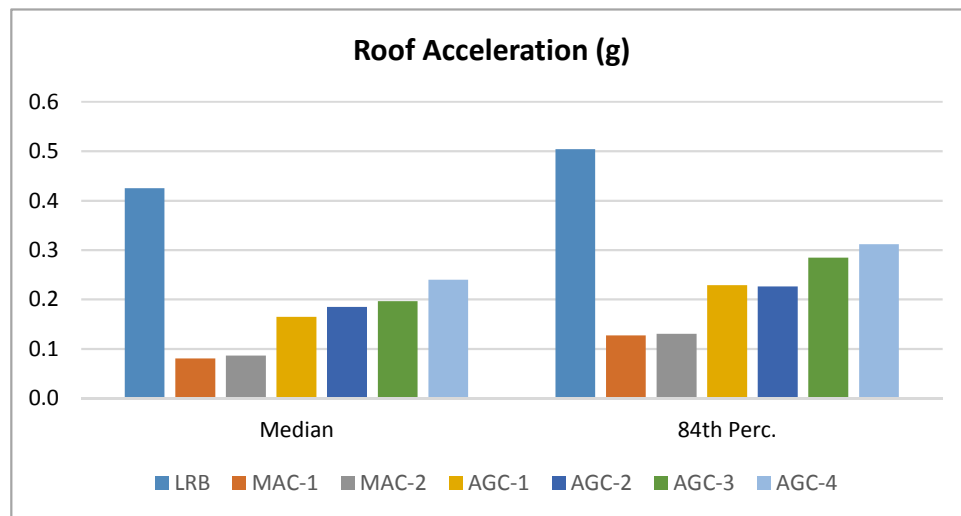
Figure 3.32: Summary of the far-field roof total acceleration response.
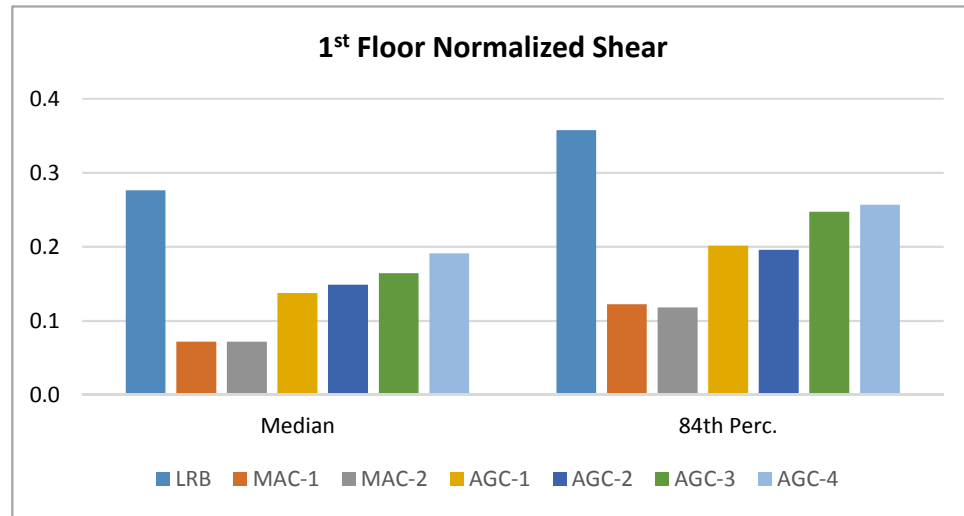
Figure 3.33: Summary of the far-field 1st floor shear response.

3.7.2 Response to the Near-Fault Records

The fourteen pairs of the scaled ground motions given in Table 3.3 are used in this section to evaluate the efficacy of the proposed semi-active control algorithms under the effect of near-fault excitations. The displacement response-history and the isolation system force-displacement relationship of the structure with the MAC against the passive LRB system subjected to the *1998 Loma Prieta*, EQ05, are shown in Figures 3.34 and 3.35, respectively. Figures 3.36 and 3.37 show the displacement response-history and the isolation system force-displacement relationship for the system with AGC under the same earthquake record. From the figures, the MAC algorithm results in residual displacement in the base slab as in the case under the far-field records. This behavior was observed under most of the considered ground motions. In this case however, increasing the maximum stiffening ratio (from $\alpha_{max} = 0.7$ for MAC-1 to $\alpha_{max} = 2.0$ for MAC-2) provides a slight improvement in the base displacement but with an increased residual displacement (Figure 3.34b). In contrast, the AGC has self-centering feature that was observed under the effect of all the considered

ground motions. The AGC system also results in less base displacement demand than the MAC system. The effect of higher stiffening ratio on the performance of the AGC is noticeable on the base displacement response history, as can be observed in Figures 3.36 and 3.37.

The base displacement can be controlled by increasing the acceleration gain used for the AGC (see Figures 3.12 to 3.14). However, increasing the gain will only lead to the full capacity of the isolation system, which is basically limited by the maximum allowable stiffening ratio of the variable stiffness device. Although increasing the acceleration gain reduces the base displacement, it leads to minimal reduction of the seismic demands on the structural system compared to the LRB. Comparing the isolation system force-displacement relationships for the systems with the same maximum stiffening ratio (*e.g.* algorithms AGC-1 versus AGC-3 and AGC-2 versus AGC-4) that are shown in Figure 3.37, as in the case under the far-field ground motions the effect of increasing the acceleration gain (G) is less significant on the base displacement response than the maximum allowable stiffening ratio. The latter is the most effective parameter in controlling the base displacement. This can also be concluded by studying the force-displacement relationship of the systems with the same acceleration gain and different maximum stiffening ratios (*e.g.* algorithms AGC-1 versus AGC-2 and AGC-3 versus AGC-4).

Studying the statistical summary of the base displacement peak responses that is shown in Figure 3.38, the same observation regarding the effect of the increased acceleration gain and the upper bound of the stiffening ratio, holds true. On the other hand, the effect of the maximum stiffening ratio on the base acceleration is insignificant with either MAC or AGC algorithms. This can be seen in Figure 3.39 where the base acceleration barely changes with the increased stiffening ratio.

In terms of response reduction, the MAC systems are capable of achieving up to
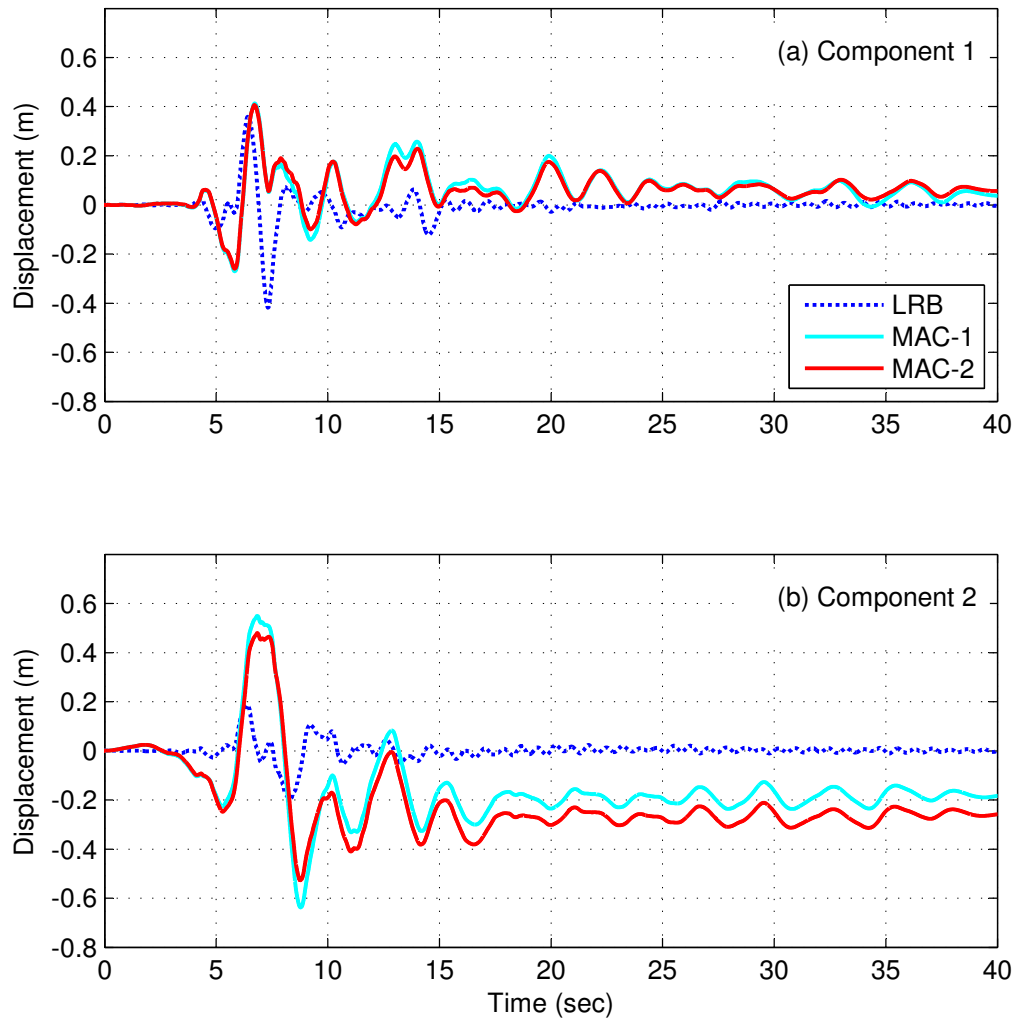
Figure 3.34: Base displacement response history for MAC systems versus LRB under near-fault EQ05 (1989 Loma Prieta)
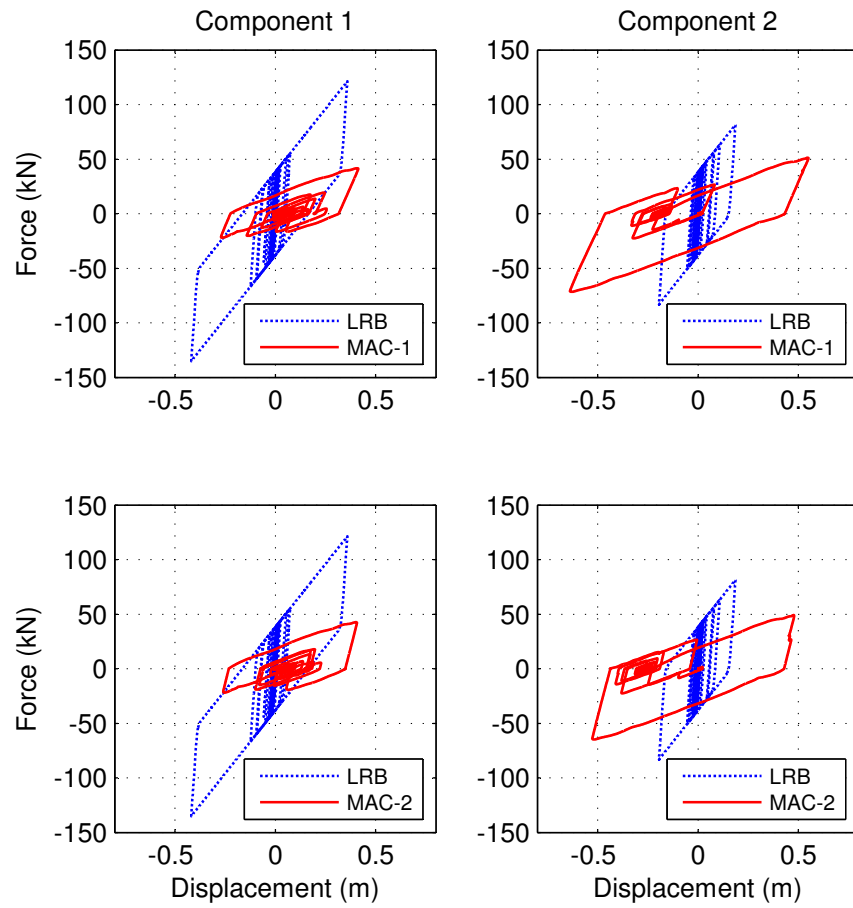
Figure 3.35: Passive LRB vs MAC isolation systems force-displacement relationship, under near-fault EQ05 (1989 Loma Prieta)
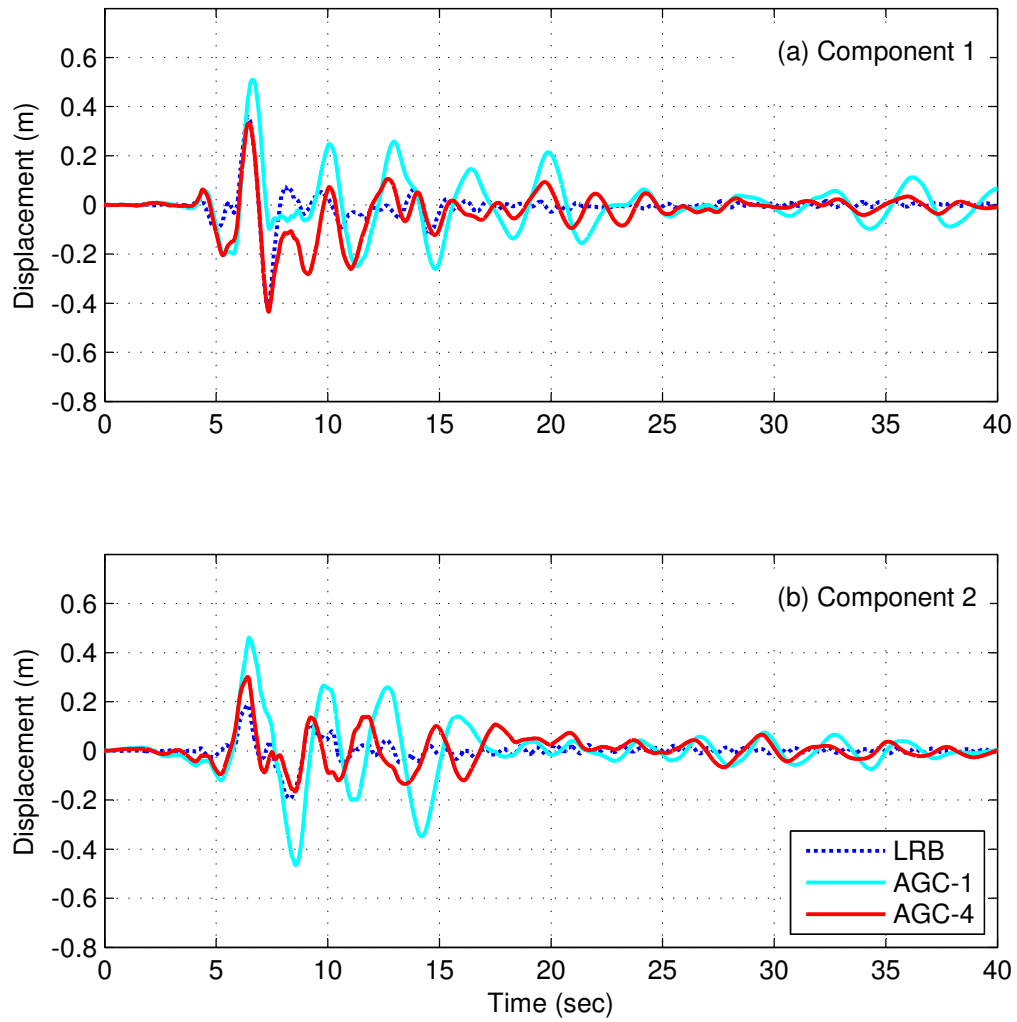
Figure 3.36: Base displacement response history for AGC systems versus LRB under near-fault EQ05 (1989 Loma Prieta)
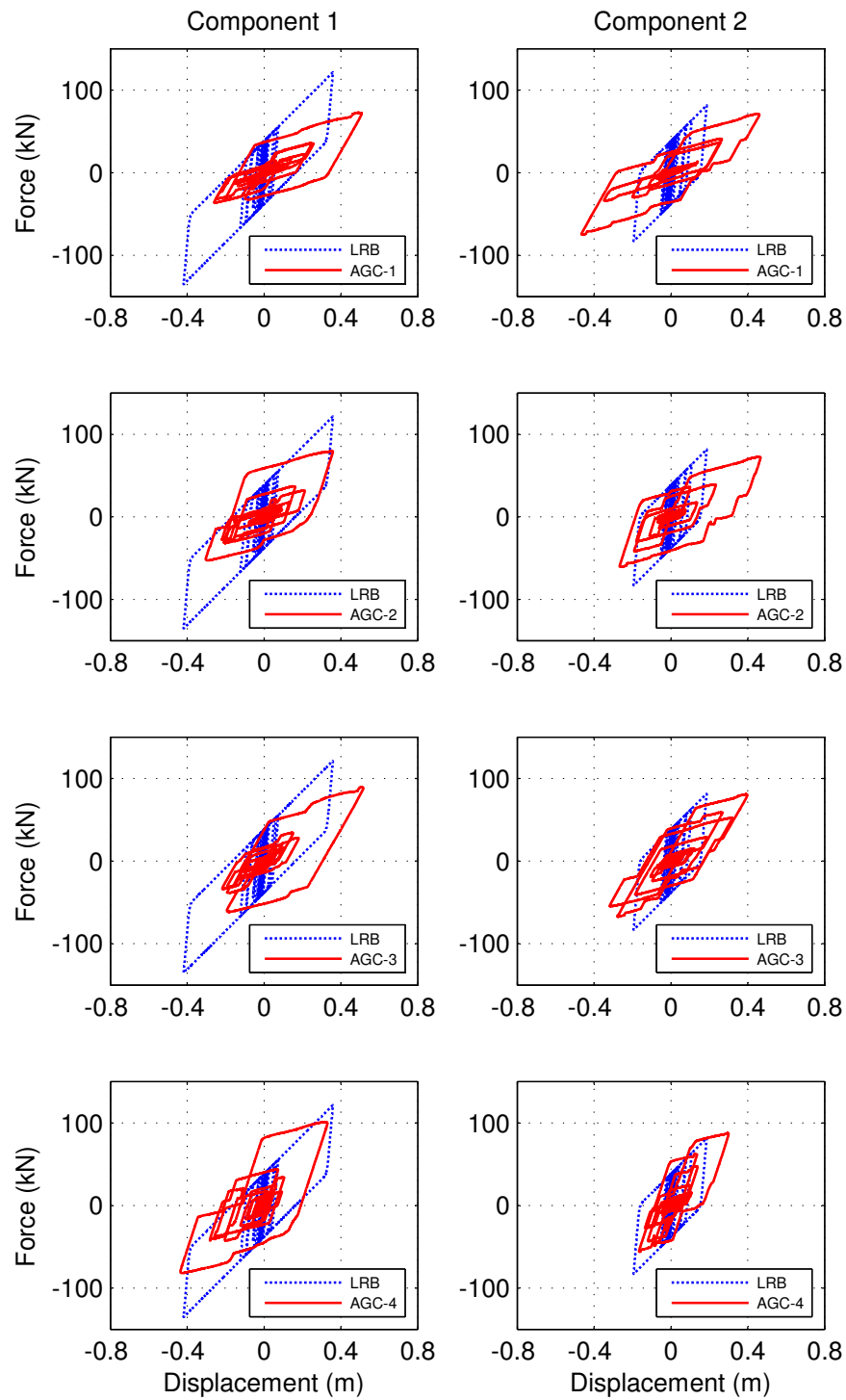
Figure 3.37: Passive LRB vs AGC isolation systems force-displacement relationship, under near-fault EQ05 (1989 Loma Prieta)
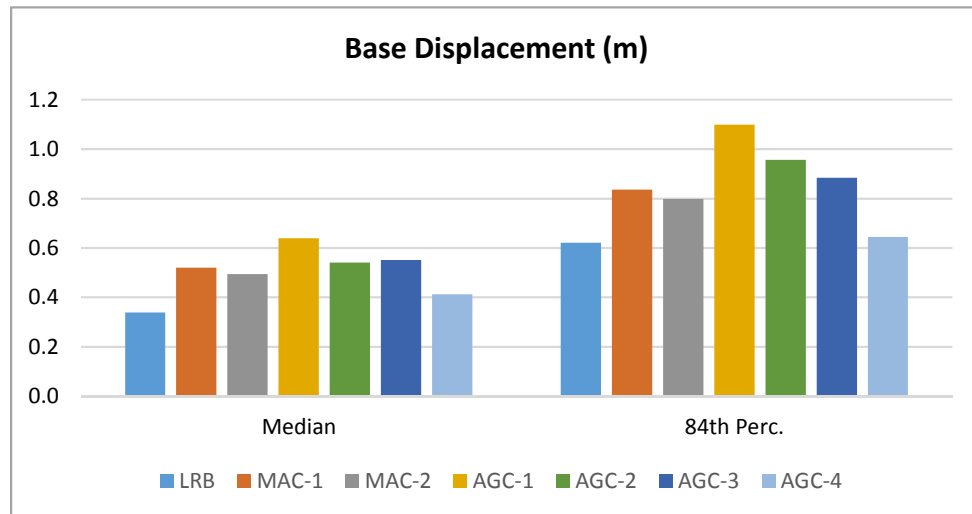
Figure 3.38: Summary of the near-fault base displacement response.
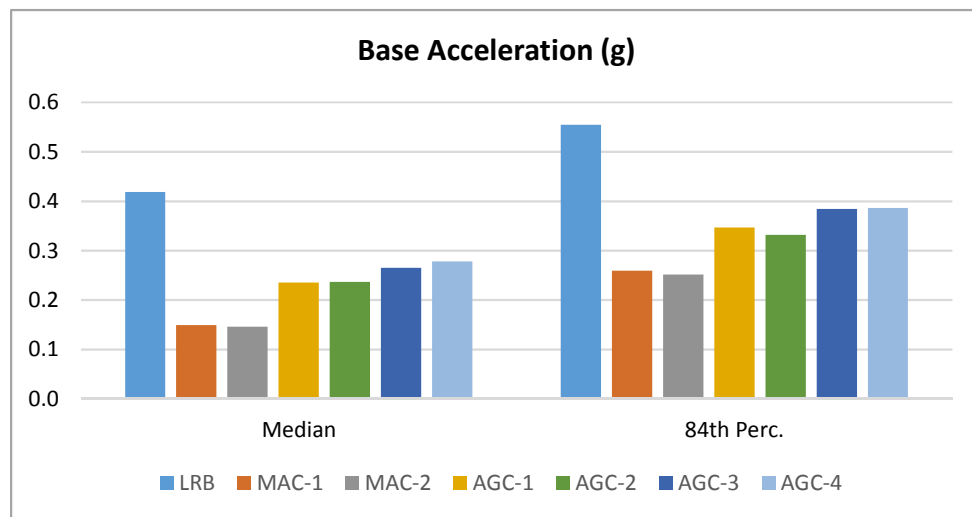
Figure 3.39: Summary of the near-fault base total acceleration response.

Table 3.7: Superstructure seismic demands normalized to the fixed base structure under the near-fault records.

Demand	LRB	MAC-1	MAC-2	AGC-1	AGC-2	AGC-3	AGC-4
Roof Displacement	0.220	0.084	0.082	0.131	0.130	0.146	0.151
Roof Acceleration	0.210	0.071	0.069	0.112	0.113	0.126	0.134
1st floor shear	0.236	0.097	0.093	0.150	0.147	0.166	0.169

65% reduction in the base acceleration compared to the passive LRB system, while the AGC systems provide less reduction of up to 44% only, as shown in Table 3.8. Also Figures 3.40 and 3.41 show an example of the base acceleration response history under the effect of EQ05 (*1989 Loma Prieta*). The effect of increased stiffening ratio on the base acceleration response history is not significant for the system with the MAC algorithms. However, a slight increase in the base acceleration, compared to the LRB system, is noticeable when the stiffening ratio or the acceleration gain are increased.

In terms of the superstructure seismic demands, the MAC law provides significant reduction in both the acceleration and displacement demands on the superstructure, as shown in Figures 3.42 to 3.44. A comparison of the superstructure seismic demands on the considered systems normalized to the demands on the fixed base structure is given in Table 3.7. The structural seismic demands of the proposed control strategies normalized to the seismic demands of the LRB system are given in Table 3.8. As can be inferred from the tables, the proposed smart base isolation strategies provide significant reduction to the seismic demands on near-fault structures compared to fixed base and conventionally isolated structures. As an example of the superstructure performance, Figures 3.45 and 3.46 show the fifth story drift and the roof total acceleration response histories, respectively, under the EQ05 (*1989 Loma Prieta*) for different control strategies.

In the preceding analyses, the proposed semi-active control strategies showed good

Figure 3.40: Base acceleration response history for LRB versus MAC under near-fault EQ05 (1989 Loma Prieta)

Table 3.8: Structural seismic demands normalized to the LRB system under the near-fault records.

Demand	MAC-1	MAC-2	AGC-1	AGC-2	AGC-3	AGC-4
Base Displacement	1.539	1.463	1.893	1.599	1.632	1.219
Base Acceleration	0.357	0.349	0.563	0.566	0.633	0.664
Roof Displacement	0.384	0.372	0.597	0.591	0.667	0.687
Roof Acceleration	0.337	0.331	0.533	0.540	0.603	0.640
1st floor shear	0.412	0.394	0.636	0.622	0.703	0.717
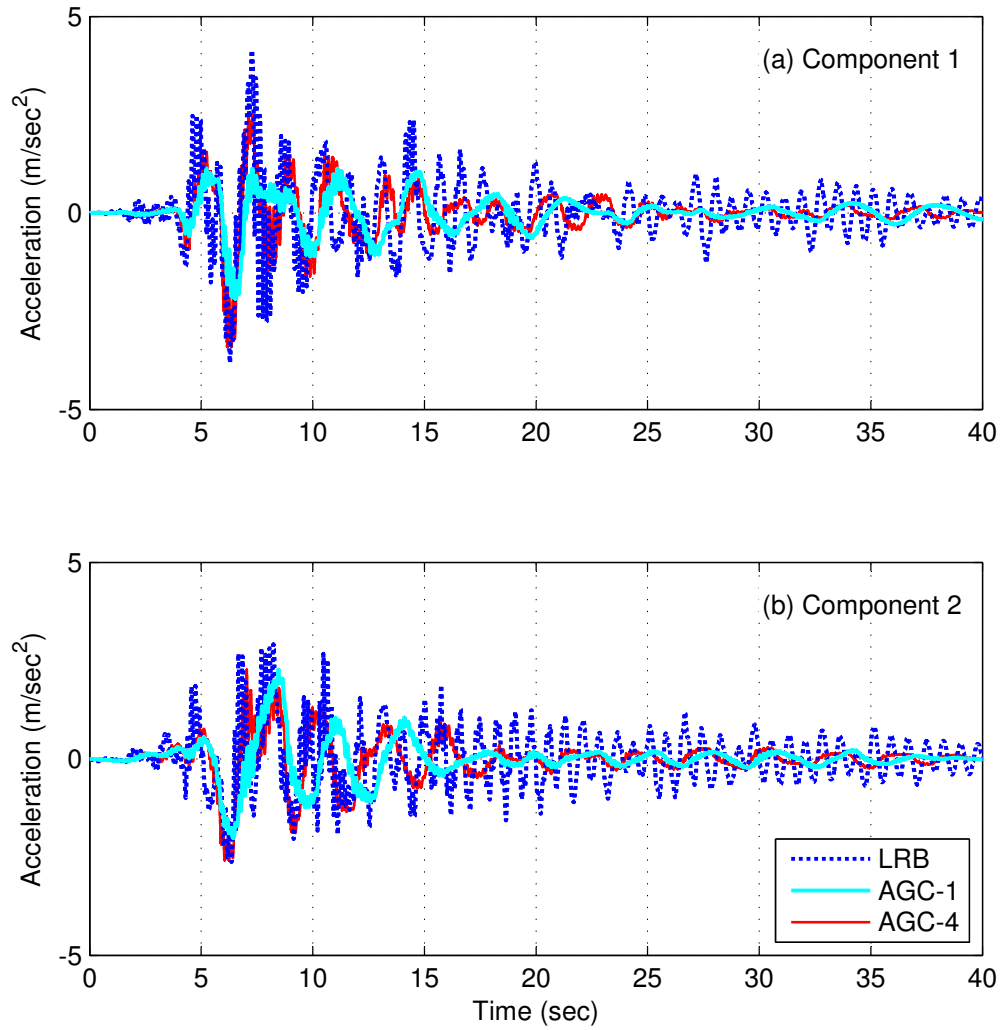
Figure 3.41: Base acceleration response history for LRB versus AGC under near-fault EQ05 (1989 Loma Prieta)
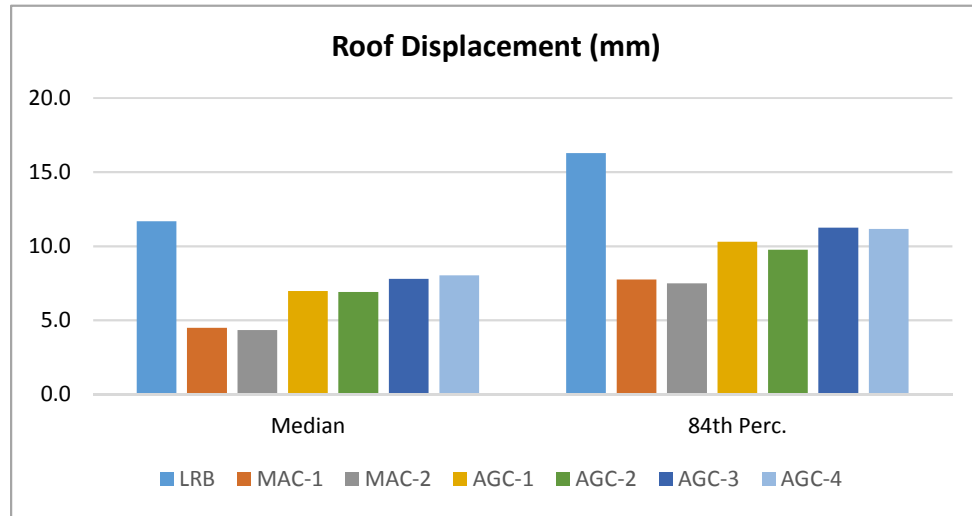
Figure 3.42: Summary of the near-fault roof displacement response relative to the base slab.
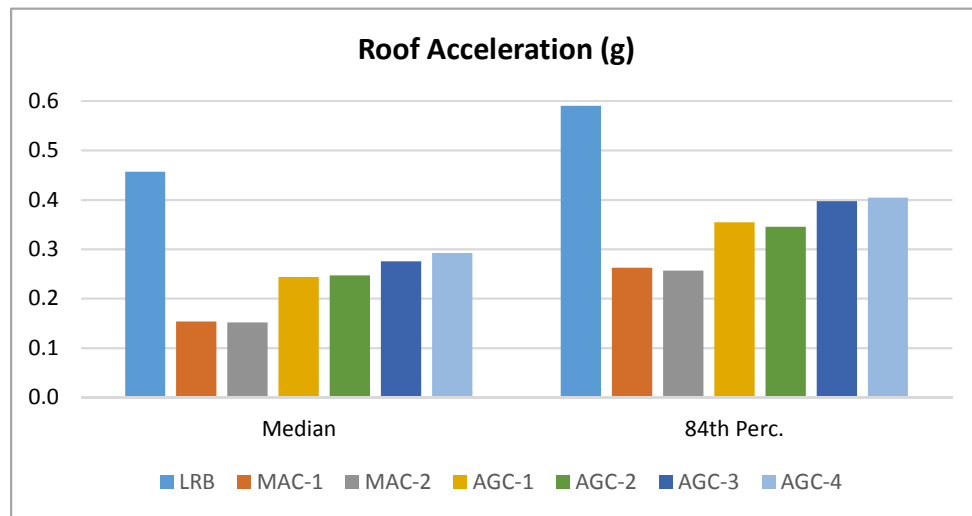
Figure 3.43: Summary of the near-fault roof total acceleration response.
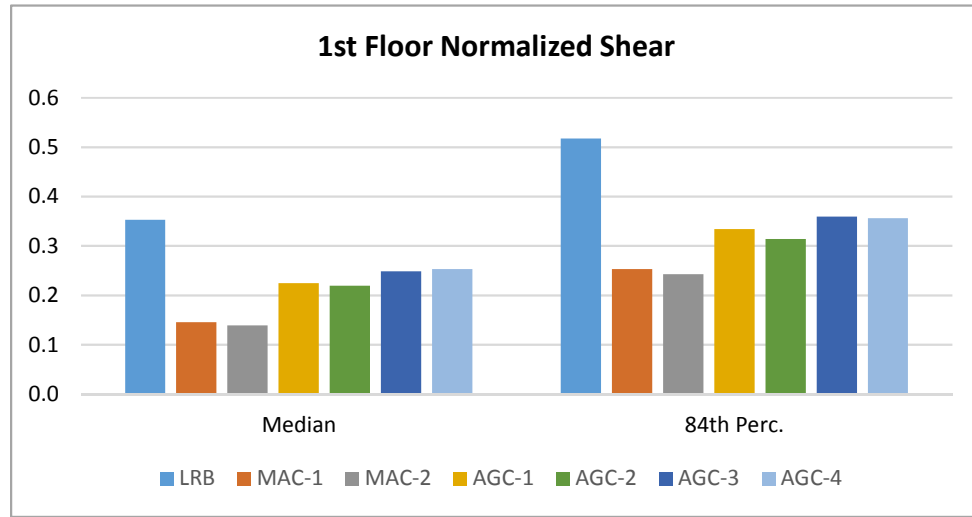
Figure 3.44: Summary of the near-fault 1st floor shear response.

improvement to the seismic demands on structures located near active faults. However, the near-fault ground motions are characterized by long velocity pulses accompanied by large ground displacement. This phenomena leads to limited implementation of the base isolation systems for the near-fault sites. This is due to the fact that the isolated structures have relatively long period of vibration that may cause resonance with the near-fault motions. Large ground displacement increases the possibility of destabilizing the isolators that may need to be uneconomically large in size to overcome the large base displacement demand. The proposed control strategies are developed for variable stiffness base isolation systems employing MR elastomers (Usman et al., 2009). Because of the limited range of stiffness variation of such devices, there was no reduction of the near-fault base displacement demand. But there are other variable stiffness devices with wider range of stiffening ratio, for instance the MRE 35% Fe that can provide a stiffening ratio of up to 50 (Winthrop et al., 2005).

Assuming a maximum change of the isolation system stiffness as high as ten times the base material stiffness, the base displacement demand can be reduced by up to 35% of the conventional isolation systems by implementing the AGC, without
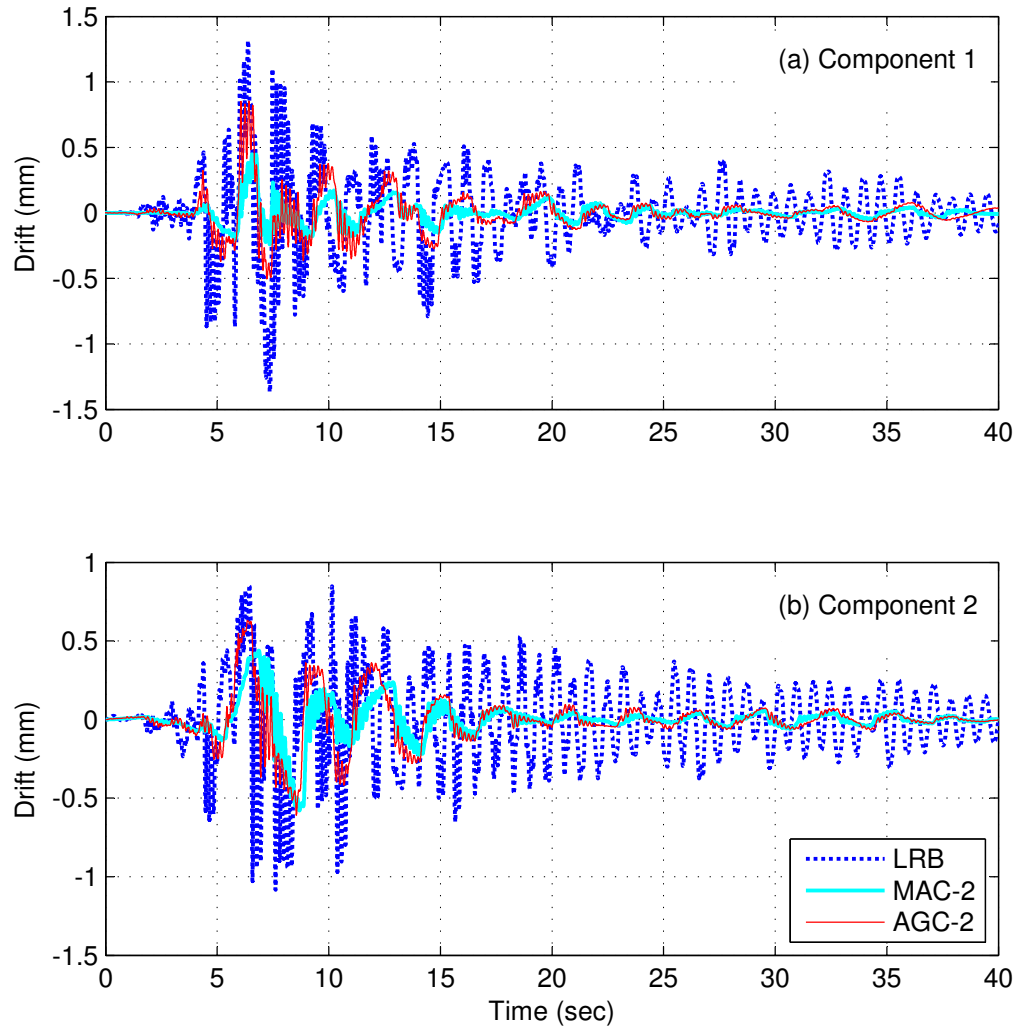
Figure 3.45: Fifth story drift response history for LRB versus controlled systems under near-fault EQ05 (1989 Loma Prieta)

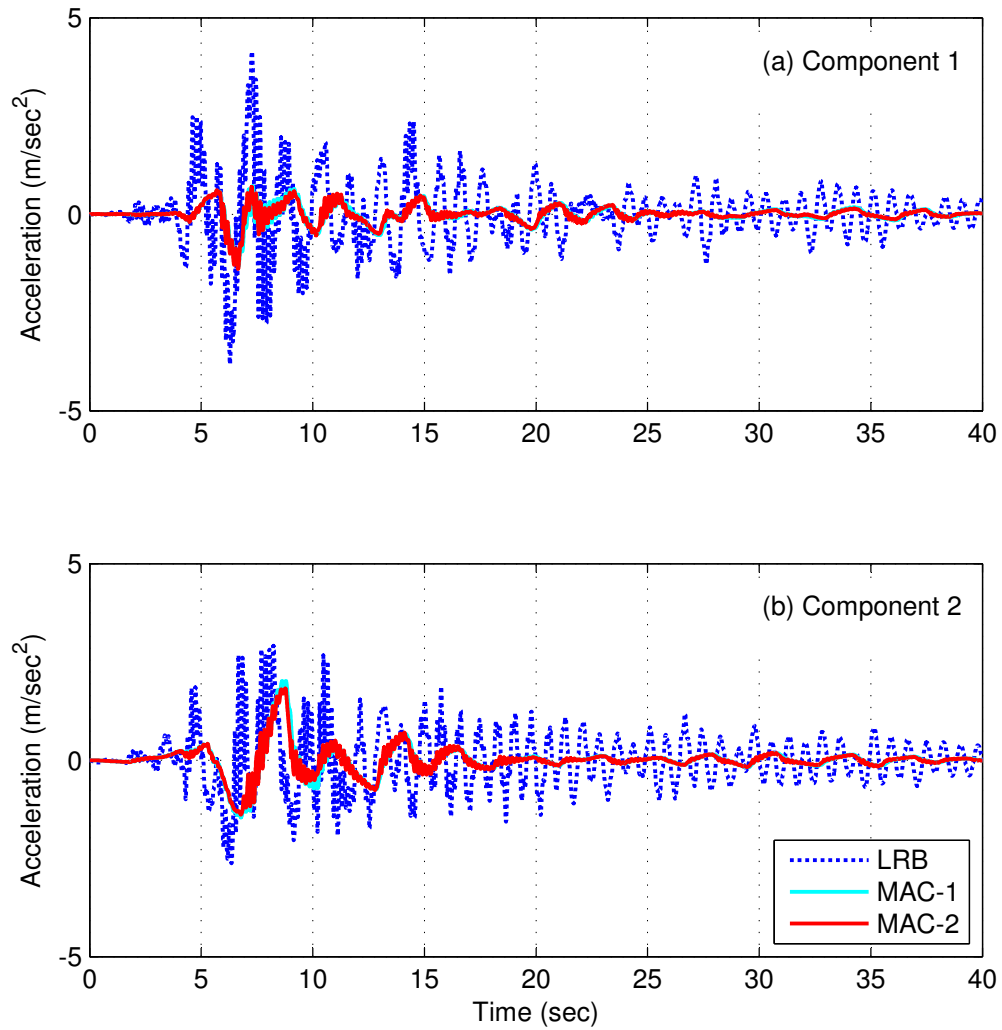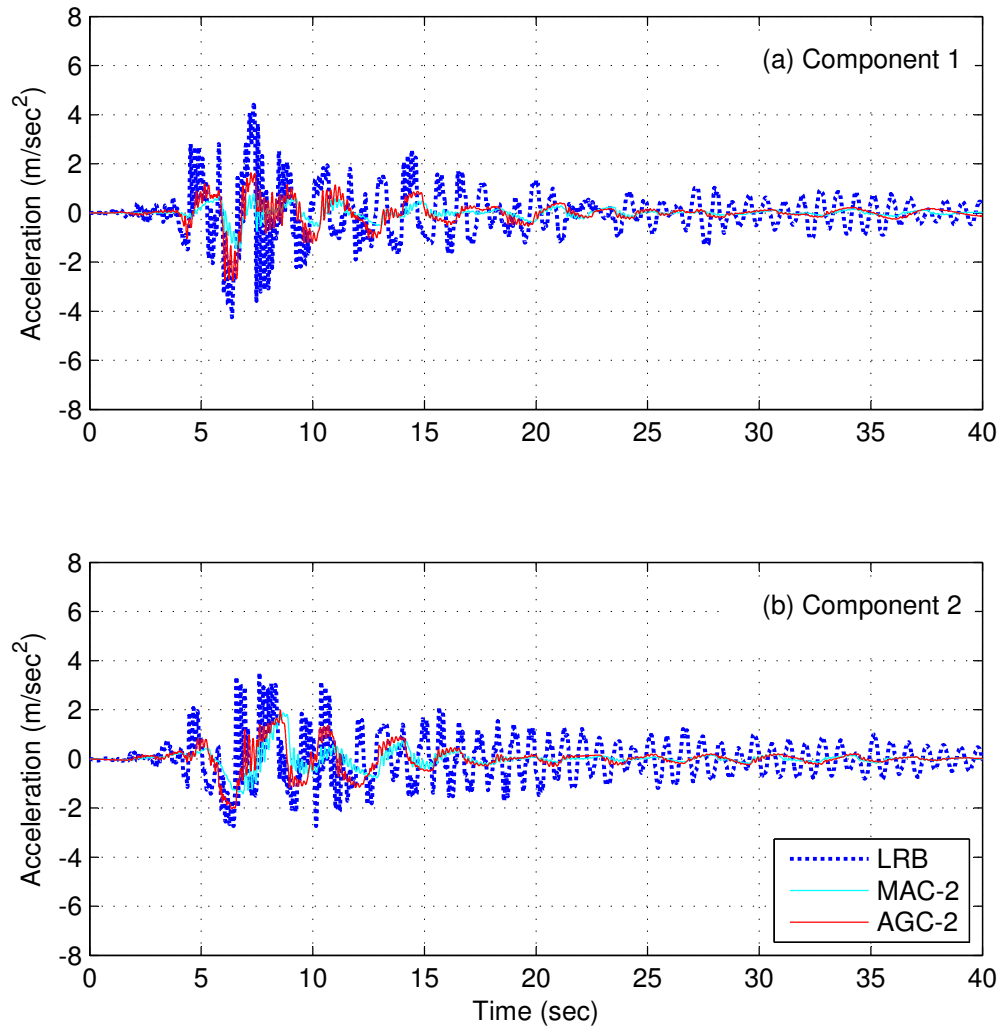**Figure 3.46:** Roof acceleration response history for LRB versus controlled systems under near-fault EQ05 (1989 Loma Prieta)

Table 3.9: Superstructure seismic demands normalized to the fixed base structure under the near-fault records, considering higher stiffening ratio for the isolation system.

Demand	LRB	MAC-3	AGC-5
Roof Displacement	0.220	0.080	0.208
Roof Acceleration	0.210	0.082	0.210
1st floor shear	0.236	0.089	0.218

Table 3.10: Structural seismic demands normalized to the LRB system under the near-fault records, considering higher stiffening ratio for the isolation system.

Demand	MAC-3	AGC-5
Base Displacement	1.437	0.676
Base Acceleration	0.362	0.977
Roof Displacement	0.364	0.948
Roof Acceleration	0.391	1.004
1st floor shear	0.377	0.924

compromising the reduced seismic demands obtained by the conventionally isolated structures, as shown in Tables 3.9 and 3.10, where MAC-3 and AGC-5 are assumed with maximum stiffening ratio ($\alpha_{max} = 10$). As it can be noticed from the tables, the effect of increased stiffening ratio is limited on the MAC algorithm behavior.

3.8 Semi-Active Control Based on LQR

Active control theory of structures has been widely implemented in the design of passive energy dissipation devices, as well as in the design of semi-active control algorithm (Agrawal and Yang, 1999; Li and Ou, 2006; Li et al., 2008; Usman et al., 2009). This is achieved by deriving the active control forces then command the semi-active control device to change its properties (stiffness and/or damping) so that the desired control force could be achieved. Classical linear optimal control (Soong, 1990) depends on modifying the structural parameters (stiffness and damping) so that

the structure behaves more favorably when subjected to external seismic excitation. Consider a base isolated structure with a controllable device located at the isolation level, as shown in Figure 3.1b. The equation of motion for this structure can be written as

$$\mathbf{M}\ddot{\mathbf{x}} + \mathbf{C}\dot{\mathbf{x}} + \mathbf{K}\mathbf{x} = -\mathbf{M}\mathbf{E}_g\ddot{x}_g + \mathbf{E}_cf_c \tag{3.33}$$

where $\mathbf{x}$, $\dot{\mathbf{x}}$, and $\ddot{\mathbf{x}}$ are the displacement, velocity, and acceleration vectors, relative to the ground, respectively; $\mathbf{M}$, $\mathbf{C}$, and $\mathbf{K}$ are the mass, damping, and stiffness matrices of the dynamic system; $\ddot{x}_g$ is the ground acceleration; f_c is the control force developed by the controllable device; $\mathbf{E}_g$ is the influence array of the ground motion on the superstructure DOFs, and $\mathbf{E}_c$ is the location matrix of the control force. Equation 3.33 can be written in state space form as follows

$$\dot{\mathbf{z}} = \mathbf{A}\mathbf{z} + \mathbf{B}f_c + \mathbf{E}\ddot{x}_g \tag{3.34}$$

where $\mathbf{z} = [\mathbf{x}^T\ \dot{\mathbf{x}}^T]^T$ is the state vector; and the state matrices $\mathbf{A}$, $\mathbf{B}$, and $\mathbf{E}$ are

$$\mathbf{A} = \begin{bmatrix} \mathbf{0} & \mathbf{I} \\ -\mathbf{M}^{-1}\mathbf{K} & -\mathbf{M}^{-1}\mathbf{C} \end{bmatrix} \ , \ \mathbf{B} = \begin{bmatrix} \mathbf{0} \\ \mathbf{M}^{-1}\mathbf{E}_c \end{bmatrix} \ , \ \mathbf{E} = \begin{bmatrix} \mathbf{0} \\ -\mathbf{E}_g \end{bmatrix} \tag{3.35}$$

In the linear quadratic optimal control, the control force f_c is chosen to minimize the performance index, J, which can take the form

$$J = \int_0^\infty \left[\mathbf{z}^T\mathbf{Q}\mathbf{z} + \mathbf{R}f_c^2\right] dt \tag{3.36}$$

where $\mathbf{Q}$ and $\mathbf{R}$ are the weighting matrices that define the relative importance between the state variables and the control force, respectively. By assigning large values for the matrix $\mathbf{Q}$, the performance is given higher priority than the control force magnitude.

Table 3.11: Range of the stiffening ratio used for the LQG algorithm.

Control	Stiffening Ratio	
ID	α_{min}	α_{max}
LQG-1	-0.7	0.7
LQG-2	-0.7	2.0
LQG-3	-0.7	10

In the considered example, the control force, f_c, is scalar, as the control force is only developed at the isolation level, thus $\mathbf{R}$ is also a scalar. The linear quadratic regulator (LQR) control law is

$$f_c = -\mathbf{Gz} \tag{3.37}$$

where $\mathbf{G}$ is the control gain that is obtained by solving the matrix Ricatti equation

$$\mathbf{PA} - \frac{1}{2}\mathbf{PBR}^{-1}\mathbf{B}^T\mathbf{P} + \mathbf{A}^T\mathbf{P} + 2\mathbf{Q} = 0 \tag{3.38}$$

The control gain $\mathbf{G}$ can be calculated as

$$\mathbf{G} = \frac{1}{2}\mathbf{R}^{-1}\mathbf{B}^T\mathbf{P} \tag{3.39}$$

The control force obtained from Equation 3.37 can then be used to regulate the variable stiffness of the base isolation system by substituting for the desired control force into Equation 3.15 in real-time.

The semi-active control algorithm developed according to the LQR control theory is subjected to the near-fault earthquake records (Table 3.3). The considered isolation system variable stiffness range is summarized in Table 3.11. Next, the structural response with the LQR control is compared to the corresponding cases of the MAC and AGC algorithms.

With stiffening ratio ($\alpha_{max} = 0.7$), the LQR algorithm fails to reduce the seismic

demands on the isolated structure. However, under the same constrains, the MAC and the AGC successfully reduce the superstructure accelerations and drifts at the expense of increased base displacement. This can be observed from the statistical summary shown in Figure 3.47. With a higher stiffening ratio ($\alpha_{max} = 2.0$) the LQR-2 slightly reduces the superstructure accelerations and drifts without compromising the base displacement of the LRB. The base displacement and base acceleration response history of the isolated building with the LQR-1 and LQR-2 subjected to the EQ05 (*1989 Loma Prieta*) are shown in Figures 3.48 and 3.49, respectively. It is evident from the figures that a wider stiffening ratio range gives more room for the controller to develop control forces that are closer to the desired active control forces. Figure 3.50 clearly shows how the wider range of stiffness helps achieving the performance of the actively controlled structure. The plots show the desired control force versus the achieved force for different ranges of stiffening ratio.

As mentioned earlier, if the stiffening ratio of the variable stiffness isolation system is as high as ten, the AGC-5 successfully reduces the base displacement of the LRB isolated structure by up to 35%. Comparing the performance of the AGC-5 to the LQR-3, as shown in Figure 3.51, the LQR-3 slightly reduces both base displacement and superstructure accelerations and drifts. Yet the AGC-5 outperforms the LQR-3 as it reduces the undesirable large base displacement of the near-fault ground motions while maintaining the same level of other seismic demands as in the conventionally isolated structure.

As an illustration for the potential of the AGC-5 to control the base displacement of the near-fault ground motion without compromising the performance of the conventionally isolated structure, Figure 3.52 shows the base displacement response history under the EQ01 (*1979 Imperial Valley-06*). Figure 3.53 shows the effect of this control algorithm on the base acceleration. Significant reduction in the base dis-
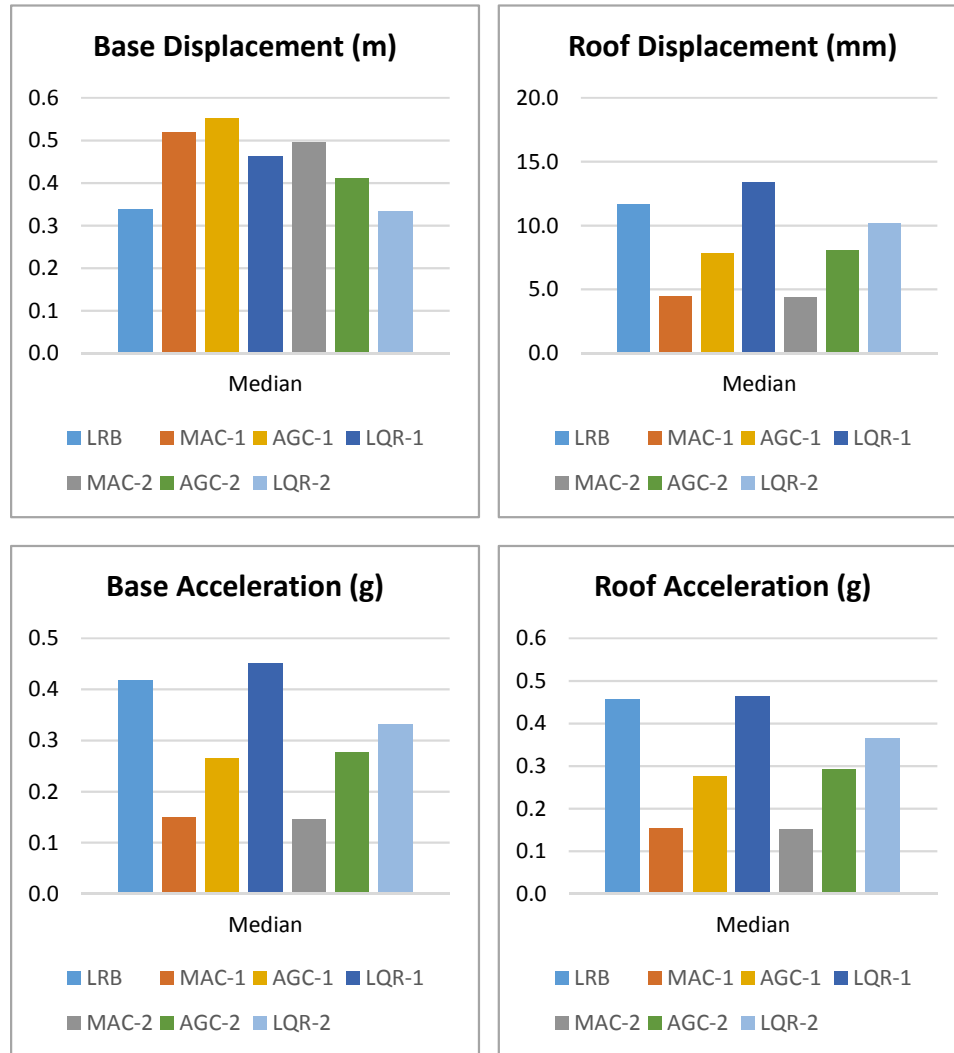
Figure 3.47: Median of the near-fault seismic response for the isolated structure with limited stiffening ratio.
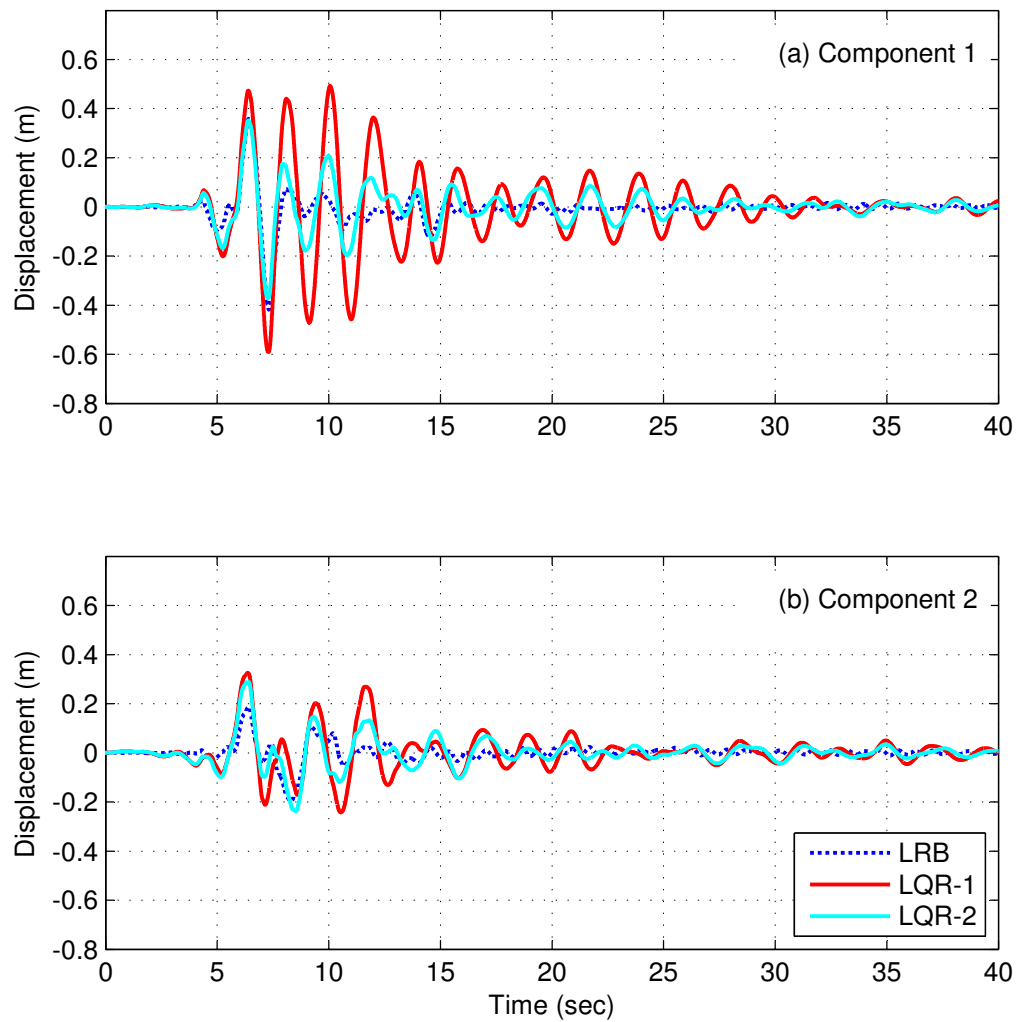
Figure 3.48: Base displacement response history for LRB versus LQR systems under near-fault EQ05 (1989 Loma Prieta)
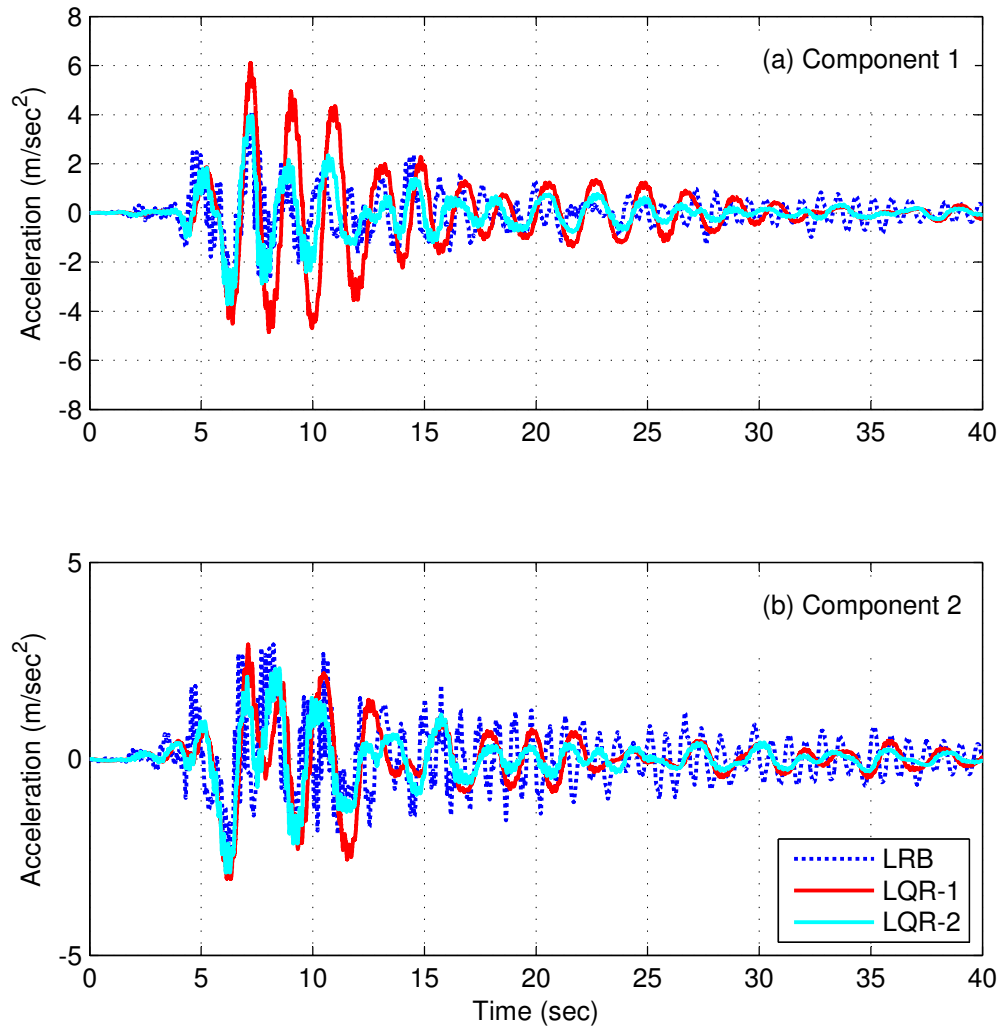
Figure 3.49: Base acceleration response history for LRB versus LQR systems under near-fault EQ05 (1989 Loma Prieta)
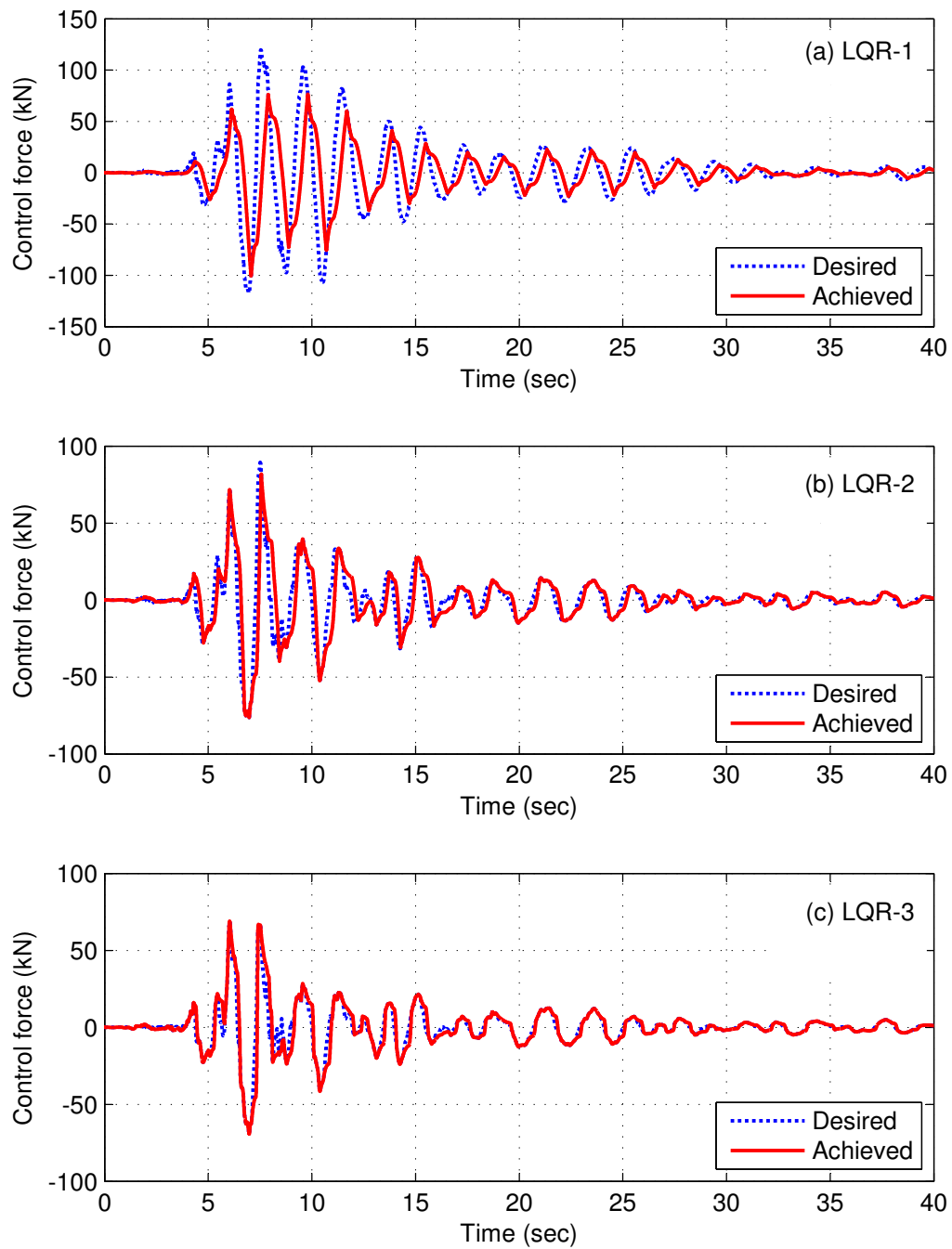
Figure 3.50: Desired and achieved control forces with different stiffening range under near-fault EQ05 (1989 Loma Prieta)
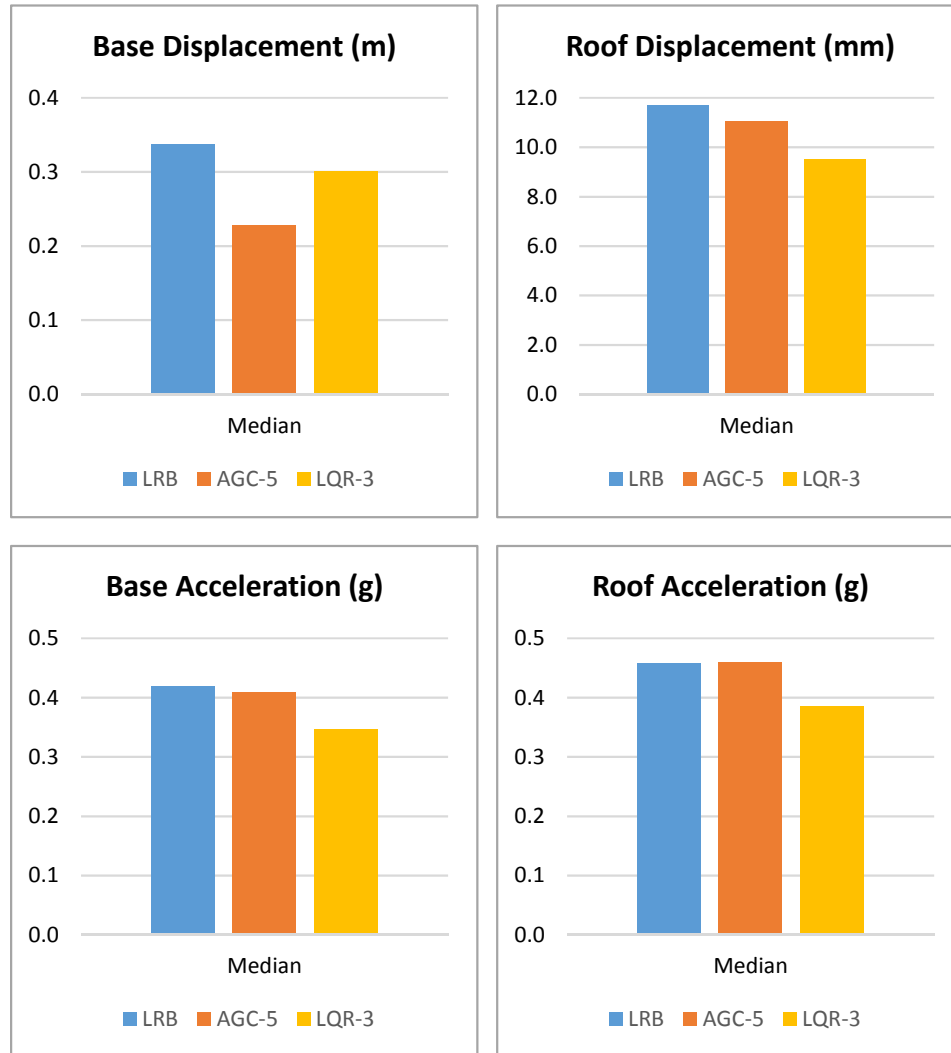
Figure 3.51: Median of the near-fault seismic response for the isolated structure with stiffening ratio $\alpha = 10$.
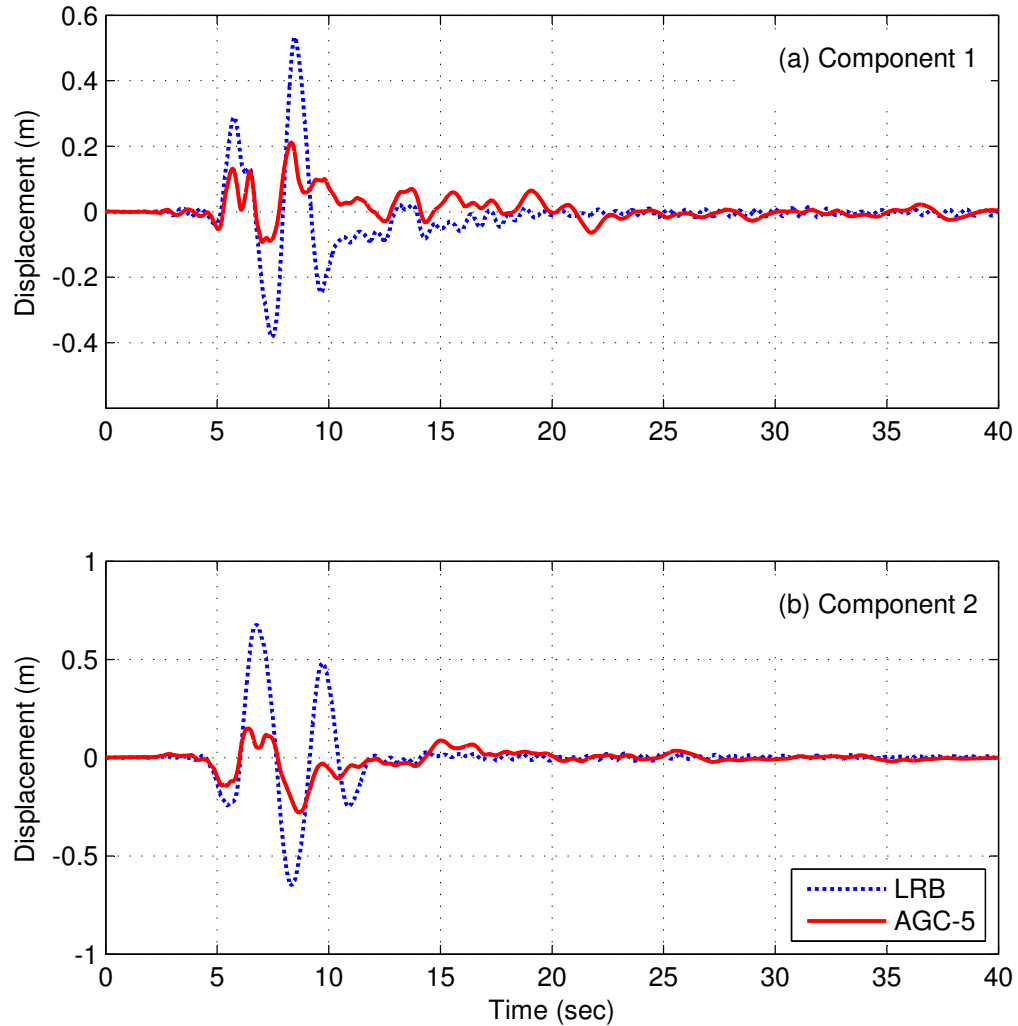
Figure 3.52: Base displacement response history for AGC-5 system versus LRB under near-fault EQ01 (1979 Imperial Valley-06)

placement is achieved, while the base acceleration remains at the same level of the LRB system.

In terms of the superstructure response, Figure 3.54 shows the response history for the inter-story drift of the 5th story, and Figure 3.55 shows the roof total acceleration response history under the same earthquake record.
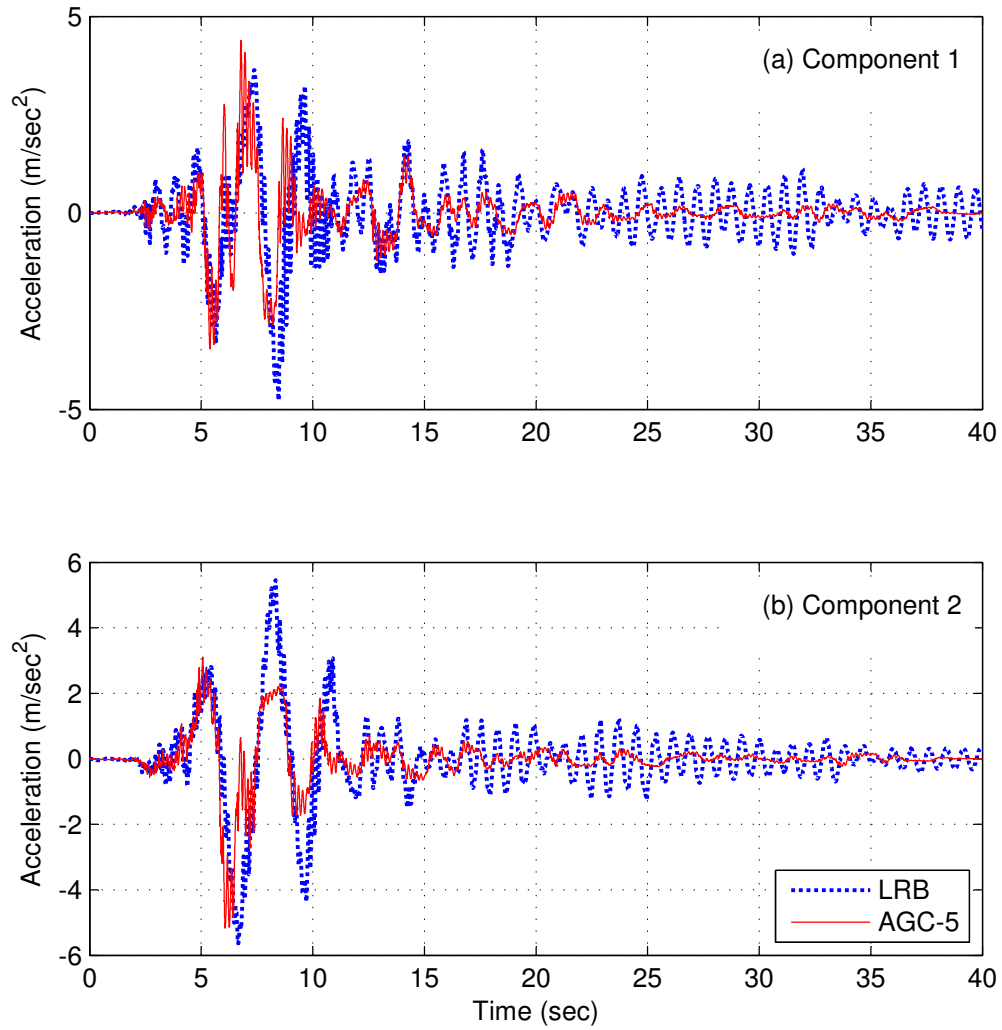
Figure 3.53: Base acceleration response history for AGC-5 system versus LRB under near-fault EQ01 (1979 Imperial Valley-06)
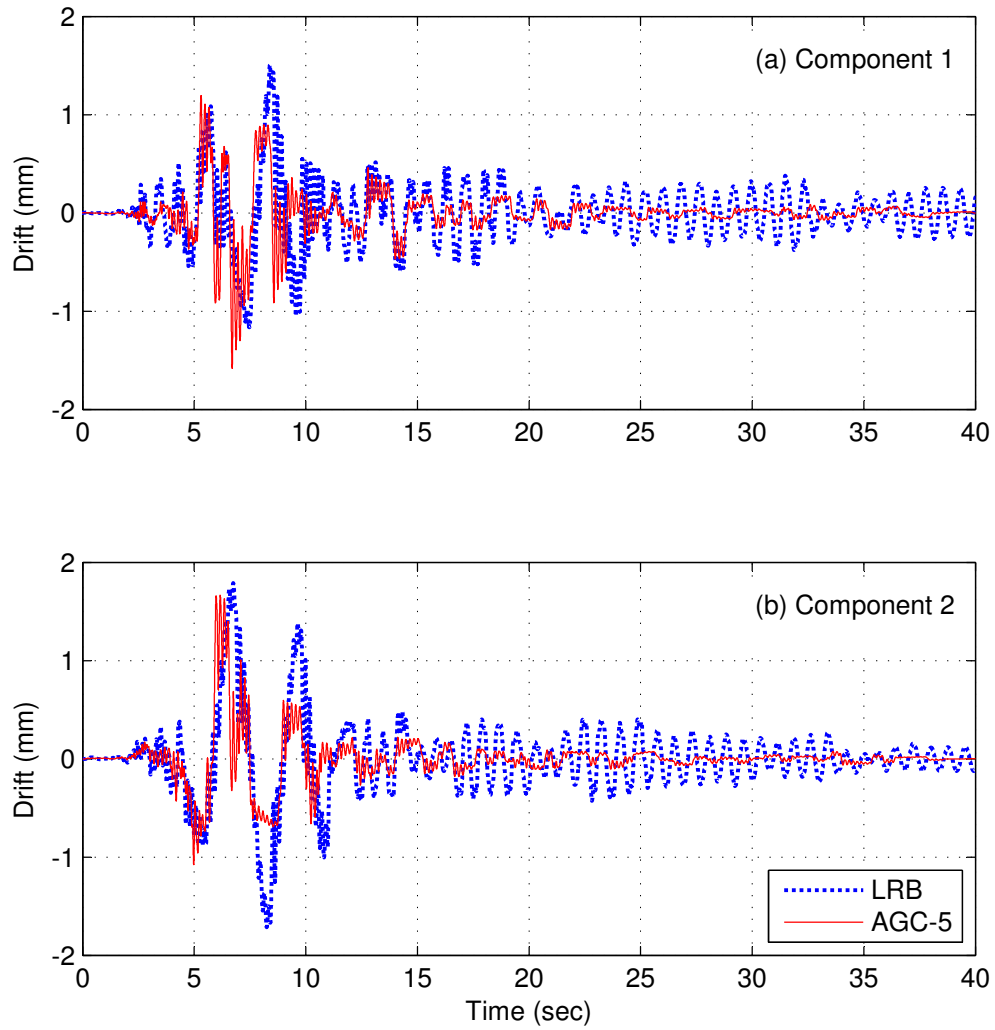
Figure 3.54: Fifth story drift response history for AGC-5 system versus LRB under near-fault EQ01 (1979 Imperial Valley-06)
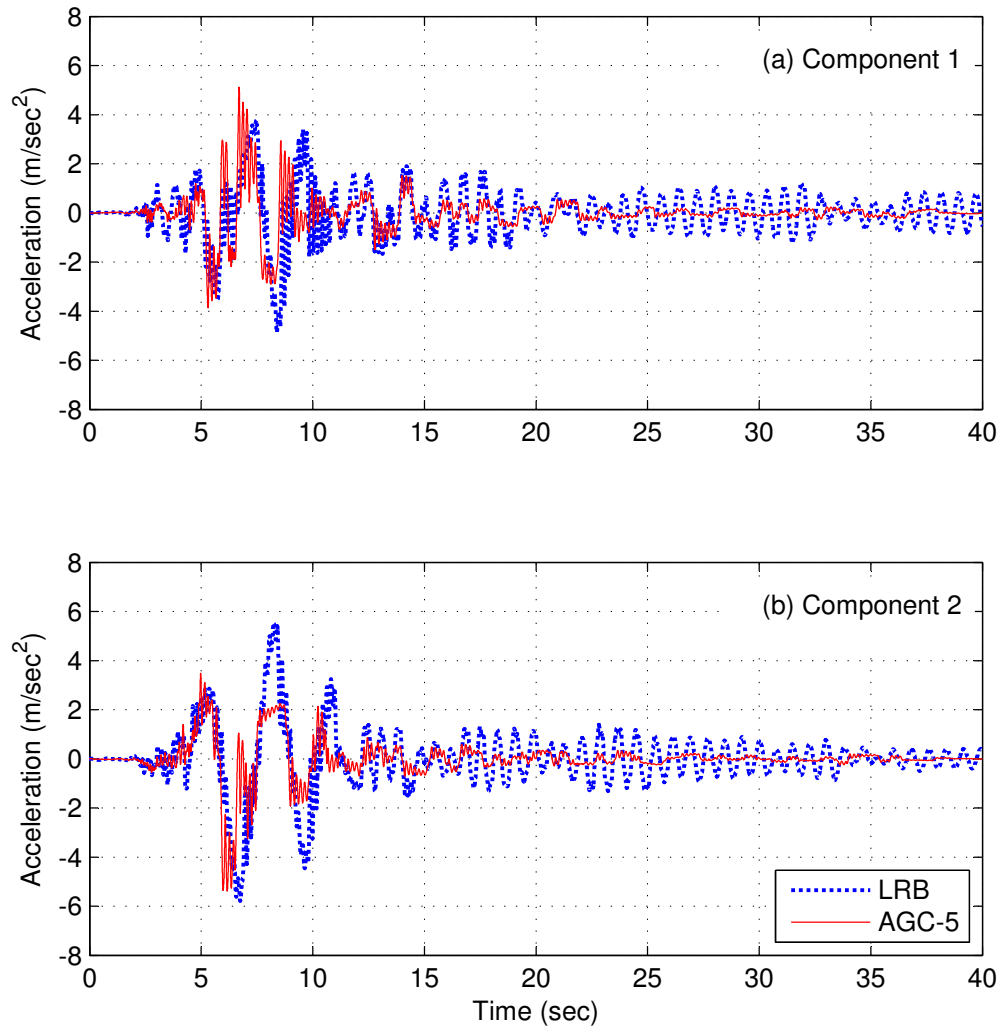
Figure 3.55: Roof acceleration response history for AGC-5 system versus LRB under near-fault EQ01 (1979 Imperial Valley-06)

3.9   Summary

In this chapter, semi-active control strategies for smart base isolation systems employing Magneto-Rheological Elastomers (MREs) were developed. The proposed control algorithms were designed to minimize the superstructure and the substructure accelerations. Two semi-active control algorithms were proposed, the Minimal Acceleration Control (MAC) and the Acceleration Gain Control (AGC). Both methods led to significant reduction of the seismic demands on base isolated structures. Under the effect of far-field ground motions, the MAC algorithm can reduce the overall structural accelerations and the superstructure displacements by up to 75% compared to the seismically isolated structure with conventional lead rubber bearing (LRB) system. However, up to 30% increase in the base displacement demand is possible. The AGC on the other hand, provides up to 40% reduction in the seismic demands with only 12% increase in the base displacement, or up to 50% reduction in the seismic demands with 34% increase in the base displacement. The selection of the acceleration gain, G, is the responsible parameter for the trade-off between the desired seismic response reduction and the base displacement. In addition, the AGC has self-centering capability that leaves no residual displacement in the base slab as in the case with the MAC algorithm.

For the near-fault excitations, almost the same reduction of the seismic demands can be achieved. The MAC algorithm provides up to 65% reduction in the overall structural acceleration as well as the superstructure's displacements relative to the LRB system. Up to 46% increase in the base displacement is possible with a tendency to leave residual displacement in the base slab. However, the increased base displacement demand on near-fault isolated structures is too critical, as the base displacement demand on near-fault seismically isolated structures is typically high, and may cause instability of the isolation system. To overcome this issue, a variable stiffness device

that is capable of providing stiffening ratio of up to ten is needed. Such a device can achieve up to 33% reduction in the base displacement of the conventionally isolated structure with the AGC algorithm, without compromising the reduced demands on the isolated structure, which is within the range of 70% to 80% of the fixed base case. However, the MRE base isolation system with the current properties of limited stiffening ratio can achieve up to 34% reduction in the overall structural accelerations and the superstructure's displacements with 22% increase in the base displacement.

For a better reduction of the seismic demands on the superstructure, the base displacements achieved using the proposed control algorithms tend to exceed the base displacement of the conventionally isolated structure. This makes the proposed systems more suitable for far-field ground motions (low displacement demands) and for the isolation of acceleration sensitive structural and non-structural components, unless isolation systems with higher stiffening ratios are available.

Chapter 4

Stiffening Bracing System

The conventional design of steel braced frames utilizes bracing systems that are initially stiff, with the capability of providing energy dissipation once the braces yield in tension. The stiff bracing systems lead to structures with relatively short period that experience high floor accelerations under frequent (moderate) earthquakes and wind loads. Under strong seismic events, these systems are designed to yield to allow energy dissipation by means of hysteretic behavior of the bracing elements. Structures located in the vicinity of an active fault are likely to experience high displacement demands, which may lead to large inter-story drifts, especially for those with bracing systems that are intentionally designed to yield. The excessive inter-story drift usually leads to permanent deformations and/or instability issues caused by the $P - \Delta$ effect on the columns. Gravity columns, which are subjected to the same lateral deformation of the lateral load resisting systems, are more likely to experience serious damage due to the $P - \Delta$ effect.

This chapter presents a design procedure for Stiffening Bracing System (SBS). This bracing system is designed so that it initially provides a relatively low stiffness and the stiffness increases once a predefined inter-story drift ratio is reached. The increase of the bracing stiffness can be achieved by installing elements that are engaged in the seismic resisting system once a certain displacement is reached. The stiffening

behavior can also be achieved by using controllable stiffness devices, as discussed in Section 2.3, or by a combination of both alternatives. However, this chapter focuses on the design and behavior of the passive stiffening bracing system. The assembly and details of the devices that are capable of providing this kind of stiffening behavior are not covered in this dissertation.

The main goal of this design alternative is to provide a relatively flexible braced frame that would experience low floor accelerations during low seismic events. However, the system will develop larger stiffness once a desired inter-story drift is reached. This behavior is believed to limit the increasing inter-story drift, which in turn will reduce the permanent deformations and the $P - \Delta$ effect. In addition, the proposed design methodology maintains a uniform inter-story drift ratio throughout the building's height by introducing an optimization process for the vertical distribution of stiffness as well as the controlling parameters of the stiffening bracing system.

4.1   Introduction

The presumed stiffening force-displacement relationship for the SBS is shown in Figure 4.1. This behavior can be achieved by using controllable variable stiffness device (VSD), such as the semi-active stiffness damper (SASD) or the active variable stiffness (AVS) device (Kobori et al., 1993; Yang et al., 1996; Yang and Agrawal, 1999; Yang et al., 2000; Nasu et al., 2001; Agrawal et al., 2003) or the semiactive independently variable stiffness (SAIVS) device (Nagarajaiah and Mate, 1998; Narasimhan and Nagarajaiah, 2005; Sahasrabudhe and Nagarajaiah, 2005a; Nagarajaiah and Sahasrabudhe, 2006) that were described and discussed in Section 2.3. Alternatively, the stiffening behavior can be achieved by mechanically engaging and disengaging additional elements. Figure 4.2 shows an example of mechanical stiffening bracing system, where two groups of added damping and stiffness (ADAS) devices are in-
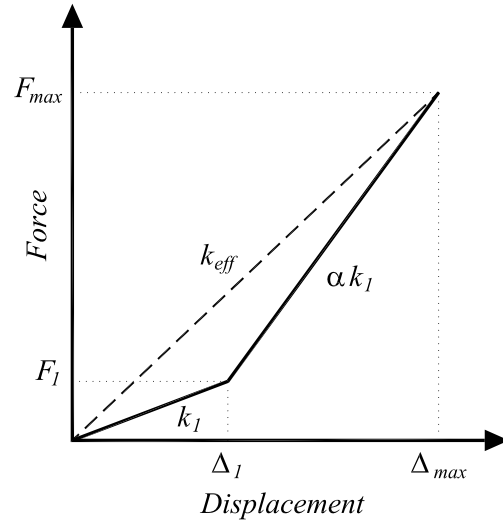
Figure 4.1: Stiffening brace, Force-Displacement relationship

stalled between the braces and the floor beam. The two ADAS groups are separated by a slotted hole at the top connecting plate, so that only one group is always engaged in the lateral force resisting system, while the other group participates in the stiffness once the deformation exceeds the slotted hole tolerance. Figure 4.3 shows another example, where a scissors-jack is attached to a moment frame, with the diagonal member attached to the other members by means of a slotted connection, so that the stiffness of the scissors-jack brace will only be activated once a desired inter-story drift is reached.

In the following sections, the design procedure, selection of the SBS parameters, and the optimal stiffness distribution over the building's height are illustrated.

4.2 Design Concept of the SBS

The seismic demand on structures depends mainly on the fundamental period of vibration as well as the equivalent damping ratio of the system. A small damping ratio is inherent in civil structures considering the friction between the structural and
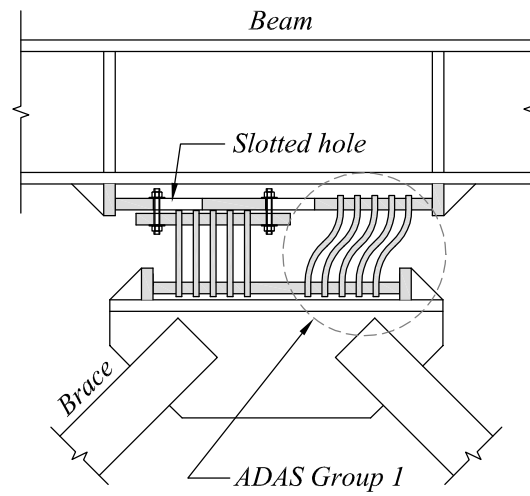
Figure 4.2: Stiffening bracing system using two groups of ADAS
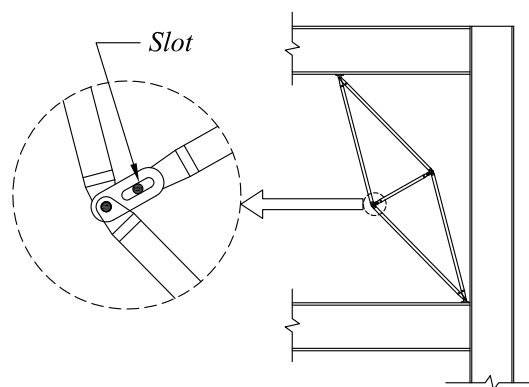
Figure 4.3: Stiffening bracing system using Scissor Jack brace with slotted connection

nonstructural elements, such as the frictional forces developed through the interaction between the partition walls and the structural system during lateral vibrations. However, larger damping ratios are obtained due to hysteretic energy dissipated by inelastic deformation of the structural members. Although the inelastic deformation dissipates large portion of the seismic energy, it may lead to permanent deformation of the structures. As an alternative, supplemental damping and energy-absorbing devices are used to dissipate the seismic energy while minimizing the damage to the main structural system (Soong and Spencer Jr., 2002; Yang et al., 2010; Kim et al., 2006).

Near-fault ground motions are dominated by a long velocity pulse that develops pulse type displacement for long period structures (Hall et al., 1995). High spectral acceleration components are observed in the long period range for the fault-normal direction (Jangid and Kelly, 2001). However, the near-fault high seismic energy in the long period range together with improper stiffness distribution may lead to local damage or soft-story failure mechanism (Mohammadi et al., 2004). As an attempt to resolve this issue, the proposed system is designed so that it provides initially a relatively long period structure but with an optimized stiffness and damping distribution. The stiffness optimization takes into account the effect of higher modes on the overall deformation of the structure. Thus, it is possible to achieve a more uniform inter-story drift ratio over the building's height, which results in a more uniform seismic demand distribution and avoids local floor damage and soft-story failure mechanism. Furthermore, the reduction that could be achieved in floor accelerations reduces the internal stresses on the structural elements and hence allows for an economical design. With the initially soft structure, the lateral deformations are expected to be large, however, the SBS is presumed to stiffen up at a desired inter-story drift ratio to limit the excessive lateral deformations. In addition, supplemental viscous damping

devices are distributed over the floors for the same reason.

The design concept of the proposed stiffening bracing system can be summarized as follows:

- Relatively long period structure subjected to lower seismic forces than conventional braced frames or moment frames.

- Variable stiffness characteristic that reduces the probability of resonance with the ground excitation, and limits excessive deformations.

- Performance based design to achieve uniform inter-story drift ratio that reduces the chance of local story damage and nonlinear deformation.

- Low floor accelerations that reduces the seismic demand on nonstructural and internal contents of the building, in addition to cost effective design.

Reinhorn et al. (2005) and Viti et al. (2006) proposed a strength reduction procedure for retrofitting of an existing hospital with similar objectives. The method relies on reducing the strength of the existing structure (weakening) that would result in reduced acceleration demands. However, the strength reduction leads to an increase in the structural deformations. Therefore, supplemental damping devices are used in conjunction with the weakened structure to maintain the deformations within acceptable range. The weakening of the structure is achieved by removing some of the lateral force resisting elements, such as shear walls, bracing members, *etc.*, or by reducing the moment capacity of some of the moment connections. A schematic representation of the weakening and damping procedure is shown in Figure 4.4. The figure shows the demand-capacity curves of a typical yielding structure, designated "Original". The performance point of the original structure is defined as the intersecting point between the capacity curve and the inelastic spectral demand curve (point 1). Applying the weakening concept to the original structure, the capacity
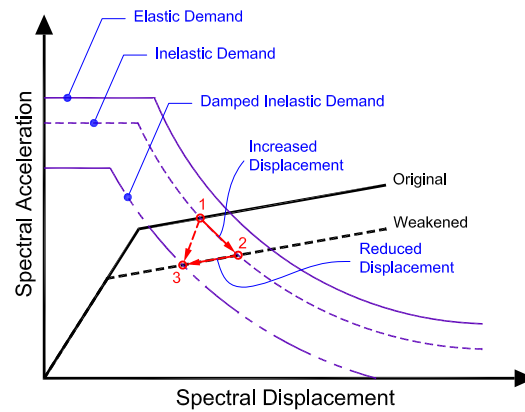
Figure 4.4: Schematic representation of the weakening and damping procedure

of the structure reduces, leading to the capacity curve designated "Weakened". The performance point of the weakened structure (point 2) shows that the resulting weak system experiences less acceleration demand but at the expense of increased displacement. With the addition of viscous damping devices, the demand curve reduces to the damped inelastic spectral demand curve, leading to performance point 3, which shows that both acceleration and displacement demands on the new structure are reduced.

In order to calculate the amount of weakening and added damping, Lavan et al. (2008) developed a noniterative procedure to optimize the parameters involved in the weakened system, such as the amount and location of weakened elements and damping devices. The procedure depends on developing a nonlinear active control using the theory of sliding mode control. Once the active control forces are obtained, they can be translated to an equivalent passive system by applying the appropriate amount of weakening to the structural elements and determining the required added damping. The location and magnitude of the weakening and damping are selected so that the error between the forces acting on each degree of freedom in the two systems (the actively controlled and the weakened and damped systems) is minimized.
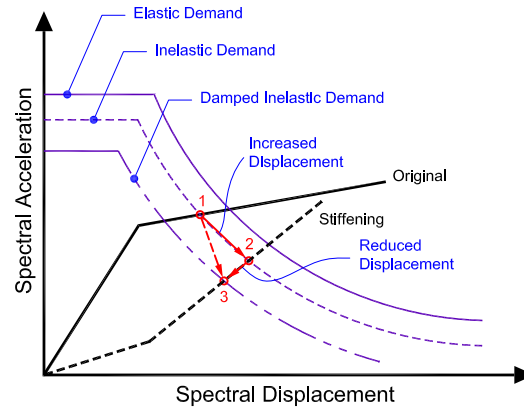
Figure 4.5: Schematic representation of the stiffening bracing system

In contrast to the weakening and damping procedure, the proposed stiffening system provides relatively flexible structure, compared to the regular yielding system. This flexible structure will experience reduced acceleration demands, as shown by point 2 on the schematic representation of the SBS shown in Figure 4.5. However, the reduced acceleration demands will be accompanied by increased displacement demands. Therefore, additional damping is needed to control the increased displacement to an acceptable limit. Thus, the performance point can be dragged form point 2 to point 3 on the capacity-demand curves shown in the figure. The design procedure is based on an optimized distribution for the stiffening and damping so that uniform inter-story drift is achieved throughout the building's height. The performance point of the final structure (point 3) is not necessarily experiencing less displacement demand as this point is set to the maximum allowable displacement, which ensures reduced acceleration demands and satisfies the system stability.

The proposed stiffening procedure is not only implementable for design of new structures, but also for retrofit of existing structures. This can be done by introducing the weakening technique to the existing structure, so that the retrofitted structure relies mainly on the added stiffening bracing system for its lateral force resisting

capacity.

## 4.3   Optimization Process for the SBS

The first step of the optimization process is to define the site design response spectra that would be used with the equivalent lateral force procedure described in ASCE 7-10 (ASCE, 2010). Because no significant yielding is expected in the proposed procedure, the response modification coefficient is taken as, $R = 1$. The story shear is then calculated based on the known lateral force distribution. This story shear is used to specify the initial stiffness of the bracing system, k_1, by selecting a hypothetical inter-story drift value, d_1, as shown in Figure 4.6. However, d_1 should be selected so that the resulting stiffening ratio, α, per floor remains a practical value and the stiffness of the system does not change drastically. Sudden sharp change in the brace stiffness may lead to an amplified floor accelerations. Therefore, it is suggested that d_1 be assumed within the range of twice the maximum inter-story drift, Δ_{max}. The initial stiffness per floor, k_{x1}, for the SBS is given by

$$k_{x1} = \frac{V_x}{d_{x1}} \tag{4.1}$$

where the subscript x refers to the xth floor.

By defining the initial stiffness per floor, a modal analysis is then performed and the story drift ratios, $D_{x_j}^{(i)}$, for the xth floor due to the jth mode in the ith iteration are evaluated. The maximum expected story drift ratios, D_x^i, are then estimated based on the square-root-of-the-sum-of-squares (SRSS) for the dominant modes, as follows

$$D_x^{(i)} = \sqrt{\sum_{j=1}^{n} D_{x_j}^2} \tag{4.2}$$
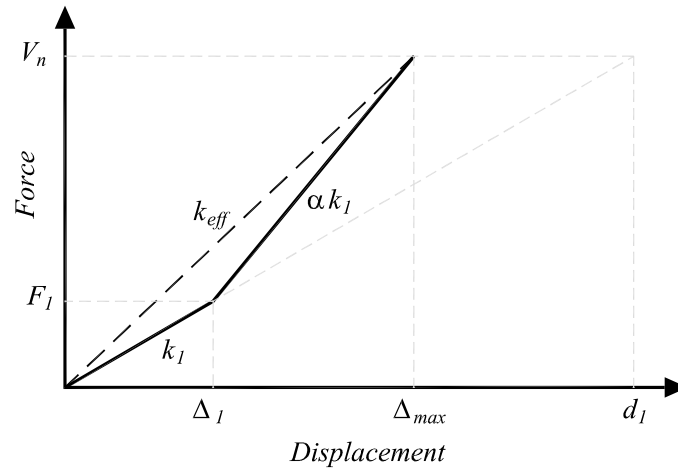
Figure 4.6: Parameters definition for a typical stiffening brace

The stiffening ratio per floor, $\alpha_x^{(i)}$, can now be updated for the next iteration as

$$\alpha_x^{(i+1)} = \alpha_x^{(i)} \frac{D_x^{(i)}}{D_{max}} \tag{4.3}$$

where D_{max} is the maximum allowable drift ratio as defined by ASCE 7-10. The effective stiffness for the SBS per floor can be calculated and updated for the $(i+1)$ step as

$$k_{x_{eff}}^{(i+1)} = \frac{k_{x1}\Delta_{x1} + \alpha_x^{(i+1)} k_{x1}(\Delta_{max} - \Delta_{x1})}{\Delta_{max}} \tag{4.4}$$

where the displacement Δ_1 is defined as the displacement where the brace starts to stiffen, Figure 4.6. In this dissertation, Δ_1 is assumed to be $(0.25 \ to \ 0.3)\Delta_{max}$.

With the newly defined effective stiffness, the entire process is repeated based on the updated stiffness until convergence with the maximum allowable drift ratio, D_{max}, for all floors is achieved.

After the convergence is reached, a pushover analysis is performed on the structure, and the performance point (the intersection between the capacity and demand curves) is observed. This performance point also defines the effective period of the structure,
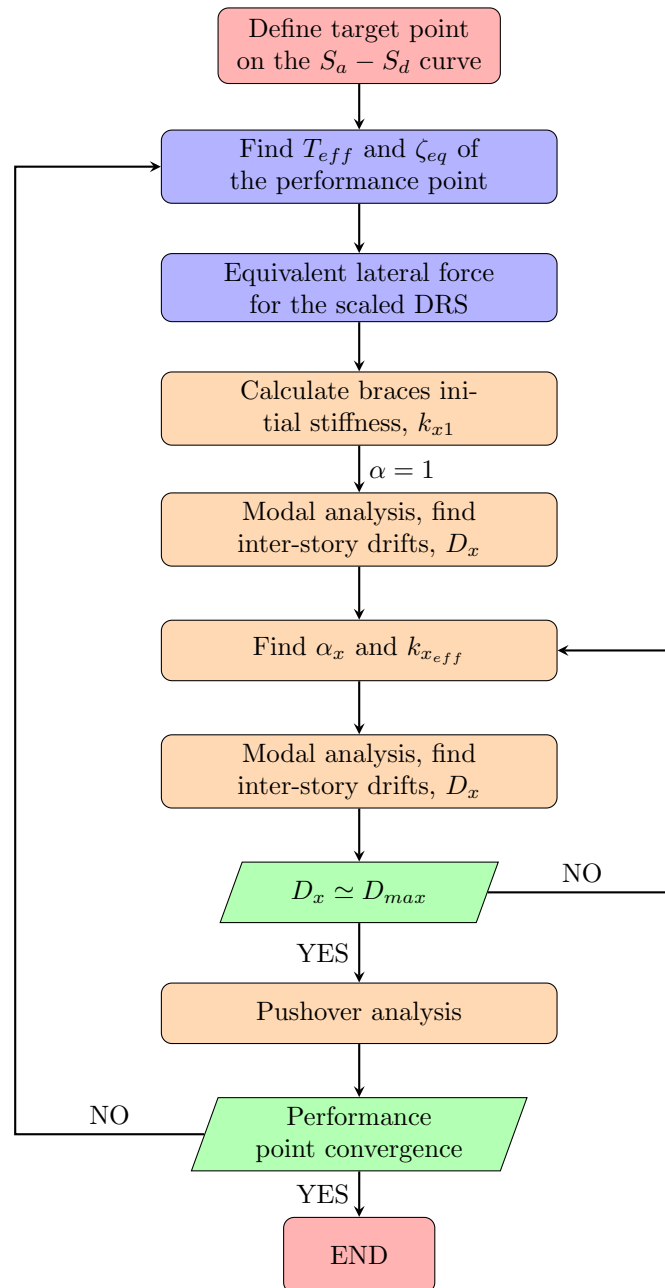
Figure 4.7: Flowchart for the SBS parameters optimization

which is then used to update the equivalent lateral force at the beginning of the optimization process. Figure 4.7 shows a flowchart for the optimization process.

It should be pointed out here that the stiffness optimization process depends on determining an effective story stiffness that can be achieved with the bilinear behavior. If a linear elastic brace is used, the same effect can be achieved. However, linear elastic brace might be impractical. The stiffening bilinear behavior is suggested here as it is possible to achieve this behavior through variety of variable stiffness devices, as discussed earlier.

4.4   Damping Distribution

In the preceding section, the stiffness optimization is based on a desired performance that defines a damped response spectra which is given by scaling the elastic response spectra (5% damped) by the demand reduction factor specified by the ATC-40 (1996) as

$$SR_A = \frac{3.21 - 0.68\ln(\zeta_{eff})}{2.12} \tag{4.5a}$$

$$SR_V = \frac{2.31 - 0.41\ln(\zeta_{eff})}{1.65} \tag{4.5b}$$

where SR_A and SR_V are the spectral reduction factor for the constant acceleration and constant velocity regions in the linear elastic design response spectra, respectively, and ζ_{eff} represents the effective or equivalent damping ratio in the system that can be defined as

$$\zeta_{eff} = \zeta_0 + \zeta_{hy} + \zeta_d \tag{4.6}$$

where ζ_0 is the inherent damping, ζ_{hy} and ζ_d represent the effective hysteretic damping and the damping provided by supplemental damping devices, respectively. In the

current study, the main system is assumed to remain in the elastic range ($\zeta_{hy} = 0$), and the required added damping is assumed to be provided by viscous dampers. The following paragraph describes the procedure used to define the viscous damping coefficients per floor to assist achieving the desired performance. Although most of the supplemental energy dissipating devices are nonlinear velocity-dependent, it is assumed here that the used dampers are linear velocity-dependent. However, it is possible to transfer the damping coefficient of the linear viscous damper to its nonlinear counterpart using the equivalent power consumption approach proposed by Pekcan et al. (1999), or other methods.

The device damping coefficient per floor should be defined so that the desired added damping ratio (ζ_d) is achieved. The added damping that needs to be supplemented by the dampers can be obtained from the desired equivalent viscous damping ratio defined in Section 4.3 after subtracting the inherent damping in the system (ζ_0).

In order to find the damping device viscous damping coefficient per floor, the nonlinear static procedure as per FEMA (1997) is used. The equivalent damping supplemented by the energy dissipation devices can be calculated as (Chopra, 1995; FEMA, 1997)

$$\zeta_d = \frac{E_D}{4\pi E_s} \tag{4.7}$$

where E_D is the energy dissipated by the energy dissipation devices, and E_s is the strain energy stored in the building. At the predefined performance level, these energies can be calculated as (FEMA, 1997; Kim et al., 2003)

$$E_D = \frac{2\pi^2}{T} \sum_j c_j \cos^2 \theta_j (\Delta_i - \Delta_{i-1})^2 \tag{4.8a}$$

$$E_s = \frac{2\pi^2}{T^2} \sum_i m_i \Delta_i^2 \tag{4.8b}$$

where c_j is the damping coefficient of the jth damper, θ_j is the jth damper inclination angle, Δ_i is the maximum desired displacement of the ith floor relative to the ground, as shown in Figure 4.8, T is the effective period of the structure at the desired performance, and m_i is the ith floor mass. Substituting from Equation 4.8 into Equation 4.7, the added damping provided by the supplemental energy dissipation devices can be calculated as

$$\zeta_d = \frac{T \sum_j c_j \cos^2 \theta_j (\Delta_i - \Delta_{i-1})^2}{4\pi \sum_i m_i \Delta_i^2} \tag{4.9}$$

With the desired added damping ratio, ζ_d, the sum of the damping coefficients $(\sum_j c_j)$ can be calculated from Equation 4.9 and then equally distributed per floor devices, as will be done through the following analyses.

4.5 Implementation of the SBS

To illustrate the effectiveness of the proposed stiffening bracing system (SBS) in seismic mitigation of far-field and near-fault structures, the Los Angles benchmark buildings designed for the SAC joint venture are used (FEMA, 2000). The buildings have been redesigned with the SBS being the lateral force resisting system in lieu of the special moment resisting frames. For performance assessment, the same benchmark structures were also designed with buckling restrained braced frames (BRBF).
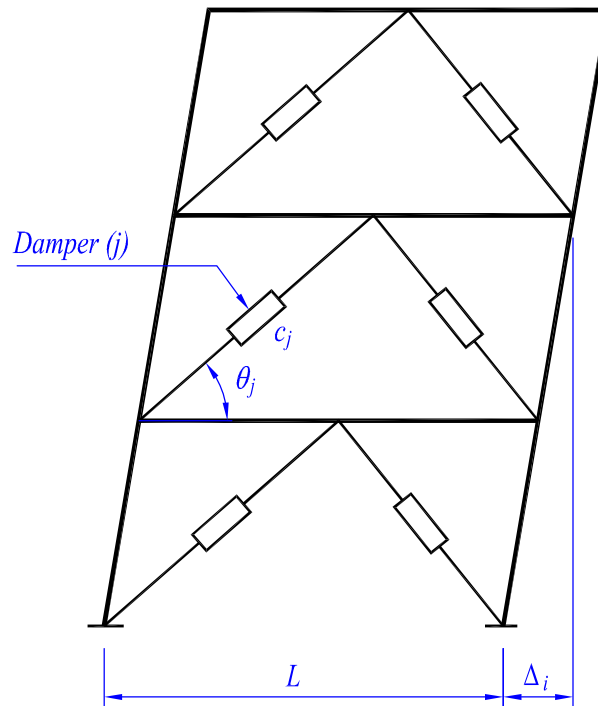
Figure 4.8: Deformed Chevron braced frame with viscous damping devices

4.6 Ground Motions and Scaling

The design response spectra originally used for the design of the SAC buildings were adopted for the design of the SBS and BRBF systems. The site mapped spectral acceleration for the short period and 1-second period are ($S_S = 1.65g$), and ($S_1 = 0.64g$) respectively. The ground motion sets for the 10% probability of being exceeded in 50 years (return period of 475 years) designated (10/50) and the 2% probability of being exceeded in 50 years (return period of 2475 years) designated (2/50) are used for the response history analyses of the two systems. Unscaled 10/50 records set is used to examine the structures under the effect of the design earthquake, as the median of the 5% damped elastic response spectra was found to be matching the design response spectra, as shown in Figure 4.9. However, the 2/50 records set, which is used to investigate the behavior of the SBS under the effect of the maximum considered
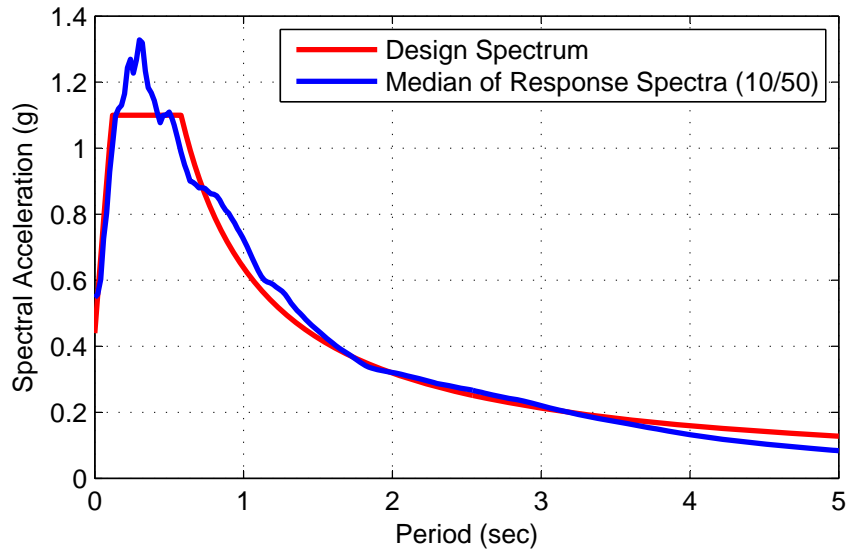
Figure 4.9: Median of the 5% damped elastic response spectra of the 10/50 ground motion records and design spectrum

earthquake, was scaled so that the median of the square root of the sum of squares (SRSS) spectrum, constructed for each pair of the ground motions by taking the SRSS of the 5% damped response spectra of the scaled components, does not fall below 1.4 times the design spectrum in the range of the period of interest. This period range is considered $0.2T$ to $1.5T$ (ASCE, 2010), where T is the fundamental period of vibration of the structure. Because the scaled ground motions used by Gupta and Krawinkler (1999); FEMA (2000) were found to be exceeding the considered maximum response spectra, only the ground motion records were used with the scaling described above. The median of the SSRS of the 5% damped elastic response spectra constructed for each pair of the scaled 2/50 ground motion records is shown in Figure 4.10. The characteristics of the 10/50 and 2/50 ground motion sets and scale factors used for the nonlinear response history analyses are given in Tables 4.1 and 4.2, respectively. These ground motion sets are rich with near-fault and far-field records, however the individual component of each record is rotated to 45 deg to the fault trace to minimize the effect of directivity (FEMA, 2000).

Table 4.1: Details of the 10/50 ground motion records (FEMA, 2000).

Record ID	Record Name	Duration (sec)	Magnitude (M_w)	R (km)	PGA (in/sec^2)
LA01	Imperial Valley, 1940	39.38	6.9	10.0	178.0
LA02	Imperial Valley, 1940	39.38	6.9	10.0	261.0
LA03	Imperial Valley, 1979	39.38	6.5	4.10	152.0
LA04	Imperial Valley, 1979	39.38	6.5	4.10	188.4
LA05	Imperial Valley, 1979	39.08	6.5	1.20	116.4
LA06	Imperial Valley, 1979	39.08	6.5	1.20	90.60
LA07	Landers, 1992	79.98	7.3	36.0	162.6
LA08	Landers, 1992	79.98	7.3	36.0	164.4
LA09	Landers, 1992	79.98	7.3	25.0	200.7
LA10	Landers, 1992	79.98	7.3	25.0	139.1
LA11	Loma Prieta, 1989	39.98	7.0	12.4	256.9
LA12	Loma Prieta, 1989	39.98	7.0	12.4	374.4
LA13	Northridge, 1994, Newhall	59.98	6.7	6.70	261.8
LA14	Northridge, 1994, Newhall	59.98	6.7	6.70	253.7
LA15	Northridge, 1994, Rinaldi	14.95	6.7	7.50	206.0
LA16	Northridge, 1994, Rinaldi	14.95	6.7	7.50	223.9
LA17	Northridge, 1994, Sylmar	59.98	6.7	6.40	219.9
LA18	Northridge, 1994, Sylmar	59.98	6.7	6.40	315.5
LA19	North Palm Springs, 1986	59.98	6.0	6.70	393.5
LA20	North Palm Springs, 1986	59.98	6.0	6.70	380.9
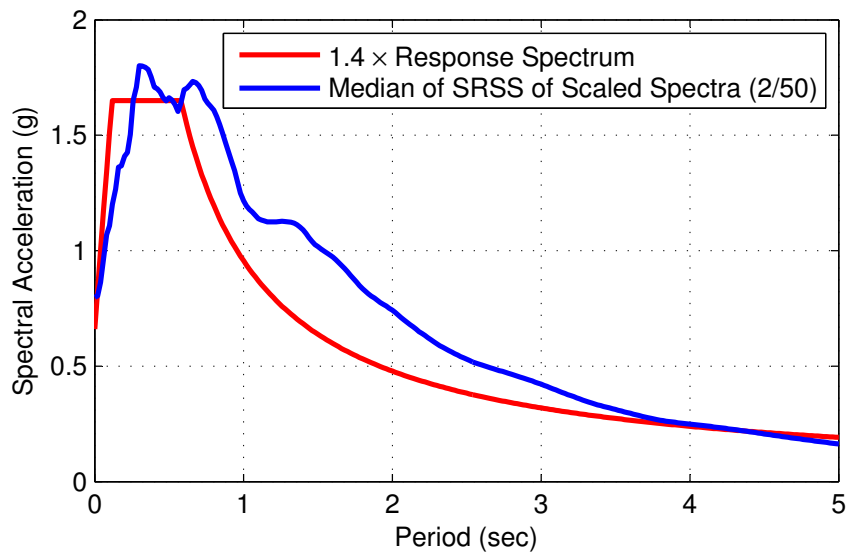
Figure 4.10: Median of the SSRS of the 5% damped elastic response spectra constructed for each pair of the scaled 2/50 ground motion records

Table 4.2: Details of the 2/50 ground motion records and scaling (FEMA, 2000).

Record ID	Record Name	Duration (sec)	Magnitude (M_w)	R (km)	PGA (in/sec^2)	Scale
LA21	Kobe, 1995	59.98	6.9	3.40	495.3	0.72
LA22	Kobe, 1995	59.98	6.9	3.40	355.4	0.72
LA23	Loma Prieta, 1989	24.99	7.0	3.50	161.4	0.69
LA24	Loma Prieta, 1989	24.99	7.0	3.50	182.6	0.69
LA25	Northridge, 1994	14.95	6.7	7.50	335.3	0.95
LA26	Northridge, 1994	14.95	6.7	7.50	364.3	0.95
LA27	Northridge, 1994	59.98	6.7	6.40	357.8	1.20
LA28	Northridge, 1994	59.98	6.7	6.40	513.4	1.20
LA29	Tabas, 1974	49.98	7.4	1.20	312.4	0.90
LA30	Tabas, 1974	49.98	7.4	1.20	382.9	0.90
LA31	Elysian Park, simulated	29.99	7.1	17.5	500.5	0.85
LA32	Elysian Park, simulated	29.99	7.1	17.5	458.1	0.85
LA33	Elysian Park, simulated	29.99	7.1	10.7	302.1	0.43
LA34	Elysian Park, simulated	29.99	7.1	10.7	262.8	0.43
LA35	Elysian Park, simulated	29.99	7.1	11.2	383.1	0.35
LA36	Elysian Park, simulated	29.99	7.1	11.2	424.9	0.35
LA37	Palos Verdes, simulated	59.98	7.1	1.50	274.7	0.48
LA38	Palos Verdes, simulated	59.98	7.1	1.50	299.7	0.48
LA39	Palos Verdes, simulated	59.98	7.1	1.50	193.1	0.55
LA40	Palos Verdes, simulated	59.98	7.1	1.50	241.4	0.55

4.7 LA 3-story Building

The design of the BRBF as well as the SBS is based initially on the equivalent lateral force procedure as per ASCE 7-10 (ASCE, 2010). The response modification coefficient, R, is taken as eight for the case of BRBF and unity for the SBS. The distribution of the viscous damping devices for the structure with the SBS was determined such that the effective damping ratio of the structure is 10%. The layout of the Los Angeles 3-story office building is shown in Figure 4.11. The analyses of the braced frame systems is conducted for the north-south direction and the external bays are chosen to be Chevron braced bays as shown in the figure. The seismic mass per braced frame is taken as half of the building's total mass, which is given by FEMA-355C (FEMA, 2000) as shown in Table 4.3.
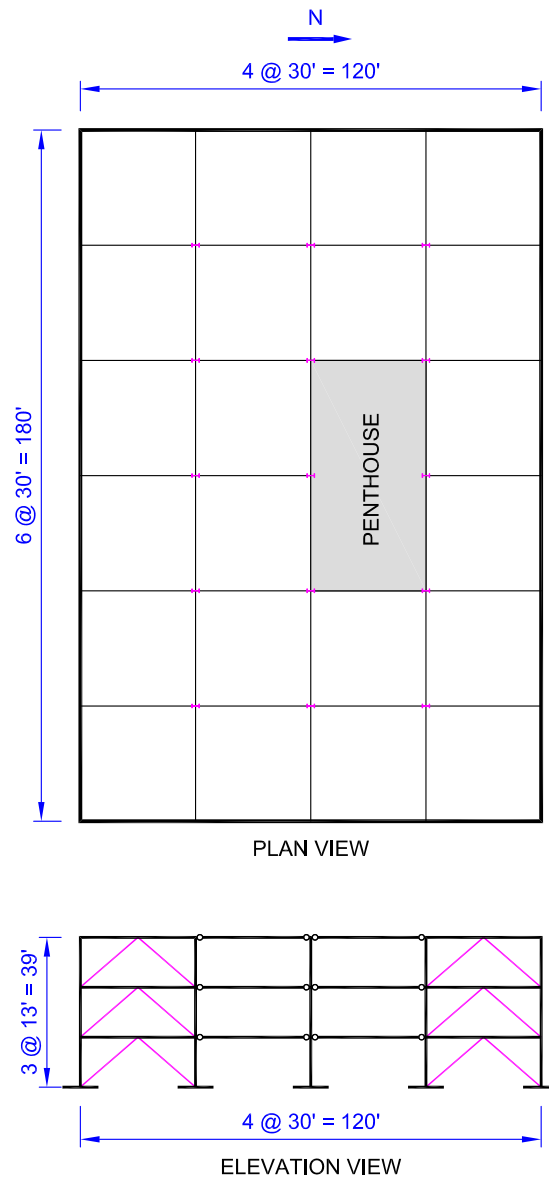
Figure 4.11: Layout of the Los Angeles 3-story braced frame building

Table 4.3: Total floor mass for the 3-story office building.

Floor Level	Total Mass $(kips.sec^2/ft)$
Roof	70.90
Floors 2 & 3	65.53

4.7.1 Design of LA 3-story Building with SBS

The preliminary design of the stiffening bracing system is based on the equivalent lateral force procedure as per ASCE (2010). However, the approximate period (T_a) is not involved in the proposed procedure, as the target performance point with a particular period (T) is assumed. The equivalent lateral force as well as the desired effective viscous damping ratio (ζ_{eff}) are determined based on this period. For the design of the LA 3-story building, the structural period is initially assumed as $(T_{initial} = 1.50 sec)$ and the effective damping ratio is $(\zeta_{eff} = 10\%)$. Based on the assumed damping ratio, the demand reduction factors for the constant acceleration (SR_A) and constant velocity (SR_V) regions are given by (ATC-40, 1996)

$$SR_A = \frac{3.21 - 0.68 \ln(\zeta_{eff})}{2.12} = 0.776 \tag{4.10a}$$

$$SR_V = \frac{2.31 - 0.41 \ln(\zeta_{eff})}{1.65} = 0.828 \tag{4.10b}$$

Therefore, the reduced maximum considered earthquake spectral response accelerations for short period (S_{MS}) and for 1-sec period (S_{M1}) become as follows (ASCE, 2010)

$$S_{MS} = F_a(SR_A S_S) = (1.0)(0.776)(1.650g) = 1.280g \tag{4.11a}$$

$$S_{M1} = F_v(SR_V S_1) = (1.5)(0.776)(0.638g) = 0.792g \tag{4.11b}$$

and the design response accelerations at short and 1-sec periods become

$$S_{DS} = \frac{2}{3}S_{MS} = 0.853g \tag{4.12a}$$

$$S_{D1} = \frac{2}{3}S_{M1} = 0.528g \tag{4.12b}$$

4.7.2　Seismic Base Shear

With response modification coefficient $(R = 1)$, importance factor $(I = 1)$, and the initially assumed structural period $(T = 1.50sec)$, the seismic response coefficient, C_s, is calculated as

$$C_s = \frac{S_{DS}}{R/I} = 0.853g \tag{4.13}$$

the seismic response coefficient should not exceed

$$C_s = \frac{S_{D1}}{(R/I)T} = \frac{0.528g}{(1/1)1.5} = 0.352g \tag{4.14}$$

note that the seismic response coefficient should not be less than the maximum of the following

$$C_s = 0.044S_{DS}I = 0.038g \tag{4.15a}$$

$$C_s = \frac{0.5S_1}{R/I} = 0.264g \tag{4.15b}$$

Thus the seismic response coefficient, C_s, is governed by Equation 4.14, and the seismic base shear, V, becomes

$$V = C_s W \tag{4.16}$$

where W is the effective seismic weight of the structure.

Table 4.4: Vertical distribution of shear for the LA 3-story building.

Level	w_x (kips)	$\sum w$ (kips)	h_x (ft)	$w_x h_x^k$ (kip − ft)	$w_x h_x^k / (w_x h_x^k)$	F_x (kips)	V_x (kips)
Roof	2283	2283	39	556036	0.595	1362	
3	2110	4393	26	279732	0.299	685	1362
2	2110	6503	13	98900	0.106	242	2047
1							2290
Total	6503			934668		2290	

4.7.3 Vertical Distribution of Seismic Forces

The seismic base shear, V, is distributed as a lateral force per floor (F_x) which is given by

$$F_x = C_{vx}V \tag{4.17a}$$

$$C_{vx} = \frac{w_x h_x^k}{\sum_{i=1}^{n} w_i h_i^k} \tag{4.17b}$$

where C_{vx} is the vertical distribution factor, w_x is the effective seismic weight of xth floor, h_x is the level of floor x^{th} measured from the base of the structure, and k is an exponent related to the structure period so that for structures with a period of $0.5 sec$ or less, $k = 1$, and for structures with period of $2.5 sec$ or more, $k = 2$. For other periods, k is determined by linear interpolation. For the structure analyzed herein, the exponent k is calculated as

$$k = 1 + \frac{1.5 - 0.5}{2} = 1.50$$

The typical floor height of the LA 3-story benchmark building is ($h = 13 ft$), as shown in Figure 4.11, the vertical distribution of shear is as given in Table 4.4.

Considering the accidental torsional moment, the lateral floor forces and floor shear per braced frame are adjusted as shown in Table 4.5.

Table 4.5: Braced frame shear forces for the LA 3-story building.

Level	Story force F_x (kips)	Story shear V_x (kips)	Frame force $F_{x,f}$ (kips)	Frame shear $V_{x,f}$ (kips)
Roof	1362		731	
3	685	1362	368	731
2	242	2047	130	1099
1		2290		1229
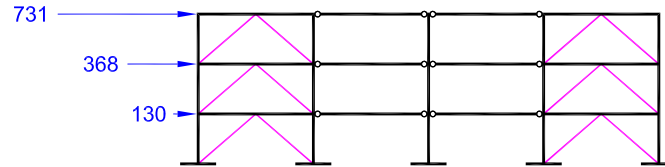
Figure 4.12: Lateral force distribution on the LA 3-story building.

4.7.4 Stiffening Bracing System Properties

4.7.4.1 Brace Initial Stiffness

The initial stiffness per floor for the SBS is calculated so that d_1 corresponds to an assumed drift ratio of 4% (see Figure 4.6). The initial stiffness distribution for the SBS is calculated from Equation 4.1. Assuming four identical braces per braced frame, as shown in Figure 4.12, the individual brace initial stiffness, k_{x_1}, can be calculated as

$$k_{x_1} = \frac{V_{x,f}}{n_b d_1 \cos^2(\theta_{b_x})} \tag{4.18}$$

where $V_{x,f}$ is the braced frame shear force at floor x, n_b is the number of braces per braced frame, d_1 is the assumed inter-story drift, and θ_{b_x} is the brace angle with respect to horizontal. A summary of the individual brace stiffness per braced frame is given in Table 4.6.

Table 4.6: Initial stiffness distribution of the SBS for the LA 3-story building.

Floor	Height (h_x) (in)	Brace Angle θ_{b_x} (rad)	Story shear $(kips)$	Brace Initial Stiff. k_{x_1} (k/in)
3	156	0.714	731	51.3
2	156	0.714	1099	77.1
1	156	0.714	1229	86.2

4.7.4.2 Brace Stiffening Ratios

The floor braces' stiffening ratios are calculated through the iterative process so that uniform inter-story drift ratio of 2% is achieve. This is done by calculating the mass and the effective stiffness matrices of the braced frame, then calculating the maximum expected inter-story drift that is obtained from the modal properties of the structure, as described in Section 4.3. The system matrices as well as the optimization process for the selection of the floor brace stiffening ratio, α_x, are performed using MATLAB (2013). In the calculation of the braced frame stiffness matrix, the floors are considered as rigid diaphragm, while the columns flexibility are taken into consideration. The degrees of freedom for the chevron braced bay are as shown in Figure 4.13.

With the parameters set forth, together with the stiffening ratio per floor, α_x, a nonlinear static pushover analysis is carried out on the final structure and the demand capacity curves are obtained (Freeman, 1998), as shown in Figure 4.14. From the figure, the performance point of *Iteration 01* falls beyond the target performance point (intersection between 10% damped demand curve and the targeted spectral displacement), therefore, the fundamental period of the structure should be updated to a shorter period. Thus, the period of the structure is updated to $(T = 1.42sec)$. The effective period of the structure is calculated from the demand capacity curves as

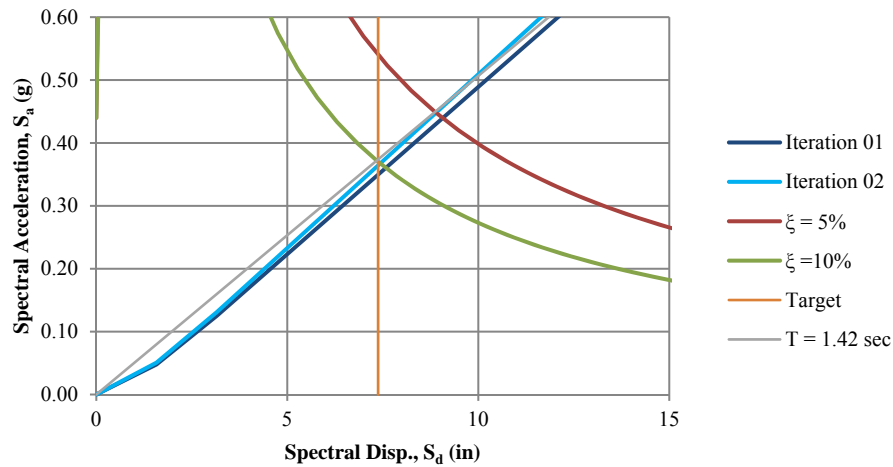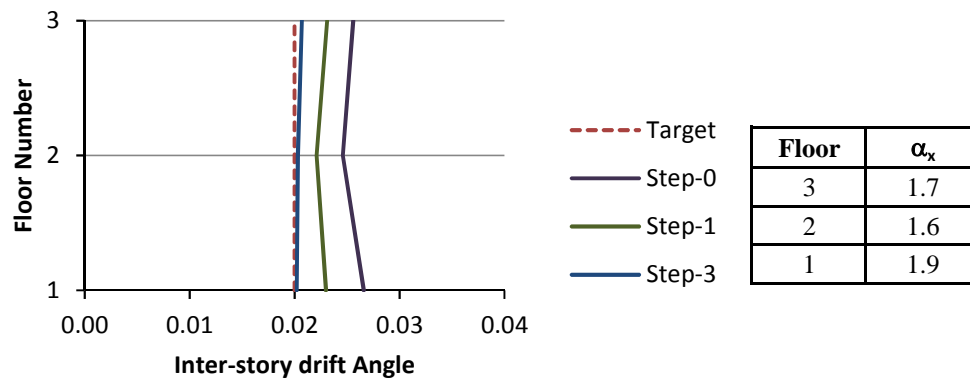$$T_{eff} = 2\pi\sqrt{\frac{S_d}{S_a}} \tag{4.19}$$
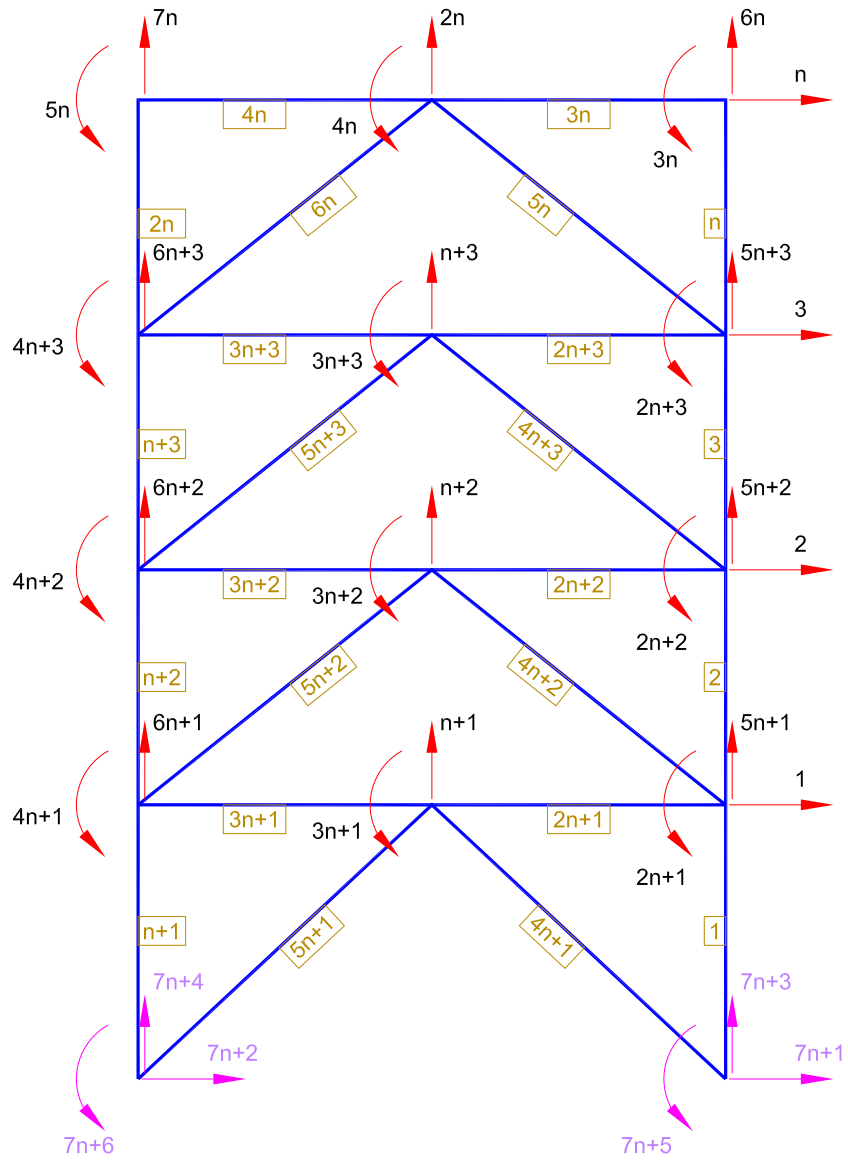
Figure 4.13: Degrees of freedom considered for the braced bay.

Figure 4.14: Capacity demand curves obtained during the optimization pross of the SBS.

Figure 4.15: Design steps for the 3-story braced frame stiffening ratio optimization.

With the updated period, the analysis starts over from the base shear calculation described in Section 4.7.2. As shown in Figure 4.14, the performance point of the updated structure (*Iteration 02*) has converged to the desired performance point with an acceptable tolerance, and hence the analysis stops. The optimization steps for the selection of the stiffening ratios during *Iteration 02* (final iteration) and the final stiffening ratios per floor, α_x, are shown in Figure 4.15.

Table 4.7: Properties of the SBS used with the 3-story building.

Floor	Δ_1/h_x (%)	θ_{b_x} (rad)	k_{x_1} (k/in)	α_x	c_x (k.s/in)
3	0.50	0.714	53.7	1.70	4.25
2	0.50	0.714	81.1	1.60	4.25
1	0.50	0.714	91.1	1.90	4.25

4.7.4.3 Distribution of Viscous Damping Devices

After setting all the stiffness parameters of the SBS, viscous damping devices are needed to be designed and distributed over the building height. These devices should provide the structure with the desired viscous damping ratio that the design of the SBS is based on. As mentioned earlier, the desired damping ratio for the system was set to 10%. It is assumed that the structure possesses 2% inherent damping ratio, and the viscous damping devices need to add the remaining 8% damping. Substituting into Equation 4.9 and assuming identical viscous damping devices placed parallel to each brace, the typical viscous damping coefficient is found to be ($c_j = 4.25k.sec/in$). The final properties of the SBS for the 3-story building are shown in Table 4.7.

To ensure that the distributed damping devices indeed provide the desired effective damping to the system, a free vibration analysis is carried out. A short period pulse excitation is applied at the base of the structure and the roof displacement response history is observed, as shown in Figure 4.16. The effective damping ratio of the structure can be calculated from the decaying roof displacement as follows

$$\zeta = \frac{1}{2\pi j} \ln\left(\frac{u_i}{u_{i+j}}\right) \tag{4.20}$$

where j is the number of considered cycles of vibration, u_i is the peak displacement at cycle i, and u_{i+j} is the peak displacement after j cycles from i. From Figure 4.16 and Equation 4.20, the effective damping ratio of the structure is found to be ($\zeta_{eff} \simeq 10\%$),
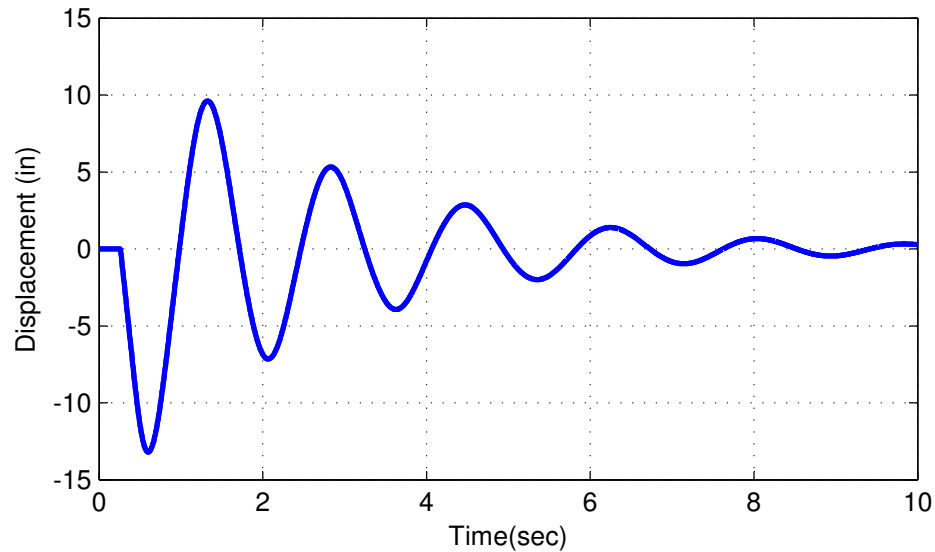
Figure 4.16: Decay of the 3-story building roof displacement response history under free vibration.

which matches the desired value.

4.8 LA 9-story Building

In this section, the implementation of the SBS in the Los Angeles 9-story benchmark building is presented (FEMA, 2000). The benchmark building was redesigned once as buckling restrained braced frame (BRBF) and with the proposed stiffening bracing system (SBS). As mentioned earlier, the response modification factor, R, is taken as eight for the case of BRBF and unity for the SBS. The distribution of the viscous damping devices has been determined to achieve an effective damping ratio of 10%. The layout of the Los Angeles 9-story office building with the moment resisting frame being replaced by the proposed braced frame is shown in Figure 4.17. The analyses of the braced frame systems is conducted for the north-south direction. Two intermediate bays are chosen to be Chevron type braced bays, as shown in the figure. The seismic mass per braced frame is taken as half of the building's total mass, which is

Table 4.8: Total floor mass for the 9-story office building.

Floor Level	Total Mass $(kips.sec^2/ft)$
Roof	73.10
Floors 9 to 3	67.86
Floor 2	69.04

given by FEMA-355C (FEMA, 2000) as shown in Table 4.8.

4.8.1 Design of LA 9-story Building with SBS

As mentioned in the design of the 3-story building with the SBS, the initial step is to assume a performance point on the demand-capacity curves and find the corresponding structural period of vibration. In this section, only the final iteration results are presented. The effective damping ratio is assumed ($\zeta_{eff} = 10\%$). In the last iteration, the structural period of vibration was found to be ($T = 3.90sec$). This period together with the assumed viscous damping ratio are used to calculate the seismic base shear and the equivalent lateral force distribution.

With response modification coefficient ($R = 1$), importance factor ($I = 1$), and structural period ($T = 3.90sec$), the seismic response coefficient (C_s) is governed by the lower bound as follows

$$C_s = \frac{0.5S_1}{(R/I)} = \frac{0.5 \times 0.528g}{(1/1)} = 0.264g$$

As the structure period is more than $2.5sec$, the exponent k is taken as ($k = 2.0$). The final vertical distribution of seismic forces is given in Table 4.9. Considering the accidental torsional moment, the lateral floor forces and floor shear per braced frame become as shown in Table 4.10.

A summary of the individual brace stiffness per braced frame is given in Table 4.11.
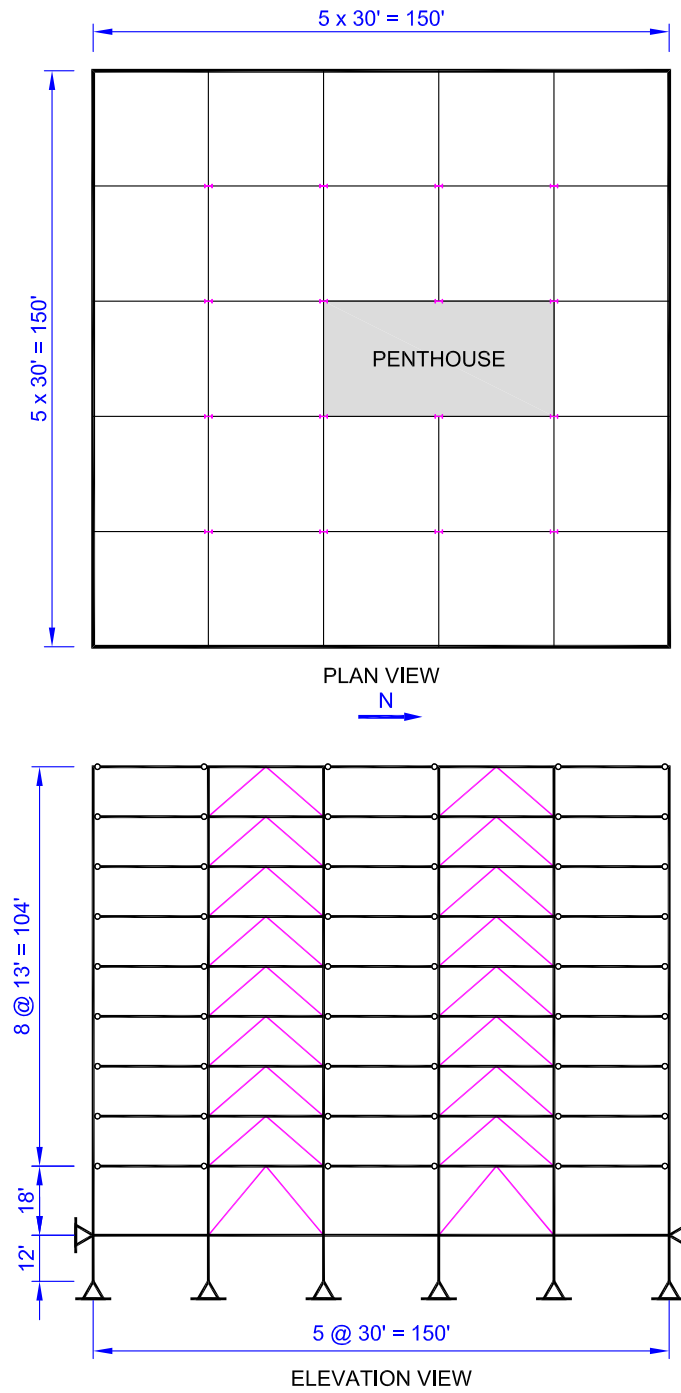
Figure 4.17: Layout of the Los Angeles 9-story braced frame building

Table 4.9: Vertical distribution of shear for the LA 9-story building.

Level	w_x $(kips)$	$\sum w$ $(kips)$	h_x (ft)	$w_x h_x^k$ $(kip-ft)$	$w_x h_x^k/(w_x h_x^k)$	F_x $(kips)$	V_x $(kips)$
Roof	2354	2354	122	35036936	0.289	1519	
9	2185	4539	109	25959985	0.214	1126	1519
8	2185	6724	96	20136960	0.166	873	2645
7	2185	8909	83	15052465	0.124	653	3518
6	2185	11094	70	10706500	0.088	464	4170
5	2185	13279	57	7099065	0.059	308	4634
4	2185	15464	44	4230160	0.035	183	4942
3	2185	17649	31	2099785	0.017	91	5126
2	2223	19872	18	720252	0.006	31	5217
1							5248
Total	19872			121042108		5248	

Table 4.10: Braced frame shear forces for the LA 9-story building.

| Level	Story force F_x $(kips)$	Story shear V_x $(kips)$	Frame force $F_{x,f}$ $(kips)$	Frame shear $V_{x,f}$ $(kips)$
Roof	1519		397	
9	1126	1519	294	397
8	873	2645	228	691
7	653	3518	170	918
6	464	4170	121	1089
5	308	4634	80	1210
4	183	4942	48	1290
3	91	5126	24	1338
2	31	5217	8	1362
1		5248		1370

Table 4.11: Initial stiffness distribution of the SBS for the LA 9-story building.

Floor	Height (h_x) (in)	Brace Angle θ_{b_x} (rad)	Story shear $(kips)$	Brace Initial Stiff. k_{x_1} (k/in)
9	156	0.714	397	27.8
8	156	0.714	691	48.4
7	156	0.714	918	64.4
6	156	0.714	1089	76.4
5	156	0.714	1210	84.9
4	156	0.714	1290	90.5
3	156	0.714	1338	93.9
2	156	0.714	1362	95.6
1	216	0.876	1370	96.7

Floor	α_x
9	2.3
8	1.8
7	1.7
6	1.7
5	1.7
4	1.8
3	1.8
2	2.0
1	2.1
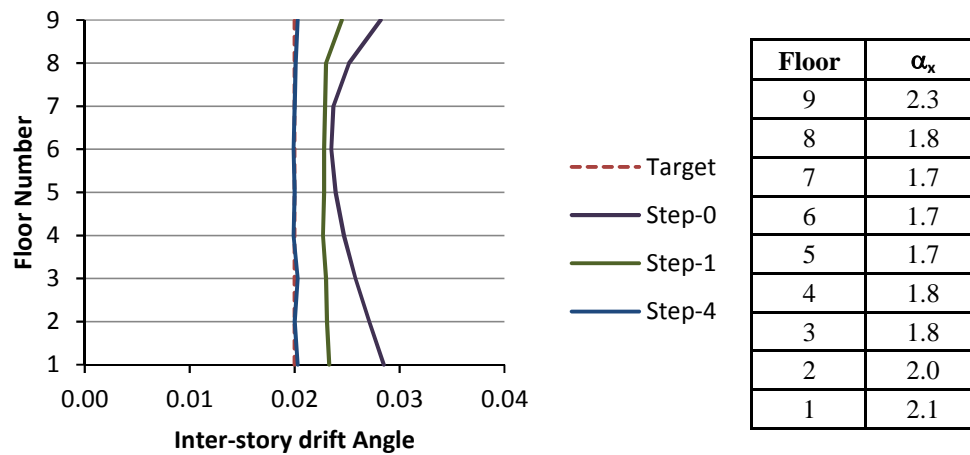
Figure 4.18: Design steps for the 9-story braced frame stiffening ratio optimization.

A 2% target inter-story drift ratio is chosen as the desired performance of the 9-story building employing the proposed SBS. Based on this assumption, the iterative process illustrated in Section 4.3 results in the braces stiffening ratios shown in Figure 4.18. The nonlinear static pushover analysis conducted for the 9-story building with the optimized parameters is shown in Figure 4.19. The capacity curve intersects the 10% damped demand curve at an effective period of 3.9sec as initially assumed.

As in the case of the 3-story building, the 9-story building is assumed to have 2% inherent damping, and the desired addition damping is being provided by means
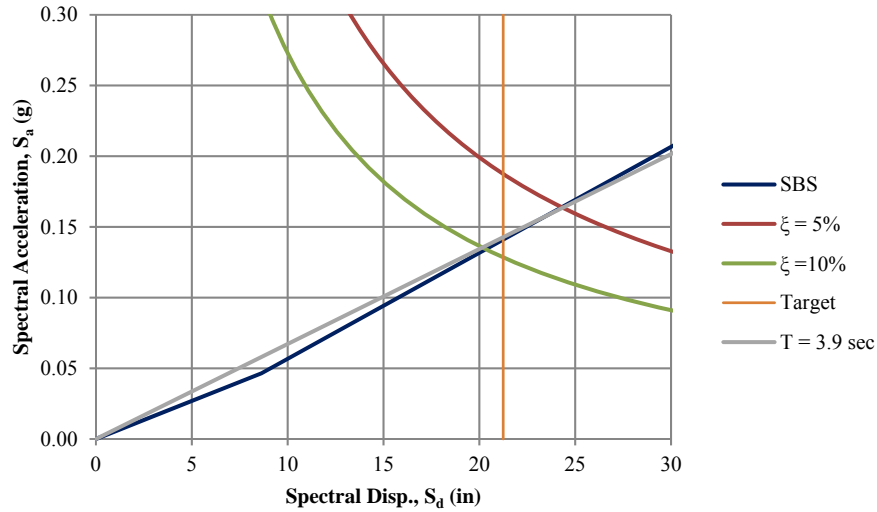
Figure 4.19: Capacity demand curves of the 9-story building with the final parameters of the SBS.

of viscous damping devices, designed and distributed as before. The dampers are installed in parallel with the braces. Based on the desired performance and the required added damping ($\zeta_d = 8\%$), Equation 4.9 leads to a typical viscous damping coefficient of ($c_j = 10.5k.sec/in$). However, the free vibration analysis showed that this value needs to be increased to achieve the desired damping level. The damping coefficient used for this building is ($c_j = 13k.sec/in$). The final properties of the SBS for the 9-story building are shown in Table 4.12.

4.9 Performance Assessment of the SBS

In the following subsections, the performance of the 3-story and 9-story buildings employing the stiffening bracing system is investigated under the effect of design earthquake (10/50) and the maximum considered earthquake (2/50) as described in Section 4.6. The nonlinear response history analyses is also carried out for a BRBF systems and compared to SBS. For this purpose, BRBFs are designed for the average

Table 4.12: Properties of the SBS used with the 9-story building.

Floor	Δ_1/h_x (%)	θ_{b_x} (rad)	k_{x_1} (k/in)	α_x	c_x (k.s/in)
9	0.50	0.714	27.8	2.30	13.0
8	0.50	0.714	48.4	1.80	13.0
7	0.50	0.714	64.4	1.70	13.0
6	0.50	0.714	76.4	1.70	13.0
5	0.50	0.714	84.9	1.70	13.0
4	0.50	0.714	90.5	1.80	13.0
3	0.50	0.714	93.9	1.80	13.0
2	0.50	0.714	95.6	2.00	13.0
1	0.50	0.876	96.7	2.10	13.0

forces induced by the design level earthquake records.

4.9.1 Performance of the 3-story building

A comparison between the BRBF and SBS systems in terms of the pushover capacity according to the first mode of vibration is shown in Figure 4.20. The peak inter-story drift angles and the peak floor accelerations for the structure with the SBS under the effect of the design earthquakes (10/50) are shown in Figure 4.21. The median, which is defined as the exponential of the average of the natural log values, as well as the 84th percentile, defined as the median times the exponent of the standard deviation of the natural logs, are overlaid on the figure. The median and 84th percentile are calculated according to Equation 3.32, which is repeated here for convenience

$$\hat{x} = e^{\frac{1}{n} \sum_{i=1}^{n} \ln x_i} \tag{4.21a}$$

$$\delta = \sqrt{\frac{\sum_{i=1}^{n} (\ln x_i - \ln \hat{x})^2}{n-1}} \tag{4.21b}$$

$$84^{th} \ percentile = \hat{x} e^{\delta} \tag{4.21c}$$

As can be seen from Figure 4.21, the proposed stiffening bracing system is capable of achieving the desired uniform inter-story drift for the structure with an acceptable accuracy around the 2% target inter-story drift angle. Note that it is allowed for the average maximum inter-story drift ratios obtained through nonlinear response history analysis to exceed the target by 25% as per ASCE 7-10. In comparison to the BRBF, Figure 4.22 shows the median and the 84th percentile of the peak floor drift angles and accelerations. It is clear that the proposed system significantly reduced the floor acceleration demands, whereas the roof acceleration was slightly increased. On the other hand, the figure indicates that the BRBF experiences less inter-story drift than the SBS. However, permanent story drift was observed under most of the considered design earthquakes set (10/50), while none of these motions resulted in any yielding to the structure with the SBS. Figure 4.23 shows the response history of the floor drift angles under the effect of the near-fault LA04 (*1979 Imperial Valley*), with a distance of 4.1km to the fault. It can be seen from the figure that the BRBF experiences permanent floors yielding, while the proposed system performs as intended without any yielding of the main frame elements, and successfully maintains the uniform inter-story drift during the entire duration of the excitation. This behavior can also be recognized by examining Figure 4.24 which shows the story shear forces versus inter-story drift under the same excitation.

Under the effect of the maximum considered earthquake (2/50), the target performance of uniform inter-story drift distribution remains unaltered for the structure with the SBS, as observed from Figure 4.25, where the system successfully maintains the uniform inter-story drift distribution under most of the considered excitations. A comparison between the median and the 84th percentile of the peak inter-story drift angles and the peak floor accelerations for the two considered systems is shown in Figure 4.26. It is evident that the target response of the proposed SBS is still achievable
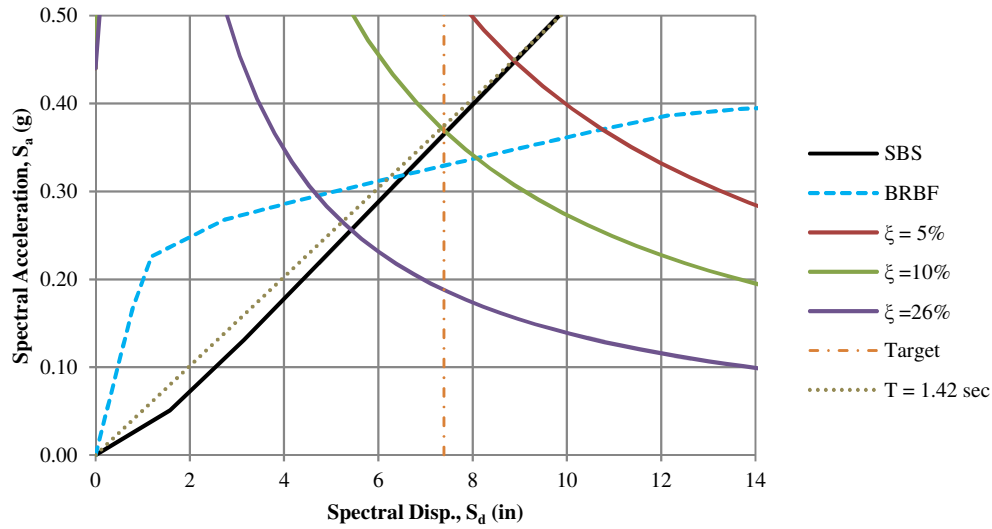
Figure 4.20: Capacity-demand curves for the LA 3-story building

under the effect of higher seismic demand, however the response is accordingly scaled. The permanent floor drifts that are observed for the BRBF do not occur for the SBS under most of the considered excitations. Figures 4.27 and 4.28 show an example of the systems performance under the effect of the LA22 (*1995 Kobe*) 3.4km away from the fault. It should be mentioned here that the BRBF analyses under LA27 and LA28 indicated near collapse condition and their responses were eliminated for both systems. Other response quantities are shown in Appendix D.

4.9.2 Performance of the 9-story building

The capacity demand curves obtained from the pushover analysis with lateral forces according to the first mode of vibration of the 9-story buildings are shown in Figure 4.29. The peak inter-story drift angles and the peak floor accelerations for the structure with the SBS under the effect of the design earthquakes (10/50) are shown in Figure 4.30. As can be seen from the figure, the proposed stiffening bracing system
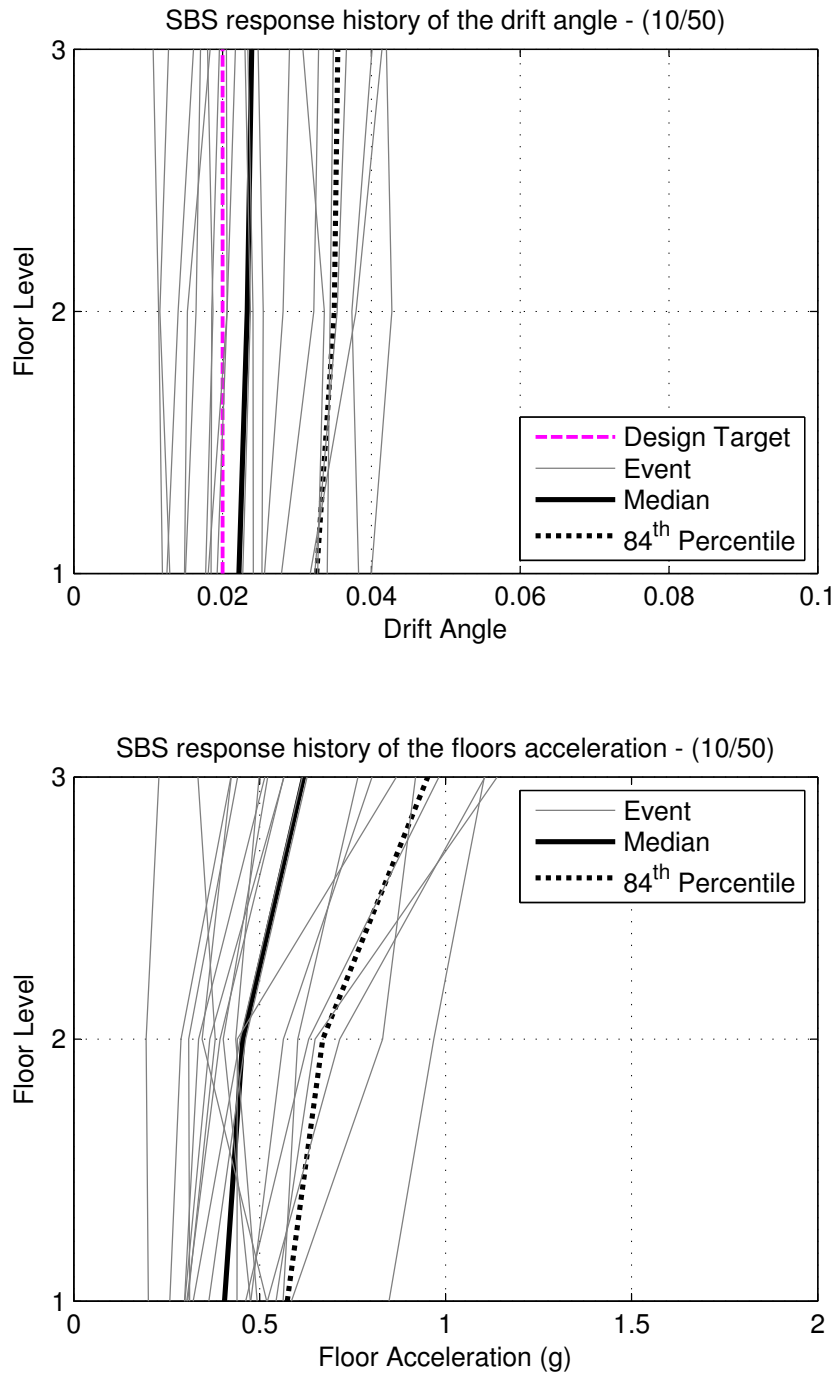
Figure 4.21: Peak response of the floor drift angles and accelerations under the 10/50 ground motions set
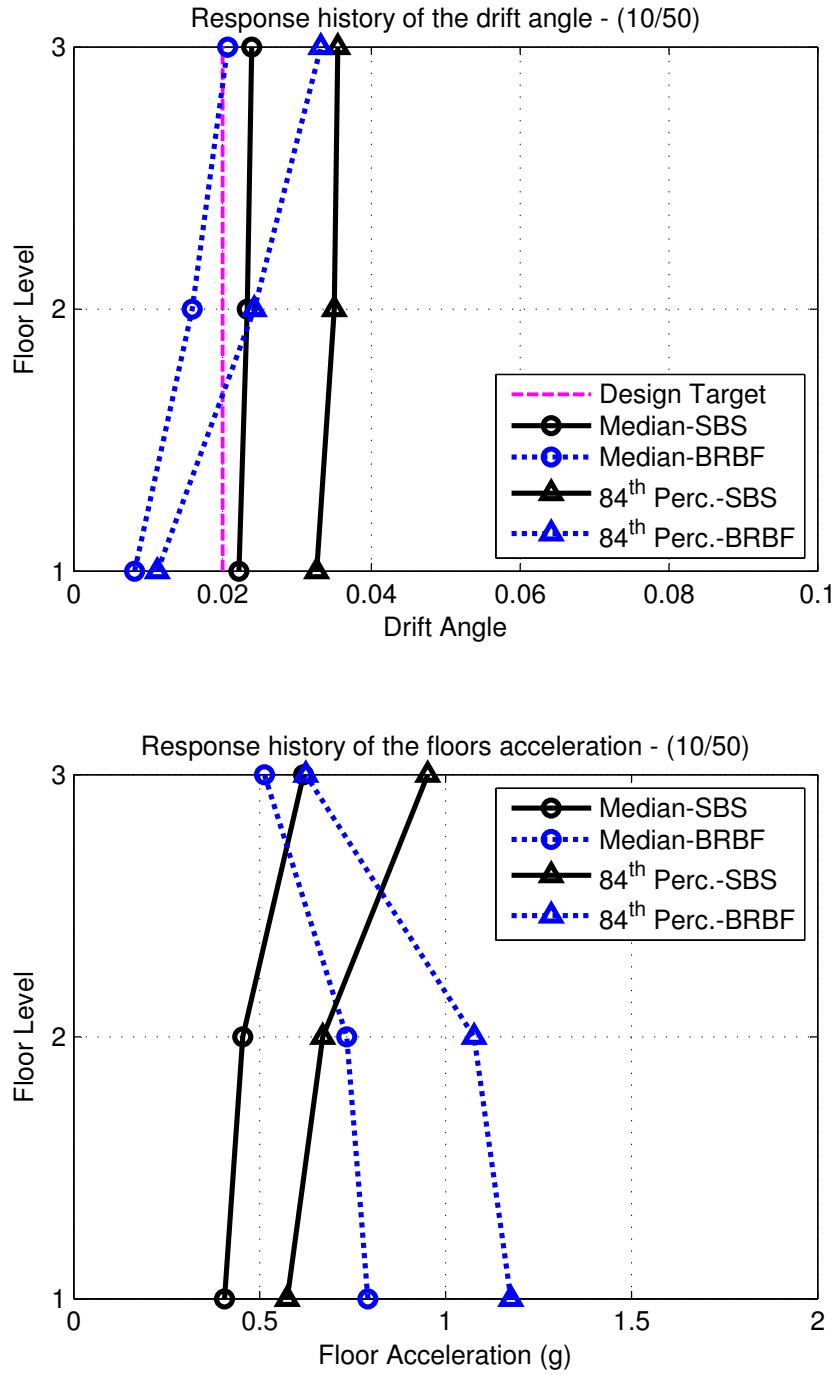
Figure 4.22: Median and 84th percentile of the peak floor drift angles and accelerations for the LA 3-story building with different bracing systems under the 10/50 ground motions set
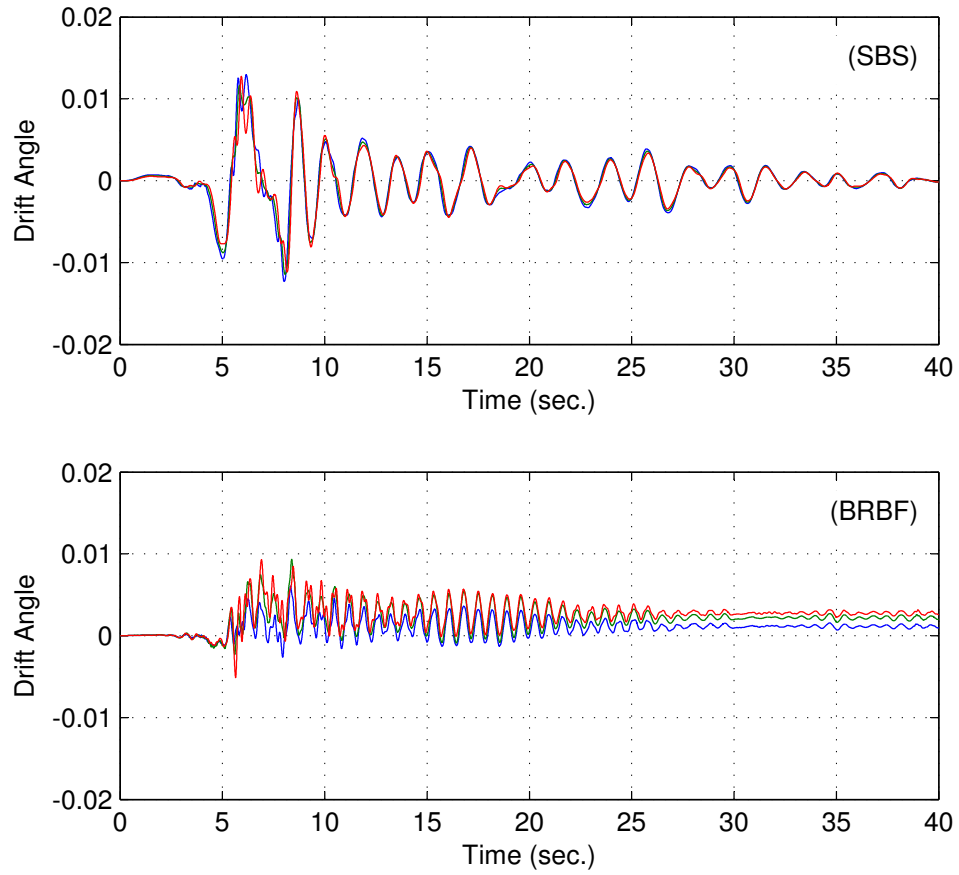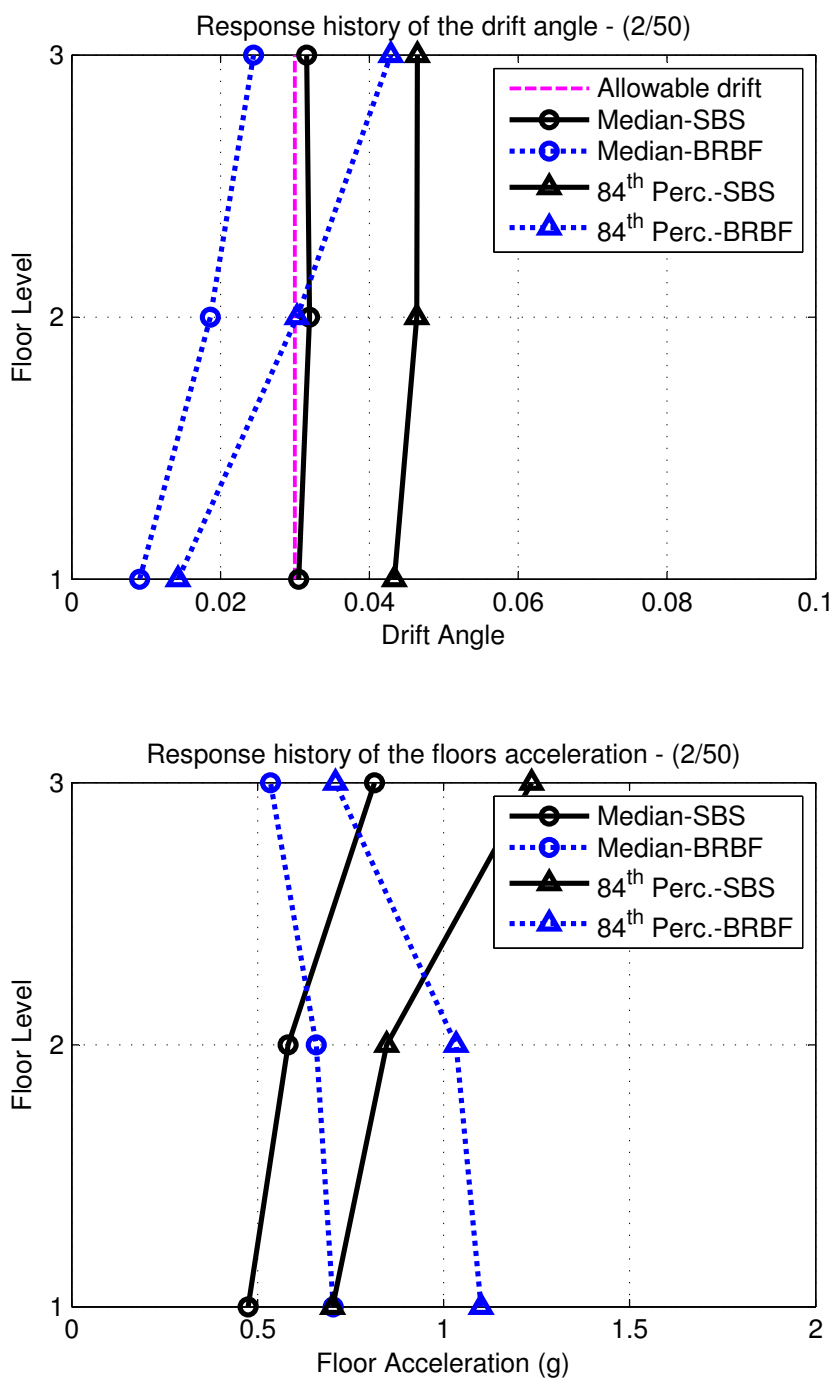
Figure 4.23: Inter-story drift angle response history under LA04 (Imperial Valley, 1979)
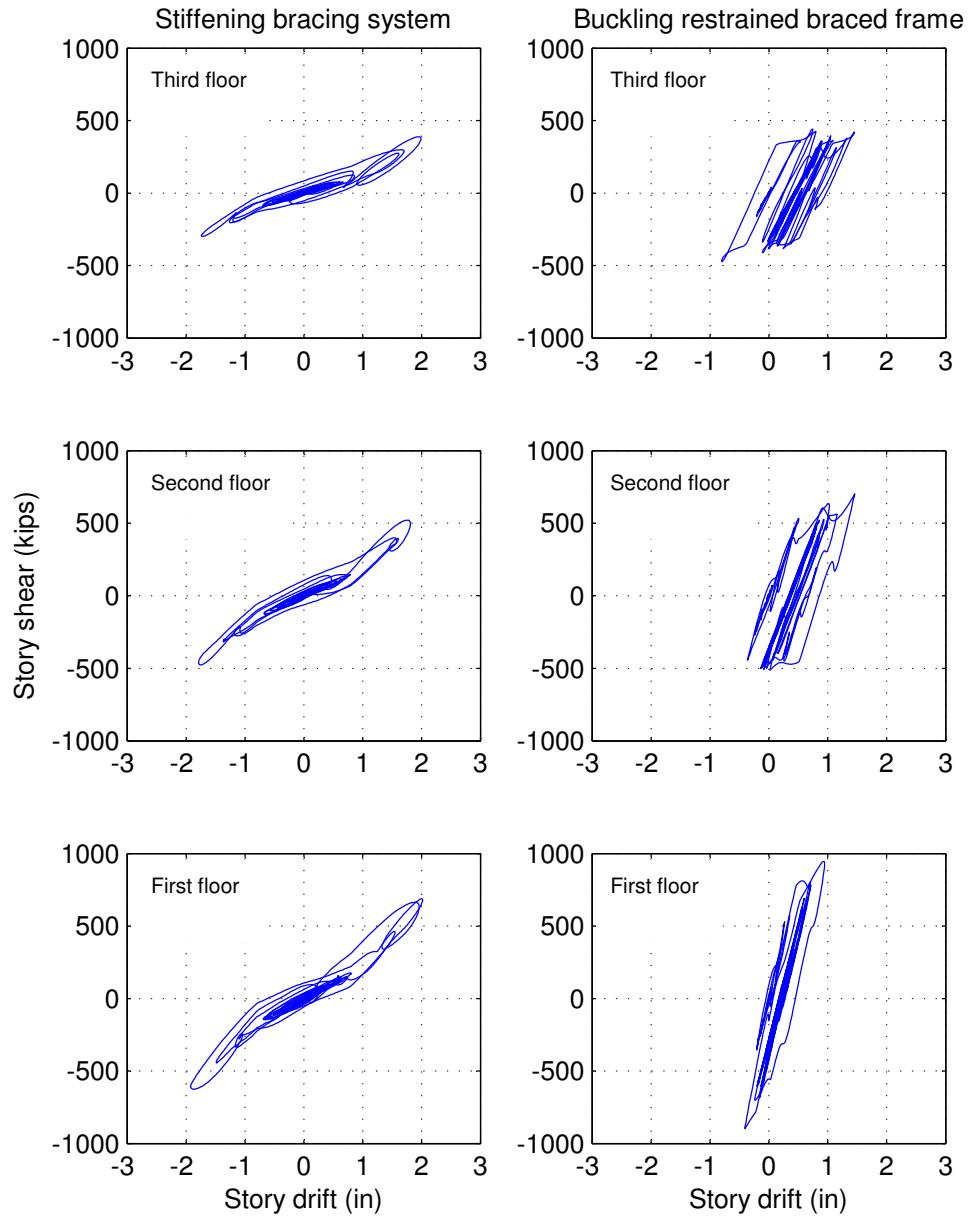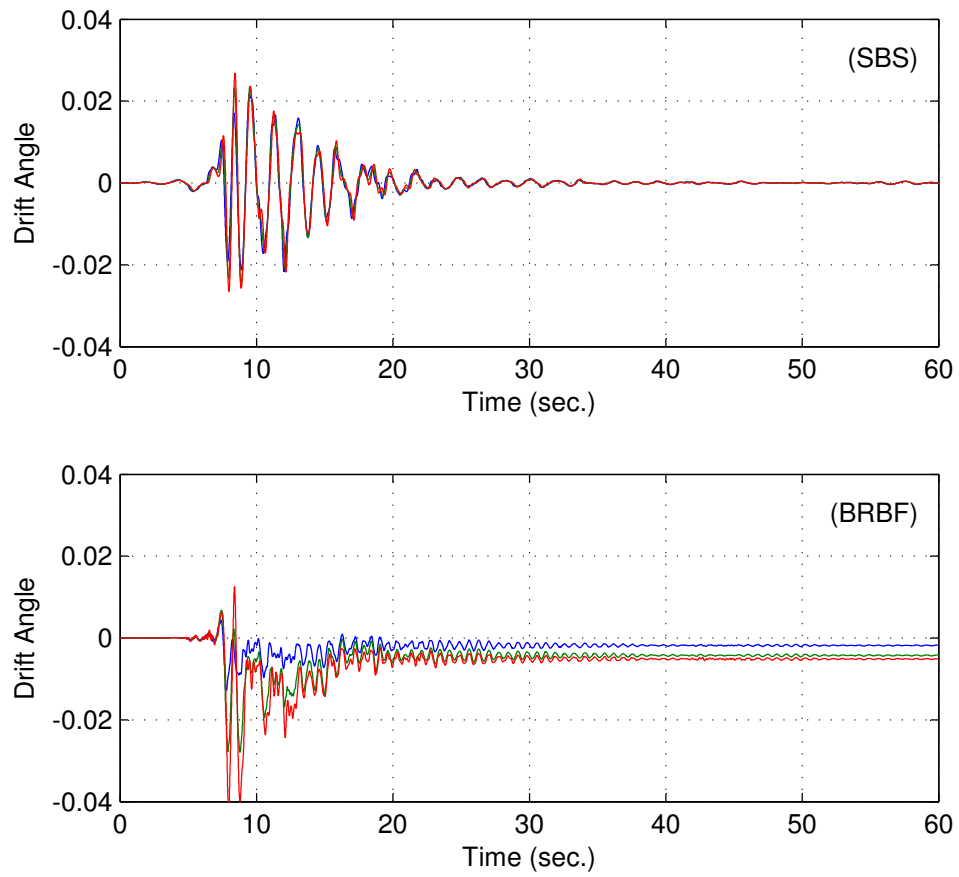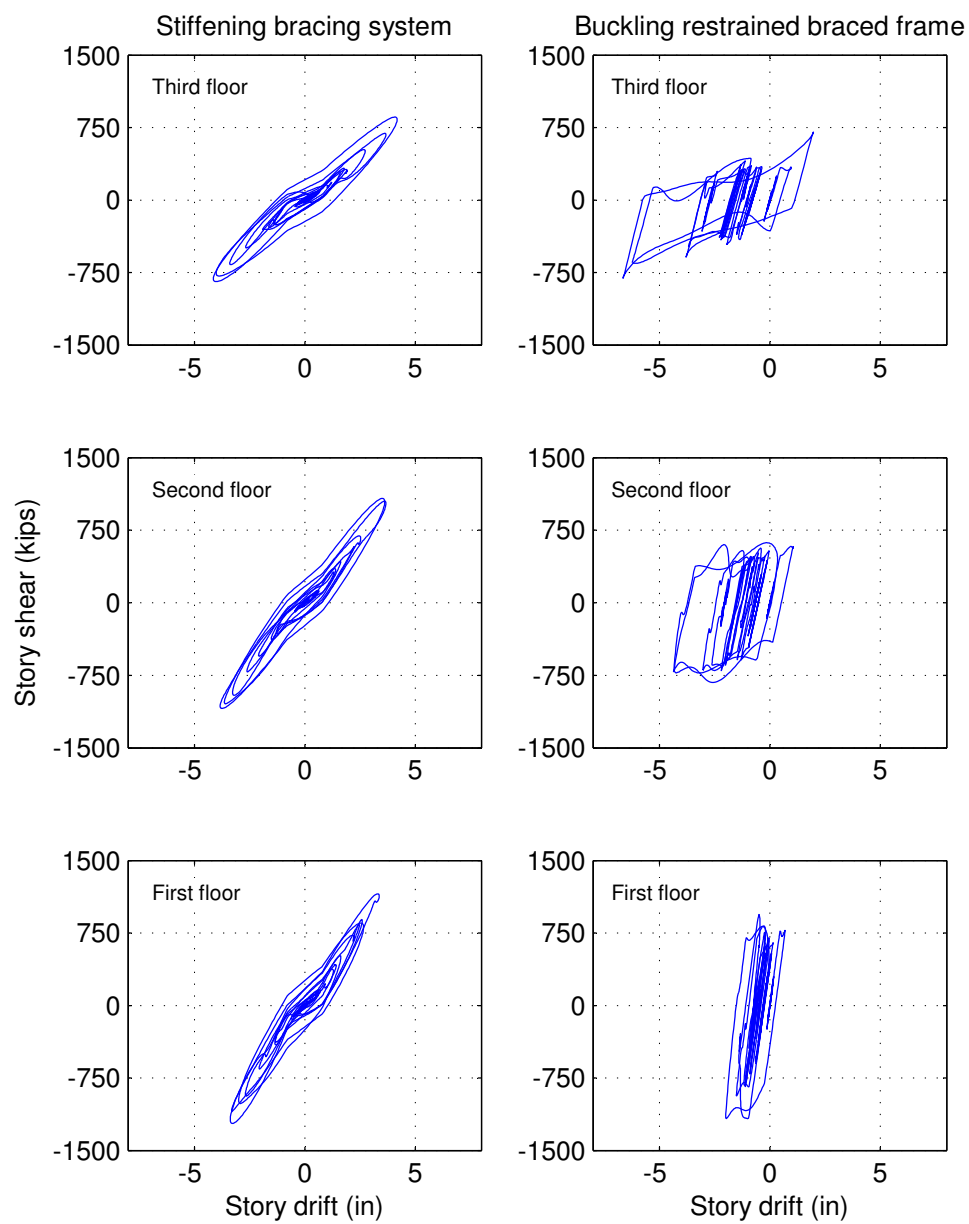
Figure 4.24: Story shear - interstory drift under LA04 (Imperial Valley, 1979)
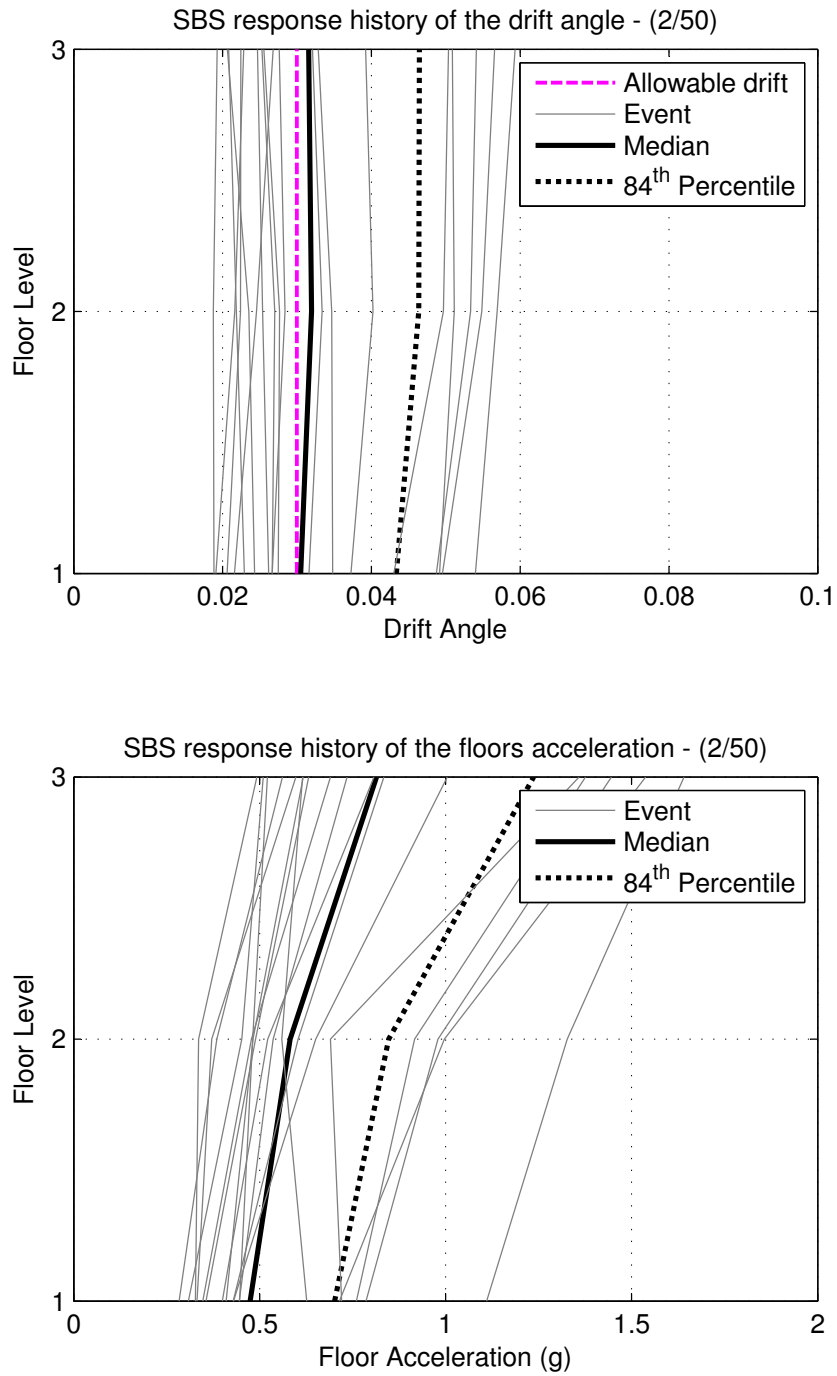
Figure 4.25: Peak response of the floor drift angles and accelerations under the 2/50 ground motions set

Figure 4.26: Median and 84th percentile of the peak floor drift angles and accelerations for the LA 3-story building with different bracing systems under the 2/50 ground motions set

Figure 4.27: Inter-story drift angle response history under LA22 (Kobe, 1995)

Figure 4.28: Story shear - interstory drift under LA22 (Kobe, 1995)

achieves the desired performance for the 9-story building, as the median of the peak inter-story drift angles for all floors is around the target drift ratio of the 2%. Figure 4.31 shows the median and the 84th percentile of the peak floor drift angles and accelerations for both systems. Clearly, the proposed system significantly reduces the floor acceleration demands compared to the BRBF. However, the BRBF experiences less inter-story drift than the SBS due to the high stiffness of the BRBF. In addition, the BRBF is primarily designed to dissipate energy through yielding. It is therefore not uncommon to observe permanent story deformations under most of the considered design earthquakes. The SBS dissipates the seismic energy through implementation and distribution of passive viscous dampers. Thus, any yielding in the SBS system would be due to main structural frame yielding, which is not permitted in the proposed methodology. According to the nonlinear response history analyses, none of the design earthquake motions resulted in any yielding to the structure with the SBS. Figure 4.32 shows the response history of the floor drift angles under the effect of LA04 (*1979 Imperial Valley*), with a distance of 4.1km to the ruptured fault. Under some cases, up to 1% permanent floor deformation is encountered on the BRBF, which can be avoided with the proposed SBS. From Figure 4.32, it can be noticed that the target uniform inter-story drift is also achieved generally. A comparison between the force-displacement characteristics for the considered systems is given in Figures 4.33 to 4.35 where the stiffening behavior of the SBS is evident.

Under the effect of the maximum considered earthquake (2/50), a slight increase in the inter-story drift ratio is anticipated. As depicted in Figure 4.36, the target uniform inter-story drift is also achieved and remained under the maximum permitted value, which is 3.0% as per ASCE 7-10. A comparison between the median and the 84th percentile of the peak inter-story drift angles and the peak floor accelerations for the two systems is shown in Figure 4.37. The figure shows reduced floor accelera-
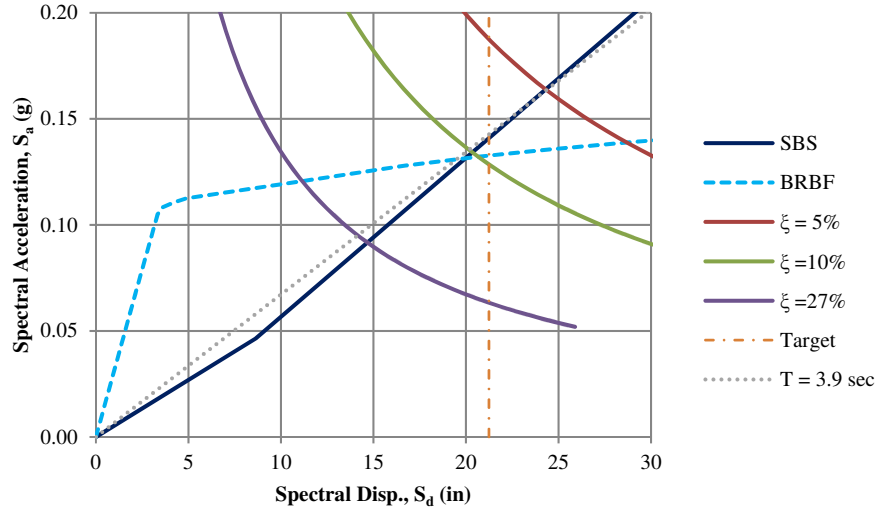
**Figure 4.29:** Capacity-demand curves for the 9-story buildings

tion demands for the structure with the SBS with almost uniform inter-story drifts. Figure 4.38 shows the response history of the inter-story drift angle under the effect of selected record, LA31 (*Elysian Park*). The inter-story drift uniformity for this record was not evident during the entire duration of the excitation, however after the 15th second, the structure started behaving uniformly as desired. The inter-story displacement inter-story shear relationships for both systems are shown in Figures 4.39 to 4.41 under the effect of the LA31 (*Elysian Park*) simulated motion with a distance of 17.5km from the ruptured fault. Appendix D shows more response quantities for the analyzed structures.
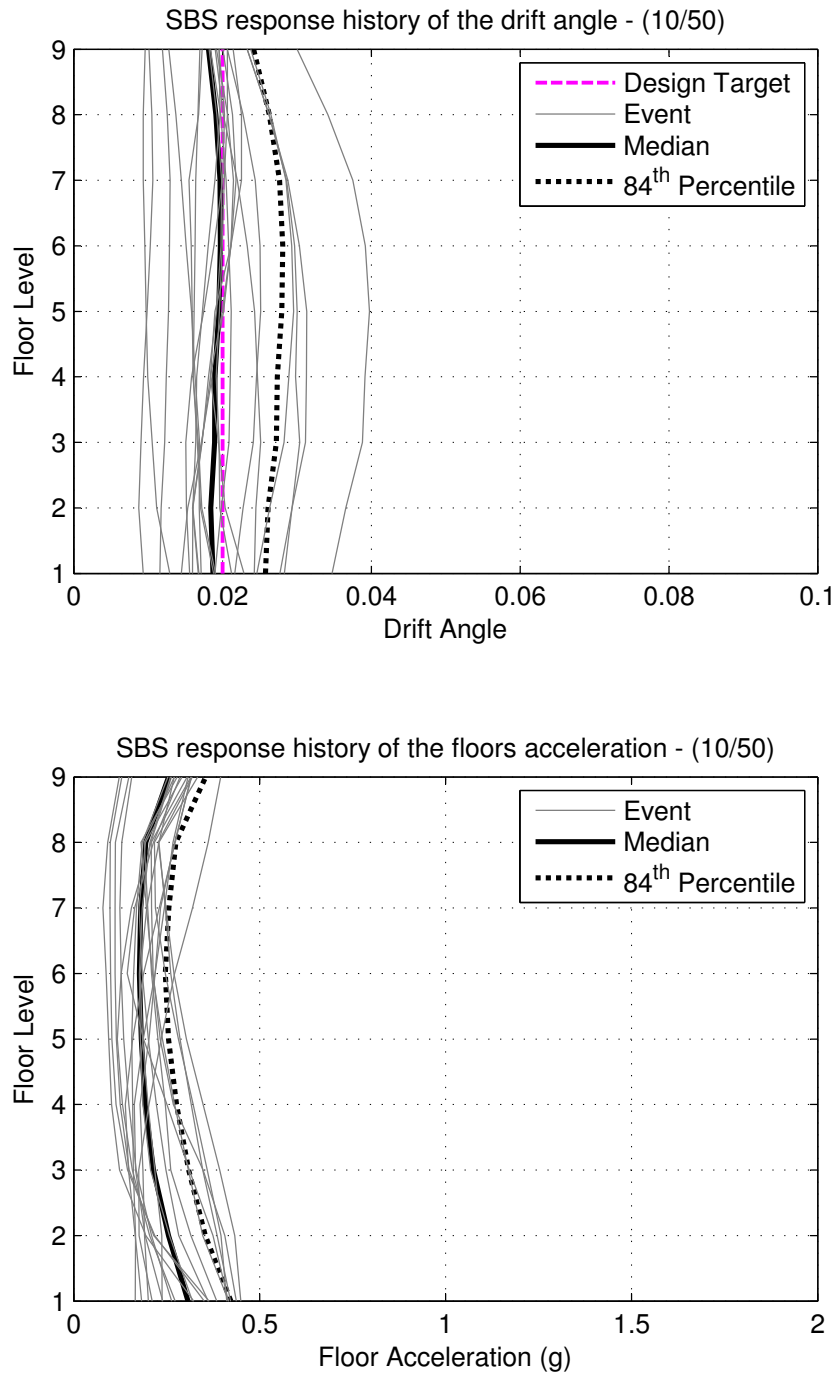
Figure 4.30: 9-story building, peak response of the floor drift angles and accelerations under the 10/50 ground motions set
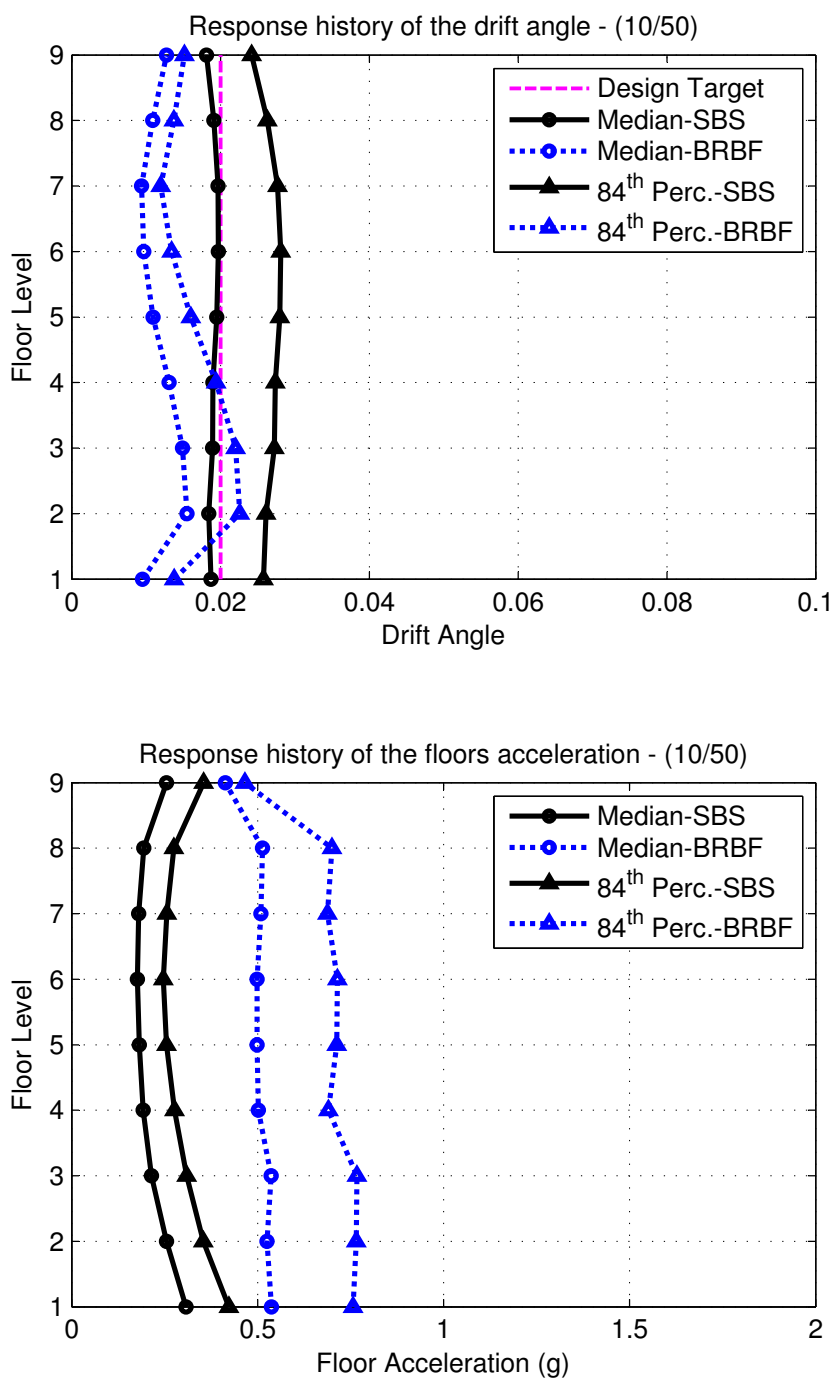
Figure 4.31: Median and 84th percentile of the peak floor drift angles and accelerations for the 9-story building with different bracing systems under the 10/50 ground motions set
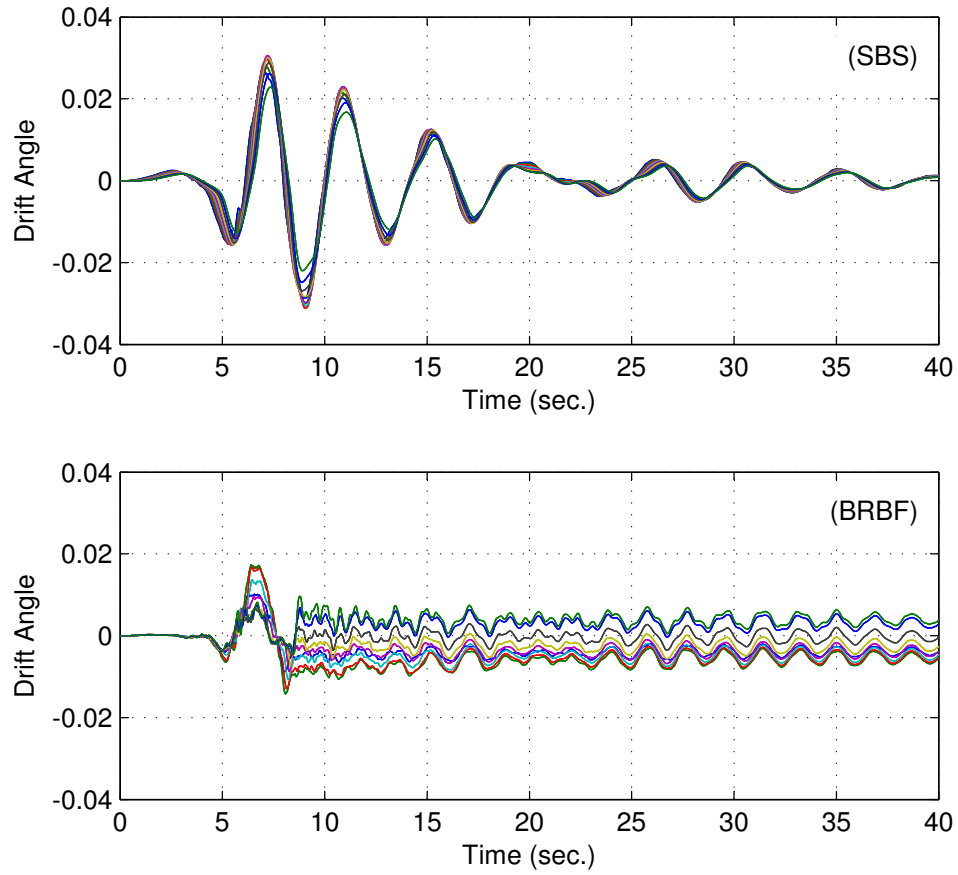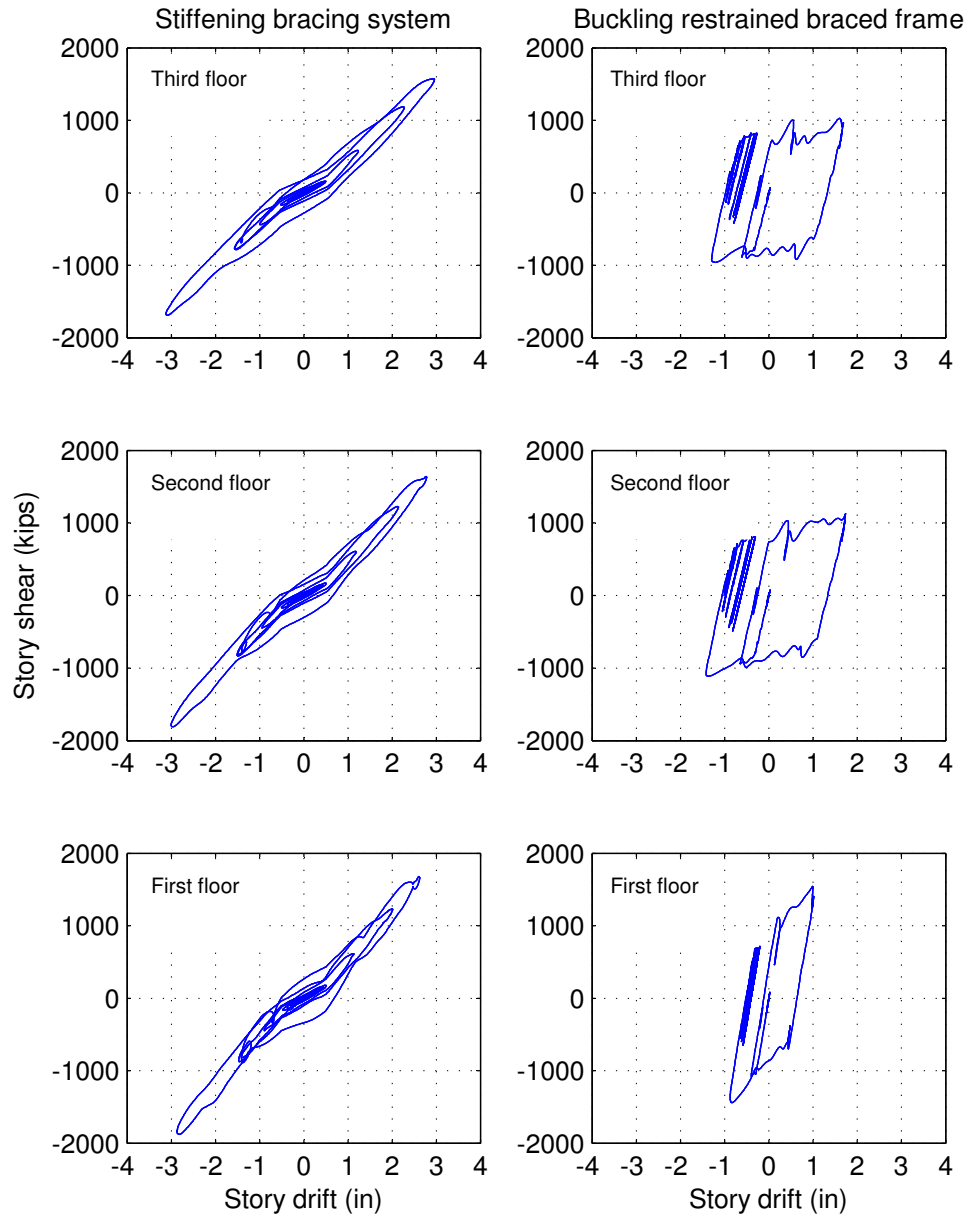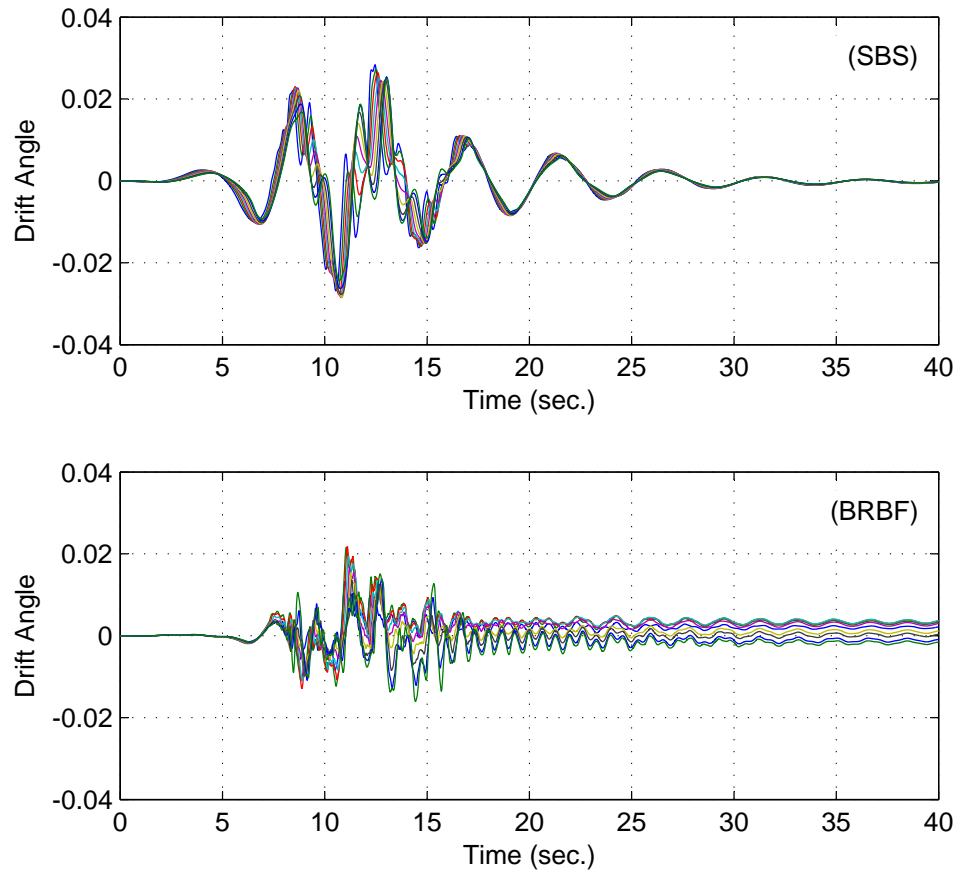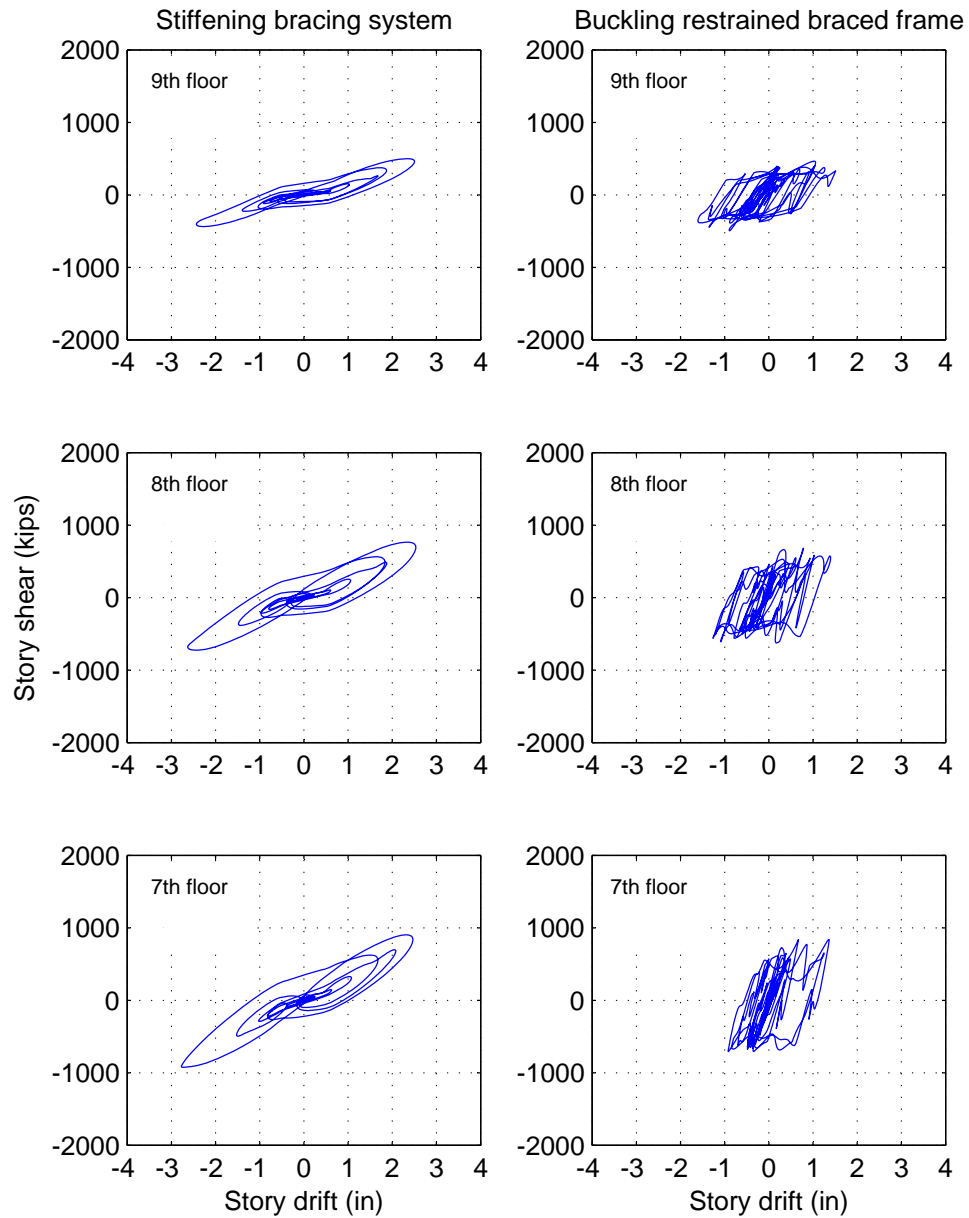
Figure 4.32: 9-story building, inter-story drift angle response history under LA04 (Imperial Valley, 1979)
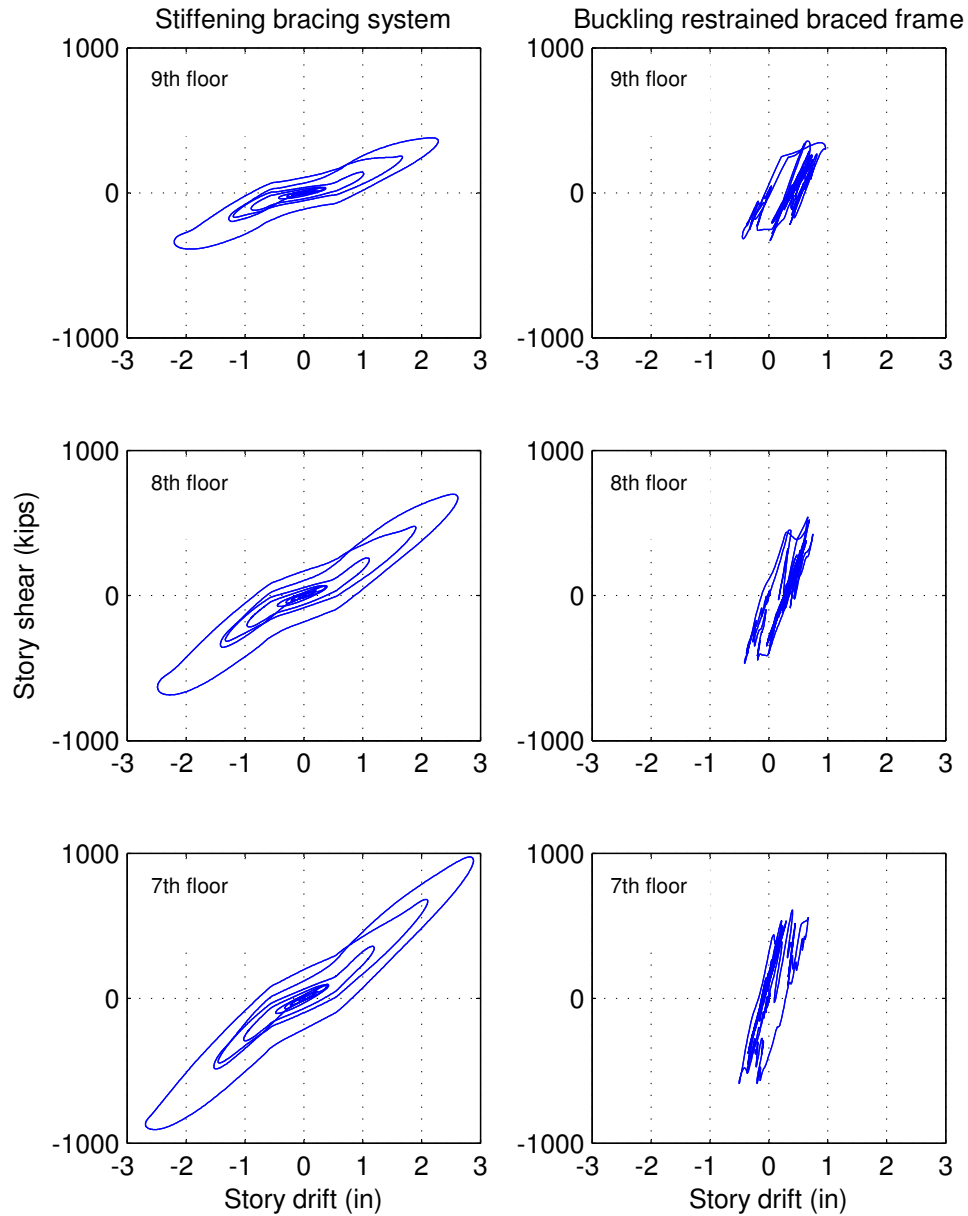
Figure 4.33: 9-story building, story shear - interstory drift for the upper three floors under LA04 (Imperial Valley, 1979)
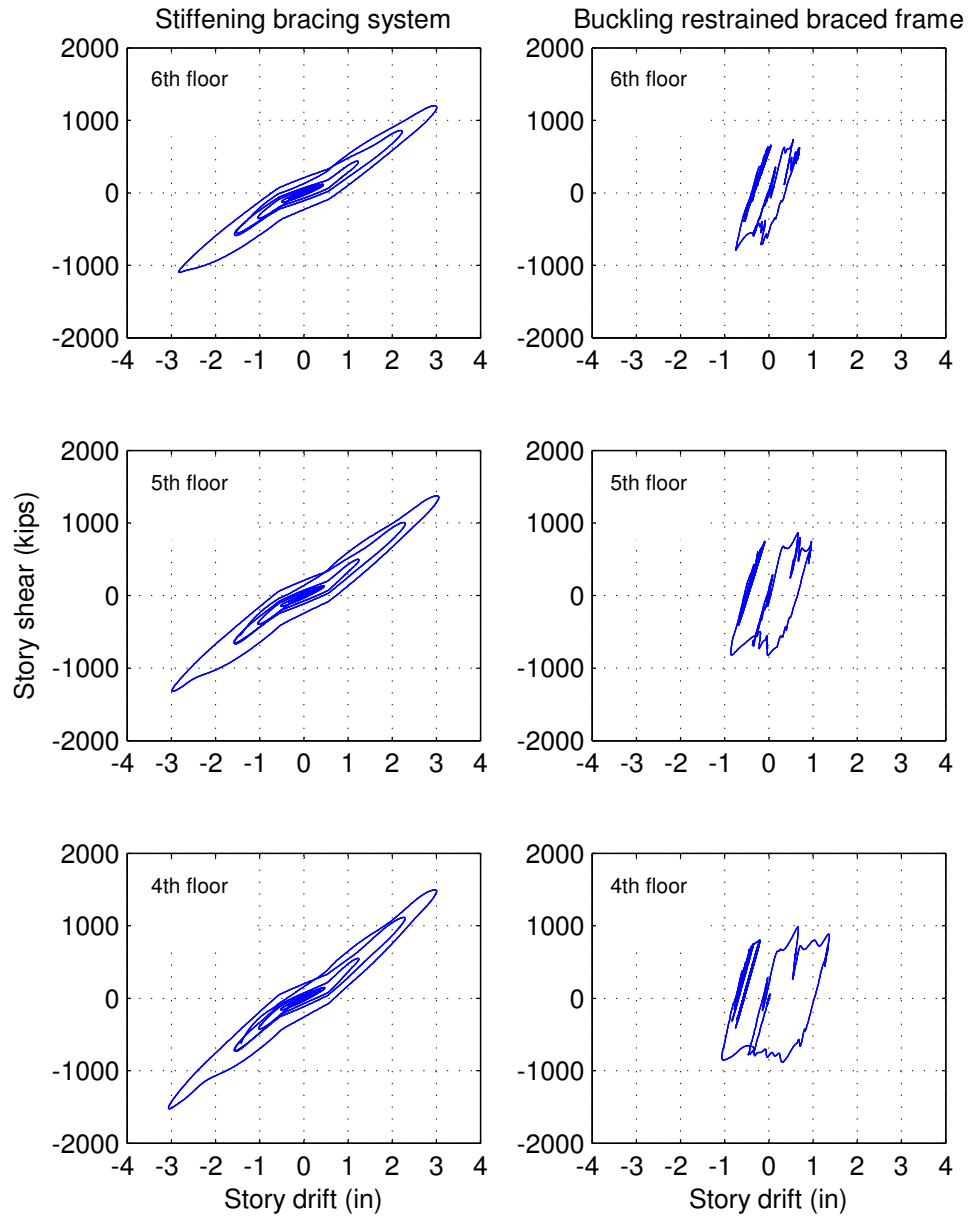
Figure 4.34: 9-story building, story shear - interstory drift for the middle three floors under LA04 (Imperial Valley, 1979)

Figure 4.35: 9-story building, story shear - interstory drift for the lower three floors under LA04 (Imperial Valley, 1979)
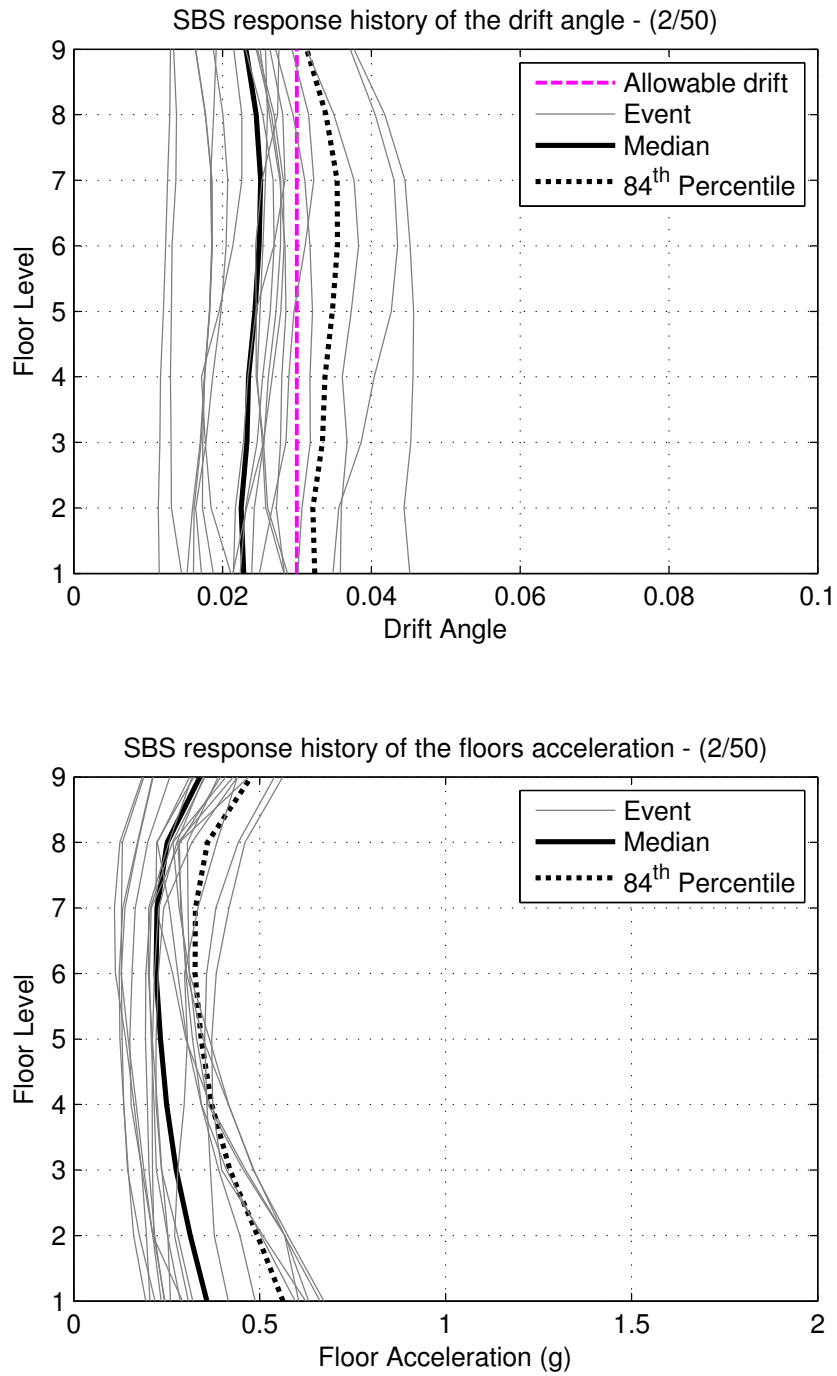
Figure 4.36: 9-story building, peak response of the floor drift angles and accelerations under the 2/50 ground motions set
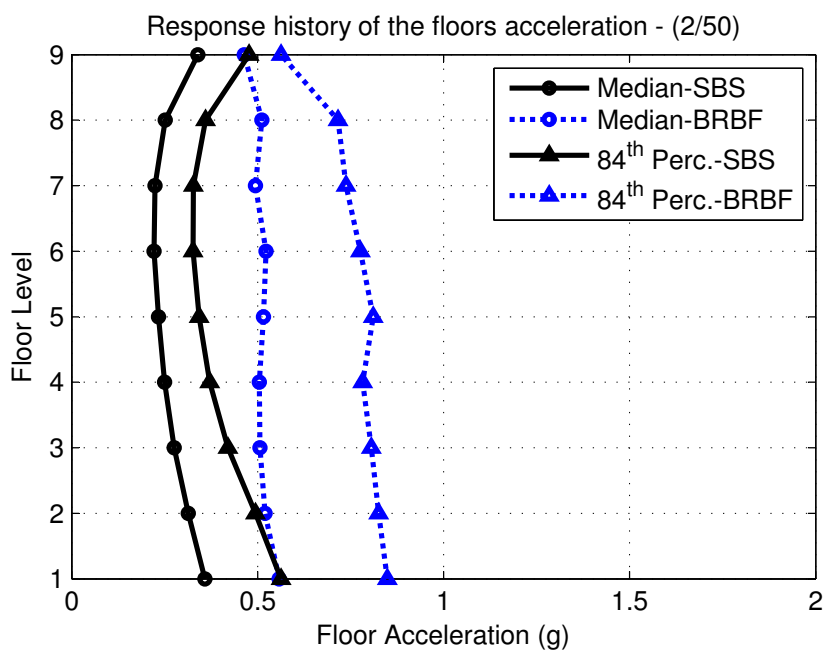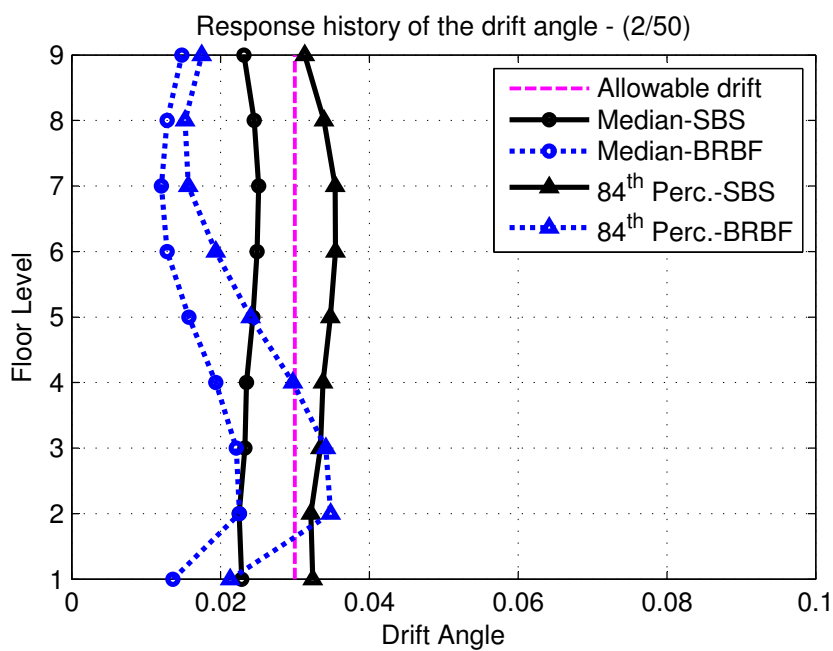
Figure 4.37: Median and 84th percentile of the peak floor drift angles and accelerations for the 9-story building with different bracing systems under the 2/50 ground motions set
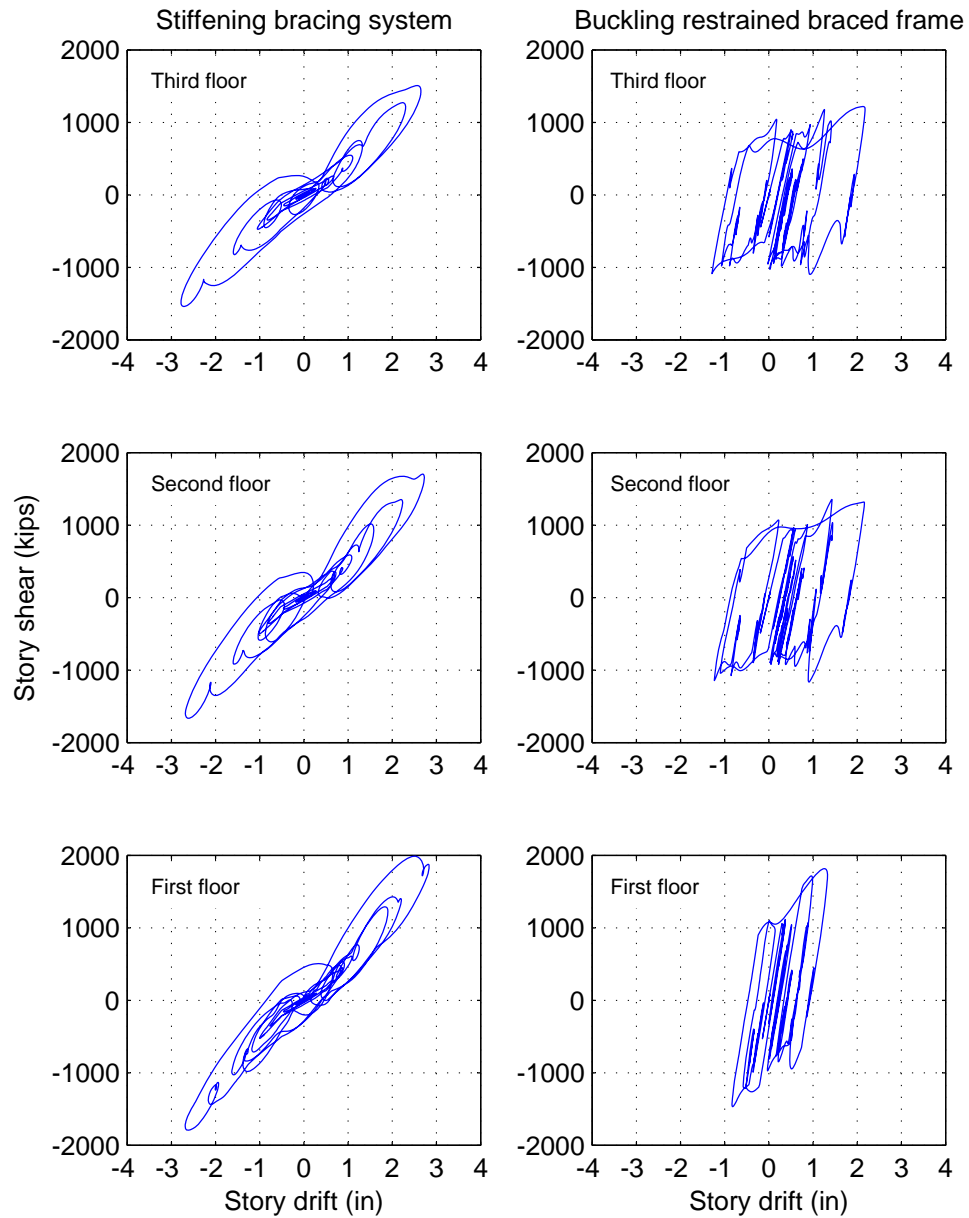
Figure 4.38: 9-story building, inter-story drift angle response history under LA31 (Elysian Park, simulated)

Figure 4.39: 9-story building, story shear - interstory drift for the upper three floors under LA31 (Elysian Park, simulated)
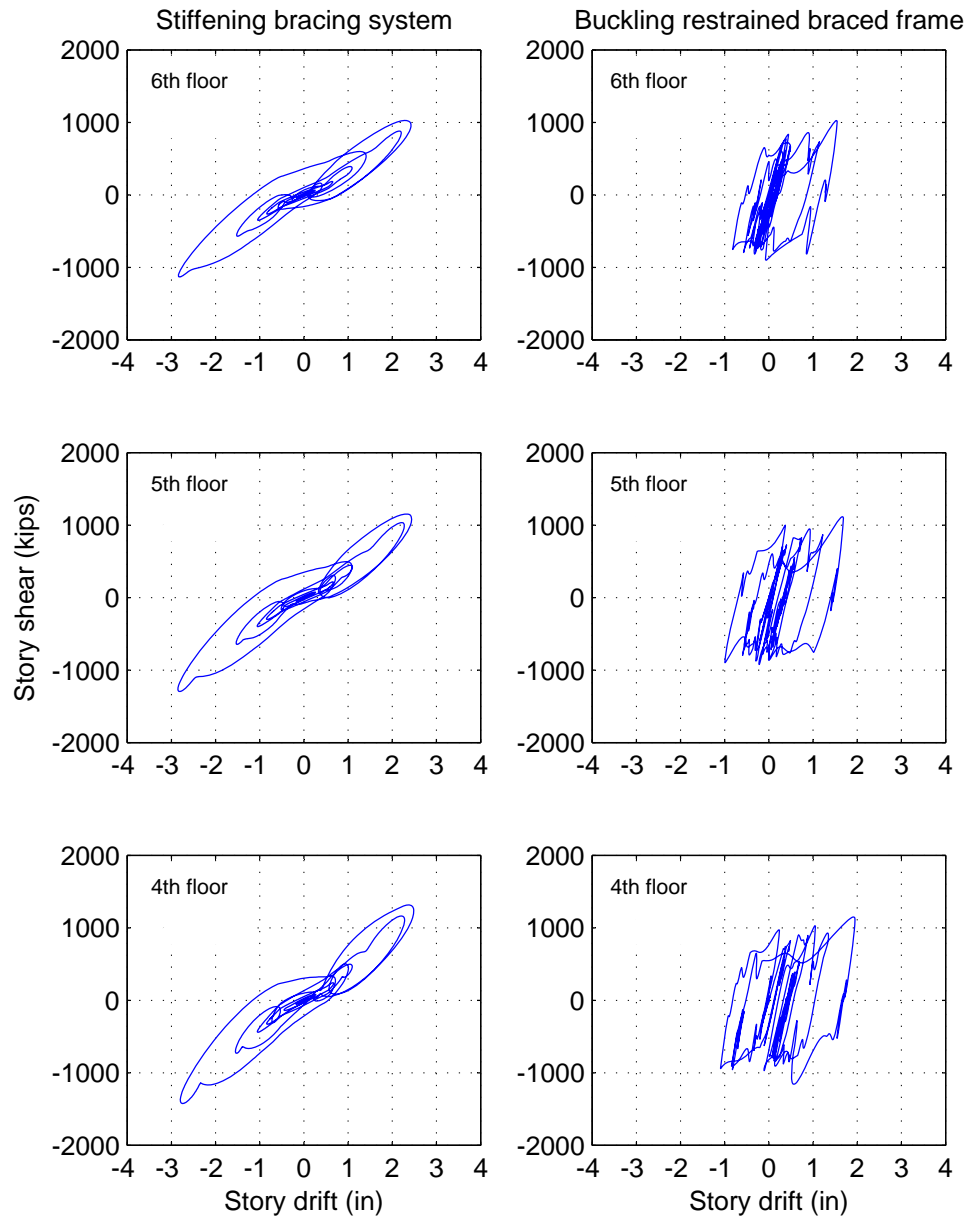
Figure 4.40: 9-story building, story shear - interstory drift for the middle three floors under LA31 (Elysian Park, simulated)

Figure 4.41: 9-story building, story shear - interstory drift for the lower three floors under LA31 (Elysian Park, simulated)

Chapter 5

Effectiveness of SBS for Tall Buildings

As it was discussed earlier in Chapter 4, the proposed stiffening bracing system relies on softening existing structures when used as a retrofit alternative, and tends to design for a relatively soft long period structure when used for new design. For the cases of tall buildings and structures with relatively long fundamental period, the proposed design methodology may not lead to a significant improvement to the system response compared to conventional methods. This can be inferred by studying a typical response spectrum as shown in Figure 5.1. For short to medium height buildings, the SBS design tends to shift the fundamental period of the structure so that the acceleration demands can be significantly reduced, as the difference between points 1 and 2 indicates. However, for tall buildings that typically have long fundamental periods, as shown by point 3, the implementation of the SBS leads to a structure with much longer period. This is shown by point 4 where the effectiveness of reduced acceleration demands is not essential. In addition, the effect of added damping is not tangible between points 3 and 4.

In order to investigate the efficacy of the SBS implementation in tall buildings, the 20-story benchmark building given by FEMA (2000) for the Los Angeles region
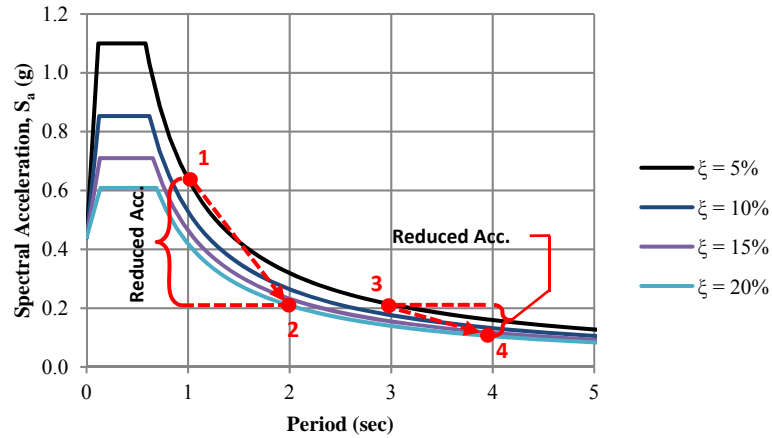
Figure 5.1: Schematic representation for the effect of SBS on different structures

**Table 5.1:** Total floor mass for the 20-story office building.

Floor Level	Total Mass $(kips.sec^2/ft)$
Roof	40.06
Floors 20 to 3	37.76
Floor 2	38.63

is used. Redesign of the building was carried out with the four SBS braced bays installed in each direction (2 braced bays per frame) as shown in Figure 5.2. The seismic mass per braced frame is taken as half of the building's total mass, which is summarized in Table 5.1.

5.1 Design of the 20-story Building with SBS

The design of the 20-story building is carried out so that the structure with the SBS has a fundamental period of vibration after all required iterations of 5.70 sec. Total effective damping ratio of $\zeta_{eff} = 10\%$, which is the summation of 2% inherent damping plus 8% added damping by viscous damping devices, is considered. Based on these parameters, and response modification factor $(R = 1)$, importance factor
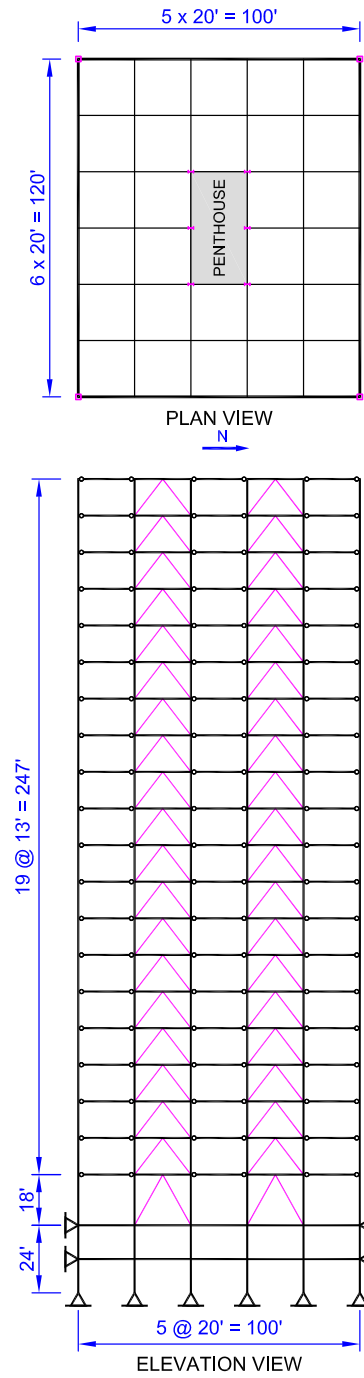
Figure 5.2: Layout of the 20-story braced frame building

Table 5.2: Vertical distribution of shear for the 20-story building.

Level	w_x (kips)	$\sum w$ (kips)	h_x (ft)	$w_x h_x^k$ (kip − ft)	$w_x h_x^k/(w_x h_x^k)$	F_x (kips)	V_x (kips)
Roof	1290	1290	265	90590250	0.144	929	
20	1216	2506	252	77220864	0.123	792	929
19	1216	3722	239	69459136	0.110	712	1721
18	1216	4938	226	62108416	0.099	637	2434
17	1216	6154	213	55168704	0.088	566	3071
16	1216	7370	200	48640000	0.077	499	3636
15	1216	8586	187	42522304	0.068	436	4135
14	1216	9802	174	36815616	0.059	378	4571
13	1216	11018	161	31519936	0.050	323	4949
12	1216	12234	148	26635264	0.042	273	5272
11	1216	13450	135	22161600	0.035	227	5546
10	1216	14666	122	18098944	0.029	186	5773
9	1216	15882	109	14447296	0.023	148	5958
8	1216	17098	96	11206656	0.018	115	6107
7	1216	18314	83	8377024	0.013	86	6222
6	1216	19530	70	5958400	0.009	61	6308
5	1216	20746	57	3950784	0.006	41	6369
4	1216	21962	44	2354176	0.004	24	6409
3	1216	23178	31	1168576	0.002	12	6433
2	1244	24422	18	403056	0.001	4	6445
1							6449
Total	24422			628807002		6449	

$(I = 1)$, the seismic response coefficient, C_s, is governed by the lower bound and is calculated as

$$C_s = \frac{0.5S_1}{(R/I)} = \frac{0.5 \times 0.528g}{(1/1)} = 0.264g$$

As the structure period is higher than $2.5sec$, the exponent k is taken as $(k = 2.0)$. The final vertical seismic force distribution is given in Table 5.2. Considering the accidental torsional moment, the lateral floor forces and floor shear per braced frame become as shown in Table 5.3.

The initial stiffness per floor for the SBS is calculated so that d_1 corresponds to an assumed drift ratio of 2% (see Figure 4.6). A summary of the individual brace

Table 5.3: Braced frame shear forces for the LA 20-story building.

Level	Story force F_x (kips)	Story shear V_x (kips)	Frame force $F_{x,f}$ (kips)	Frame shear $V_{x,f}$ (kips)
Roof	929		247	
20	792	929	211	247
19	712	1721	190	458
18	637	2434	169	648
17	566	3071	151	817
16	499	3636	133	968
15	436	4135	116	1100
14	378	4571	100	1216
13	323	4949	86	1317
12	273	5272	73	1403
11	227	5546	60	1476
10	186	5773	49	1536
9	148	5958	39	1585
8	115	6107	31	1625
7	86	6222	23	1655
6	61	6308	16	1678
5	41	6369	11	1695
4	24	6409	6	1705
3	12	6433	3	1712
2	4	6445	1	1715
1		6449		1716

stiffness per braced frame is given in Table 5.4. A 1.5% target inter-story drift angle is chosen as the desired performance. The viscous damping coefficient per each floor damper calculated based on Equation 4.9 and updated to achieve the desired damping ratio is ($c_j = 300k/sec/in$). The final properties of the SBS designed for the 20-story building are shown in Table 5.5. The capacity-demand curves for both systems are shown in Figure 5.3. It can be noticed that the capacity curve intersects the 10% damped demand curve at an effective period of $5.7sec$ as initially assumed.

Table 5.4: Initial stiffness distribution of the SBS for the LA 20-story building.

Floor	Height (h_x) (in)	Brace Angle θ_{b_x} (rad)	Story shear $(kips)$	Brace Initial Stiff. k_{x_1} (k/in)
20	156	0.915	247	106.6
19	156	0.915	458	197.4
18	156	0.915	648	279.1
17	156	0.915	817	352.2
16	156	0.915	968	417.1
15	156	0.915	1100	474.3
14	156	0.915	1216	524.3
13	156	0.915	1317	567.7
12	156	0.915	1403	604.7
11	156	0.915	1476	636.1
10	156	0.915	1536	662.1
9	156	0.915	1585	683.4
8	156	0.915	1625	700.4
7	156	0.915	1655	713.6
6	156	0.915	1678	723.5
5	156	0.915	1695	730.5
4	156	0.915	1705	735.1
3	156	0.915	1712	737.9
2	156	0.915	1715	739.3
1	216	1.064	1716	842.1
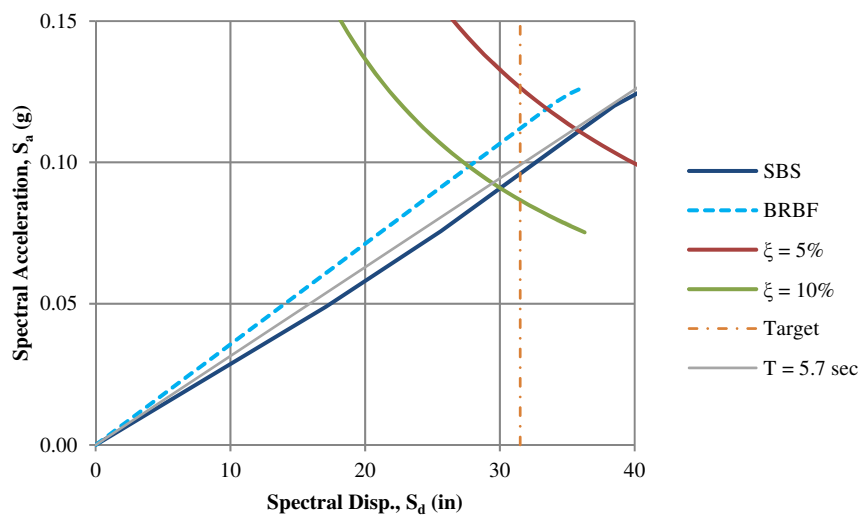
Figure 5.3: Capacity demand curves of the 20-story building with the final parameters of the SBS.

Table 5.5: Properties of the SBS used with the 20-story building.

Floor	Δ_1/h_x (%)	θ_{b_x} (rad)	k_{x_1} (k/in)	α_x
20	0.35	0.915	106.6	3.1
19	0.35	0.915	197.4	2.5
18	0.35	0.915	279.1	2.1
17	0.35	0.915	352.2	2.0
16	0.35	0.915	417.1	1.8
15	0.35	0.915	474.3	1.8
14	0.35	0.915	524.3	1.7
13	0.35	0.915	567.7	1.7
12	0.35	0.915	604.7	1.7
11	0.35	0.915	636.1	1.7
10	0.35	0.915	662.1	1.8
9	0.35	0.915	683.4	1.8
8	0.35	0.915	700.4	1.8
7	0.35	0.915	713.6	1.9
6	0.35	0.915	723.5	1.9
5	0.35	0.915	730.5	2.0
4	0.35	0.915	735.1	2.1
3	0.35	0.915	737.9	2.1
2	0.35	0.915	739.3	2.2
1	0.35	1.064	842.1	2.3

5.2 Performance of the 20-story Building

In this section, the performance of the 20-story building employing the stiffening bracing system is investigated under the effect of the design earthquake (10/50) and the maximum considered earthquake (2/50) as described in Section 4.6. The peak inter-story drift angles and the peak floor accelerations for the structure with the SBS under the effect of the design earthquakes (10/50) are shown in Figure 5.4. The median as well as the 84th percentile are overlaid on the figure. Obviously, the SBS could not effectively maintain the desired uniform inter-story drift angle over the height of the tall 20-story structure. However, it is clear that the proposed system outperforms the BRBF in terms of inter-story drift and floor accelerations, as depicted

in Figure 5.5. The figure shows the median and 84th percentile of the peak inter-story drift angles and absolute floor accelerations for the two systems under the effect of the 10/50 ground motion records. The comparison between the two systems indicates the significant reduction that has been achieved on the floor acceleration demands. In terms of inelastic permanent deformation, the BRBF is expected to experience such deformations as can be observed from Figure 5.6. The figure shows the response history of the inter-story drift angle under the effect of the near-fault LA04 (*1979 Imperial Valley*), with a distance of 4.1km to the fault. However, the proposed SBS outperforms the BRBF, as the main structural elements (steel columns and beams) remain elastic and the structure reaches the occupants comfort level then rest much faster than the BRBF. This can be noticed from the figure where starting from the 20th second the SBS vibrates with less than 0.5% inter-story drift ratio, while the BRBF exhibits vibration with more than 1.0% inter-story drift ratio up to the end of the excitation duration. In addition, two floors experienced permanent deformation of about 0.5% of the floor's height. The median permanent deformation in addition to other responses are shown in Appendix D.

Under the effect of the maximum considered earthquake (2/50), the target performance of uniform inter-story drift distribution was not effectively achieved for the tall 20-story building with the implementation of the SBS, as can be observed from Figure 5.7. Nevertheless, the overall response of the entire structure is under the maximum permissible inter-story drift. A comparison between the median and the 84th percentile of the peak inter-story drift angles and the peak floor accelerations for the two systems is shown in Figure 5.8. Although the proposed system does not achieve the desired uniform inter-story drift distribution for tall buildings, it still can achieve significant reduction in the inter-story drift and floor acceleration demands. Figure 5.9 shows a comparison between the two systems in terms of the inter-story
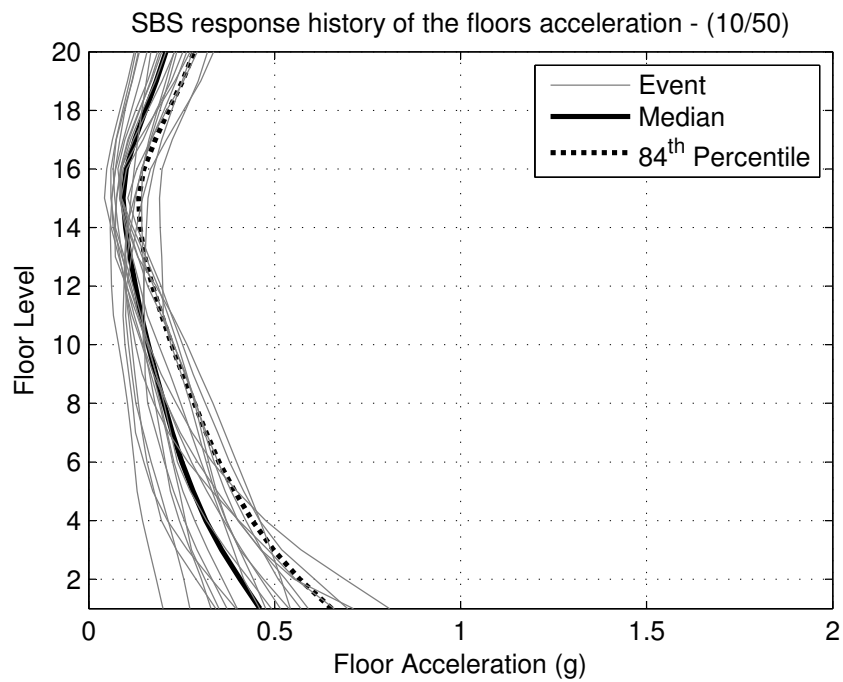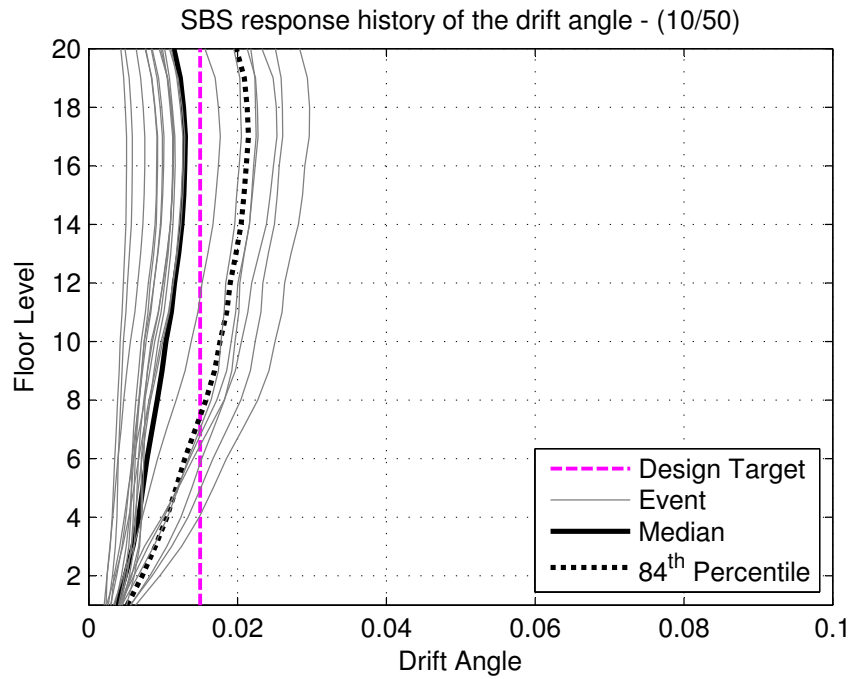
Figure 5.4: Peak response of the floor drift angles and accelerations under the 10/50 ground motion records
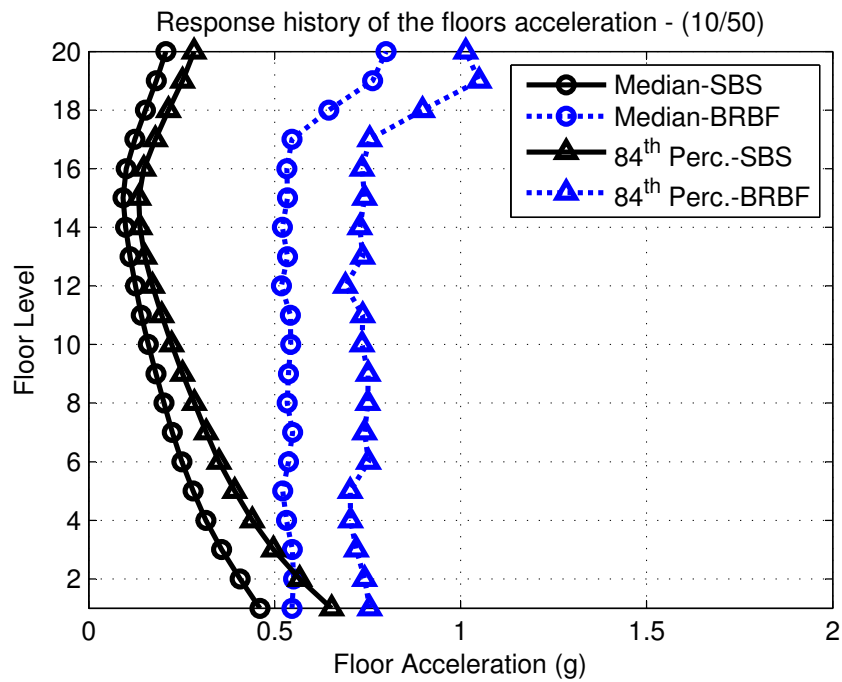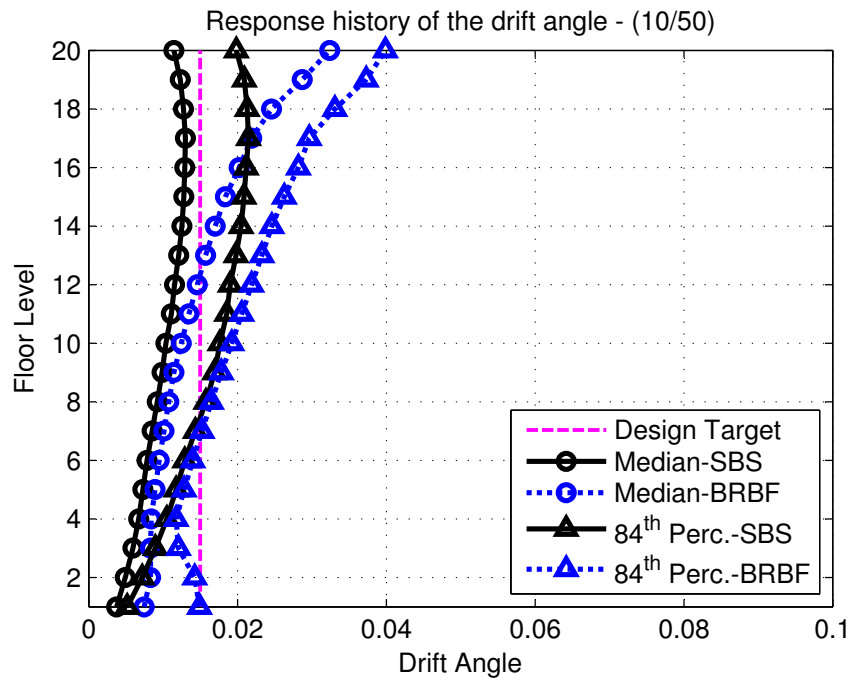
Figure 5.5: Median and 84th percentile of the peak floor drift angles and accelerations for the 20-story building with different bracing systems under the 10/50 ground motion records
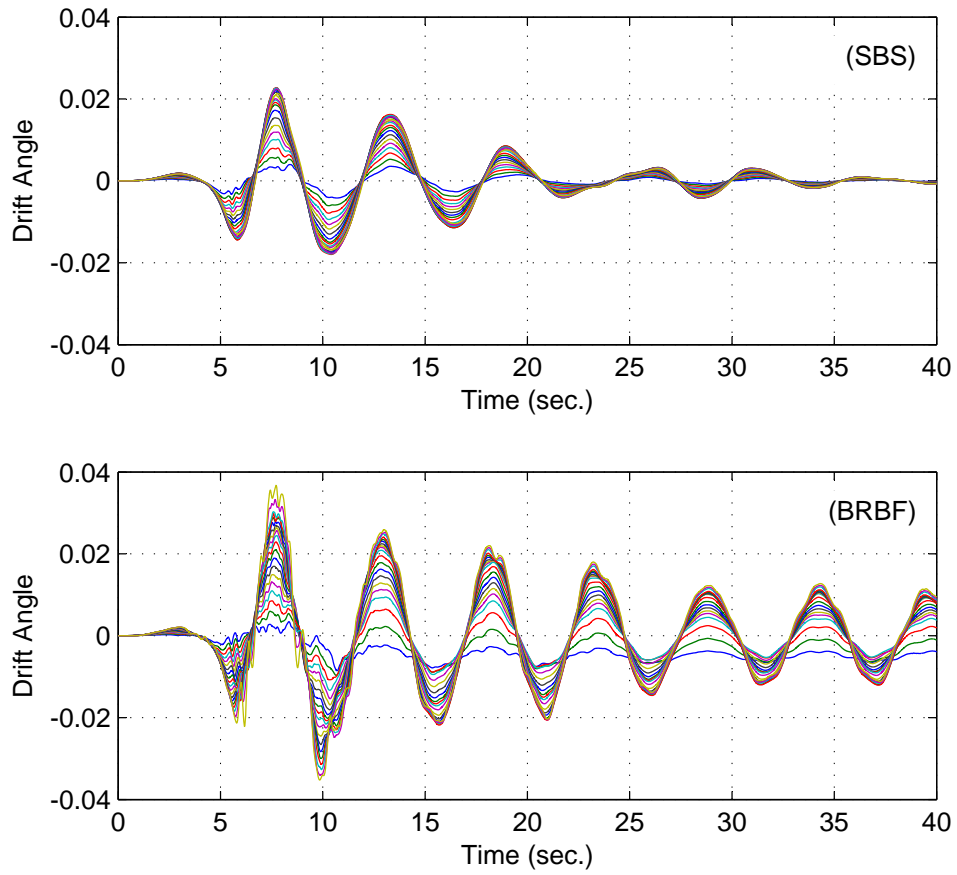
Figure 5.6: 20-story building, inter-story drift angle response history under LA04 (Imperial Valley, 1979)

drift angle response history under the effect of the LA27 (*1994 Northridge*). Clearly, the proposed system reaches steady-state in very short time without any permanent deformation under the effect of the maximum considered earthquake.
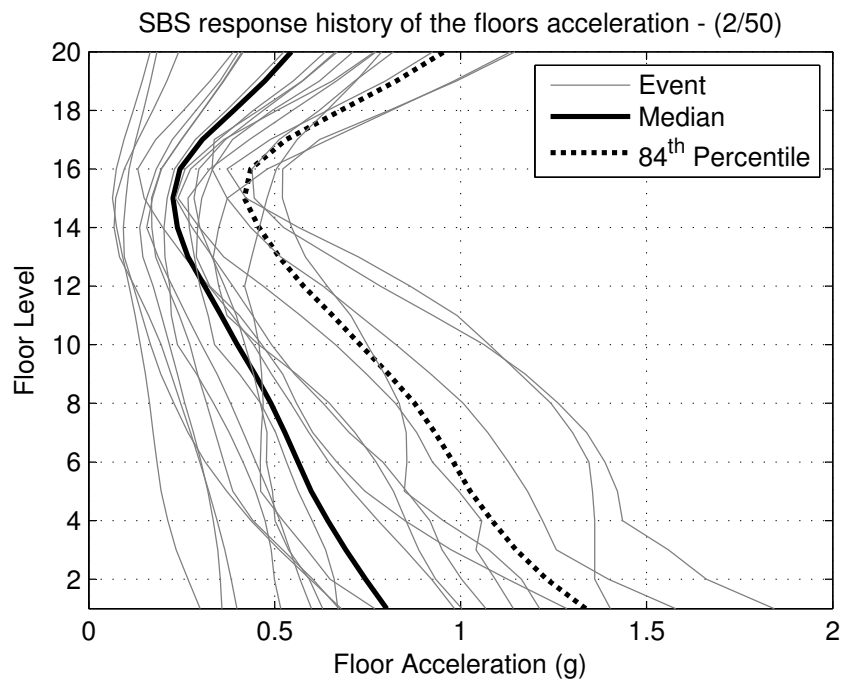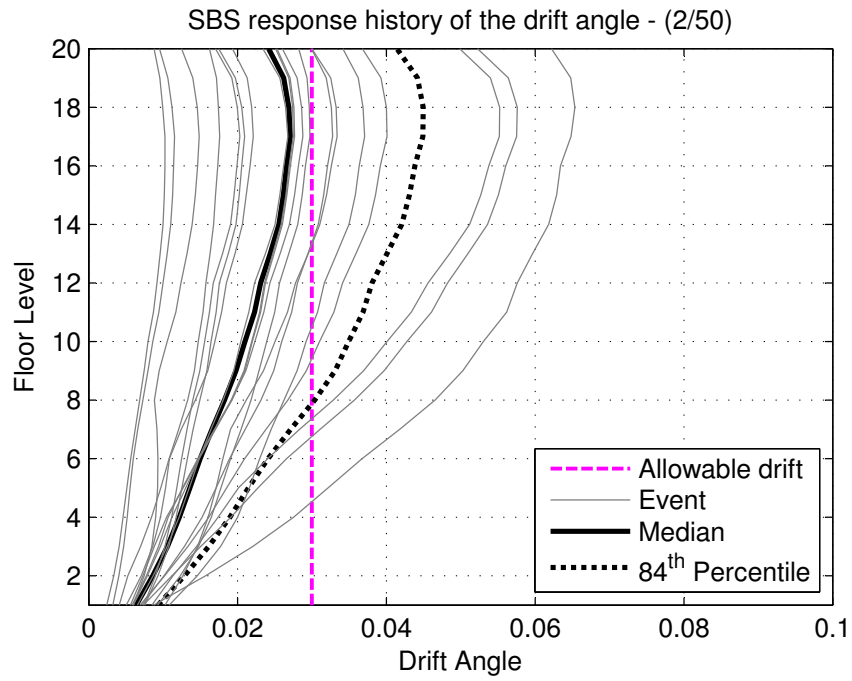
Figure 5.7: Peak response of the floor drift angles and accelerations of the 20-story building under the 2/50 ground motion records
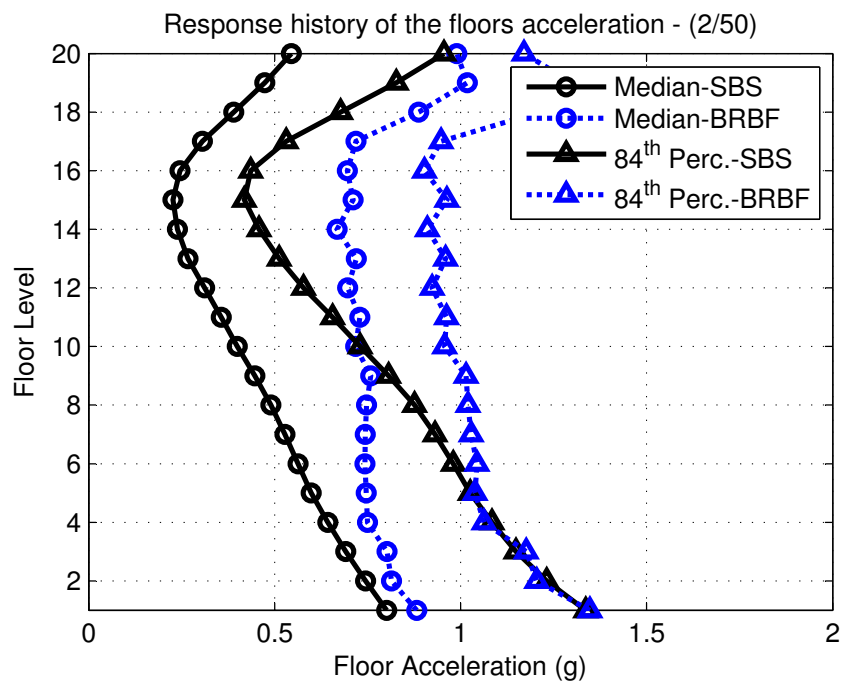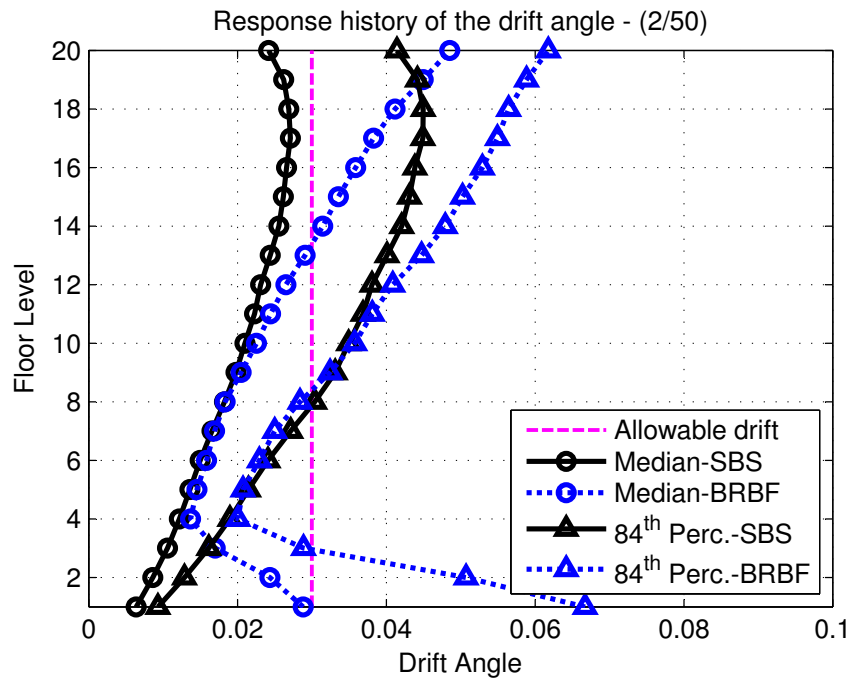
Figure 5.8: Median and 84th percentile of the peak floor drift angles and accelerations of the 20-story building with different bracing systems under the 2/50 ground motion records
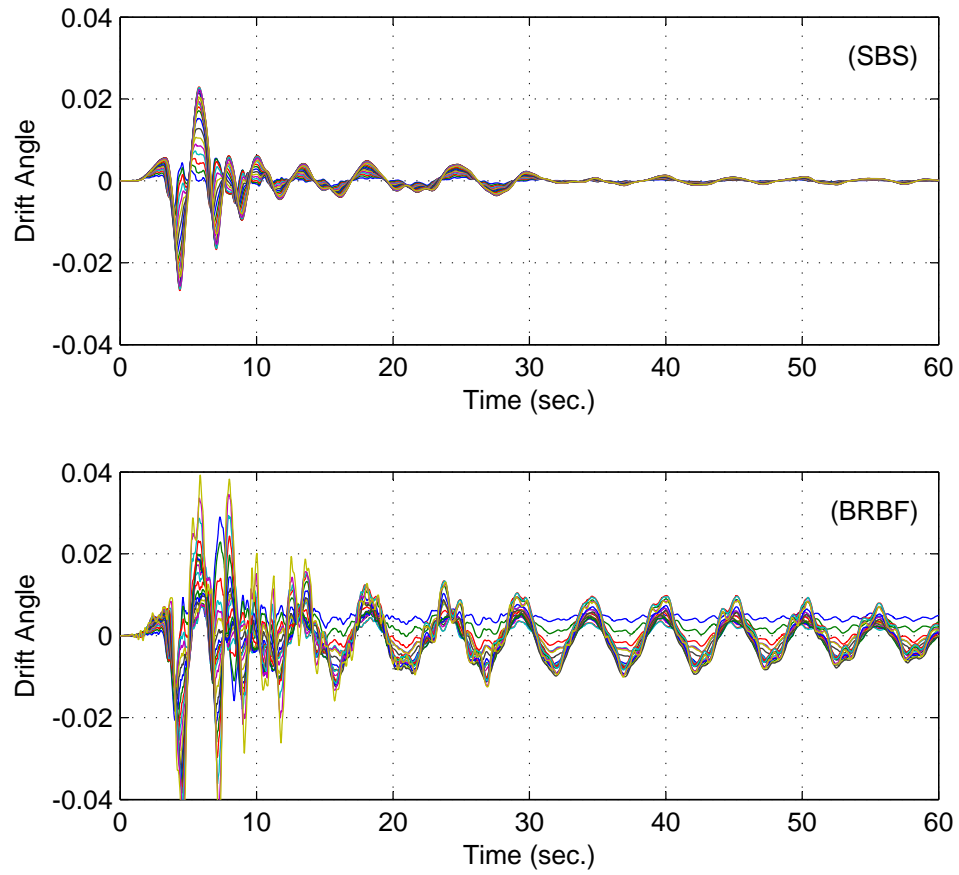
Figure 5.9: Inter-story drift angle response history of the 20-story building under LA27 (Northridge, 1994)

Chapter 6

Integrated Design of Steel Frames Employing SBS

For practical design consideration, it is essential to represent the seismic demands on structures using an equivalent lateral force distribution. These static forces can be used for the design of members and for the prediction of the structural performance under the effect of seismic loads. However, the equivalent lateral force procedures adopted by most of the seismic design codes (NEHRP, 2003; ASCE, 2010; International Code Council, 2012) do not precisely take into account the nonlinear behavior that structures undergo. Instead, the elastic seismic demands are reduced to account for the structural ductility, while the elastic structural deformations are magnified for the same reason. This method however, does not lead to a reliable seismic performance prediction, especially for structures experiencing high nonlinearity and those with damping devices, as for the stiffening bracing system with viscous damping devices. On the other hand, the equivalent lateral force procedures are mostly dependent on the first mode of vibration and do not explicitly consider the effect of higher modes. Researchers realize the need of more rigorous equivalent lateral force distribution for different types of structures. On this regard, Lee et al. (2004) proposed a new seismic lateral force distribution based on nonlinear dynamic analyses where the seismic base

shear was derived from a modified energy balance equation. The proposed seismic base shear and lateral force distribution showed good agreement with the nonlinear dynamic response history analysis. Consequently, it is more favorable for the purpose of seismic design and seismic performance assessment. Chao et al. (2007) investigated the adequacy of the proposed lateral force distribution on a number on framed structures under a wide variety of earthquake ground motions. It was shown that the proposed lateral force pattern is more rational and gives a reliable prediction of the the inelastic seismic demands on different structures. They concluded that the structures designed according to the proposed loading pattern experience maximum story shear through the nonlinear dynamic analyses that agrees well with the expected values. In addition, the structures experience more uniform maximum inter-story drifts compared to those designed following the code's equivalent lateral force procedure. Chopra and Goel (2001a) developed a Modal Pushover Analysis (MPA) procedure to account for the effect of higher modes for a better prediction of the seismic demands for inelastic structures. The response history analysis of a 9-story building showed that the proposed methodology is more accurate in estimating the drift demands and plastic hinge rotations than all FEMA's force distribution patterns.

For the case of SBS, it is also essential to derive an equivalent lateral force distribution that can predict the structural performance and the seismic demands on the framing elements.

In the previous chapters, the steel frame design was based on averaging the members internal forces obtained from the nonlinear time history analyses. In this chapter, an integrated design methodology is proposed. The method is based on deriving lateral force distribution that is relevant to the performance of structures incorporating stiffening bracing system. With the appropriate lateral force distribution and maximum expected inter-story shear, the design and the seismic performance prediction

of the frames become easier than relying on the nonlinear time history analyses. In order to evaluate the adequacy of the derived lateral force distribution, the three buildings described in Chapters 4 and 5 are redesigned with the proposed procedure. In addition, more structures are added and designed to cover a wider range of building heights. The median of the maximum inter-story shear forces obtained from the nonlinear time history analyses is then compared to the suggested inter-story shear distribution.

6.1 Integrated Design Procedure

The proposed integrated design procedure can be subdivided into three stage. In the first stage, a preliminary design is obtained according to the lateral force distribution provided by any design code in conjunction with the desired structural performance. In the second stage, the SBS is introduced and the optimization process for the SBS properties takes place. With the known SBS properties, the expected inter-story shear at the predefined inter-story drift can be back calculated, and hence a lateral force distribution pattern is achieved. This lateral force pattern is used to model the structure with any commercially available software that accounts for the $P - \Delta$ effect. The frame members' design is then updated based on the internal member forces. In the third stage, the properties of the SBS are further enhanced. This is done by using the lateral force distribution obtained in the previous stage to model the initial stiffness of the braces. Thus, the stiffening ratios of the braces become almost identical for all floors.

6.1.1 Stage (A): Preliminary Design

In this section, a preliminary design for the steel frame equipped with the SBS is developed. This preliminary design relies on the desired performance, where the inter-story drift angle is assumed to fall within the range of the target value.

6.1.1.1 Design of Braces

Starting with the target inter-story drift, the effective stiffness of the braces at floor x, k_{eff}^x, can be calculated in view of Figure 6.1 as

$$k_{eff}^x = \frac{F_{br}^x}{\Delta_{max}^x \cos \theta_x} = \frac{V_x}{2\Delta_{max}^x \cos^2 \theta_x} \tag{6.1}$$

where F_{br}^x is the axial force of the brace in the x story at the maximum desired inter-story drift Δ_{max}^x, θ_x is the angle of the brace to the horizontal, and V_x is the shear force at story x, which can be calculated as the sum of the lateral forces acting on the floors above the considered one. The lateral stiffness of the columns is ignored in Equation 6.1 as more than 90% of the lateral stiffness of braced frames is usually provided by the bracing system.

Obviously, the lateral force pattern must be known before calculating the braces effective stiffness according to Equation 6.1. Therefore, the equivalent lateral force procedure given by any design code can be used in this stage. However, the lateral force distribution employed by ASCE (2010) is used in this dissertation.

After defining the effective stiffness of the bracing system per floor, the internal force induced on the columns and beams can be evaluated.

6.1.1.2 Design of Columns

To evaluate the maximum axial force induced on columns due to lateral force effect, consider the vertical section shown in Figure 6.2. The earthquake induced axial force
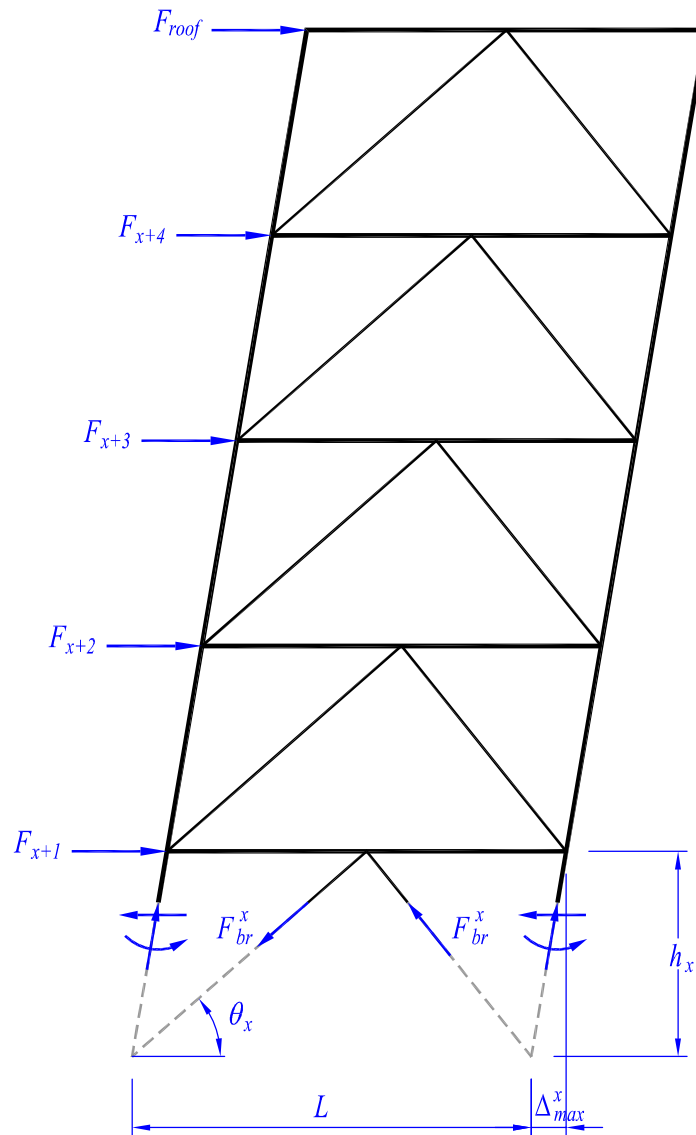
Figure 6.1: Horizontal section cut through floor x of inverted V braced bay

on the xth floor column, P_E^x, can be determined as the sum of the vertical components of the braces axial forces for all floors above. The axial force on the xth floor brace at the desired inter-story drift can be calculated from Equation 6.1 as

$$F_{br}^x = \frac{V_x}{2\cos\theta_x} \tag{6.2}$$

Hence, the seismically induced axial force on the column at floor x is

$$P_E^x = \sum_{i=x+1}^{n} F_{br}^i \sin\theta_i = \sum_{i=x+1}^{n} V_i \tan\theta_i \tag{6.3}$$

where n is the total number of floors. Based on Equation 6.3, the earthquake axial load on the nth floor column will be zero. However, to be conservative, it is recommended to shift the axial forces on columns by one floor (International Code Council, 2012) so that Equation 6.3 can be rewritten as

$$P_E^x = \sum_{i=x}^{n} F_{br}^i \sin\theta_i = \sum_{i=x}^{n} V_i \tan\theta_i \tag{6.4}$$

The column's axial load due to the seismic load effect is then added to the gravity loads acting on the column so that the design axial load can be calculated as

$$P_u = (1.2 + 0.2S_{DS})P_D + P_E + 0.5P_L \tag{6.5}$$

where P_D, P_L, and P_E are the axial column's force due to dead load, live load, and seismic load respectively, and S_{DS} is the design response spectral acceleration at short periods. The term $(0.2S_{DS}P_D)$ is added in the load combination to account for the vertical seismic load effect as specified by ASCE (2010).
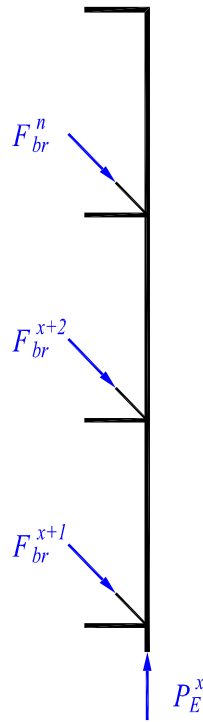
Figure 6.2: Evaluation of Column's axial load due to lateral effect

6.1.1.3   Design of Beams

It is assumed that the brace elements do not participate in resisting the gravity loads (dead and live loads). Therefore, the bending moment on the floor beams is calculated according to the applied dead and live loads on the entire span of the braced bay, L. Floor beams are also assumed to be pin connected to the columns.

In addition to the gravity loads, the floor beams must resist the axial force resulting from the horizontal components of the forces in the connected braces, as shown in Figure 6.3. Therefore, the horizontal force in the floor beam, Q_h, can be calculated as

$$Q_h^{x+1} = 2F_{br}^x \cos \theta_x \tag{6.6}$$

This horizontal force is permitted to be distributed according to the elastic force
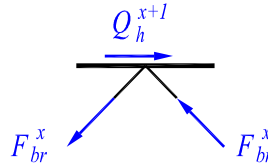
Figure 6.3: Axial load on floor beams due to seismic effect

distribution, where 60% is resisted by one side and 40% is resisted by the other side of the beam (International Code Council, 2012). Clearly, the horizontal force developed in the floor beam is equivalent to the seismic shear developed in the story below the considered beam. Hence the design axial load for the $(x+1)^{th}$ floor beam, P_b^{x+1}, can be determined as

$$P_h^{x+1} = 0.6V_x \qquad (6.7)$$

With the preliminary design obtained in this stage, the dynamic properties of the structure can be evaluated and the SBS stiffness optimization can then take place as in the following design stage.

6.1.2 Stage (B): SBS Design and Optimization Process

In this stage, the bracing system is replaced with the SBS and the optimization process described in Section 4.3 is employed. The optimization process yields the properties of the stiffening bracing system. Hence, the effective stiffness of each brace at the desired structural performance can be obtained. The effective stiffness of a typical floor brace (see Figure 4.1) is given by

$$k_{eff} = \frac{k_1\Delta_1 + \alpha k_1(\Delta_{max} - \Delta_1)}{\Delta_{max}} \qquad (6.8)$$

Once the effective stiffness of the floor's braces is defined, the story shear can be

back calculated as

$$V_x = 2\Delta_{max}^x k_{eff}^x \cos^2 \theta_x \tag{6.9}$$

The story shear updated by Equation 6.9 can now replace the preliminary design inter-story shear in Equation 6.2, and the design of columns and beams can be revised and updated as necessary. Also the lateral force distribution can be calculated from the inter-story shear given by Equation 6.9 as

$$F_{x+1} = V_x - V_{x+1} \tag{6.10}$$

The lateral force distribution defined by Equation 6.10 along with the braces effective stiffness are used to model the structure so that the $P - \Delta$ effect is taken into consideration when redesigning the columns. In this study, SAP2000 (2011) is used for the analysis of the second order effect.

6.1.3   Stage (C): Enhancement of the SBS Properties

This stage is concerned on further enhancement of the SBS properties. This is done by updating the initial stiffness, k_1, of the braces based on the lateral force distribution obtained by Equation 6.10. However, the optimization process of the SBS takes place once again to update the stiffening ratios, α_x, that are relevant to the new brace initial stiffness. This stage does not need any redesign of the frame elements, as the effective stiffness used for the design of members are barely changed. A flowchart of the integrated design procedure is shown in Figure 6.4.
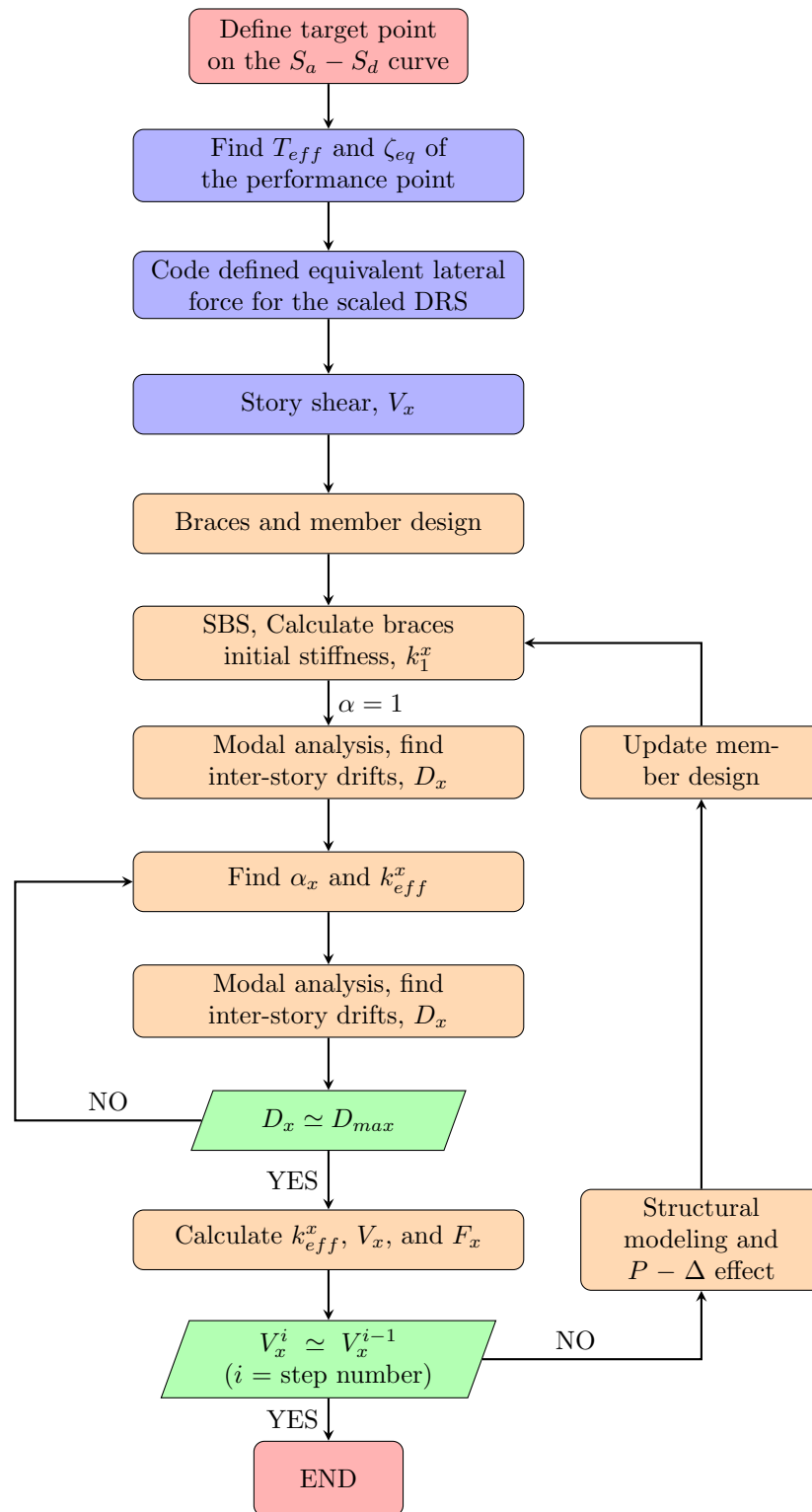
Figure 6.4: Flowchart for the integrated design os steel frames employing SBS

6.2 Implementation of the Integrated Design Procedure

In this section, the proposed integrated design procedure is implemented for the previously described SAC buildings, in addition to more structures of different heights. The structures designed and discussed in this section are 3, 5, 7, 9, 12, 15, and 20 stories. The 3, 9, and 20-story structures are the same as those discussed in the Chapters 4 and 5. However the new buildings are assumed to have the same layout of the 9-story SAC building with the same floor seismic weights and structural system. The dynamic properties of these structures are summarized in Appendix C, which include the modal periods as well as the mass participation factors for the pre-stiffening and post-stiffening cases.

As mentioned earlier, the proposed design procedure leads to almost identical stiffening ratio for the braces in all floors, as can be seen from the design summary given in Tables B.1 to B.7.

6.2.1 Story Shear and Lateral Force Distribution

The design story shear calculated according to ASCE 7-10, designated (ASCE), and the maximum expected design value for the story shear calculated according to the proposed procedure, designated (Expected), are compared to the median maximum story shear resulted from the response history analyses with the design earthquake (10/50). The comparison is shown in Figure 6.5 through 6.11. The lateral force distribution on the considered buildings is shown in Figure 6.12 through 6.18.

It can be observed from the story shear and lateral force distribution shown in Figure 6.5 through 6.18 that the proposed procedure is capable of predicting the structural performance of the SBS more accurately than the ASCE 7-10 equivalent
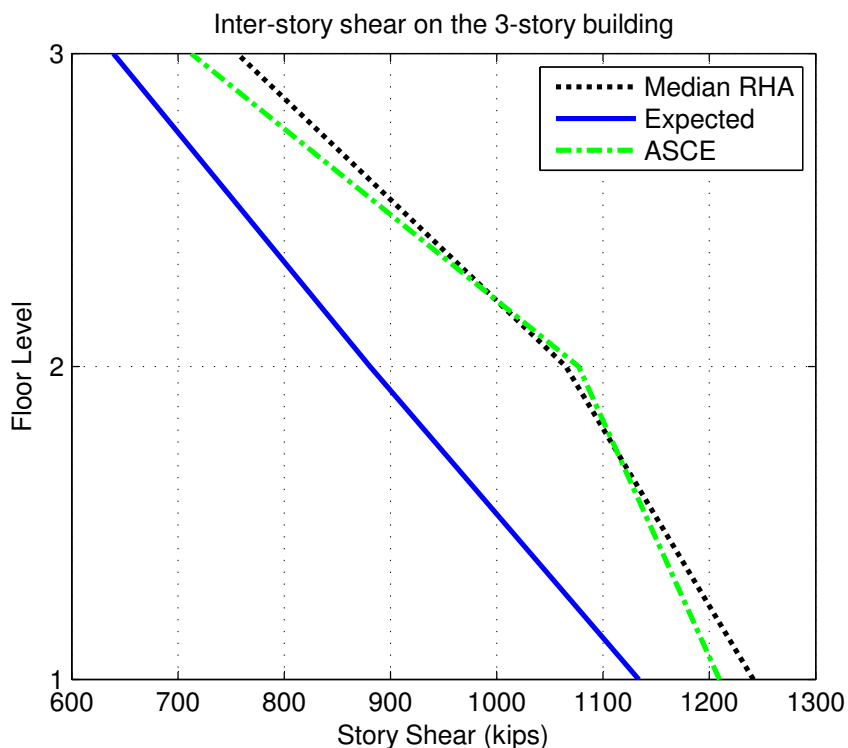
Figure 6.5: Maximum story shear of the 3-story building

lateral force procedure. It should be mentioned here that the ASCE lateral force distribution is not really the original lateral force distribution prescribed by ASCE (2010) but is rather a modified version where the limitations on the upper and lower bounds of the seismic response coefficient, C_s, have been omitted. In addition, the actual effective period of the structures under consideration is taken into account instead of the approximate structural period strictly specified by the code. However, it is noticeable that the proposed methodology under estimates the base shear for the 3, 5, and 7-story buildings, and over estimates the base shear for the 12, 15, and 20-story buildings. For the case of the 9-story building, the expected inter-story shear shows an excellent agreement with the results of the response history analyses, as can be seen in Figure 6.8. Clearly, the proposed lateral force distribution precisely traces the lateral forces induced on the building during the nonlinear response history
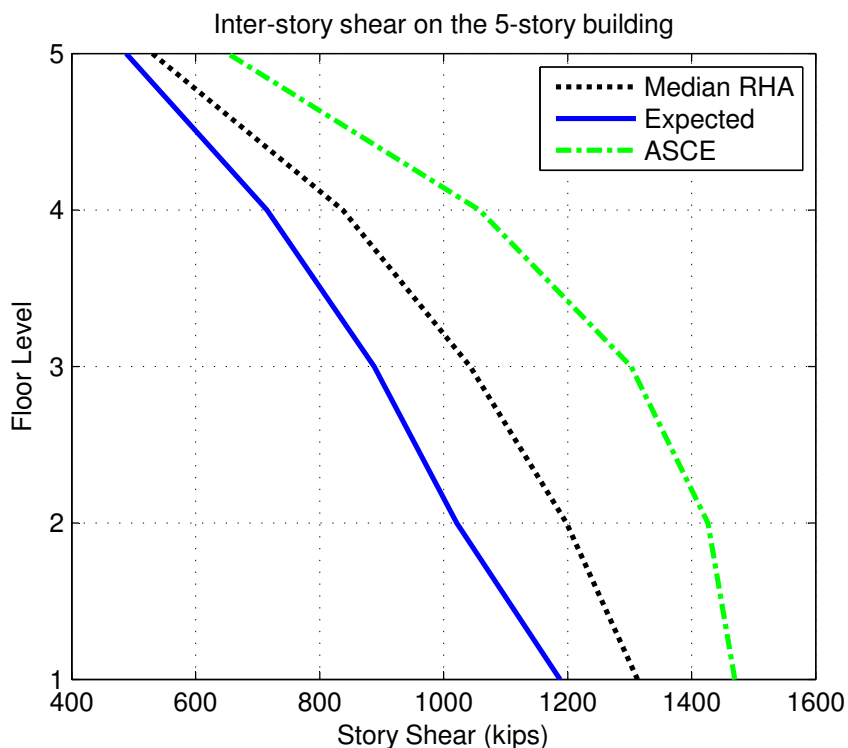
Figure 6.6: Maximum story shear of the 5-story building

analyses, as depicted in Figure 6.15. However, the tendency of tracing the actual structural behavior of the other cases is still noticeable but with less accuracy, as can be seen in Figure 6.12 through 6.18.

6.2.2 Seismic Performance under the Design and Maximum Earthquake Records

The seismic performance of the structures designed in accordance with the proposed methodology under the effect of the design earthquake records (10/50), (Figure 6.19 through 6.25), shows that the proposed procedure sufficiently leads to structural design that ends up with a performance sufficiently close to the desired target. From Figure 6.22, the median peak inter-story drift angle of the 9-story building is not only uniform throughout the building's height, but also falls on the target drift that it was
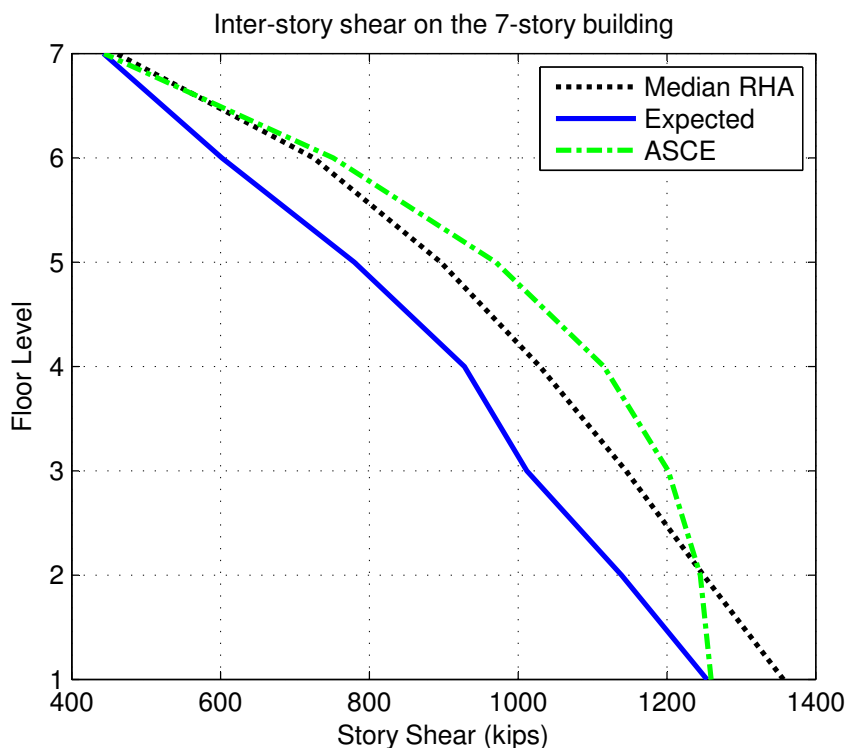
Figure 6.7: Maximum story shear of the 7-story building

designed for. However, for the other structures where the design base shear is under estimated, the nonlinear time history analyses resulted in an inter-story drift angle for these buildings that is slightly higher than the target design value. This is applicable to the 3, 5, and 7-story buildings, as shown in Figure 6.19 to 6.21. On the other hand, the structures designed for an overestimated base shear led to an inter-story drift angle that is slightly below the design target. This is applicable to the 12, 15, and 20-story buildings, as shown in Figure 6.23 to 6.25. Although the inter-story drift of the considered structures could be slightly higher or lower than the target value, the desired uniform inter-story drift is still achievable in all cases. Table 6.1 shows the seismic base shear of the considered structures with the percentage of the error in estimating the seismic base shear. It is noticeable from the table that the seismic performance of the structures is reflected by how accurately the design base shear is
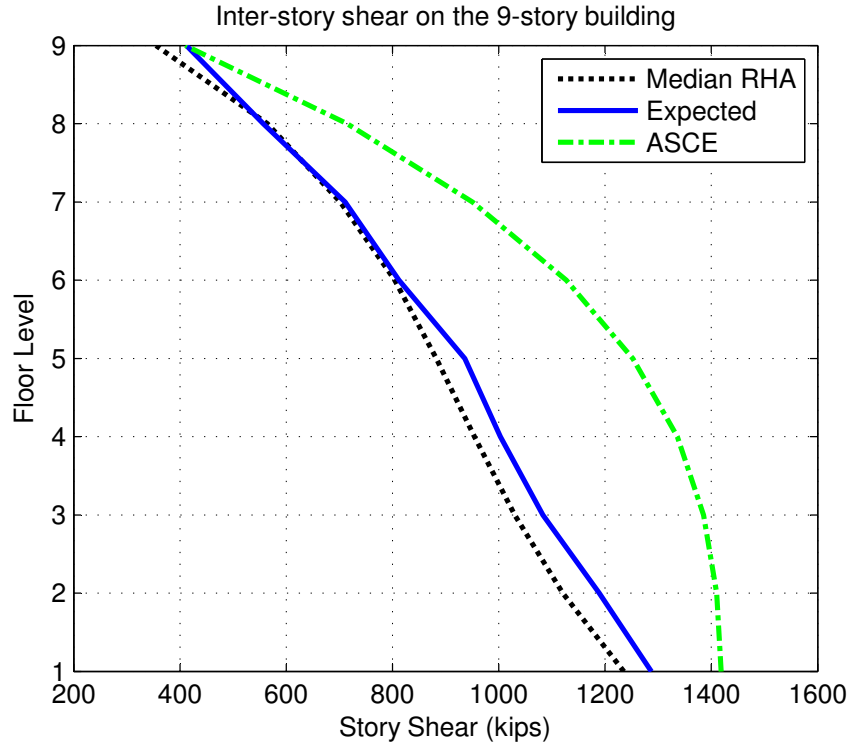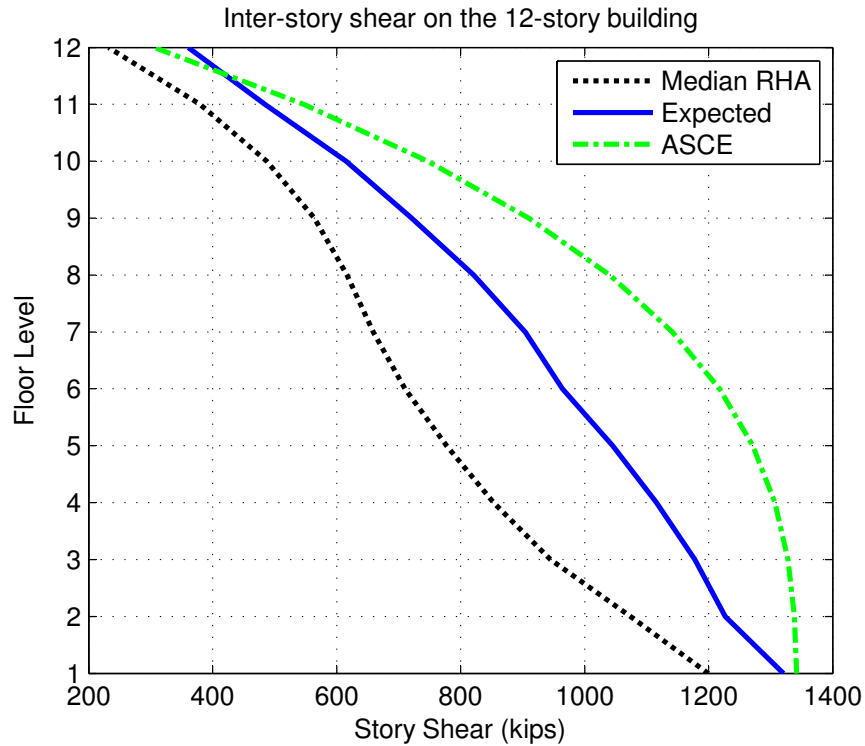
Figure 6.8: Maximum story shear of the 9-story building

Table 6.1: Base shear induced on the considered structures.

Building	Effective Period	Base Shear (kips)		$C_s = V/W$		Estimation
ID	T_{eff} (sec)	THA	Expected	THA	Expectd	Error (%)
3-story	1.42	1242	1134	0.382	0.349	-8.69
5-story	2.40	1313	1188	0.236	0.213	-9.50
7-story	3.20	1357	1254	0.175	0.162	-7.56
9-story	4.00	1236	1287	0.124	0.130	4.16
12-story	5.20	1200	1321	0.091	0.100	10.13
15-story	5.20	1570	1714	0.095	0.104	9.14
20-story	5.50	1268	1417	0.104	0.116	11.73

estimated.

For the case of maximum considered earthquake (2/50) records, the seismic performance of the considered structures is again achieves the desired target of uniform inter-story drift and falls within the allowable code specified range. The median peak inter-story drift angle as well as the total floor acceleration obtained from the

Figure 6.9: Maximum story shear of the 12-story building

nonlinear response history analyses under the 2/50 earthquake records are shown in Figure 6.26 through 6.32. The inter-story drift as well as the floor acceleration for the common buildings, which were designed according to the integrated design procedure and the response history procedure (3, 9, and 20-story buildings), are overlaid on Figures 6.19, 6.22, and 6.25 for the (10/50) analyses, and Figures 6.26, 6.29, and 6.32 for the (2/50) analyses. From the figures, the seismic performance of each pair is about the same. However, for the 20-story building, the integrated design methodology leads to a more uniform inter-story drift than the response history based design. In addition, the floor accelerations are slightly better, especially for the lower floors. Generally, the integrated design procedure is much easier and less time consuming than the response history approach. It also provides a straightforward design methodology that is reliable in terms of structural performance and prediction.
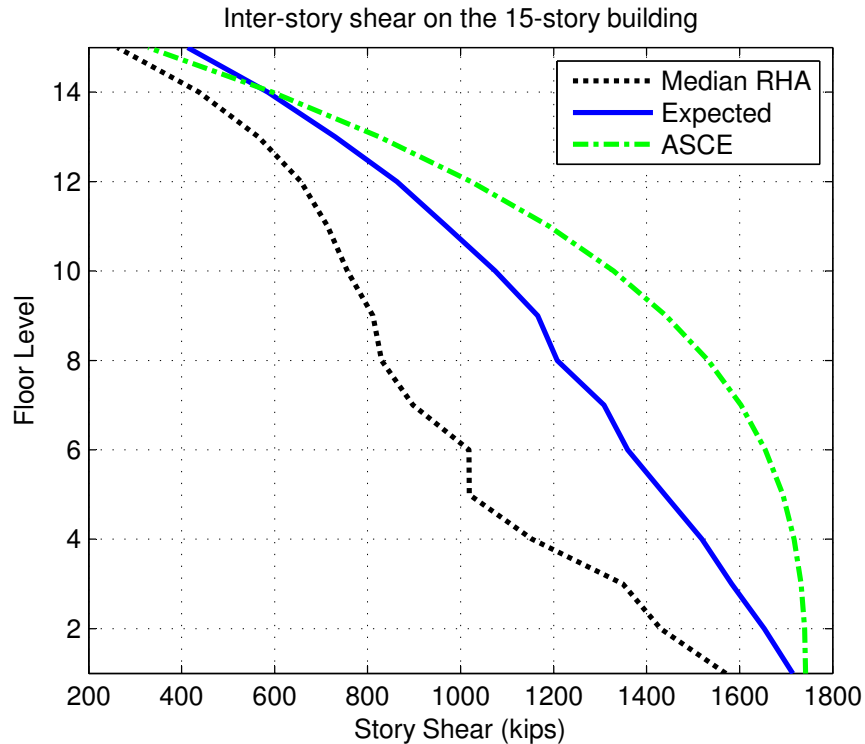
Figure 6.10: Maximum story shear of the 15-story building

6.3 Effect of Stiffness and Damping

The performance of the SBS relies on the stiffness optimization as well as the supplemental damping provided by the viscous damping devices, however. In order to investigate the effect of stiffness and damping, the 5, 9, and 15-story buildings were subjected to the 10/50 ground motion records. The response history analyses are carried out on the buildings with the supplemental viscous dampers being eliminated, so that the stiffening braces act individually. Thus the total effective damping in the systems is the inherent damping only (2%). As can be seen from Figure 6.33, the optimized stiffness alone, without any supplemental dampers, successfully achieves the desired uniform inter-story drift for the 5-story building. However the drift ratio is higher than the target because of the higher seismic demand. As the building's height increases, the effectiveness of the stiffness alone becomes less. For the 9-story
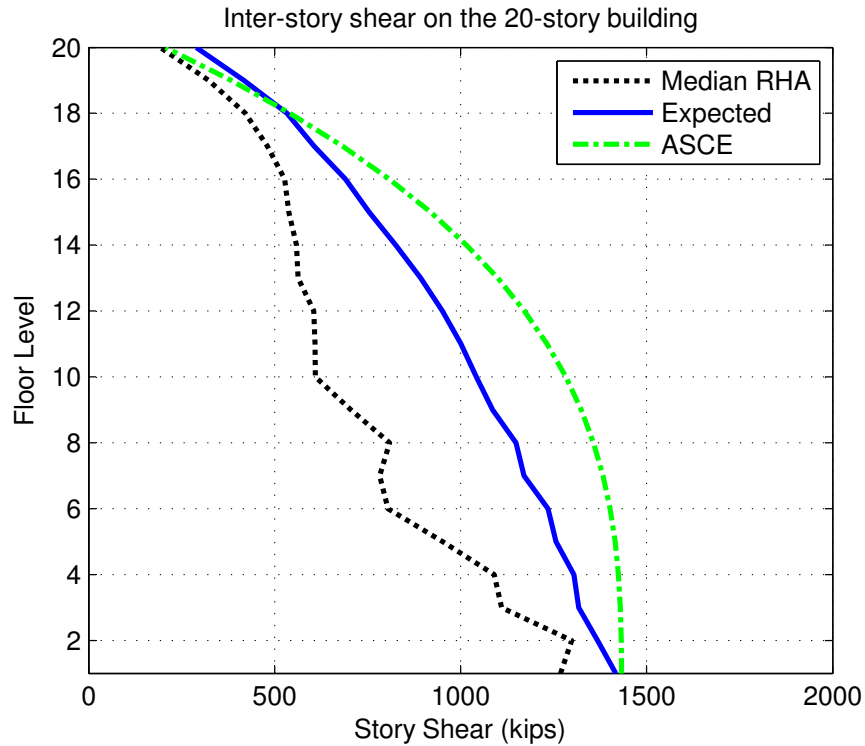
Figure 6.11: Maximum story shear of the 20-story building

building, the optimized stiffness alone partially achieves the uniform inter-story drift target, as can be seen in Figure 6.34. While for the 15-story building, the stiffness alone fails to achieve the desired target and the added supplemental damping becomes essential for the SBS to behave as desired. Therefore, the SBS procedure is robust, with or without the supplemental viscous damping devices, for low rise buildings. For tall buildings, the SBS cannot achieve the desired target performance without supplemental viscous damping devices.
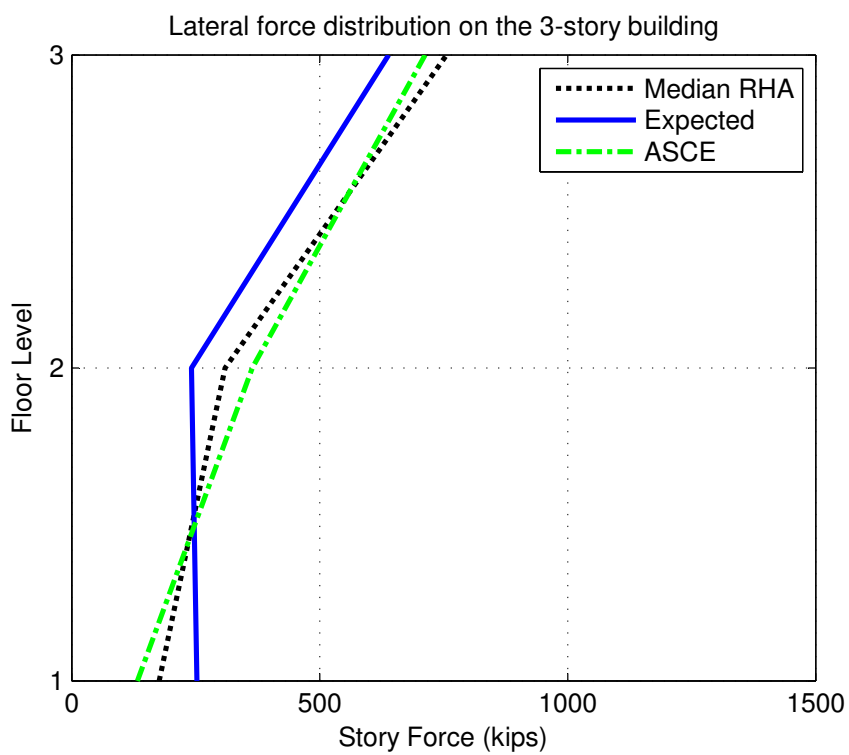
Figure 6.12: Lateral force distribution on the 3-story building
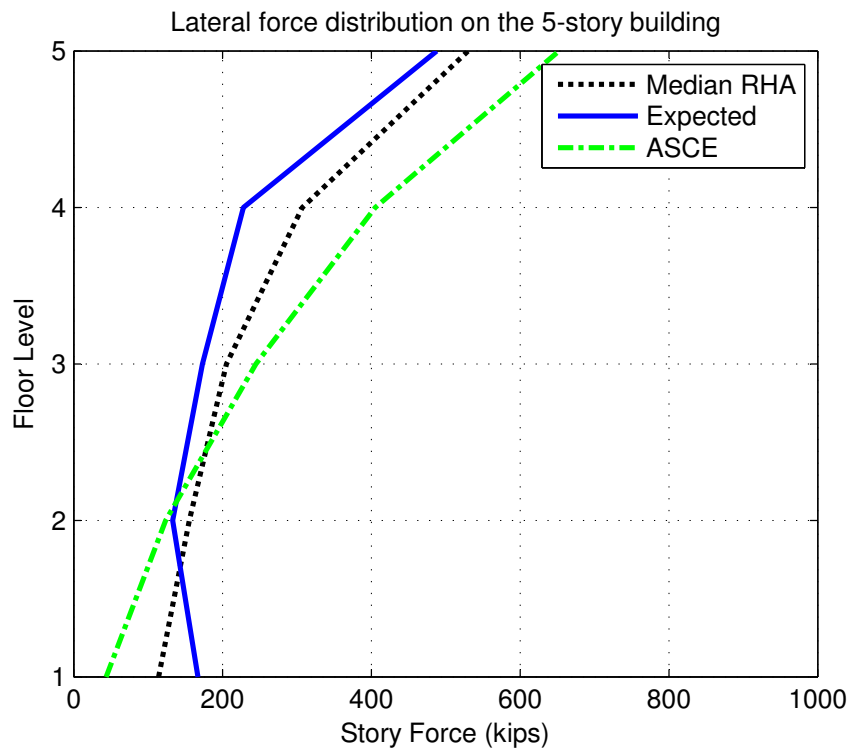
Figure 6.13: Lateral force distribution on the 5-story building
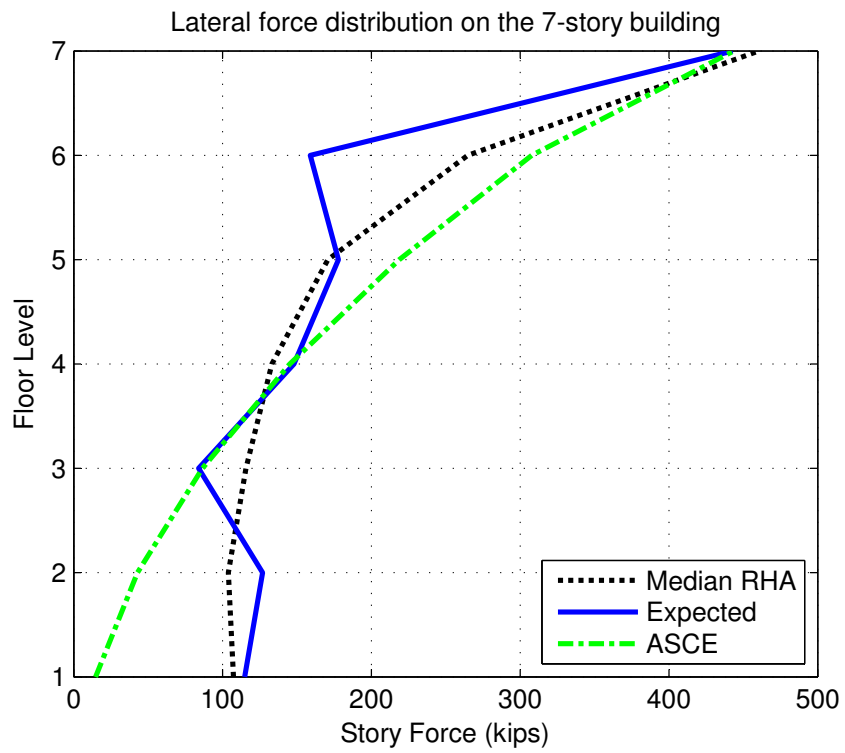
Figure 6.14: Lateral force distribution on the 7-story building
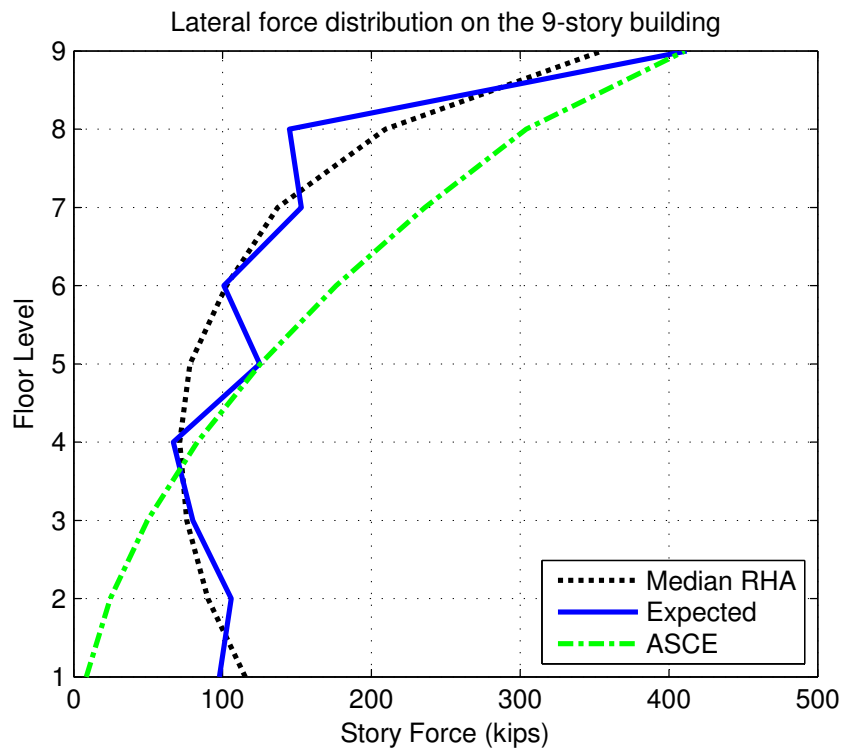
Figure 6.15: Lateral force distribution on the 9-story building
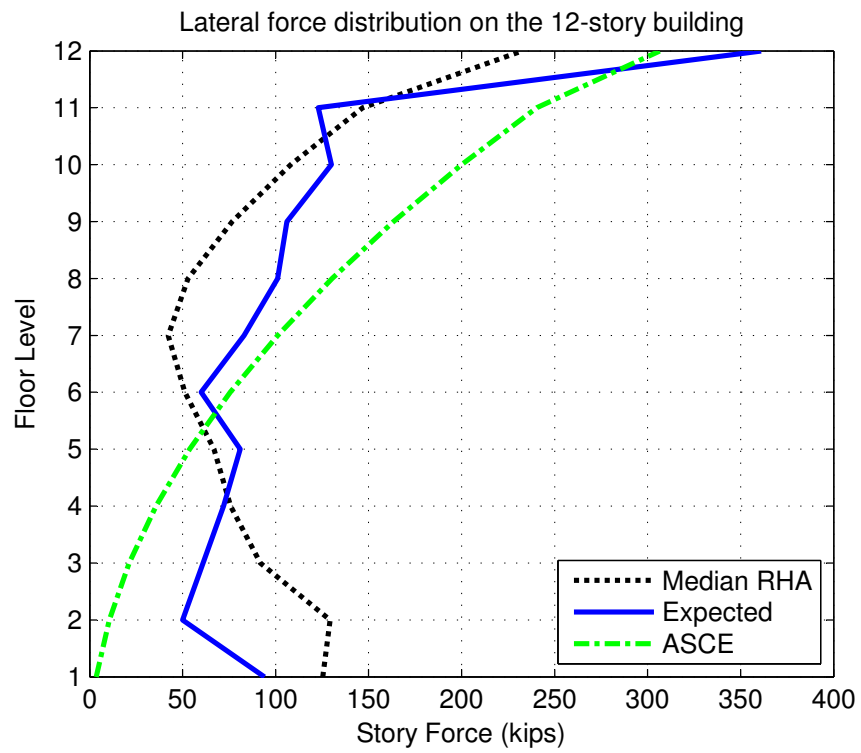
Figure 6.16: Lateral force distribution on the 12-story building
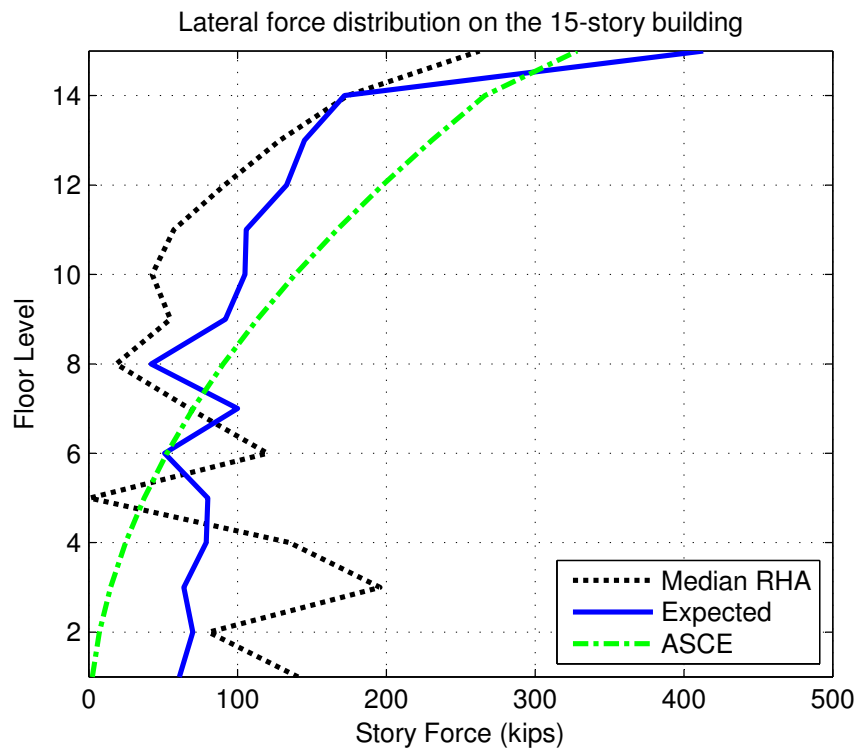
Figure 6.17: Lateral force distribution on the 15-story building
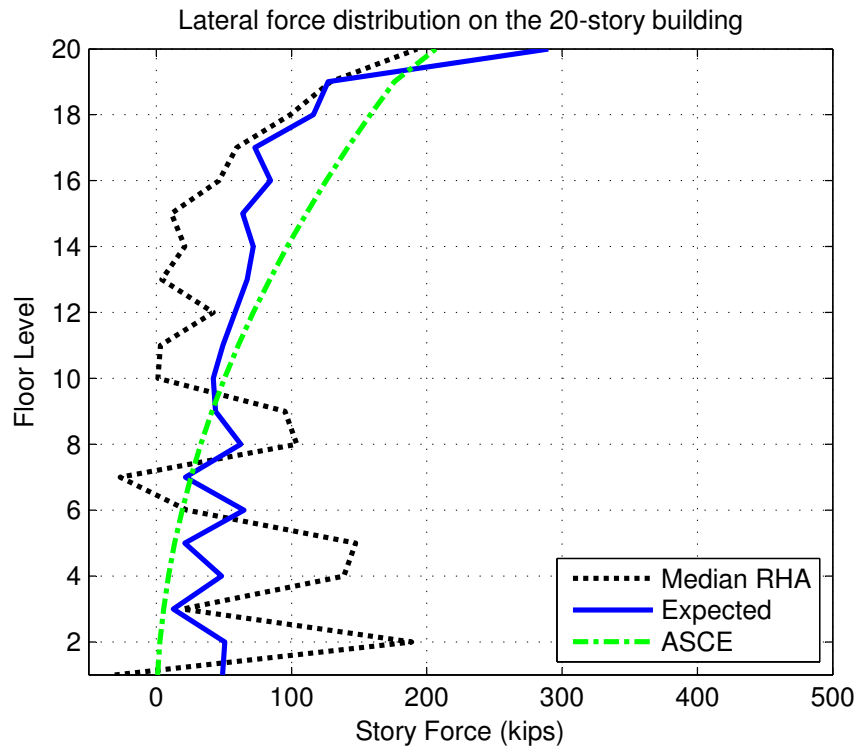
Figure 6.18: Lateral force distribution on the 20-story building
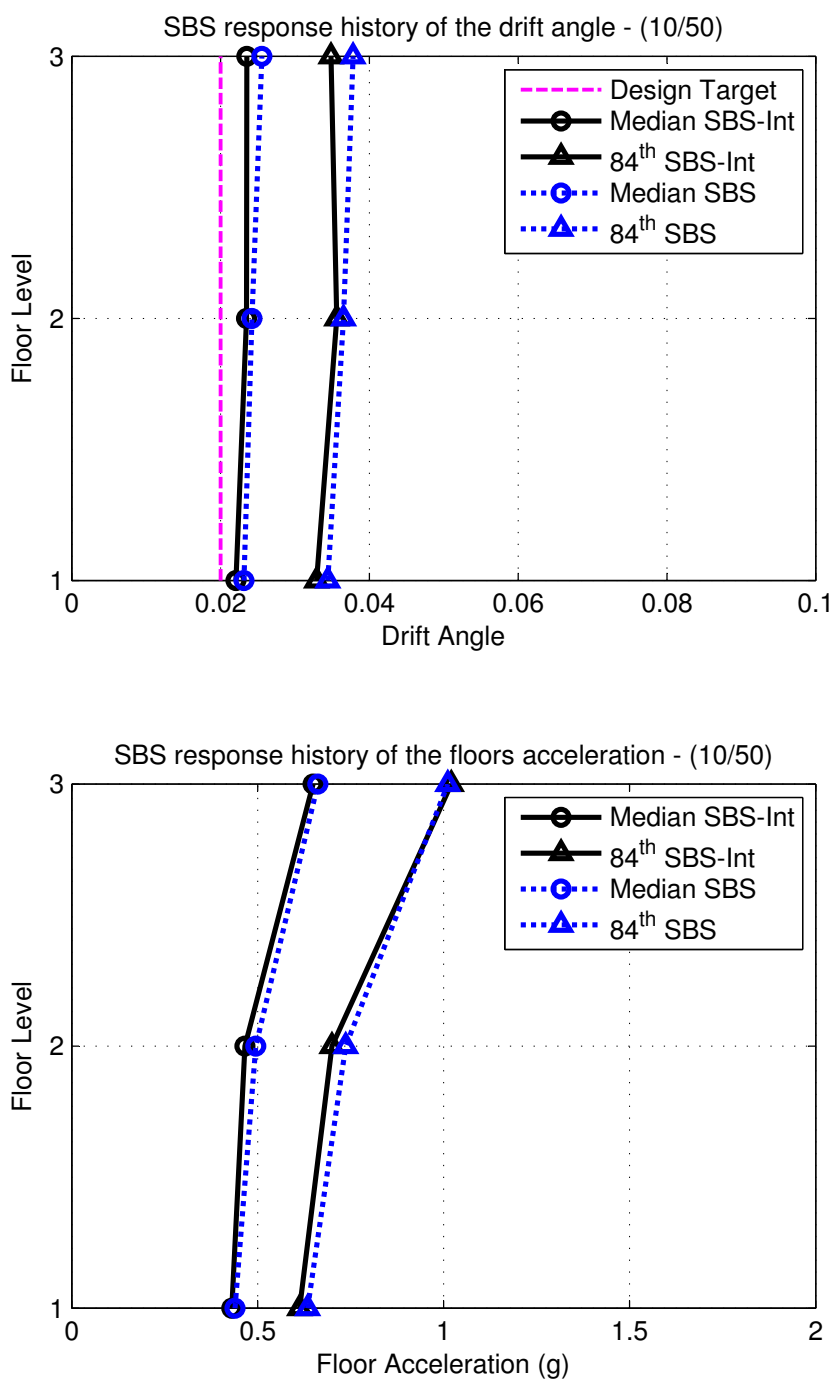
Figure 6.19: Median of the peak inter-story drift angle and peak floor acceleration for the 3-story building under the 10/50 ground motion records
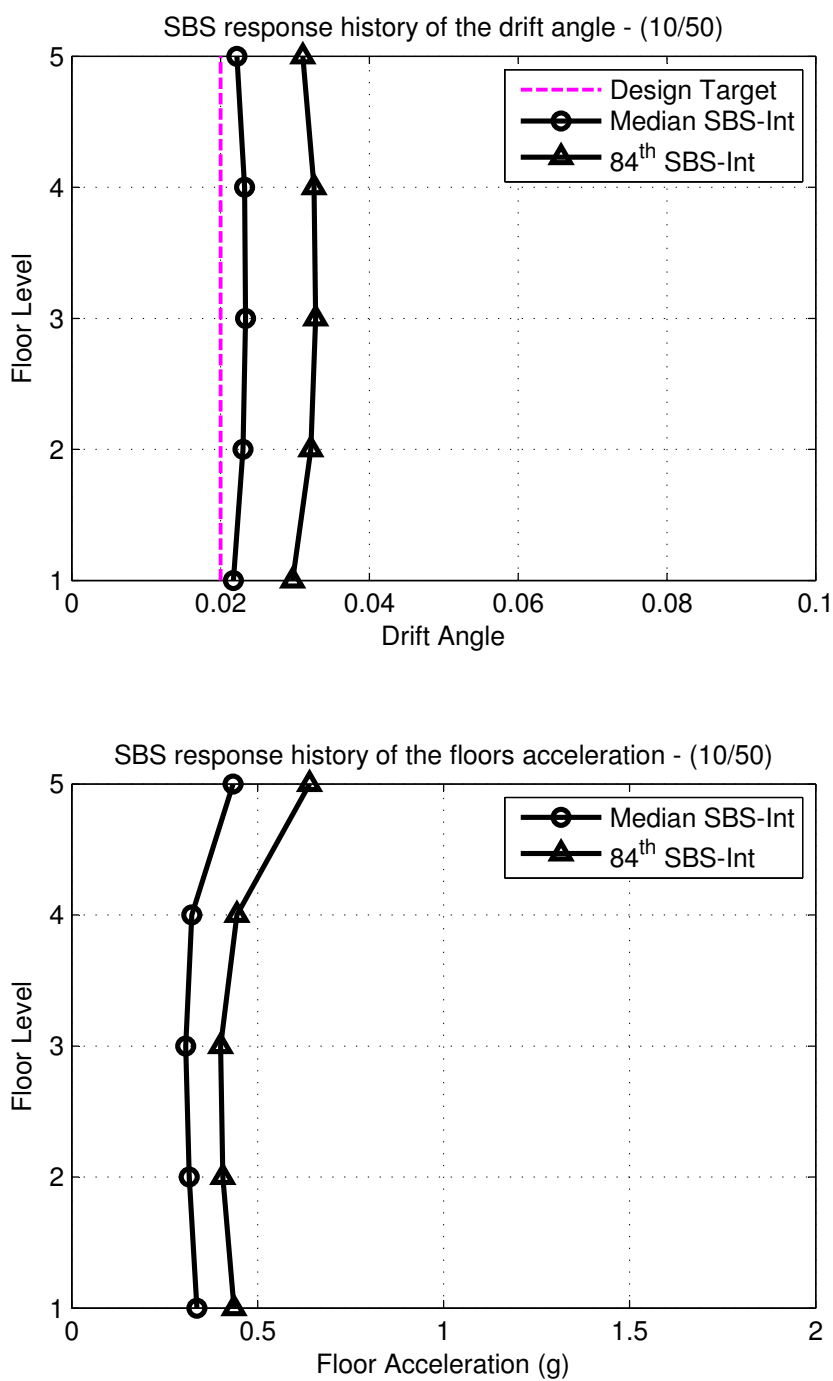
Figure 6.20: Median of the peak inter-story drift angle and peak floor acceleration for the 5-story building under the 10/50 ground motion records

Figure 6.21: Median of the peak inter-story drift angle and peak floor acceleration for the 7-story building under the 10/50 ground motion records

Figure 6.22: Median of the peak inter-story drift angle and peak floor acceleration for the 9-story building under the 10/50 ground motion records

Figure 6.23: Median of the peak inter-story drift angle and peak floor acceleration for the 12-story building under the 10/50 ground motion records
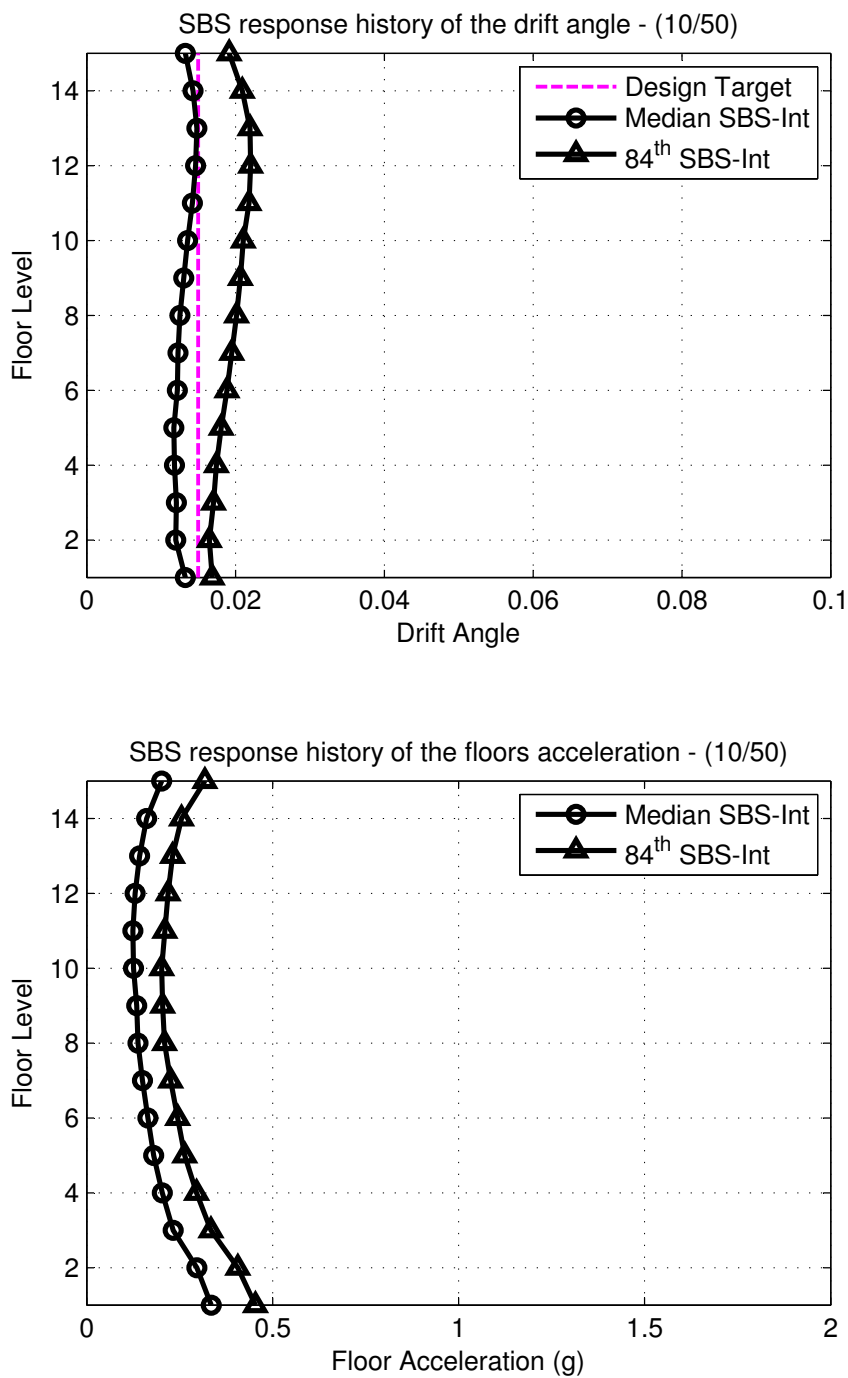
Figure 6.24: Median of the peak inter-story drift angle and peak floor acceleration for the 15-story building under the 10/50 ground motion records
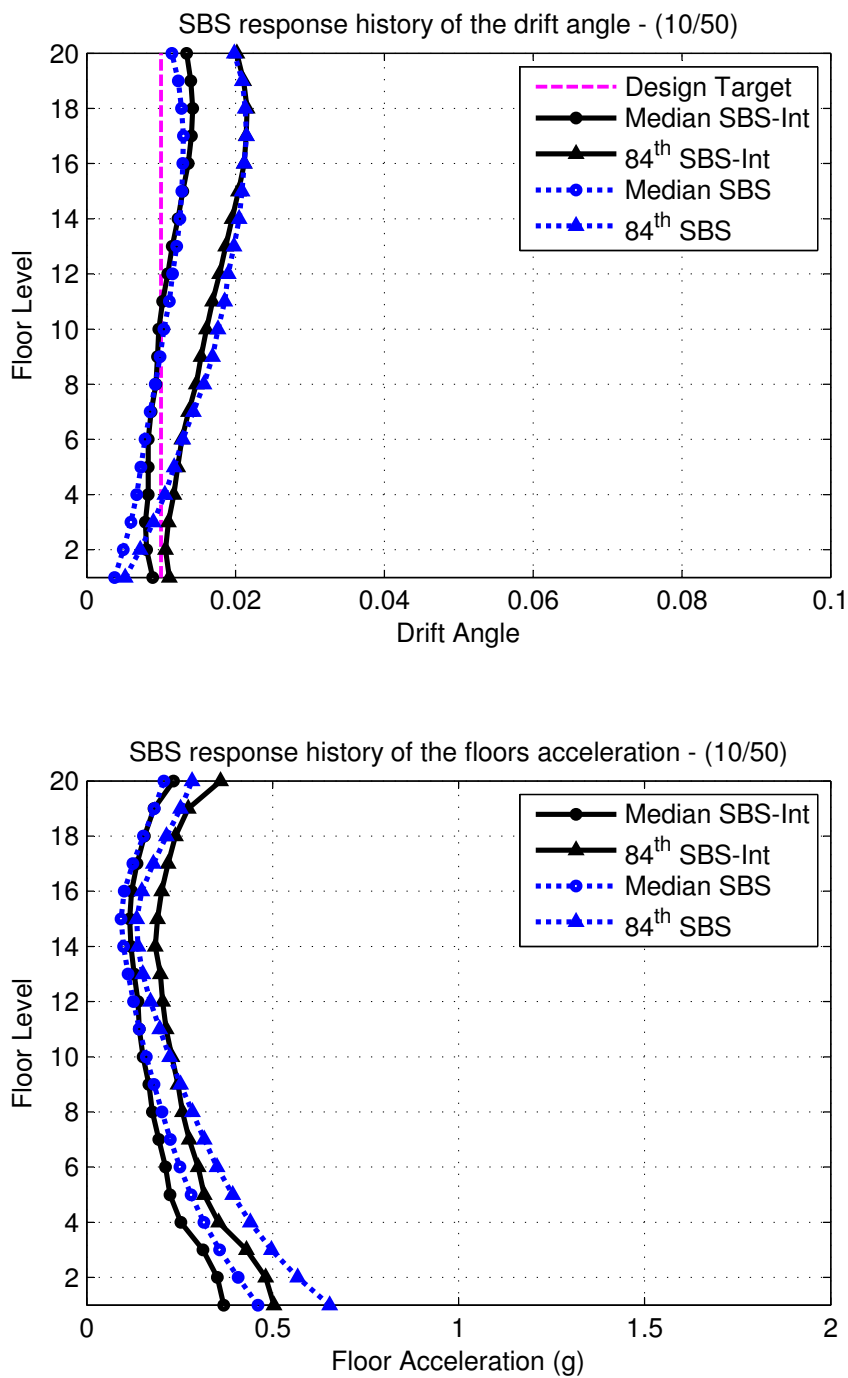
Figure 6.25: Median of the peak inter-story drift angle and peak floor acceleration for the 20-story building under the 10/50 ground motion records
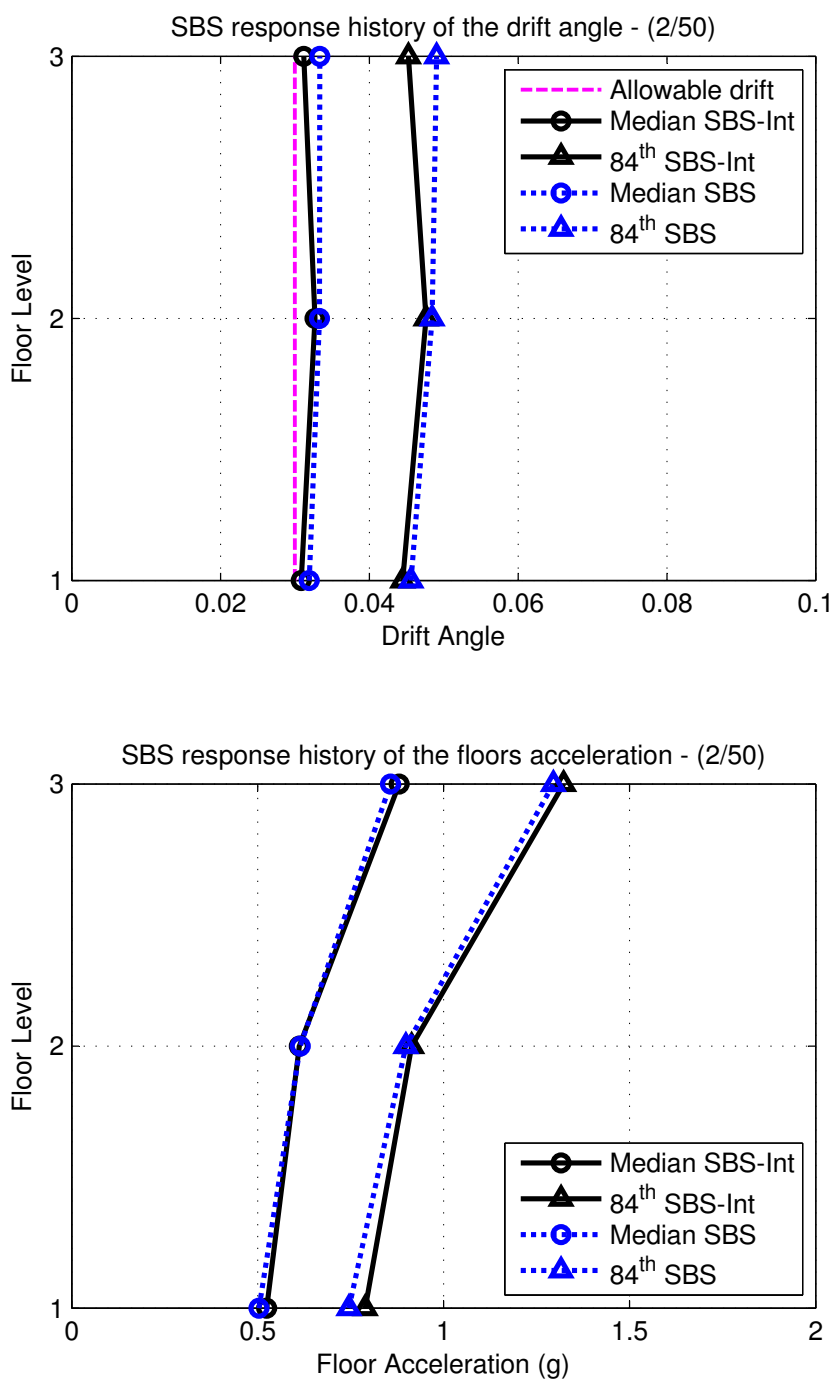
Figure 6.26: Median of the peak inter-story drift angle and peak floor acceleration for the 3-story building under the 2/50 ground motion records
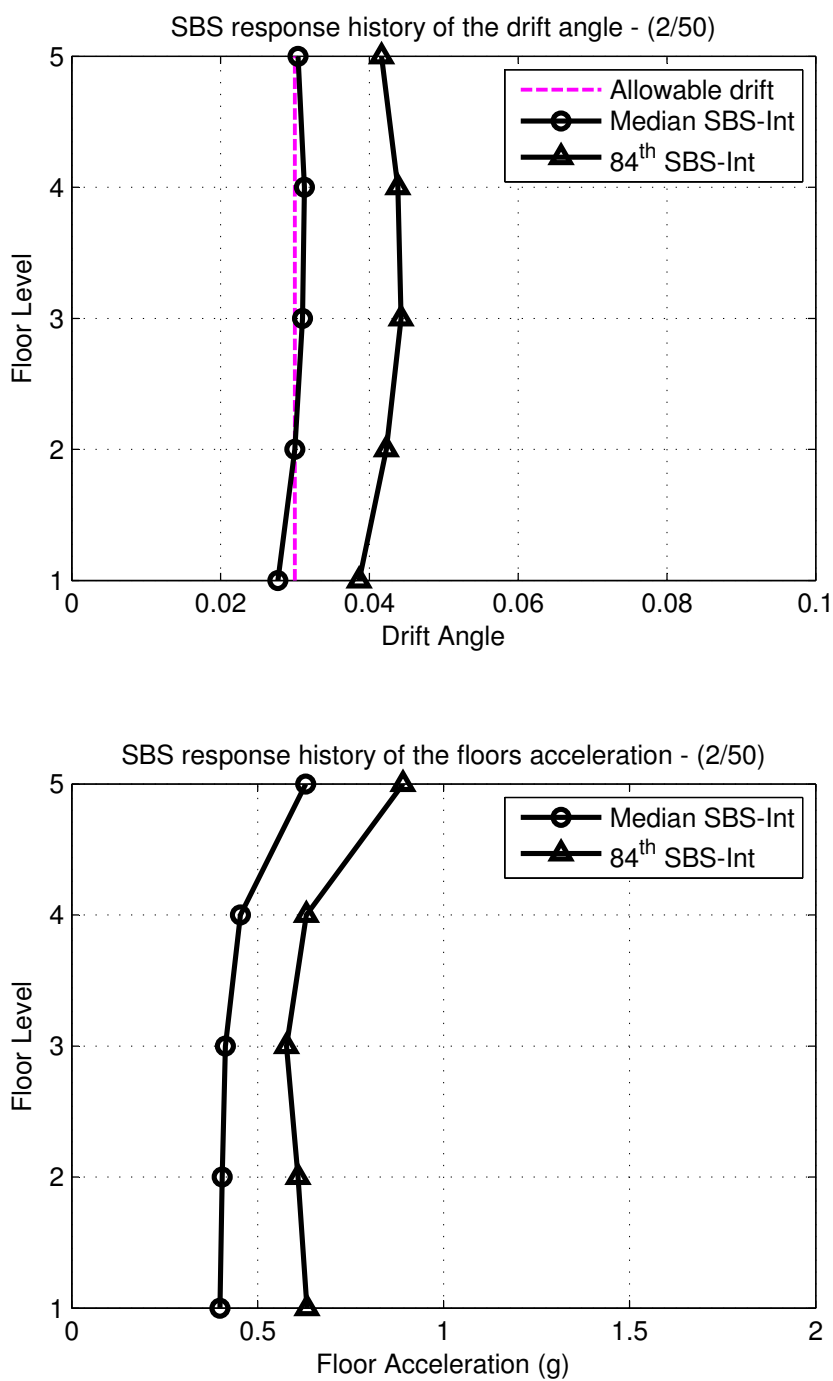
Figure 6.27: Median of the peak inter-story drift angle and peak floor acceleration for the 5-story building under the 2/50 ground motion records
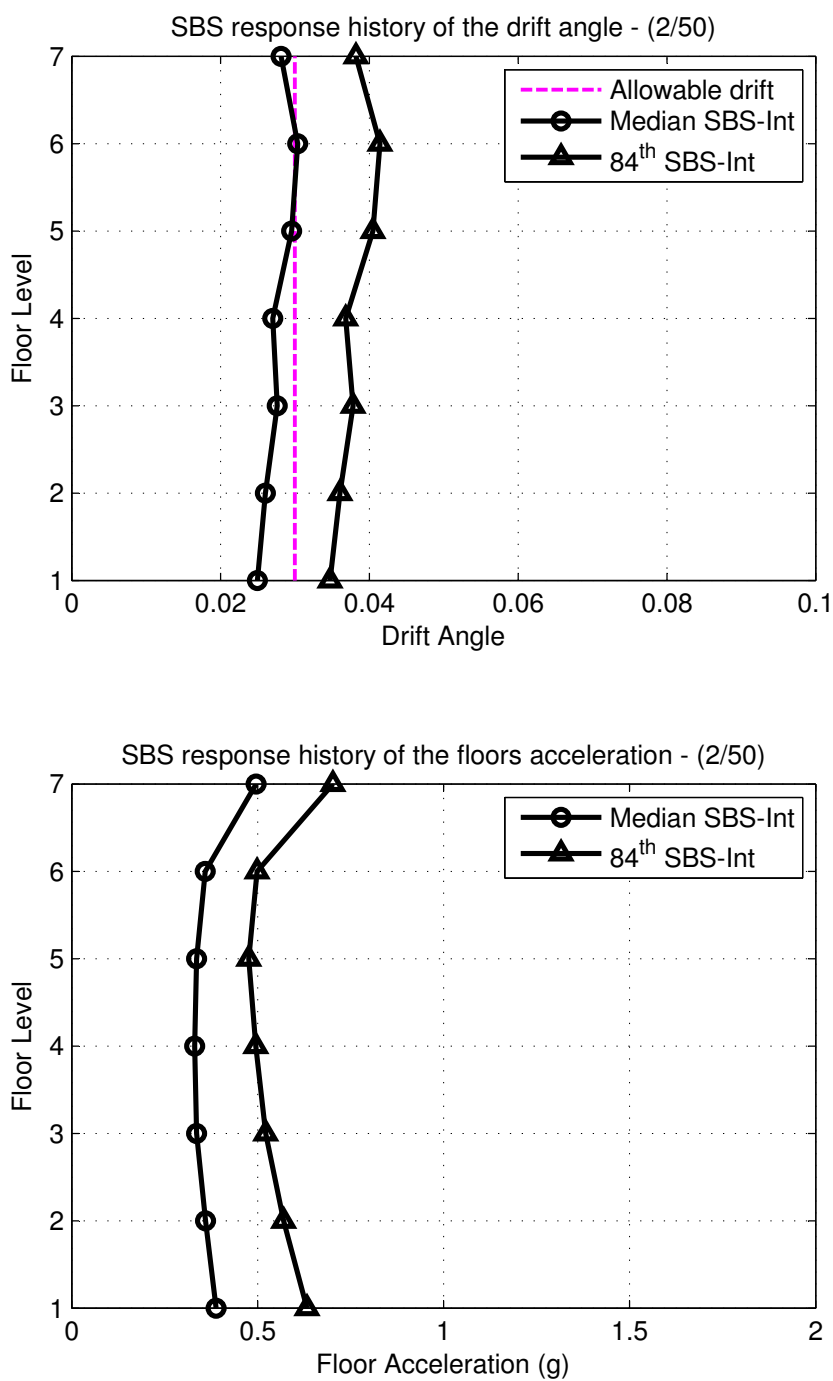
Figure 6.28: Median of the peak inter-story drift angle and peak floor acceleration for the 7-story building under the 2/50 ground motion records
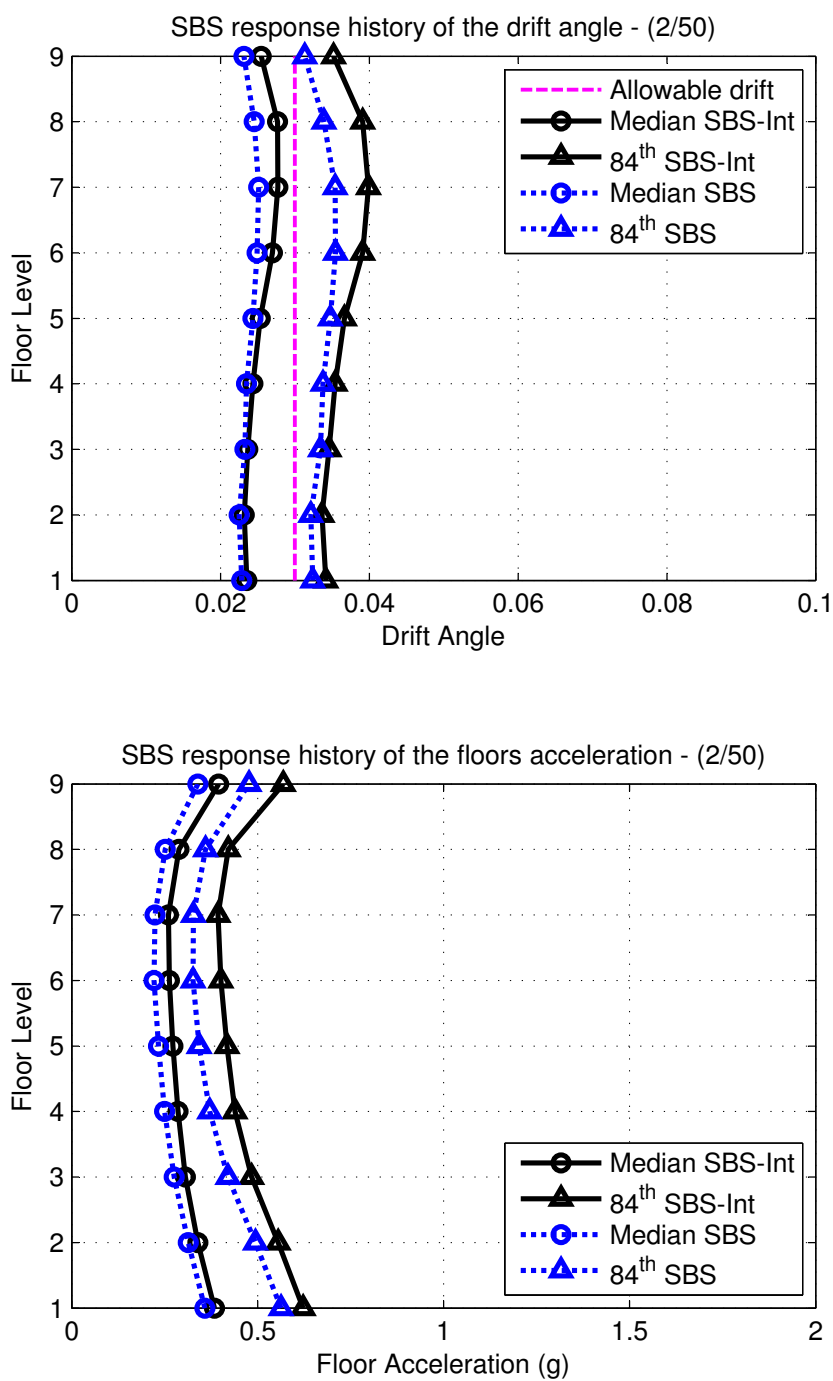
Figure 6.29: Median of the peak inter-story drift angle and peak floor acceleration for the 9-story building under the 2/50 ground motion records
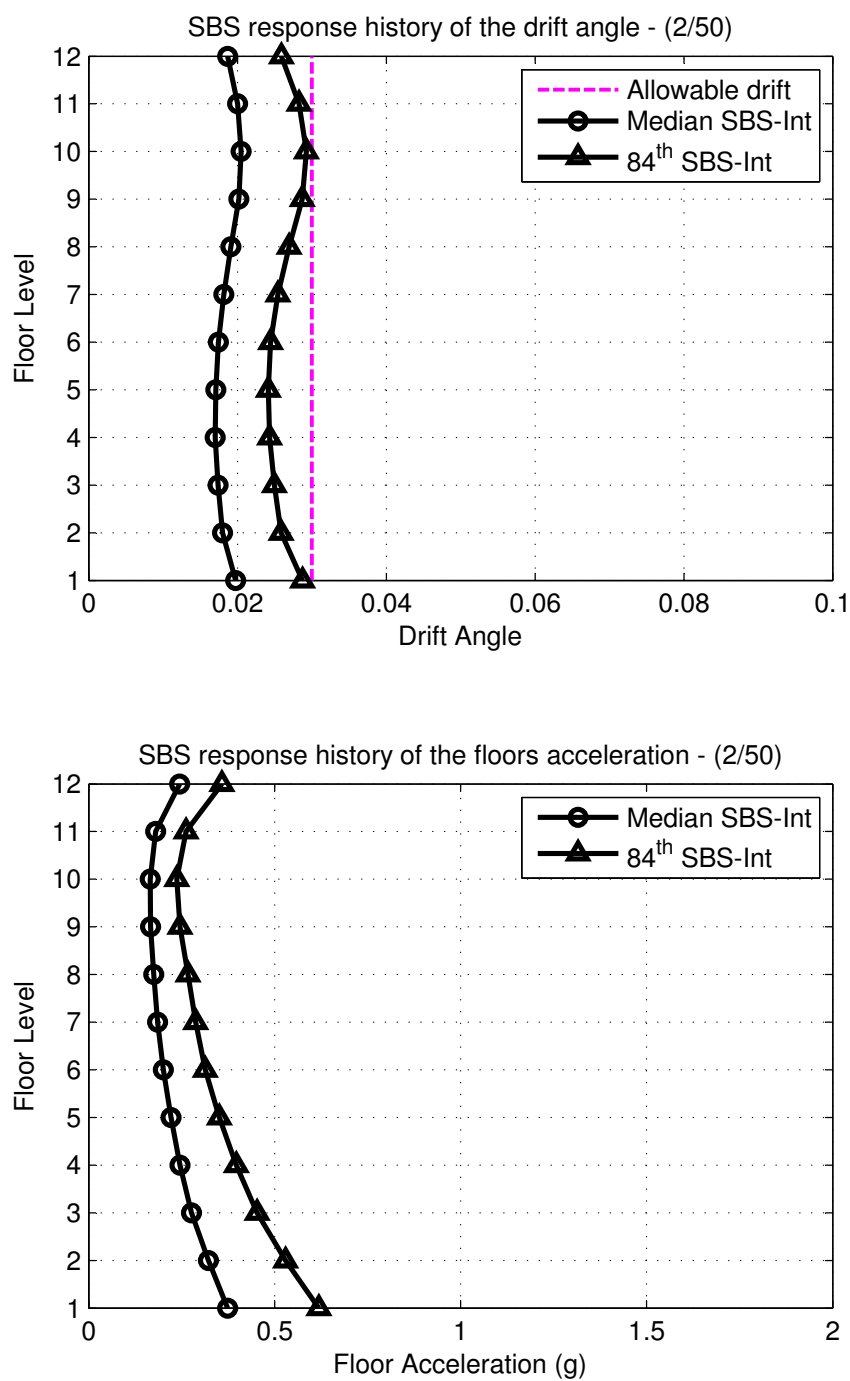
Figure 6.30: Median of the peak inter-story drift angle and peak floor acceleration for the 12-story building under the 2/50 ground motion records
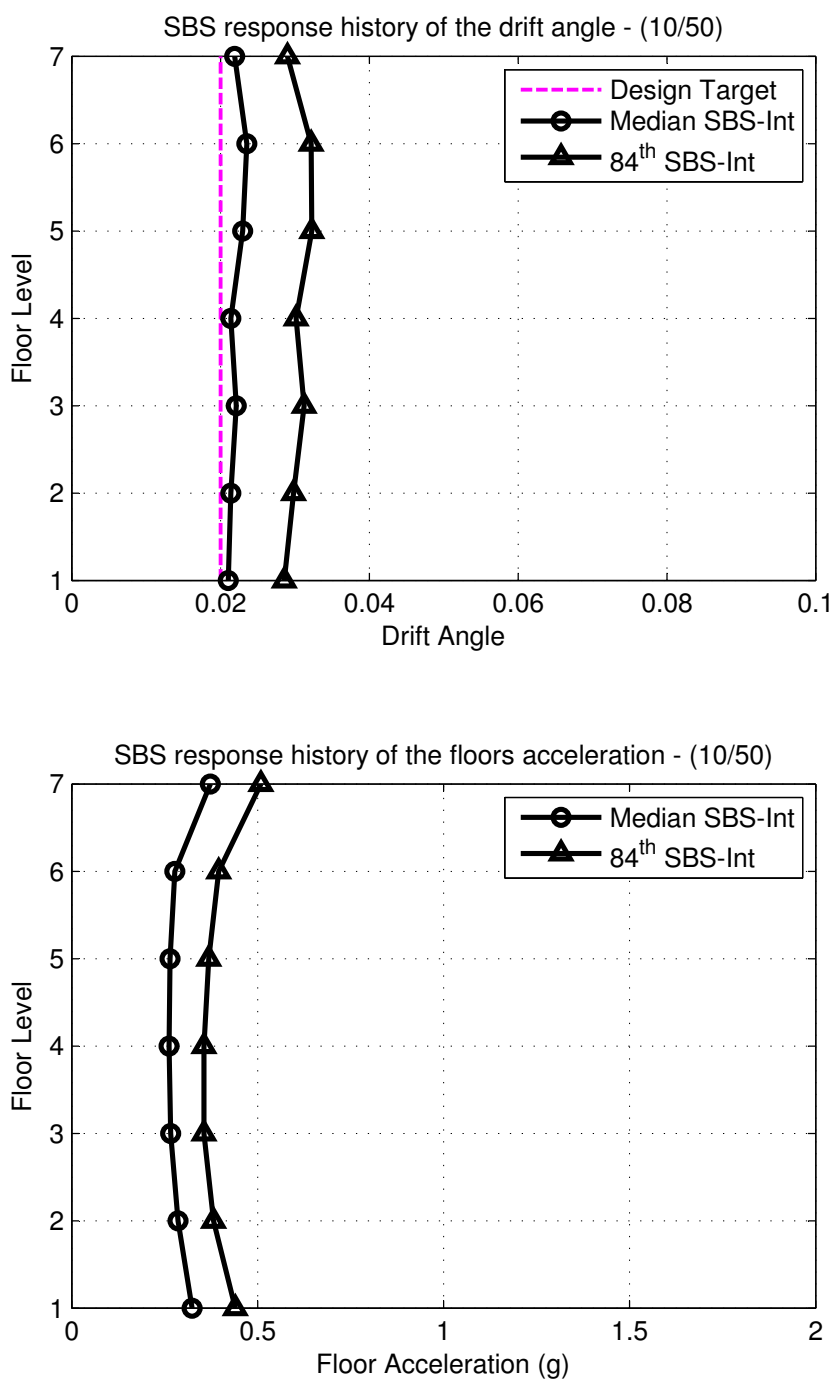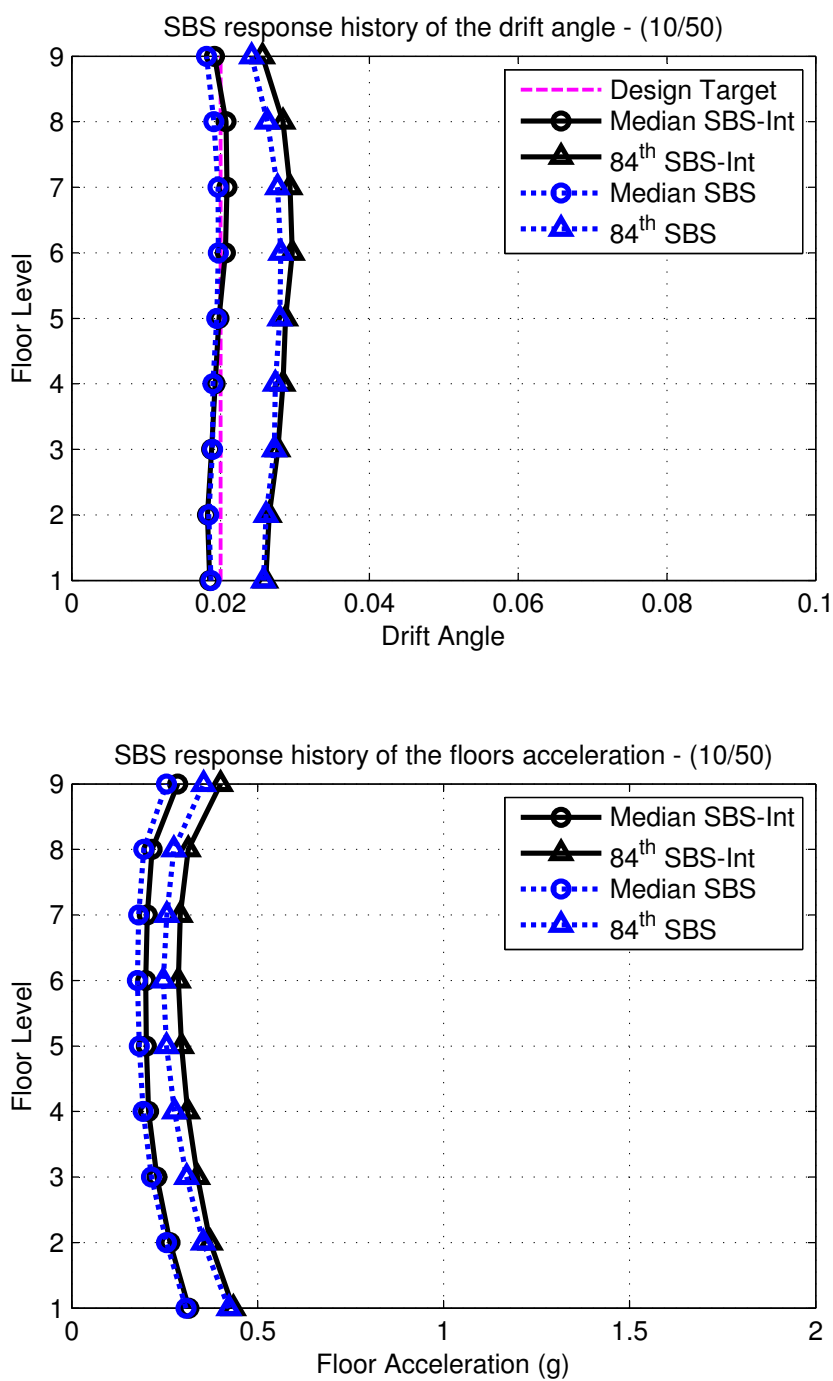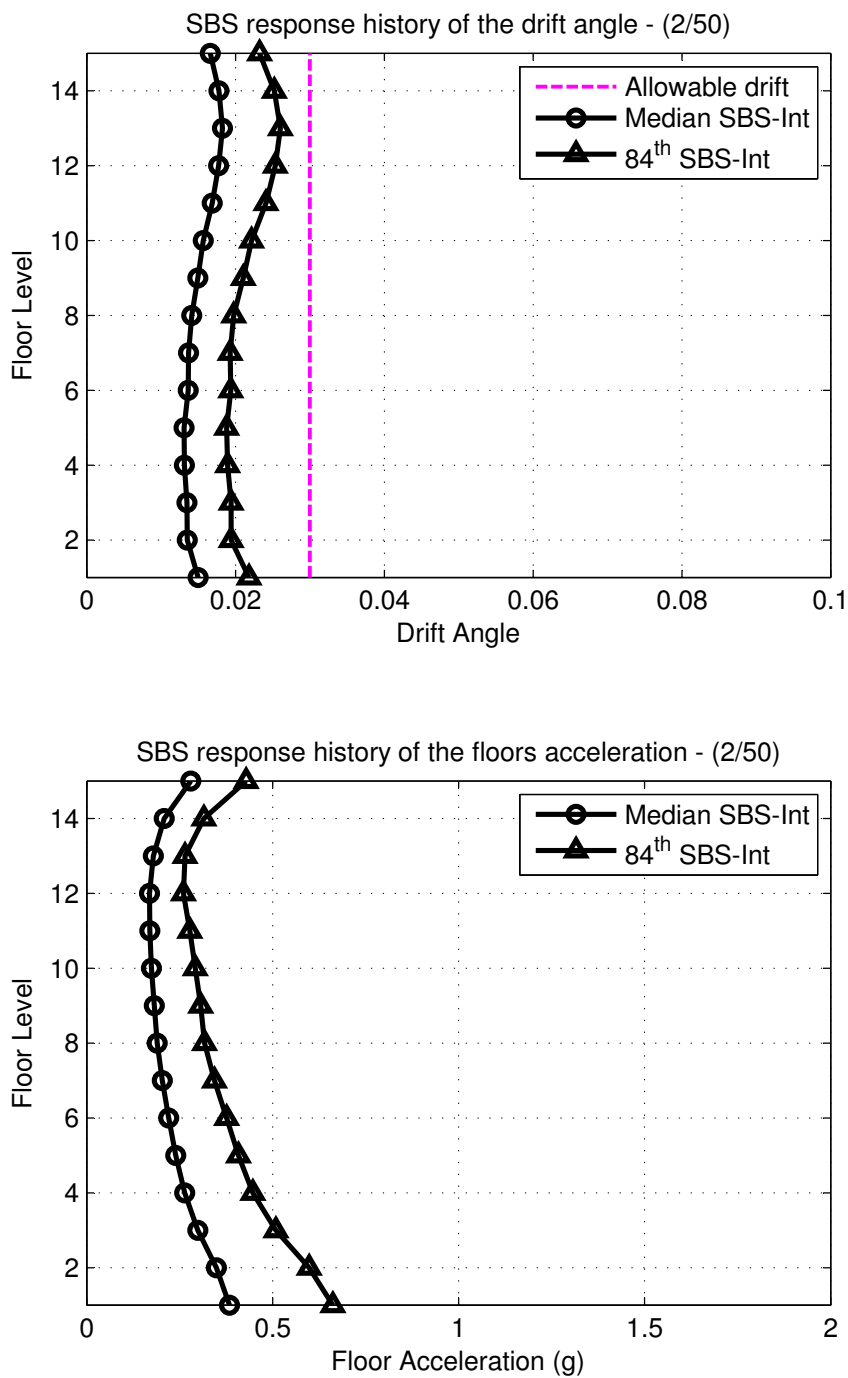
Figure 6.31: Median of the peak inter-story drift angle and peak floor acceleration for the 15-story building under the 2/50 ground motion records

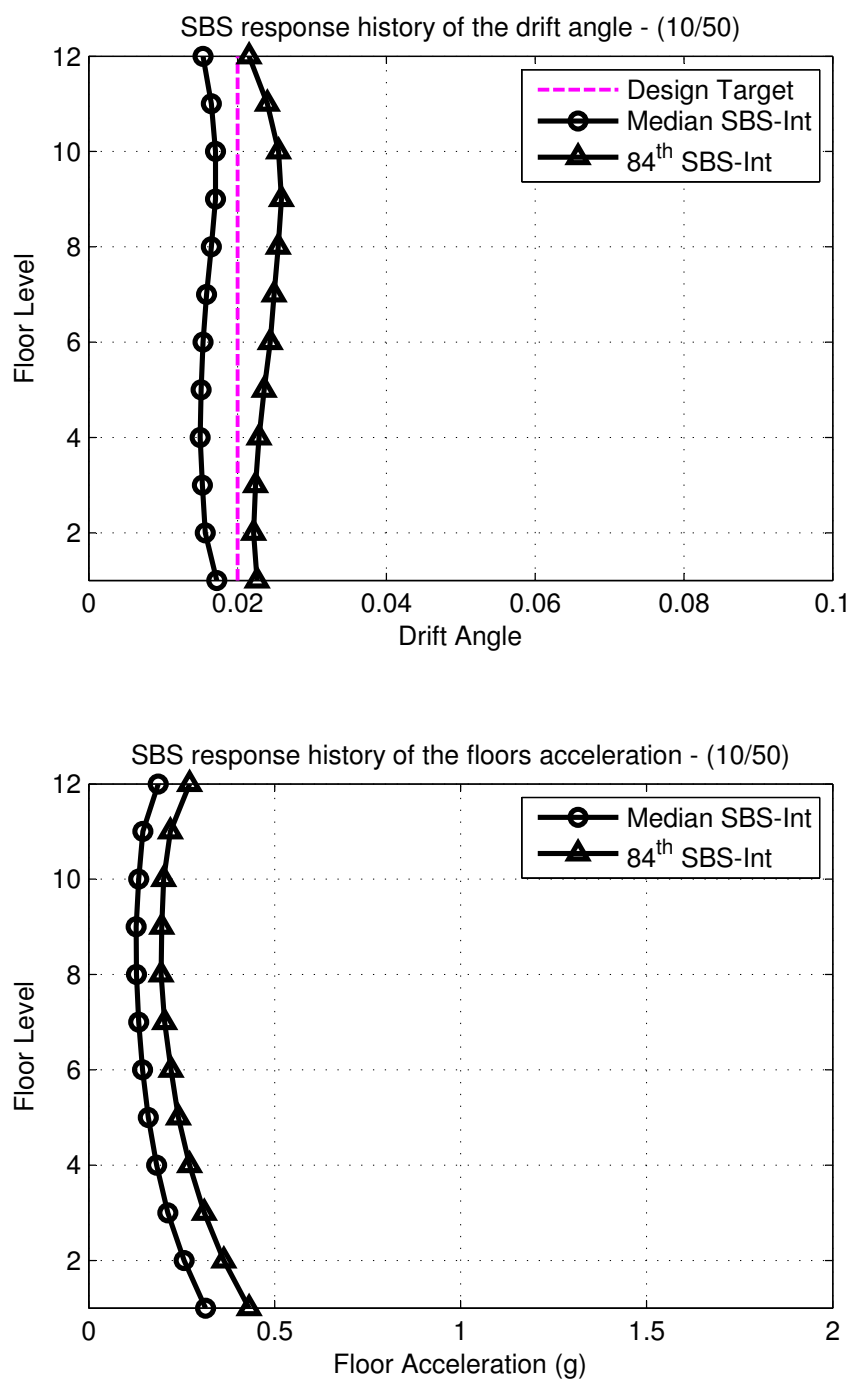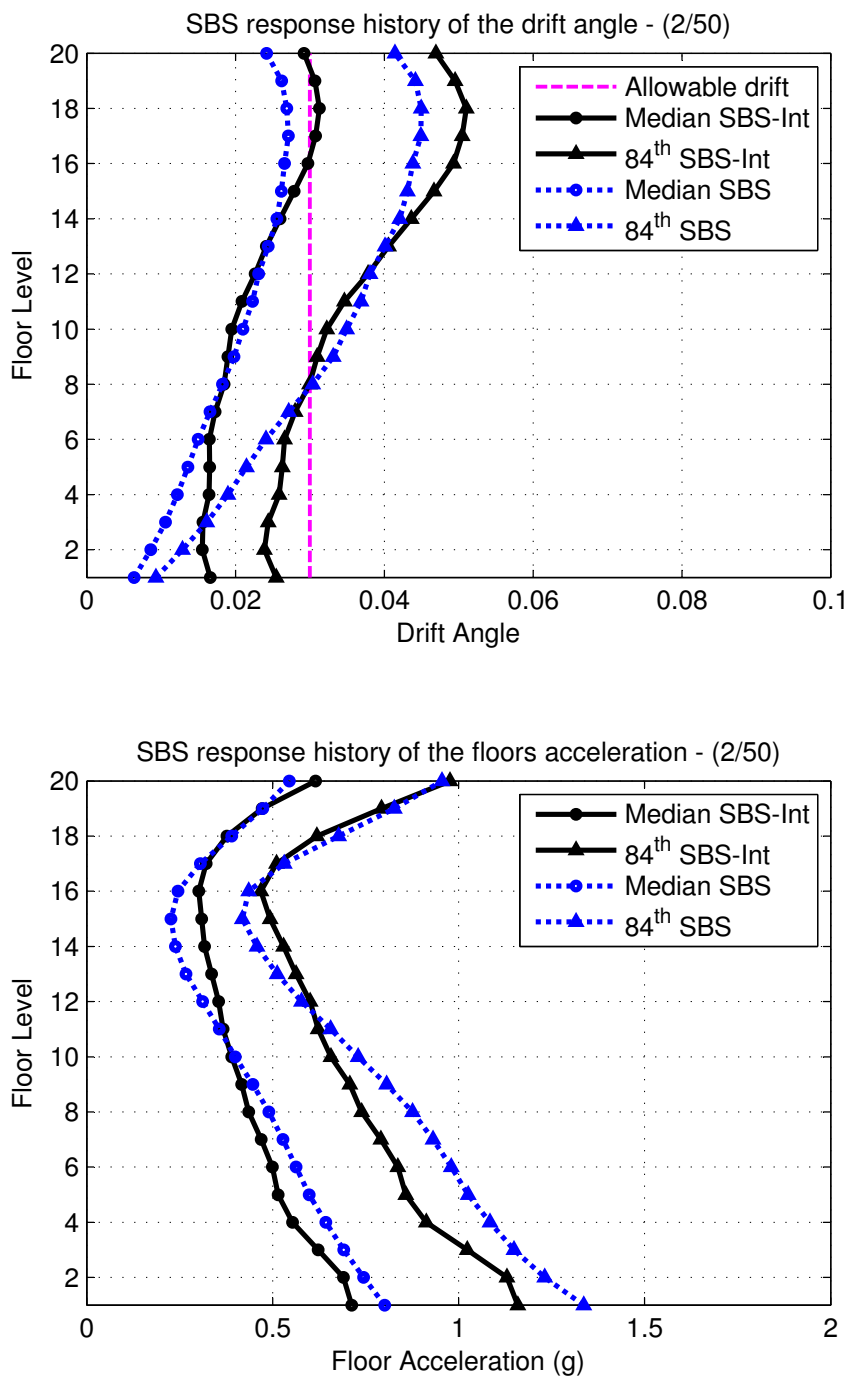**Figure 6.32:** Median of the peak inter-story drift angle and peak floor acceleration for the 20-story building under the 2/50 ground motion records
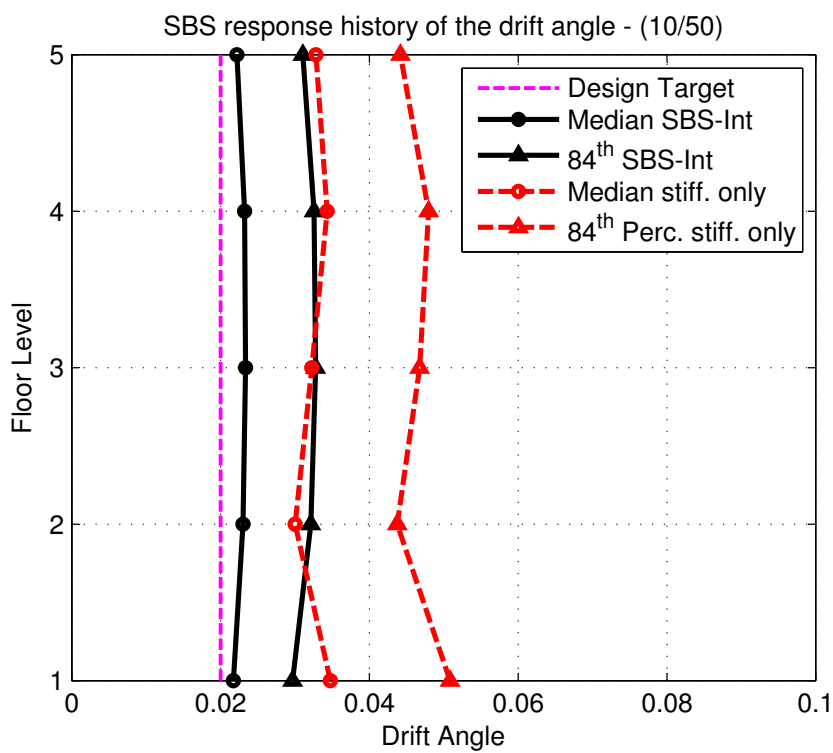
Figure 6.33: Effect of stiffness and damping on the peak inter-story drift of the 5-story building under the 10/50 ground motions
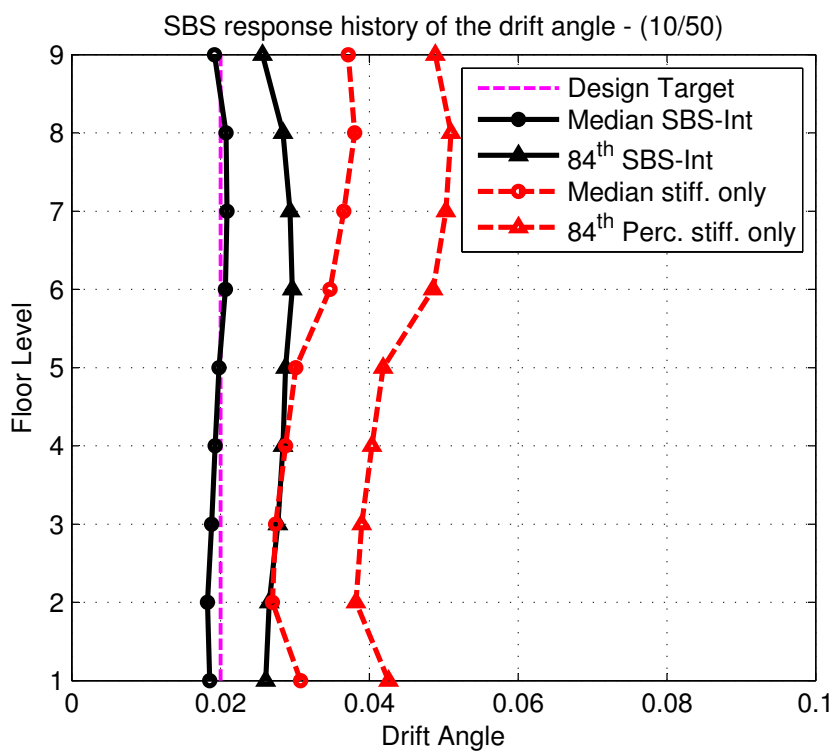
Figure 6.34: Effect of stiffness and damping on the peak inter-story drift of the 9-story building under the 10/50 ground motions
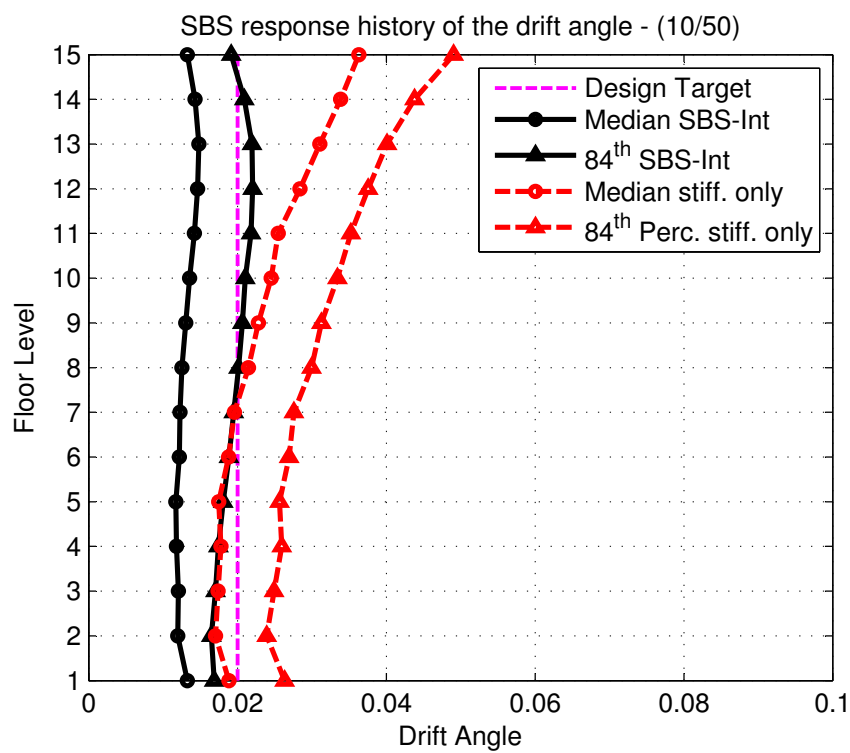
Figure 6.35: Effect of stiffness and damping on the peak inter-story drift of the 15-story building under the 10/50 ground motions

Chapter 7

Conclusions

Semi-active control strategies for smart base isolation systems employing Magneto-Rheological Elastomer (MRE) have been developed. The two proposed control algorithms were designed to minimize the superstructure and the substructure accelerations, namely, the Minimal Acceleration Control (MAC) and the Acceleration Gain Control (AGC). It was shown that both methods can significantly reduce the seismic demand on a benchmark base isolated structure. Under the effect of far-field ground motions, the MAC algorithm can reduce the overall structural accelerations and the superstructure's displacements by up to 75% compared to the seismically isolated structure with conventional lead rubber bearing (LRB) system. However, up to 37% increase in the base displacement demand is possible. The AGC on the other hand, provides up to 50% reduction in the seismic demand with only 25% increase in the base displacement. In addition, the AGC tends to minimize or eventually eliminate any residual displacement in the base slab that was observed in the cases with the MAC algorithm.

For near-fault excitations, similar levels of reduction of the seismic demand can be achieved. The MAC algorithm provides up to 65% reduction in the overall structural accelerations as well as the superstructure displacements, compared to the LRB system. However, up to 54% increase in the base displacement and a tendency to

leave residual displacement in the base slab is possible. Near-fault ground motions are dominated by large velocity pulses that induce large base displacements on seismically isolated structures. The large base displacement may lead to structural instability. Clearly, further increase of the base displacement is not favorable. To overcome this issue, a hypothetical variable stiffness device capable of providing stiffening ratio of up to ten is proposed. Such a device controlled with the AGC can achieve up to 33% reduction in the base displacement compared to the conventionally isolated structure without compromising the behavior of the LRB. However, the MRE base isolation system with the current properties of limited stiffening ratio can achieve up to 35% reduction in the overall structural accelerations and the superstructure displacements with only 22% increase in the base displacement.

It is important to note that for a better reduction of the seismic demands on the superstructure, the base displacement in both of the proposed control algorithms tends to exceed the base displacement of the conventionally isolated structure. This fact makes the proposed systems more suitable for far-field ground motions (low displacement demands) and for the isolation of acceleration sensitive structural and non-structural components, unless isolation systems with higher stiffening ratios are available.

The use of variable stiffness devices in multistory structures has also been investigated. A stiffening bracing system (SBS) has been proposed to replace the conventional bracing systems for braced frames. The SBS is primarily suggested to possess relatively low stiffness initially. This would allow for lengthened period of vibration and hence drags the structural performance to a lower level of seismic demands. After a predefined inter-story drift angle is reached, the SBS stiffens up in an attempt to limit the increase in the inter-story drift. This limitation to the inter-story drift minimizes the $P - \Delta$ effect on the columns. An optimization procedure for the SBS

parameters has been developed. The main objective of the optimization process is to maintain a uniform inter-story drift angle over the building's height. In turn, this results in evenly distributed seismic demand over the building's height. This behavior is essential for avoiding excessive damage from being concentrated in a single story. In addition, all the supplemental viscous damping devices that accompany the stiffening braces work more efficiently at their maximum capacity, which eventually leads to a cost efficient design. Structures designed according to the code-specified lateral force procedures experience nonuniform inter-story drift during seismic events. This is due to the fact that these procedures do not take into account the higher mode effects. Although the initial stiffness of the SBS is designed based on the code-specified equivalent lateral force, the optimization process explicitly accounts for the instantaneous dynamic properties of the structure as well as the higher mode effects.

In order to investigate the adequacy of the proposed system, the three SAC buildings designed for Los Angeles area were redesigned with the SBS. In addition, the buildings were redesigned as buckling restrained braced frames (BRBF) for comparison purpose. Twenty pairs of recorded ground motions were applied to both structures through a nonlinear response history analyses. The ground motion records are subdivided into two groups to represent design level earthquake and maximum considered earthquake. Under the effect of the design earthquake records, the proposed methodology successfully achieved the desired performance. The median of the twenty records showed uniform inter-story drift for the 3-story and 9-story buildings. However, for the 20-story building, the upper floors experienced higher inter-story drifts than the lower floors.,On average, the overall performance was quite uniform and below the target. In contrast, the BRBFs showed a nonuniform inter-story drift distribution for all of the considered cases. In terms of maximum floor acceleration, the SBS system showed significant reduction of up to 50% compared to the BRBFs.

This implies higher comfort level to the building occupants and lower seismic demand on acceleration sensitive nonstructural components. On the other hand, the main framing elements (Beams and Columns) stayed in their elastic region for structures with the SBS, while significant yielding and permanent story drift are observed for the BRBFs.

Under the effect of the maximum considered earthquake records, the performance of the 3-story and 9-story buildings equipped with the SBS preserved the uniformity of the inter-story drift within acceptable limit. For the 20-story building, again the upper floors experienced higher inter-story drifts than the lower floors, however the maximum inter-story drift did not exceed the allowable limit. The other merits of the SBS remained true for all cases, where similar levels of reduction of the floor acceleration demand could be achieved with no yielding of the framing elements.

Finally, an integrated and comprehensive design procedure that can be adopted by the seismic design codes is developed. An equivalent lateral force pattern has been developed by back calculating the story shear based on the optimized SBS and the desired structural performance. This pattern explicitly accounts for the higher mode effects, the dynamic properties of the structure, the damping level provided by the supplemental viscous damping devices, and the site specific seismic hazard. Therefore, the proposed lateral force procedure is reliable in terms of prediction of structural performance and seismic demand on structural elements.

The integrated design methodology was used to design seven structures with different heights. The nonlinear response history analyses showed that the proposed procedure predicts with a good agreement the structural performance as well as the seismic demand on the structural elements. However, the procedure under estimates the seismic base shear on the low-rise buildings and over estimates it for the high-rise buildings. This error in the base shear prediction did not exceed 12% in general.

Recommendations for Future Study

The following topics are recommended for future work and further investigation:

- Experimental studies should be conducted on smart base isolation systems employing stiffness controllable devices, such as MRE base isolators, to verify the performance of the proposed control algorithms.

- The mechanical properties of the MRE base isolation devices should be improved so that higher shear stains could be accommodated and higher stiffening ratios could be achieved.

- In this study, the acceleration gain used with the AGC algorithm was assumed to be constant. However, considering time variant gain may lead to further improvement of the structural performance.

- The superstructure nonlinearities of the smart base isolated structure that may take place during severe seismic events should be investigated.

- A physical device capable of achieving the desired behavior of the SBS should be developed and experimentally tested.

- The applicability of the proposed SBS in retrofitting existing structures should be experimentally studied.

References

Agrawal, A. K. and Yang, J. N. Design of passive energy dissipation systems based on lqr control methods. *Journal of Intelligent Material Systems and Structures*, 10 (12):933–944, 1999.

Agrawal, A. K.; Yang, J. N., and He, W. L. Applications of some semiactive control systems to benchmark cable-stayed bridge. *Journal of Structural Engineering*, 129 (7):884–894, 2003.

ASCE, . *Minimum Design Loads for Buildings and Other Structures*. ASCE 7-10, 2010. Structural Engineering Institute, ASCE/SEI.

ATC-40, . Seismic evaluation and retrofit of concrete buildings. Technical report, Applied Technology Council, 1996.

Bani-Hani, Khaldoon A. and Sheban, Mashal A. Semi-active neuro-control for base-isolation system using magnetorheological (MR) dampers. *Earthquake Engineering & Structural Dynamics*, (35):1119–1144, 2006.

Barbat, A. H.; Rodellar, J.; Ryan, E. P., and Molinares, N. Active control of nonlinear base-isolated buildings. *Engineering Mechanics*, pages 676–684, 1995.

Behrooz, Majid; Wang, Xiaojie, and Gordaninejad, Faramarz. Modeling of a new semi-active/passive magnetorheological elastomer isolator. *Smart Materials And Structures*, 23, 2014a.

Behrooz, Majid; Wang, Xiaojie, and Gordaninejad, Faramarz. Performance of a new magnetorheological elastomer isolation system. *Smart Materials And Structures*, 23, 2014b.

Buckle, Ian G. New zealand seismic base isolation concepts and their application to nuclear engineering. *Nuclear Engineering and Design*, pages 313–326, 1985.

Buckle, Ian G. and Mayes, Ronald L. Seismic isolation: History, application, and performance - a world view. *Earthquake Spectra*, 6:161–201, 1990.

Carlson, J.D. and Spencer Jr., B.F. Magneto-rheological fluid dampers for semi-active seismic control. volume III, pages 35–40, Chiba, Japan, September 1996. 3rd International Conference on Motion and Vibration Control.

Chao, Shih-Ho and Goel, Subhash C. Performance-based seismic design of EBF using target drift and yield mechanism as performance criteria. Technical report, University of Michigan, 2005.

Chao, Shih-Ho and Goel, Subhash C. Performance-based plastic design of special truss moment frames. *Engineering Journal*, pages 127–150, 2008.

Chao, Shih-Ho; Goel, Subhash C., and Lee, Soon-Sik. A seismic design lateral force distribution based on inelastic state of structures. *Earthquake Spectra*, 23(3):547–569, August 2007. Earthquake Engineering Research Institute.

Chopra, Anil K. *Dynamics Of Structures, Theory and Applications to Earthquake Engineering.* Prentice Hall, 1995.

Chopra, Anil K. and Goel, Rakesh K. A modal pushover analysis procedure to estimate seismic demands for buildings: Theory and preliminary evaluation. Technical Report CMS-9812531, Pacific Earthquake Engineering Research Center (PEER), U.S.-Japan Cooperative Research in Urban Earthquake Disaster Mitigation, 2001a.

Chopra, Anil K. and Goel, Rakesh K. Modal pushover analysis of sac buildings. *Proceeding* SEAOC *Convention, San Diego, California*, 2001b.

Constantinou, Michael C.; Soong, Tsu T., and Dargush, Gary F. *Passive Energy Dissipation Systems For Structural Design and Retrofit.* Research Foundation of the State University of New York and the Multidisciplinary Center for Earthquake Engineering Research, 1998.

Cui, Shenlei; Bruneau, Michel, and Kasalanati, Amarnath. Behavior of bidirectional spring unit in isolated floor systems. *ASCE*, pages 944–952, 2010.

Davis, L. C. Model of magnetorheological elastomers. *Journal Of Applied Physics*, 85(6):3348–3351, 1999.

Dolce, Mauro and Marnetto, Roberto. Passive seismic devices based on shape memory alloys. Auckland, New Zealand, 2000. NZSEE.

Dyke, S.J.; Spencer Jr., B.F.; Quast, P.; Sain, M.K.; Kaspari Jr., D.C., and Soong, T.T. Experimental verification of acceleration feedback control strategies for an active tendon system. Technical Report NCEER-94-0024, National Center for Earthquake Engineering Research, Buffalo, New York, August 1994.

Dyke, S.J.; Spencer Jr., B.F.; Quast, P.; Sain, M.K.; Kaspari Jr., D.C., and Soong, T.T. Acceleration feedback control of MDOF structures. *Journal of Engineering Mechanics*, 122(9):907–918, 1996a.

Dyke, S.J.; Spencer Jr., B.F.; Sain, M.K., and Carlson, J.D. Experimental verification of semi-active structural control strategies using acceleration feedback. volume III,

pages 291–296, Chiba, Japan, 1996b. 3rd International Conference on Motion and Vibration Control.

Dyke, S.J.; Spencer Jr., B.F.; Sain, M.K., and Carlson, J.D. Modeling and control of magnetorheological dampers for seismic response reduction. *Smart Materials and Structures*, 5(5):565–575, 1996c.

Eem, S H; Jung, H J, and Koo, J H. Seismic performance evaluation of an MR elastomer-based smart base isolation system using real-time hybrid simulation. *Smart Materials And Structures*, 22, 2013.

FEMA, . NEHRP commentary on the guidelines for the seismic rehabilitation of buildings. Technical report, FEMA 274, 1997. Issued by FEMA in furtherance of the Decade for Natural Disaster Reduction.

FEMA, . State of the art report on systems performance of steel moment frames subject to earthquake ground shaking. Technical report, FEMA-355C, 2000. Prepared for the SAC Joint Venture Partnership by Helmut Krawinkler, Department of Civil Engineering, Stanford University.

FEMA, . Quantification of building seismic performance factors. Technical report, FEMA P695, 2009. prepared by Applied Technology Council for the Federal Emergency Management Agency, Washington, D.C.

Freeman, Sigmund A. Development and use of capacity spectrum method. Seattle, Washington, June 1998. 6th US NCEE Conference on Earthquake Engineering/EERI.

Ganjavi, B.; Amiri, J. Vaseghi; Amiri, G. Ghodrati, and Amrei, S.A. Razavian. Effect of seismic loading patterns on height-wise distribution of drifts, hysteretic energy and damage in reinforced concrete buildings. *Jornal of Applied Sciences*, 7(22): 3431–3441, 2007.

Gupta, Akshay and Krawinkler, Helmut. Seismic demands for performance evaluation of steel moment resisting frame structures. Report 132, Department of Civil and Environmental Engineering, Stanford University, 1999.

Gupta, Balram and Kunnath, Sashi K. Adaptive spectra-based pushover procedure for seismic evaluation of structures. *Earthquake Spectra*, 16(2):367–391, 2000.

Hall, John F.; Heaton, Thomas H.; Halling, Marvin W., and Wald, David J. Near-source ground motion and its effects on flexible buildings. *Earthquake Spectra*, 11: 569–605, 1995.

Hanson, R.D.; Xia, C., and Su, Y.-F. Design of supplementa steel damping devices for buildings. *Earthquake Engineering, 10th world conference*, 1992.

He, W.L.; Agrawal, A.K., and Yang, J.N. Novel semiactive friction controller for linear structures against earthquakes. *Journal of Structural Engineering*, 129(7): 941–950, 2003.

Ikhouane, Fayçal and Rodellar, José. *Systems with Hysteresis, Analysis, Identification and Control using the Bouc-Wen Model.* John Wiley & Sons, Ltd, 2007.

Inaudi, José A. and Kelly, James M. Hybrid isolation systems for equipment protection. *Earthquake Engineering & Structural Dynamics*, 22:297–313, 1993.

International Code Council, ICC. *Structural Seismic Design Manual.* 2006 IBC, 2006. Vol. 3 Building design examples for steel and concrete.

International Code Council, ICC. *Structural Seismic Design Manual.* 2012 IBC, 2012.

Jabbari, F.; Schmitendorf, W. E., and Yang, J. N. H_∞ control for seismic-excited buildings with acceleration feedback. *Journal of Engineering Mechanics*, 121(9): 994–1002, 1995.

Jabbari, Faryar and Bobrow, James E. Vibration suppression with resettable device. *Engineering Mechanics*, 128(9):919–924, September 2002.

Jalali, Abdolrahim; Cardone, Donatello, and Narjabadifam, Peyman. Smart restorable sliding base isolation system. *Bulletin of Earthquake Engineering*, pages 657–673, 2010.

Jangid, R. S. and Kelly, J. M. Base isolation for near-fault motions. *Earthquake Engineering & Structural Dynamics*, 30:691–707, 2001.

Jansen, Laura M. and Dyke, Shirley J. Semi-active control strategies for MR dampers: A comparative study. *Journal of Engineering Mechanics*, 126(8):795–803, 2000.

Johnson, Erik A.; Ramallo, Juan C.; Spencer, Jr., and Sain, Michael K. Intelligent base isolation systems. Kyoto, Japan, 1998. Second World Conference on Structural Control.

Jolly, Mark R.; Bender, Jonathan W., and Carlson, J. D. Properties and applications of commercial magnetorheological fluids. SPIE, 1998.

Jung, Hyung-Jo; Lee, Sung-Jin; Jang, Dong-Doo; Kin, In-Ho; Koo, Jeong-Hoi, and Khan, Fazeel. Dynamic characterization of magneto-rheological elastomers in shear mode. *IEEE Transactions On Magnetics*, 45(10):3930–3933, 2009.

Kelly, James M. The role of damping in seismic isolation. *Earthquake Engineering & Structural Dynamics*, pages 3–20, 1999.

Kelly, J.M.; Leitmann, G., and Soldatos, A.G. Robust control of base-isolated structures under earthquake excitation. *Journal of Optimization Theory and Applications*, 53(2):159–180, 1987.

Kim, Jinkoo; Choi, Hyunhoon, and Min, Kyung-Won. Performance-based design of added viscous dampers using capacity spectrum method. *Journal of Earthquake Engineering*, 7(1):1–24, 2003.

Kim, Jinkoo; Ryu, Jingook, and Chung, Lan. Seismic performance of structures connected by viscoelastic dampers. *Engineering Structures*, 28(2):183–195, 2006.

Kobori, Takuji; Takahashi, Motoichi; Nasu, Tadashi; Niwa, Naoki, and Ogasawara, Katsura. Seismic response controlled structure with active variable stiffness system. *Earthquake Engineering & Structural Dynamics*, 22(11):925–941, 1993.

Komodromos, Petros. *Seismic Isolation for Earthquake-Resistant Structures*. WIT Press, London, 2000.

Lavan, O.; Cimellaro, G. P., and Reinhorn, A. M. Noniterative optimization procedure for seismic weakening and damping of inelastic structures. *Journal of Structural Engineering*, 134(10):1638–1648, 2008.

Lee, Soon-Sik; Goel, Subhash C., and Chao, Shih-Ho. Performance-based seismic design of steel moment frames using target drift and yield mechanism. Vancouver, B.C., Canada, August 2004. 13th World Conference on Earthquake Engineering.

Li, Hui and Ou, Jinping. A design approach for semi-active and smart base-isolated buildings. *Struct. Control Health Monit.*, pages 660–681, 2006.

Li, Hui; Liu, Min, and Ou, Jinping. Negative stiffness characteristics of active and semi-active control systems for stay cables. *Structural Control and Health Monitoring*, 15(2):120–142, 2008.

Li, Yancheng; Li, Jianchun; Li, Weihua, and Samali, Bijan. Development and characterization of a magnetorheological elastomer based adaptive seismic isolator. *Smart Materials And Structures*, 22, 2013a.

Li, Yancheng; Li, Jianchun; Tian, Tongfei, and Li, Weihua. A highly adjustable magnetorheological elastomer base isolator for applications of real-time adaptive control. *Smart Materials And Structures*, 22, 2013b.

Madden, Glenn J.; Wongprasert, Nat, and Symans, Michael D. Analytical and numerical study of a smart sliding base isolation system for seismic protection of buildings. *Computer-Aided Civil and Infrastructure Engineering*, pages 19–30, 2003.

Makris, Nicos. Rigidity-plasticity-viscosity: Can electrorheological dampers protect base-isolated structures from near-source ground motions? *Earthquake Engineering & Structural Dynamics*, pages 571–591, 1997.

MATLAB, . *version 8.1.0.604 (R2013a)*. The MathWorks Inc., Natick, Massachusetts, 2013.

Mazza, Fabio and Vulcano, Alfonso. Base-isolation techniques for the seismic protection of rc framed structures subjected to near-fault ground motions. Vancouver, B.C., Canada, 2004. 13th World Conference on Earthquake Engineering.

Mohammadi, R. Karami; Naggar, M.H. El, and Moghaddam, H. Optimum strength distribution for seismic resistant shear buildings. *International Journal of Solids and Structures*, 41:6597–6612, 2004.

Morishita, Shin and Ura, Tamaki. Er fluid applications to vibration control devices and an adaptive neural-net controller. *Journal Of Intelligent Material Systems and Structures*, pages 366–372, 1993.

Naeim, Farzad and Kelly, James M. *Design of Seismic Isolated Structures: From Theory to Practice.* John Wiley & Sons, Canada, 1999.

Nagarajaiah, S. and Mate, D. Semi-active control of continuously variable stiffness system. *Proceedings Second World Conference on Structural Control, vol. 1, Kyoto, Japan*, pages 397–406, July 1998.

Nagarajaiah, Satish and Sahasrabudhe, Sanjay. Seismic response control of smart sliding isolated buildings using variable stiffness systems: an experimental and numerical study. *Earthquake Engineering & Structural Dynamics*, 35(2):177–197, 2006.

Nagarajaiah, Satish; Riley, Michael A., and Reinhorn, Andrei. Control of sliding-isolated bridge with absolute acceleration feedback. *Journal of Engineering Mechanics*, 119(11):2317–2332, 1993.

Nagarajaiah, Satish; Mao, Yuqing, and Saharabudhe, Sanjay. Nonlinear sesmic response spectra of smart sliding isolated structures with independently variable MR dampers and variable stiffness saivs system. *Structural Engineering and Mechanics*, 24(3):375–393, 2006.

Narasimhan, S. and Nagarajaiah, S. Smart base isolated buildings with variable friction systems: H_∞ controller and SAIVF device. *Earthquake Engineering & Structural Dynamics*, 35(8):921–942, 2006.

Narasimhan, Sriram and Nagarajaiah, Satish. A STFT semiactive controller for base isolated buildings with variable stiffness isolation systems. *Engineering Structures*, 27(4):514–523, 2005.

Nasu, Tadashi; Kobori, Takuji; Takahashi, Motoichi; Niwa, Naoki, and Ogasawara, Katsura. Active variable stiffness system with non-resonant control. *Earthquake Engineering & Structural Dynamics*, 30(11):1597–1614, 2001.

NEHRP, . NEHRP *Recommended Provisions for Seismic Regulations for New Buildings and Other Structures*, 2003. Building Seismic Safety Council, BSSC (FEMA 450-1).

Otsuka, K. and Wayman, C.M. *Shape Memory Materials*. Cambridge University Press, 1998.

Park, Kyungha. *Lateral Load Pattern For The Conceptaul Seismic Design of Moment-Resisting Frame Structures*. PhD thesis, University of Maryland, College Park, 2007.

Park, Kyungha and Medina, Ricardo A. Conceptual seismic design of regular frames based on the concept of uniform damage. *Journal of Structural Engineering*, 133 (7):945–955, July 2007.

Pekcan, Gokhan; Mander, John B., and Chen, Stuart S. Fundamental considerations for the design of non-linear viscous dampers. *Earthquake Engineering & Structural Dynamics*, 28(11):1405–1425, 1999.

Providakis, C.P. Effect of LRB isolators and supplemental viscous dampers on seismic isolated buildings under near-fault excitations. *Engineering Structures*, (30):1187–1198, 2008.

Ramallo, J. C.; Johnson, E. A., and Spencer Jr., B.F. "smart" base isolation systems. *Engineering Mechanics*, 128(10):1088–1100, 2002.

Reinhorn, Andrei M.; Viti, Stefania, and Cimellaro, GianPaolo. Retrofit of structures: Strength reduction with damping enhancement. In 37th *Technical Panel Meeting on Wind and Seismic Effects*, Tsukuba, Japan, 2005.

Roszkowski, A.; Bogdan, M.; Skoczynski, W., and Marek, B. Testing of vicosity of mr fluid in magnetic field. *Measurement Science Review*, pages 58–60, 2008.

Sadek, Fahim and Mohraz, Bijan. Semiactive control algorithms for structures with variable dampers. *Journal of Engineering Mechanics*, 124(9):981–990, 1998.

Sahasrabudhe, Sanjay and Nagarajaiah, Satish. Effectiveness of variable stiffness systems in base-isolated bridges subjected to near-fault earthquakes: An experimental and analytical study. *Intelligent Material Systems and Structures*, 16(9):743–756, 2005a.

Sahasrabudhe, Sanjay S. and Nagarajaiah, Satish. Semi-active control of sliding isolated bridges using MR dampers: an experimental and numerical study. *Earthquake Engineering & Structural Dynamics*, 34:965–983, 2005b.

SAP2000, . *Linear and Nonlinear Static and Dynamic Analysis and Design of Three-Dimensional Structures*. Computer and Structures, Inc., Berkeley, California, USA, 2011.

Schmitendorf, W. E.; Jabbari, Faryar, and Yang, J.N. Robust control techniques for buildings under earthquake excitation. *Earthquake Engineering & Structural Dynamics*, 23(5):539–552, 1994.

Shome, Nilesh; Cornell, C. Allin; Bazzurro, Paolo, and Carballo, J. Eduard. Earthquake records and nonlinear MDOF responses. Report RMS-29, Dep. of Civil Engineering, Stanford University, 1997.

Soong, T.T. *Active Structural Control: Theory and Practice.* John Wiley & Sons, 1990.

Soong, T.T. and Spencer Jr., B.F. Supplemental energy dissipation: state-of-the-art and state-of-the-practice. *Engineering Structures*, 24(3):243–259, 2002.

Spencer Jr., B.F.; Sain, M.K.; Won, C.-H.; Kaspari, D.C., and Sain, P.M. Reliability-based measures of structural control robustness. *Structural Safety*, 15:111–129, 1994.

Symans, Michael D; Madden, Glenn J, and Wongprasert, Nat. Experimental study of an adaptive base isolation system for buildings. Auckland, New Zealand, 2000. NZSEE.

Takewaki, Izuru. An approach to stiness-damping simultaneous optimization. *Computer methods in applied mechanics and engineering*, 189:641–650, 2000.

Thai, Khiem; Jabbari, Faryar, and Bobrow, James E. Structural control via semi-active and hybrid control. Albuquerque, New Mexico, 1997. Proceedings of the American Control Conference.

Tsai, Chong-Shien. *Advanced Base Isolation Systems for Light Weight Equipments*, chapter Earthquake-Resistant Structures - Design, Assessment and Rehabilitation, pages 79–130. ISBN 978-953-51-0123-9, InTech, Taiwan, 2012.

Tsai, Keh-Chyuan; Chen, Huan-Wei; Hong, Ching-Ping, and Su, Yung-Feng. Design of steel triangular plate energy absorbers for seismic-resistant construction. *Earthquake Spectra*, 9(3):505–528, 1993.

Usman, M; Sung, S H; Jang, D D; Jung, H J, and Koo, J H. Numerical investigation of smart base isolation system employing MR elastomer. In 11th *Conference on Electrorheological Fluids and Magnetorheological Suspensions*. IOPscience, 2009.

Viti, Stefania; Cimellaro, Gian Paolo, and Reinhorn, Andrei M. Retrofit of a hospital through strength reduction and enhanced damping. *Smart Structures and Systems*, 2(4):339–355, 2006.

Wilde, Krzysztof; Gardoni, Paolo, and Fujino, Yozo. Base isolation system with shape memory alloy device for elevated highway bridges. *Engineering Structures*, pages 222–229, 2000.

Winslow, W. M. Method and means for translating electrical impulses into mechanical force. 1947. U.S. Patent No. 2417850.

Winslow, W. M. Induced fibration of suspensions. *Journal of applied physics*, pages 1137–1140, 1949.

Winthrop, M.F.; Baker, W.P., and Cobb, R.G. A variable stiffness device selection and design tool for lightly damped structures. *Journal of Sound and Vibration*, 287 (4-5):667–682, 2005.

Yang, Chuang-Sheng Walter; DesRoches, Reginald, and Leon, Roberto T. Design and analysis of braced frames with shape memory alloy and energy-absorbing hybrid devices. *Engineering Structures*, 32(2):498–507, 2010.

Yang, G.; Spencer Jr., B.F.; Carlson, J.D., and Sain, M.K. Large-scale MR fluid dampers: modeling and dynamic performance considerations. *Engineering Structures*, 24:309–323, 2002.

Yang, Jann N. and Agrawal, Anil K. Semi-active hybrid control systems for nonlinear buildings against near-field earthquakes. *Engineering Structures*, 24(3):271–280, 2002.

Yang, Jann N. and Anil K. KimAgrawal, Jin-Hoon. A semi-active stiffness damper for vibration control of civil engineering structures. 17th Int. Modal Analysis Conf. (IMAC XVII), 1999. Society for Experimental Mechanics, Kissimmee, Fla., Feb. 8-11, 437-443.

Yang, Jann N.; Kim, Jin-H, and Agrawal, Anil K. Resetting semiactive stiffness damper for seismic response control. *Journal of Structural Engineering*, 126(12): 1427–1433, 2000.

Yang, Jian; Du, Haiping; Li, Weihua; Li, Yancheng; Li, Jianchun; Sun, Shuaishuai, and Deng, H X. Experimental study and modeling of a novel magnetorheological elastomer isolator. *Smart Materials And Structures*, 22, 2013.

Yang, J.N.; Wu, J.C., and Li, Z. Control of seismic-excited buildings using active variable stiffness systems. *Engineering Structures*, 18(8):589–596, 1996.

Yoshioka, H.; Ramallo, J. C., and Spencer Jr., B. F. "smart" base isolation strategies employing magnetorheological dampers. *Journal of Engineering Mechanics*, 128 (5):540–551, 2002.

Appendix A

Redesigned Benchmark Buildings

The dynamic properties and structural member sizes of the 3, 9 and 20-story re-designed SAC benchmark buildings discussed in Chapters 4 and 5 are summarized is this appendix. The design of the SBS and BRBF frames were based on the average demands determined according to the response history analyses. The design summary of the 3-story buildings is shown in Tables A.1 and A.2, while the dynamic properties are shown in Table A.7. The design summary of the 9-story buildings is shown in Tables A.3 and A.4, while the dynamic properties are shown in Table A.8. The design summary of the 20-story buildings is shown in Tables A.5 and A.6, while the dynamic properties of this building are shown in Table A.9. The dynamic properties summarized herein include the modal periods (T) and the mass participation factors (MPF) for the pre-stiffening and post-stiffening cases of the SBS buildings as well as for the elastic state of the BRBF buildings.

Table A.1: Summary of the SBS 3-story building (units kips, sec., in).

| Story | Floor | Braced Bay | | Outside Braced Bay | | SBS Properties | | | |
No.	No.	Column	Girder	Column	Collector	Δ_1^x/h_x	k_1^x	α_x	c_x
1	2	W 14 X 176	W 21 X 55	W 14 X 176	W 21 X 44	0.5%	91.1	1.9	4.25
2	3	W 14 X 176	W 21 X 55	W 14 X 176	W 21 X 44	0.5%	81.1	1.6	4.25
3	Roof	W 14 X 176	W 21 X 44	W 14 X 176	W 21 X 44	0.5%	53.7	1.7	4.25

Table A.2: Summary of the BRBF 3-story building.

Story No.	Floor No.	Braced Bay Column	Braced Bay Girder	Outside Braced Bay Column	Outside Braced Bay Collector	Floor Brace A_{sc} (in^2)
1	2	W 14 X 311	W 21 X 83	W 14 X 311	W 21 X 44	4.41
2	3	W 14 X 311	W 21 X 68	W 14 X 311	W 21 X 44	3.71
3	Roof	W 14 X 311	W 18 X 65	W 14 X 311	W 21 X 44	2.29

Table A.3: Summary of the SBS 9-story building (units kips, sec., in).

Story No.	Floor No.	Braced Bay Column	Braced Bay Girder	Outside Braced Bay Column	Outside Braced Bay Collector	SBS Properties Δ_1^x/h_x	k_1^x	α_x	c_x
1	2	W 14 X 233	W 24 X 62	W 14 X 132	W 24 X 62	0.5%	96.7	2.1	13
2	3	W 14 X 211	W 24 X 62	W 14 X 132	W 24 X 62	0.5%	95.6	2.0	13
3	4	W 14 X 211	W 24 X 62	W 14 X 132	W 24 X 62	0.5%	93.9	1.8	13
4	5	W 14 X 193	W 24 X 62	W 14 X 132	W 24 X 62	0.5%	90.5	1.8	13
5	6	W 14 X 193	W 24 X 62	W 14 X 132	W 24 X 62	0.5%	84.9	1.7	13
6	7	W 14 X 145	W 24 X 62	W 14 X 132	W 24 X 62	0.5%	76.4	1.7	13
7	8	W 14 X 145	W 24 X 62	W 14 X 132	W 24 X 62	0.5%	64.4	1.7	13
8	9	W 14 X 132	W 24 X 62	W 14 X 132	W 24 X 62	0.5%	48.4	1.8	13
9	Roof	W 14 X 132	W 24 X 62	W 14 X 132	W 24 X 62	0.5%	27.8	2.3	13

Table A.4: Summary of the BRBF 9-story building.

Story No.	Floor No.	Braced Bay Column	Braced Bay Girder	Outside Braced Bay Column	Outside Braced Bay Collector	Floor Brace A_{sc} (in^2)
1	2	W 14 X 500	W 24 X 94	W 14 X 311	W 21 X 44	8.24
2	3	W 14 X 500	W 24 X 84	W 14 X 145	W 21 X 44	6.85
3	4	W 14 X 311	W 24 X 84	W 14 X 145	W 21 X 44	6.60
4	5	W 14 X 311	W 24 X 84	W 14 X 145	W 21 X 44	6.20
5	6	W 14 X 257	W 24 X 76	W 14 X 145	W 21 X 44	5.65
6	7	W 14 X 257	W 24 X 76	W 14 X 145	W 21 X 44	4.92
7	8	W 14 X 211	W 21 X 73	W 14 X 145	W 21 X 44	4.01
8	9	W 14 X 211	W 21 X 68	W 14 X 145	W 21 X 44	2.91
9	Roof	W 14 X 193	W 21 X 57	W 14 X 145	W 21 X 44	1.62

Table A.5: Summary of the SBS 20-story building (units kips, sec., in).

Story	Floor	Braced Bay		Outside Braced Bay		SBS Properties			
No.	No.	Column	Girder	Column	Collector	Δ_1^x/h_x	k_1^x	α_x	c_x
1	2	W 14 X 455	W 21 X 50	W 14 X 132	W 21 X 44	0.35%	842.1	2.3	300
2	3	W 14 X 455	W 21 X 50	W 14 X 132	W 21 X 44	0.35%	739.3	2.2	300
3	4	W 14 X 398	W 18 X 46	W 14 X 132	W 21 X 44	0.35%	737.9	2.1	300
4	5	W 14 X 398	W 18 X 46	W 14 X 132	W 21 X 44	0.35%	735.1	2.1	300
5	6	W 14 X 342	W 18 X 46	W 14 X 132	W 21 X 44	0.35%	730.5	2.0	300
6	7	W 14 X 342	W 18 X 46	W 14 X 132	W 21 X 44	0.35%	723.5	1.9	300
7	8	W 14 X 311	W 18 X 46	W 14 X 132	W 21 X 44	0.35%	713.6	1.9	300
8	9	W 14 X 311	W 18 X 46	W 14 X 132	W 21 X 44	0.35%	700.4	1.8	300
9	10	W 14 X 257	W 18 X 46	W 14 X 132	W 21 X 44	0.35%	683.4	1.8	300
10	11	W 14 X 257	W 18 X 46	W 14 X 132	W 21 X 44	0.35%	662.1	1.8	300
11	12	W 14 X 211	W 18 X 46	W 14 X 132	W 21 X 44	0.35%	636.1	1.7	300
12	13	W 14 X 211	W 18 X 46	W 14 X 132	W 21 X 44	0.35%	604.7	1.7	300
13	14	W 14 X 145	W 18 X 46	W 14 X 132	W 21 X 44	0.35%	567.7	1.7	300
14	15	W 14 X 145	W 18 X 46	W 14 X 132	W 21 X 44	0.35%	524.3	1.7	300
15	16	W 14 X 132	W 18 X 46	W 14 X 132	W 21 X 44	0.35%	474.3	1.8	300
16	17	W 14 X 132	W 18 X 46	W 14 X 132	W 21 X 44	0.35%	417.1	1.8	300
17	18	W 14 X 132	W 18 X 46	W 14 X 132	W 21 X 44	0.35%	352.2	2.0	300
18	19	W 14 X 132	W 18 X 46	W 14 X 132	W 21 X 44	0.35%	279.1	2.1	300
19	20	W 14 X 132	W 18 X 46	W 14 X 132	W 21 X 44	0.35%	197.4	2.5	300
20	Roof	W 14 X 132	W 18 X 46	W 14 X 132	W 21 X 44	0.35%	106.6	3.1	300

Table A.6: Summary of the BRBF 20-story building.

Story	Floor	Braced Bay		Outside Braced Bay		Floor Brace
No.	No.	Column	Girder	Column	Collector	A_{sc} (in^2)
1	2	W 14 X 665	W 27 X 114	W 14 X 132	W 21 X 44	18.46
2	3	W 14 X 665	W 27 X 114	W 14 X 132	W 21 X 44	11.70
3	4	W 14 X 550	W 24 X 94	W 14 X 132	W 21 X 44	11.68
4	5	W 14 X 550	W 24 X 94	W 14 X 132	W 21 X 44	11.64
5	6	W 14 X 398	W 24 X 94	W 14 X 132	W 21 X 44	11.56
6	7	W 14 X 398	W 24 X 94	W 14 X 132	W 21 X 44	11.45
7	8	W 14 X 370	W 24 X 94	W 14 X 132	W 21 X 44	11.29
8	9	W 14 X 370	W 24 X 94	W 14 X 132	W 21 X 44	11.08
9	10	W 14 X 370	W 24 X 94	W 14 X 132	W 21 X 44	10.81
10	11	W 14 X 370	W 24 X 94	W 14 X 132	W 21 X 44	10.47
11	12	W 14 X 342	W 21 X 83	W 14 X 132	W 21 X 44	10.06
12	13	W 14 X 342	W 21 X 83	W 14 X 132	W 21 X 44	9.56
13	14	W 14 X 311	W 18 X 76	W 14 X 132	W 21 X 44	8.96
14	15	W 14 X 311	W 18 X 76	W 14 X 132	W 21 X 44	8.27
15	16	W 14 X 257	W 18 X 71	W 14 X 132	W 21 X 44	7.47
16	17	W 14 X 257	W 18 X 71	W 14 X 132	W 21 X 44	6.56
17	18	W 14 X 233	W 18 X 60	W 14 X 132	W 21 X 44	5.52
18	19	W 14 X 233	W 18 X 60	W 14 X 132	W 21 X 44	4.36
19	20	W 14 X 193	W 18 X 46	W 14 X 132	W 21 X 44	3.05
20	Roof	W 14 X 193	W 18 X 46	W 14 X 132	W 21 X 44	1.60

Table A.7: Dynamic properties of the 3-story buildings.

Mode No.	SBS Pre-Stiffening		SBS Post-Stiffening		BRBF	
	T (sec)	MPF	T (sec)	MPF	T (sec)	MPF
1	1.79	0.867	1.44	0.858	0.69	0.838
2	0.56	0.115	0.48	0.121	0.24	0.126
3	0.25	0.018	0.23	0.021	0.13	0.036

Table A.8: Dynamic properties of the 9-story buildings.

Mode No.	SBS Pre-Stiffening		SBS Post-Stiffening		BRBF	
	T (sec)	MPF	T (sec)	MPF	T (sec)	MPF
1	4.95	0.829	3.93	0.811	1.86	0.768
2	1.83	0.110	1.44	0.123	0.70	0.144
3	1.03	0.037	0.83	0.039	0.41	0.045
4	0.66	0.014	0.56	0.016	0.29	0.021

Table A.9: Dynamic properties of the 20-story buildings.

Mode No.	SBS Pre-Stiffening		SBS Post-Stiffening		BRBF	
	T (sec)	MPF	T (sec)	MPF	T (sec)	MPF
1	5.83	0.665	5.43	0.636	5.36	0.639
2	1.77	0.213	1.48	0.220	1.28	0.216
3	0.93	0.060	0.75	0.071	0.64	0.068
4	0.64	0.025	0.50	0.030	0.43	0.031
5	0.48	0.013	0.38	0.015	0.32	0.017
6	0.38	0.008	0.30	0.009	0.25	0.010

Appendix B

Summary of the Building's Structural Elements

The summary of the structural member sizes designed according to the integrated design procedure, as discussed in Chapter 6, is given in Tables B.1 through B.7.

Table B.1: Summary of the 3-story building design (units kips, sec., in).

Story	Floor	Braced Bay		Outside Braced Bay		SBS Properties			
No.	No.	Column	Girder	Column	Collector	Δ_1^x/h_x	k_1^x	α_x	c_x
1	2	W 12 X 96	W 18 X 60	W 12 X 96	W 18 X 50	0.5 %	77.6	2.4	4.25
2	3	W 12 X 96	W 18 X 60	W 12 X 96	W 18 X 50	0.5 %	60.3	2.4	4.25
3	Roof	W 12 X 96	W 18 X 50	W 12 X 96	W 18 X 50	0.5 %	43.8	2.4	4.25

Table B.2: Summary of the 5-story building design (units kips, sec., in).

Story	Floor	Braced Bay		Outside Braced Bay		SBS Properties			
No.	No.	Column	Girder	Column	Collector	Δ_1^x/h_x	k_1^x	α_x	c_x
1	2	W 12 X 152	W 21 X 93	W 12 X 96	W 18 X 50	0.5 %	81.8	2.4	7.0
2	3	W 12 X 152	W 21 X 83	W 12 X 96	W 18 X 50	0.5 %	72.5	2.3	7.0
3	4	W 12 X 96	W 21 X 73	W 12 X 96	W 18 X 50	0.5 %	63.1	2.3	7.0
4	5	W 12 X 96	W 21 X 62	W 12 X 96	W 18 X 50	0.5 %	49.0	2.4	7.0
5	Roof	W 12 X 96	W 21 X 55	W 12 X 96	W 18 X 50	0.5 %	34.6	2.3	7.0

Table B.3: Summary of the 7-story building design (units kips, sec., in).

Story	Floor	Braced Bay		Outside Braced Bay		SBS Properties			
No.	No.	Column	Girder	Column	Collector	Δ_1^x/h_x	k_1^x	α_x	c_x
1	2	W 14 X 211	W 21 X 68	W 12 X 96	W 18 X 50	0.5 %	86.3	2.4	10.75
2	3	W 14 X 176	W 21 X 68	W 12 X 96	W 18 X 50	0.5 %	77.9	2.4	10.75
3	4	W 14 X 176	W 21 X 68	W 12 X 96	W 18 X 50	0.5 %	71.9	2.3	10.75
4	5	W 12 X 106	W 21 X 68	W 12 X 96	W 18 X 50	0.5 %	63.5	2.4	10.75
5	6	W 12 X 106	W 21 X 68	W 12 X 96	W 18 X 50	0.5 %	55.4	2.3	10.75
6	7	W 12 X 96	W 21 X 62	W 12 X 96	W 18 X 50	0.5 %	42.8	2.3	10.75
7	Roof	W 12 X 96	W 21 X 50	W 12 X 96	W 18 X 50	0.5 %	31.4	2.3	10.75

Table B.4: Summary of the 9-story building design (units kips, sec., in).

Story	Floor	Braced Bay		Outside Braced Bay		SBS Properties			
No.	No.	Column	Girder	Column	Collector	Δ_1^x/h_x	k_1^x	α_x	c_x
1	2	W 14 X 311	W 21 X 83	W 12 X 96	W 18 X 50	0.5 %	88.7	2.4	12.25
2	3	W 14 X 233	W 18 X 76	W 12 X 96	W 18 X 50	0.5 %	81.4	2.4	12.25
3	4	W 14 X 233	W 18 X 76	W 12 X 96	W 18 X 50	0.5 %	77.0	2.3	12.25
4	5	W 14 X 159	W 21 X 68	W 12 X 96	W 18 X 50	0.5 %	71.3	2.3	12.25
5	6	W 14 X 159	W 21 X 68	W 12 X 96	W 18 X 50	0.5 %	64.1	2.4	12.25
6	7	W 12 X 106	W 21 X 68	W 12 X 96	W 18 X 50	0.5 %	57.7	2.3	12.25
7	8	W 12 X 106	W 18 X 65	W 12 X 96	W 18 X 50	0.5 %	50.5	2.3	12.25
8	9	W 12 X 96	W 18 X 65	W 12 X 96	W 18 X 50	0.5 %	39.6	2.3	12.25
9	Roof	W 12 X 96	W 18 X 60	W 12 X 96	W 18 X 50	0.5 %	28.2	2.4	12.25

Table B.5: Summary of the 12-story building design (units kips, sec., in).

Story	Floor	Braced Bay		Outside Braced Bay		SBS Properties			
No.	No.	Column	Girder	Column	Collector	Δ_1^x/h_x	k_1^x	α_x	c_x
1	2	W 14 X 455	W 21 X 83	W 12 X 96	W 18 X 50	0.5 %	91.0	2.4	18
2	3	W 14 X 398	W 21 X 83	W 12 X 96	W 18 X 50	0.5 %	88.0	2.4	18
3	4	W 14 X 398	W 21 X 83	W 12 X 96	W 18 X 50	0.5 %	80.6	2.4	18
4	5	W 14 X 311	W 21 X 83	W 12 X 96	W 18 X 50	0.5 %	76.4	2.4	18
5	6	W 14 X 311	W 21 X 83	W 12 X 96	W 18 X 50	0.5 %	74.2	2.3	18
6	7	W 14 X 233	W 21 X 83	W 12 X 96	W 18 X 50	0.5 %	68.5	2.3	18
7	8	W 14 X 233	W 21 X 83	W 12 X 96	W 18 X 50	0.5 %	64.2	2.3	18
8	9	W 14 X 145	W 21 X 83	W 12 X 96	W 18 X 50	0.5 %	58.4	2.3	18
9	10	W 14 X 145	W 21 X 83	W 12 X 96	W 18 X 50	0.5 %	51.2	2.3	18
10	11	W 14 X 132	W 21 X 68	W 12 X 96	W 18 X 50	0.5 %	43.7	2.3	18
11	12	W 14 X 132	W 21 X 62	W 12 X 96	W 18 X 50	0.5 %	34.4	2.3	18
12	Roof	W 14 X 132	W 21 X 50	W 12 X 96	W 18 X 50	0.5 %	25.7	2.3	18

Table B.6: Summary of the 15-story building design (units kips, sec., in).

Story No.	Floor No.	Braced Bay Column	Braced Bay Girder	Outside Braced Bay Column	Outside Braced Bay Collector	Δ_1^x/h_x	k_1^x	α_x	c_x
1	2	W 14 X 500	W 24 X 94	W 12 X 96	W 18 X 50	0.5 %	161.4	2.5	32
2	3	W 14 X 455	W 24 X 94	W 12 X 96	W 18 X 50	0.5 %	154.6	2.5	32
3	4	W 14 X 455	W 24 X 94	W 12 X 96	W 18 X 50	0.5 %	148.1	2.5	32
4	5	W 14 X 370	W 24 X 94	W 12 X 96	W 18 X 50	0.5 %	142.1	2.5	32
5	6	W 14 X 370	W 24 X 94	W 12 X 96	W 18 X 50	0.5 %	134.6	2.5	32
6	7	W 14 X 283	W 24 X 94	W 12 X 96	W 18 X 50	0.5 %	127.1	2.5	32
7	8	W 14 X 283	W 21 X 93	W 12 X 96	W 18 X 50	0.5 %	122.4	2.5	32
8	9	W 14 X 211	W 21 X 93	W 12 X 96	W 18 X 50	0.5 %	113.0	2.5	32
9	10	W 14 X 211	W 21 X 83	W 12 X 96	W 18 X 50	0.5 %	105.5	2.6	32
10	11	W 14 X 145	W 21 X 83	W 12 X 96	W 18 X 50	0.5 %	97.2	2.6	32
11	12	W 14 X 145	W 21 X 73	W 12 X 96	W 18 X 50	0.5 %	90.6	2.5	32
12	13	W 12 X 96	W 21 X 73	W 12 X 96	W 18 X 50	0.5 %	80.7	2.5	32
13	14	W 12 X 96	W 21 X 68	W 12 X 96	W 18 X 50	0.5 %	68.3	2.5	32
14	15	W 12 X 96	W 21 X 68	W 12 X 96	W 18 X 50	0.5 %	54.8	2.5	32
15	Roof	W 12 X 96	W 21 X 57	W 12 X 96	W 18 X 50	0.5 %	38.7	2.5	32

Table B.7: Summary of the 20-story building design (units kips, sec., in).

Story No.	Floor No.	Braced Bay Column	Braced Bay Girder	Outside Braced Bay Column	Outside Braced Bay Collector	Δ_1^x/h_x	k_1^x	α_x	c_x
1	2	W 14 X 730	W 21 X 68	W 12 X 96	W 18 X 46	0.35 %	330.3	2.7	65
2	3	W 14 X 730	W 21 X 68	W 12 X 96	W 18 X 46	0.35 %	289.0	2.6	65
3	4	W 14 X 605	W 21 X 68	W 12 X 96	W 18 X 46	0.35 %	278.3	2.6	65
4	5	W 14 X 605	W 21 X 68	W 12 X 96	W 18 X 46	0.35 %	267.2	2.7	65
5	6	W 14 X 500	W 21 X 68	W 12 X 96	W 18 X 46	0.35 %	257.3	2.7	65
6	7	W 14 X 500	W 21 X 68	W 12 X 96	W 18 X 46	0.35 %	253.0	2.7	65
7	8	W 14 X 426	W 21 X 68	W 12 X 96	W 18 X 46	0.35 %	247.3	2.6	65
8	9	W 14 X 426	W 21 X 68	W 12 X 96	W 18 X 46	0.35 %	235.3	2.7	65
9	10	W 14 X 342	W 21 X 68	W 12 X 96	W 18 X 46	0.35 %	229.6	2.6	65
10	11	W 14 X 342	W 18 X 65	W 12 X 96	W 18 X 46	0.35 %	213.5	2.7	65
11	12	W 14 X 257	W 18 X 65	W 12 X 96	W 18 X 46	0.35 %	204.9	2.7	65
12	13	W 14 X 257	W 18 X 65	W 12 X 96	W 18 X 46	0.35 %	194.8	2.7	65
13	14	W 14 X 193	W 18 X 60	W 12 X 96	W 18 X 46	0.35 %	182.8	2.7	65
14	15	W 14 X 193	W 18 X 60	W 12 X 96	W 18 X 46	0.35 %	169.1	2.7	65
15	16	W 14 X 132	W 18 X 55	W 12 X 96	W 18 X 46	0.35 %	159.3	2.6	65
16	17	W 14 X 132	W 18 X 50	W 12 X 96	W 18 X 46	0.35 %	141.3	2.7	65
17	18	W 12 X 96	W 18 X 50	W 12 X 96	W 18 X 46	0.35 %	128.0	2.6	65
18	19	W 12 X 96	W 18 X 46	W 12 X 96	W 18 X 46	0.35 %	109.1	2.7	65
19	20	W 12 X 96	W 18 X 46	W 12 X 96	W 18 X 46	0.35 %	88.1	2.6	65
20	Roof	W 12 X 96	W 18 X 46	W 12 X 96	W 18 X 46	0.35 %	59.3	2.7	65

Appendix C

Dynamic Properties of the Analyzed Structures

The dynamics properties of the structures analyzed in Chapter 6 are listed in Tables C.1 through C.7. This includes the modal periods (T) and the mass participation factors (MPF) for the pre-stiffening and post-stiffening cases.

Table C.1: Dynamic properties of the 3-story building.

Mode No.	Pre-Stiffening		Post-Stiffening	
	T (sec)	MPF	T (sec)	MPF
1	1.98	0.86	1.40	0.86
2	0.68	0.12	0.51	0.12
3	0.35	0.02	0.28	0.02

Table C.2: Dynamic properties of the 5-story building.

Mode	Pre-Stiffening		Post-Stiffening	
No.	T (sec)	MPF	T (sec)	MPF
1	3.27	0.857	2.24	0.852
2	1.19	0.107	0.87	0.110
3	0.64	0.027	0.50	0.029
4	0.41	0.007	0.33	0.008
5	0.29	0.002	0.25	0.002

Table C.3: Dynamic properties of the 7-story building.

Mode	Pre-Stiffening		Post-Stiffening	
No.	T (sec)	MPF	T (sec)	MPF
1	4.33	0.834	3.10	0.825
2	1.59	0.112	1.16	0.118
3	0.89	0.035	0.67	0.036
4	0.57	0.013	0.46	0.014

Table C.4: Dynamic properties of the 9-story building.

Mode	Pre-Stiffening		Post-Stiffening	
No.	T (sec)	MPF	T (sec)	MPF
1	5.40	0.818	3.90	0.807
2	1.99	0.115	1.45	0.123
3	1.15	0.038	0.85	0.039
4	0.76	0.016	0.59	0.017

Table C.5: Dynamic properties of the 12-story building.

Mode	Pre-Stiffening		Post-Stiffening	
No.	T (sec)	MPF	T (sec)	MPF
1	7.00	0.805	5.07	0.792
2	2.58	0.116	1.88	0.126
3	1.48	0.040	1.10	0.041
4	0.98	0.018	0.76	0.019
5	0.70	0.010	0.56	0.010

Table C.6: Dynamic properties of the 15-story building.

Mode	Pre-Stiffening		Post-Stiffening	
No.	T (sec)	MPF	T (sec)	MPF
1	6.76	0.779	5.07	0.761
2	2.50	0.130	1.85	0.145
3	1.47	0.042	1.07	0.044
4	1.03	0.020	0.76	0.020
5	0.77	0.011	0.58	0.011
6	0.61	0.007	0.47	0.007

**Table C.7:** Dynamic properties of the 20-story building.

Mode	Pre-Stiffening		Post-Stiffening	
No.	T (sec)	MPF	T (sec)	MPF
1	6.80	0.731	5.45	0.693
2	2.43	0.162	1.84	0.191
3	1.37	0.047	1.00	0.054
4	0.95	0.022	0.69	0.023
5	0.72	0.012	0.53	0.013
6	0.57	0.008	0.42	0.008

Appendix D

Residual Drift, Inter-Story Shear, and O.T.M. of the Benchmark Buildings

The residual inter-story drift of the benchmark buildings discussed in Chapters 4 and 5 under the design earthquake and the maximum considered earthquake records is shown in Figures D.1 through D.6. The median peak inter-story shear on these buildings is shown in Figures D.7 through D.12. It should be noticed that the base shear on the SBS equipped buildings may, in some cases, appear to be greater than that induced on the BRBF. This is because the total effective damping for the SBS buildings was set to 10%. While the hysteretic damping of the BRBF is higher than that. For instance, the effective damping of the 3-story BRBF building is 26%. Therefore, it is expected that the base shear and the overturning moment be higher for the SBS buildings. It should also be mentioned that the 3-story BRBF approached near collapse under earthquake records LA27 and LA28, accordingly, their results were eliminated from the statistical summary. However, the SBS building successfully sustained all the considered ground motions. The median peak overturning moment on these buildings is shown in Figures D.13 through D.18.
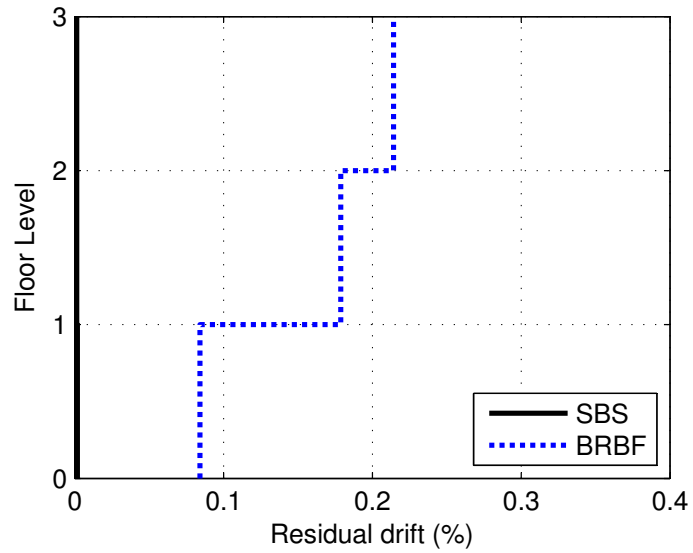
Figure D.1: Residual inter-story drift on the 3-story building under the (10/50) ground motions
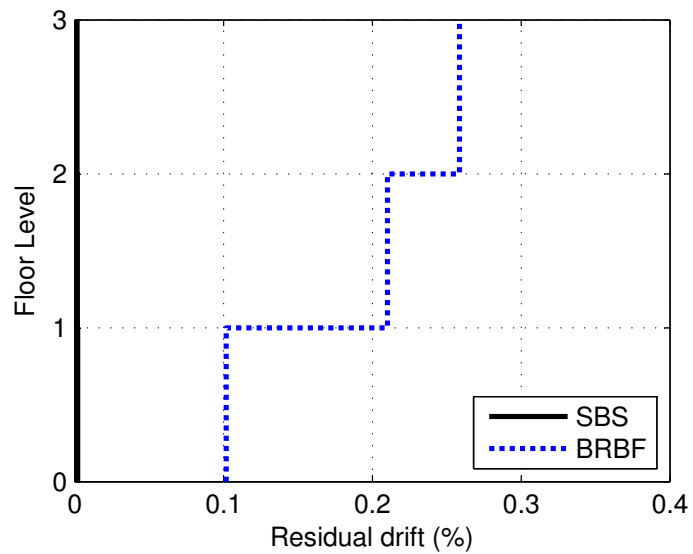
Figure D.2: Residual inter-story drift on the 3-story building under the (2/50) ground motions
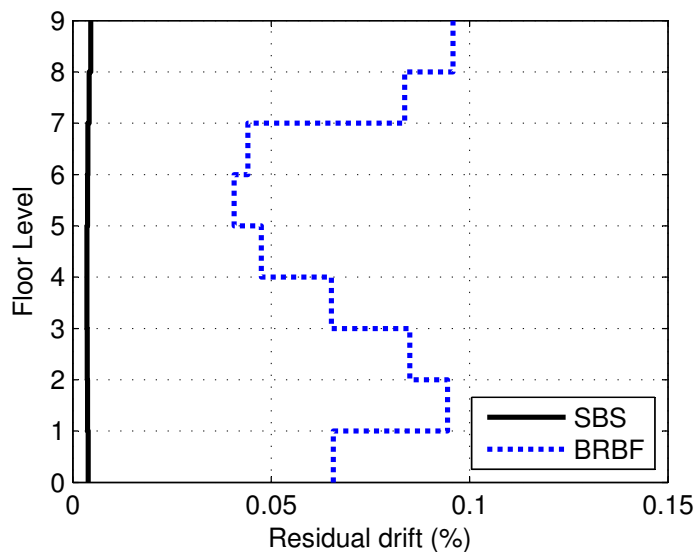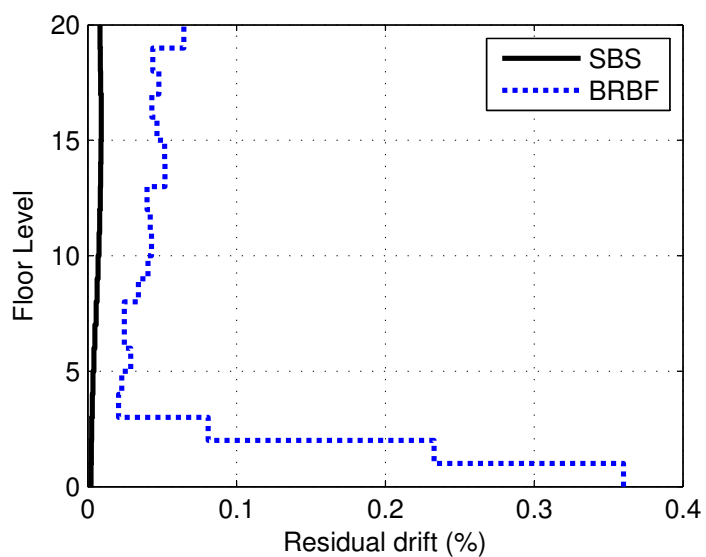
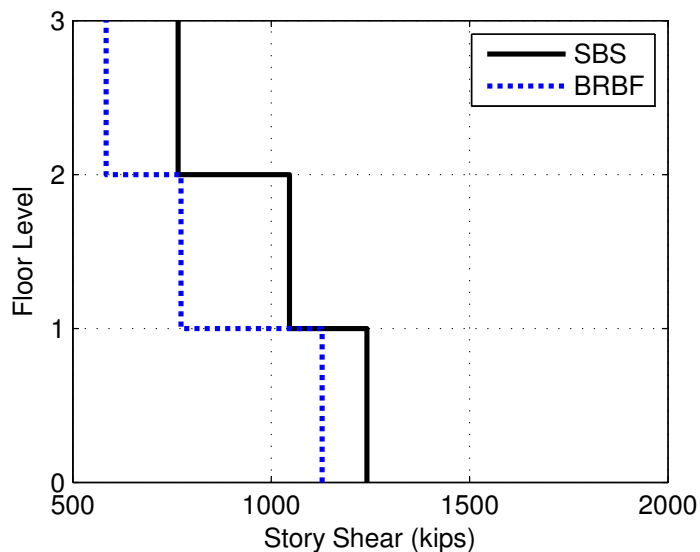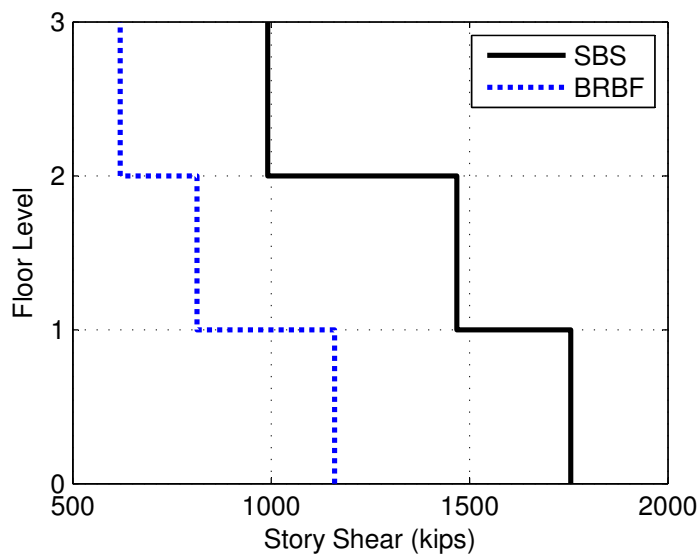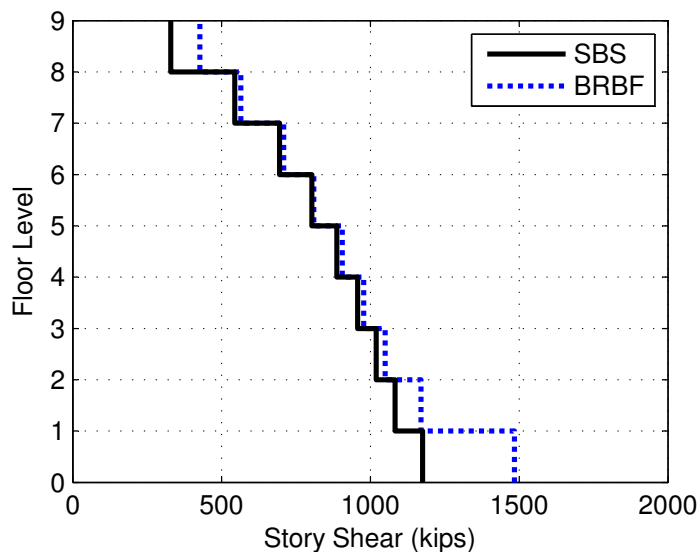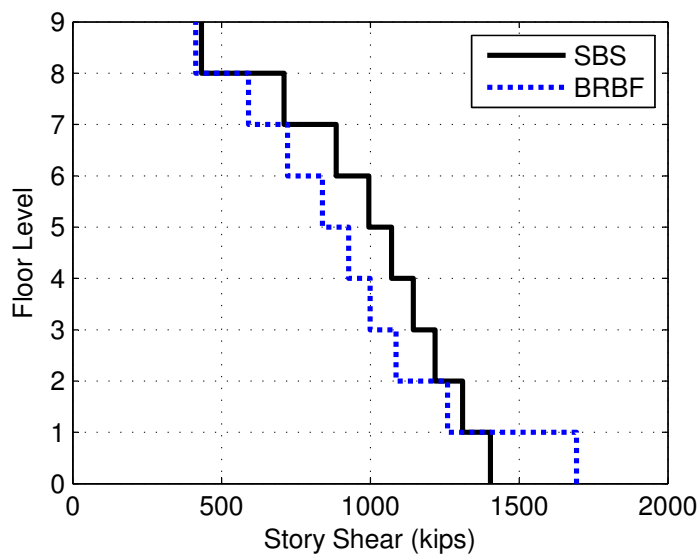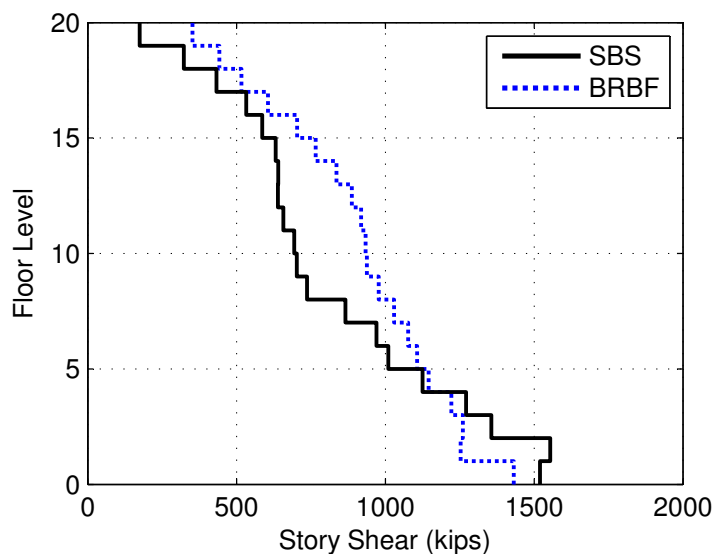**Figure D.3:** Residual inter-story drift on the 9-story building under the (10/50) ground motions
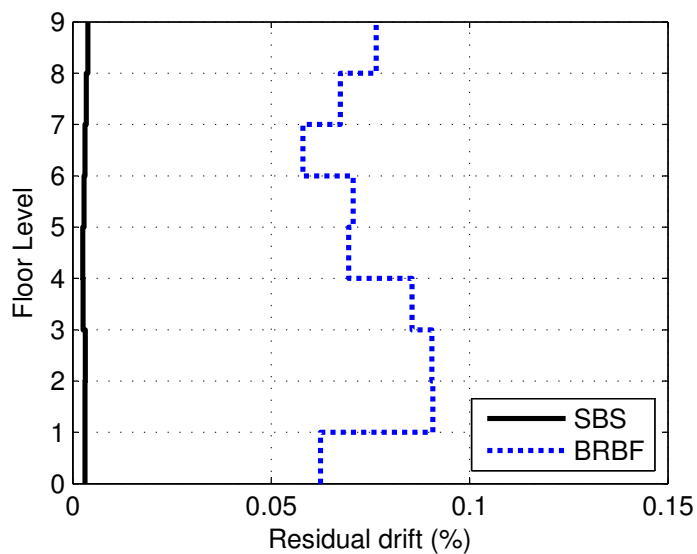
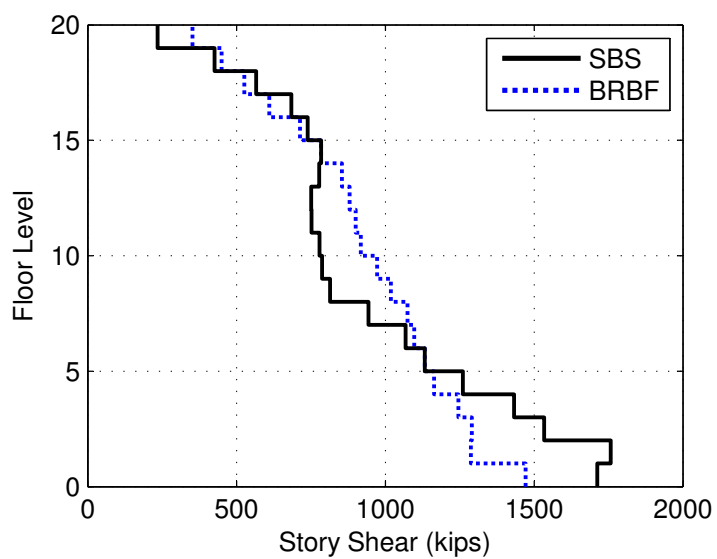**Figure D.4:** Residual inter-story drift on the 9-story building under the (2/50) ground motions
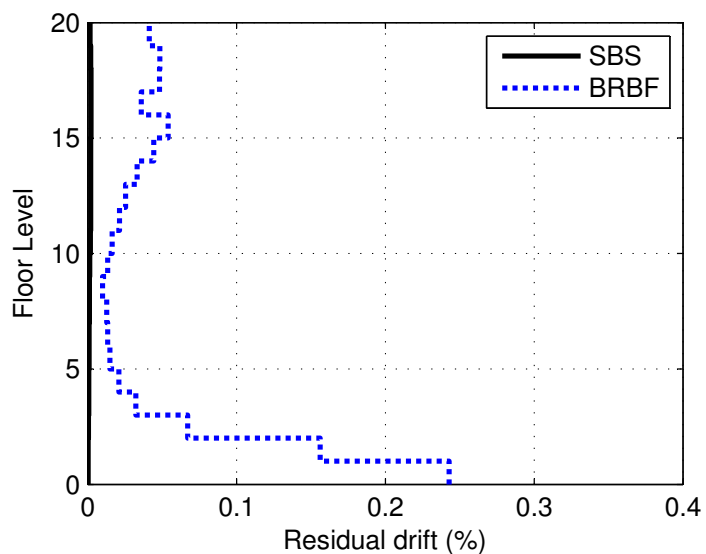
Figure D.5: Residual inter-story drift on the 20-story building under the (10/50) ground motions

Figure D.6: Residual inter-story drift on the 20-story building under the (2/50) ground motions

Figure D.7: Median inter-story shear on the 3-story building under the (10/50) ground motions
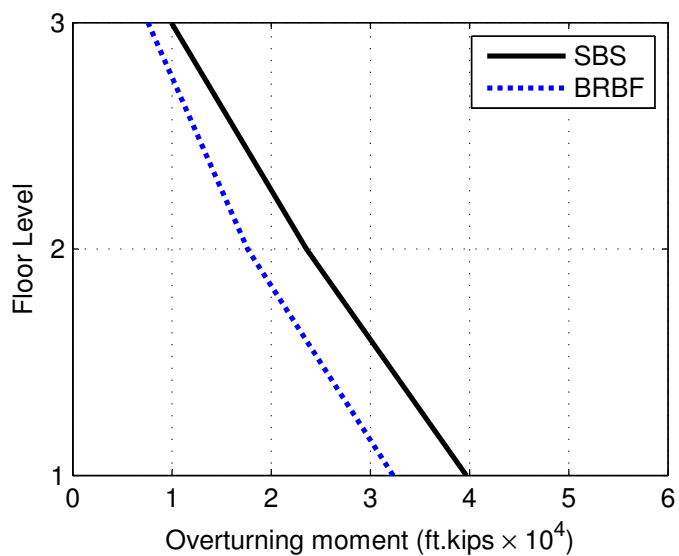

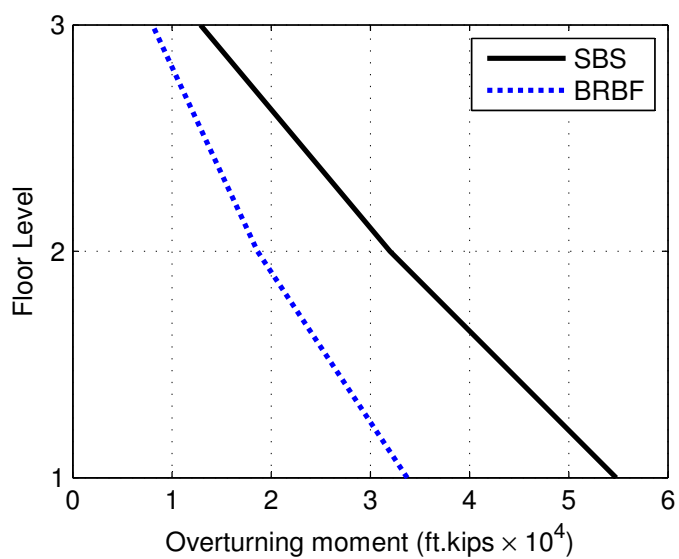**Figure D.8:** Median inter-story shear on the 3-story building under the (2/50) ground motions

Figure D.9: Median inter-story shear on the 9-story building under the (10/50) ground motions

Figure D.10: Median inter-story shear on the 9-story building under the (2/50) ground motions

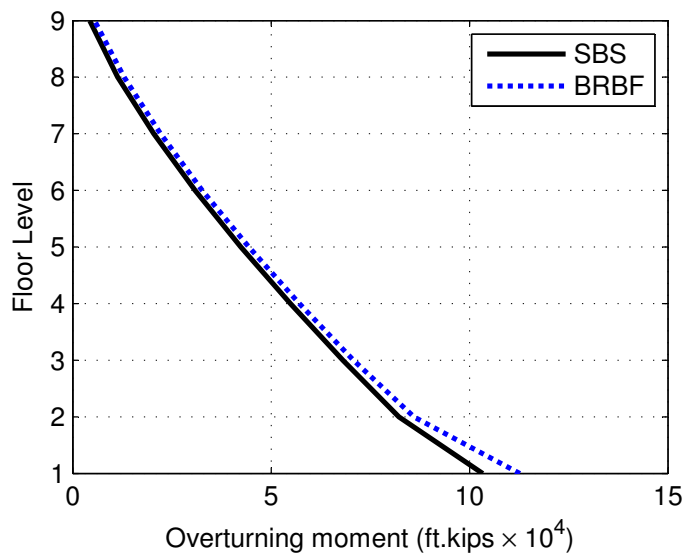**Figure D.11:** Median inter-story shear on the 20-story building under the (10/50) ground motions

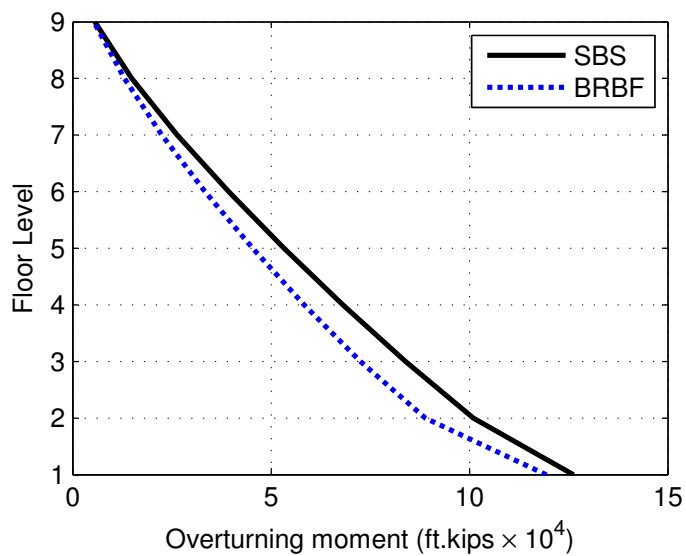**Figure D.12:** Median inter-story shear on the 20-story building under the (2/50) ground motions

Figure D.13: Median overturning moment on the 3-story building under the (10/50) ground motions

Figure D.14: Median overturning moment on the 3-story building under the (2/50) ground motions
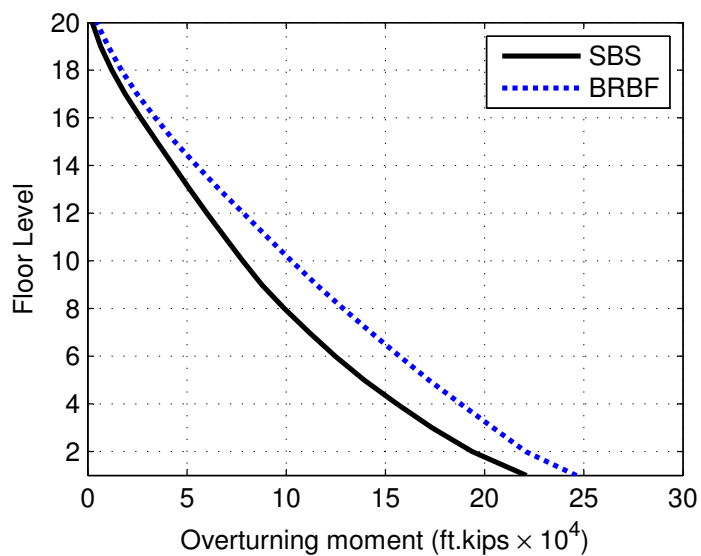
Figure D.15: Median overturning moment on the 9-story building under the (10/50) ground motions
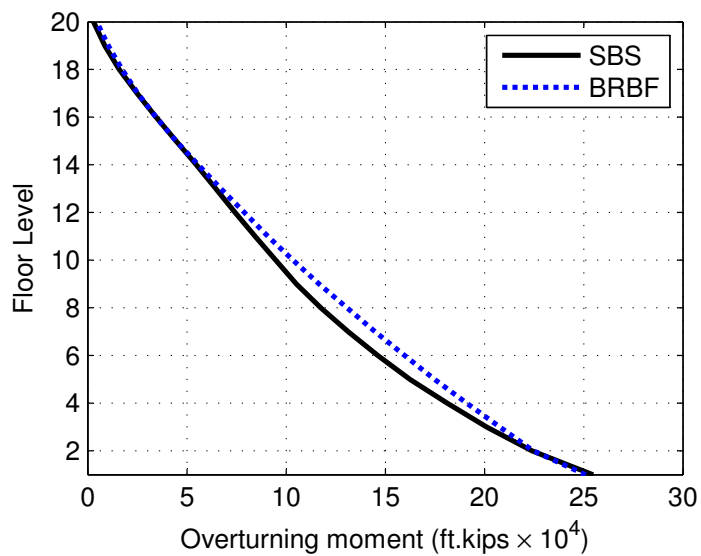

Figure D.16: Median overturning moment on the 9-story building under the (2/50) ground motions

Figure D.17: Median overturning moment on the 20-story building under the (10/50) ground motions

Figure D.18: Median overturning moment on the 20-story building under the (2/50) ground motions